Probing the Cosmic Dawn using the redshifted 21-cm bispectrum

Ph.D. Thesis

by

Mohd Kamran

Department of Astronomy, Astrophysics and Space Engineering, Indian Institute of Technology Indore, Khandwa Road, Simrol, Indore - 453552, India

Probing the Cosmic Dawn using the redshifted 21-cm bispectrum

A THESIS

Submitted in partial fulfillment of the requirements for the award of the degree

of

DOCTOR OF PHILOSOPHY

by

Mohd Kamran

Department of Astronomy, Astrophysics and Space Engineering, Indian Institute of Technology Indore, Khandwa Road, Simrol, Indore - 453552, India

INDIAN INSTITUTE OF TECHNOLOGY INDORE

I hereby certify that the work which is being presented in the thesis entitled **PROBING THE COSMIC DAWN USING THE REDSHIFTED 21-cm BISPECTRUM** in the partial fulfillment of the requirements for the award of the degree of **DOCTOR OF PHILOSOPHY** and submitted in the **DEPARTMENT OF ASTRONOMY, ASTROPHYSICS AND SPACE ENGINEERING, Indian Institute of Technology Indore**, is an authentic record of my own work carried out during the time period from July 2018 to November 2022 under the supervision of Dr. Suman Majumdar, Associate Professor, Department of Astronomy, Astrophysics and Space Engineering, Indian Institute of Technology Indore.

The matter presented in this thesis has not been submitted by me for the award of any other degree of this or any other institute.

Mohd-Kamran

29/11/2022

MOHD KAMRAN

This is to certify that the above statement made by the candidate is correct to the best of our knowledge.

Suman Majumdar

Signature of Thesis Supervisor with date

Dr. SUMAN MAJUMDAR

MOHD KAMRAN has successfully given his Ph.D. Oral Examination held on **18/11/2022**.

Suman Majumdar

Signature of Thesis Supervisor with date

Dr. SUMAN MAJUMDAR

Dedicated

to

My Family

Acknowledgements

Firstly, I am highly grateful to my supervisor Dr. Suman Majumdar for the continuous professional and personal support during my PhD. His guidance helped me a lot in order to understand how to do research and become an independent researcher over the years. I really could not have imagined having a better advisor for my PhD. I had done my M.Sc. in Physics with specialization in atomic and molecular spectroscopy. Therefore, when I joined the Astronomy PhD programme at IIT Indore, I had very little knowledge about astrophysics and cosmology. My supervisor started to teach me these subjects from the very basics, for example, the definition of cosmology and the Big Bang. During my first year, he gave me the freedom to know the basic premises of this research domain. This helped me to do a thorough literature survey. His tireless support and guidance shaped my knowledge and understanding of the subject over the years. He helped me even in improving my writing skills which has given me the confidence to write various research articles as well as this thesis. Additionally, he continuously guided me in improving my presentation skills as well. Apart from studies, we regularly used to have discussions and debates over various diverse topics. We used to go for long walks, buy vegetables and occasionally go for lunch and dinner in various good restaurants in Indore.

I would like to thanks my PSPC committee members Prof. Abhirup Datta, Dr. Somaditya Sen and Dr. Bhargav Vaidya for serving as my committee members even at hardship. I would also like to thank all of my collaborators – Dr. Raghunath Ghara, Prof. Somnath Bharadwaj, Prof. Garrelt Mellema, Dr. Jonathan R. Pritchard, Dr. Rajesh Mondal, Prof. Ilian T. Iliev for their contribution in my research. I would also like to thank M.Sc. students Anchal Saxena, Himanshu Tiwari and Aadarsh Pathak, whom I have partially supervised in their year long projects and with whom I have co-authored several journal articles.

I also thank the Indian Institute of Technology, Indore (IIT Indore) for providing the necessary computing facilities for my work and constant support during my PhD period. I would like to thank SKA-India for providing financial help to attend national and international conferences. I would like to thank the Ministry of Education (ME), Govt. of India for the financial support in the form of my PhD fellowship.

I started my PhD journey at IIT Indore with eight of my friends and this four years long journey would otherwise would have been impossible without the presence of my batch-mates Sayan Kundu, Sarvesh Mangla, Sriyasriti Acharya, Akriti Sinha, Unnati Kashyap, Parul Janagal, Sanmoy Bandopadhyay. During the first year of my PhD, I cherished a wonderful cohabitation with Sayan Kundu and Sarvesh Mangla. I thank Sriya for introducing us to the delicious vegetarian food at 'Sreemaya'.

I must thank all the friends in our department- Arnab Chakraborty, Madhurima Choudhury, Sumanjit Chakraborty, Ramij Raja, Majidul Rahman, Althaf A., Aishrila Mazumder, Deepthi Ayyagari, Swarna Chatterjee, Arghyadeep Paul, Harsha Avinash Tanti, Hemapriya R., Sanmoy Bandyopadhyay, Chandrani Chatterjee, Soumen Datta for maintaining a vibrant and friendly atmosphere in the department. A special thanks go to Sumanjit for the help regarding the LaTex template for the thesis and synopsis, which made my thesis writing easy. I would also like to give a special thanks to Abinash Kumar Shaw for providing me with a necessary plot and an illustration that helped me in elaborating the concepts. I would like to thank Chandrashekhar Murmu, Saswata Dasgupta, and Sohini Dutta for giving constructive input on my thesis.

Abstract

In the evolutionary history of our Universe, the Cosmic Dawn and Epoch of reionization (CD-EoR) is the period when the formation and evolution of the very first luminous sources took place. These first sources transitioned the state of the Universe from cold and neutral to a fully heated and ionized one. This particular phase of the Universe is largely untested via observations and thus at present we have very little insight about it. The 21-cm radiation, produced by the spin-flip transition of the electron-proton system in the 1s ground state of neutral hydrogen atom (HI), which is abundant in the inter-galactic medium (IGM), is the direct tracer of heating and ionization processes in the IGM during the CD-EoR era. This highly redshifted (cosmological) and extremely feeble signal coming from the CD-EoR is yet to be confirmatively detected via the presently operating radio telescopes. Future radio interferometric surveys with the upcoming Square Kilometre Array (SKA) are expected to be sensitive enough to detect the redshifted 21-cm signal from the CD-EoR both via Fourier statistics and tomographic images. Most of the present generation telescopes, with which imaging is almost impossible, have been trying to detect the fluctuations in this signal mainly using Fourier statistics e.g. the power spectrum. The power spectrum provides a complete statistical description of a field if it is Gaussian random in nature. However, CD-EoR 21-cm fluctuations are expected to be highly non-Gaussian. This non-Gaussianity arises and evolves with time as the heated and ionized regions form, grow, and percolate with each other during this period in the IGM. The power spectrum cannot probe this intrinsic and time-evolving non-Gaussianity. The bispectrum, being a potential probe of this non-Gaussianity, provides an opening for a comprehensive and correct interpretation of this signal. The bispectrum, in principle, can be estimated through the product of the Fourier transform of this signal for groups of three different wave numbers in the Fourier space which form closed triangles (aka k-triangle). Such higher-order statistics like the bispectrum can be detected and can also be potentially used for constraining models of CD-EoR via future SKA observations thanks to its high expected sensitivity. It is, therefore, worthwhile to develop tools to analyze and correctly interpret the CD-EoR 21-cm signal via these sophisticated statistics before the SKA becomes operational. This doctoral thesis mainly focuses on modeling and simulat-

ing the redshifted 21-cm signal observables from the CD-EoR and their statistical and physical interpretation using the bispectrum. This thesis, for the first time, presents a comprehensive and correct understanding of the CD-EoR 21-cm signal bispectrum by estimating it for triangles of all possible unique shapes and sizes in the k-space. Previous studies in the literature have considered only a few special shapes of k-triangles for the analysis of the bispectra. This thesis demonstrates that the 21-cm bispectra are non-zero for most of the triangle shapes and sizes during the entire period of the CD-EoR. This firmly establishes the high non-Gaussianity of the CD-EoR 21-cm signal. We further investigate the impact of a line of sight (LoS) anisotropy arising due to the peculiar velocity of the HI gas along the LoS direction i.e. the redshift space distortion (RSD) on the signal bispectrum. Our analysis shows that the effect of the RSD anisotropy is significant on the bispectrum magnitude and sign. We also investigate the impact of different heating sources such as mini quasars (mini-QSO) and high mass X-ray binaries (HMXB) on the 21-cm bispectrum. We observe that the redshift evolution of the bispectrum magnitude and sign follow a generic trend for both source models. For example, the redshift evolution of the bispectrum for each source model goes through two consecutive sign changes at large scales ($k_1 \sim 0.16\,\mathrm{Mpc}^{-1}$). Further, we also present an extensive analysis to connect this large-scale bispectrum's redshift evolution with two dominant IGM physical processes during CD; Lyα coupling and X-ray heating. We demonstrate that the magnitude, the sign and the sequence of sign changes in the 21-cm bispectrum can uniquely disentangle the effect of these dominant physical processes in the IGM. We further check the robustness of these features in the large-scale 21-cm bispectrum by considering various radiating sources during CD, having different source properties (parameters). We conclude that it is important to study the sequence of sign changes along with the variations in the shape and magnitude of the bispectrum throughout the CD history to arrive at a robust conclusion about the dominant IGM processes at different cosmic times.

List of Publications

Publications in peer-reviewed journals.
arXiv: http://arxiv.org/a/kamran_m_1
Google Scholar: https://scholar.google.com/citations?user=Ge5YN6wAAAAJ&hl=en&oi=ao

1. †**Kamran M.**, Ghara R., Majumdar S., Mellema G., Bharadwaj S., Pritchard J. R., Mondal R., Iliev I. T., *Redshifted 21-cm bispectrum: Impact of the source models on the signal and IGM physics from the Cosmic Dawn*, submitted to Journal of Cosmology and Astroparticle Physics; arXiv:2207.09128

   Contribution: I have formulated the problem, did the data analysis, made all of the plots, drawn most of the conclusions and written most of the manuscript.

2. Shaw A. K., Chakraborty A., **Kamran M.**, Ghara R., Choudhuri S., Ali S. S., Pal S., Ghosh A., Kumar J., Dutta P., Sarkar A. K., *Probing early universe through redshifted 21-cm signal: Modelling and observational challenges*: A review, Accepted in Journal of Astrophysics and Astronomy

   Contribution: I contributed to the theory portions of this review article and wrote three sections.

3. Pahak A., Bag S., Majumdar S., Mondal R., **Kamran M.**, Sarkar P., *Distinguishing reionization source models using the largest cluster statistics on the 21-cm maps*, Submitted to Journal of Cosmology and Astroparticle Physics; arXiv:2202.03701v2

   Contribution: I have written some of the data analysis codes, contributed in the data analysis partially, and wrote a section of the paper.

4. †**Kamran M.**, Majumdar S., Ghara R., Mellema G., Bharadwaj S., Pritchard J. R., Mondal R., Iliev I. T., *Probing IGM Physics during Cosmic Dawn using the Redshifted 21-cm Bispectrum*, Submitted to **Phys. Rev. Lett.**, arXiv:2108.08201v2

   Contribution: I have contributed in formulating the problem, designing the simulations, analysis of the simulated data and derivations of the analytical models for interpretation of the simulated statistics. I have also generated all of the plots and have written most of the paper.

5. Tiwari H., Shaw A. K., Majumdar S., **Kamran M.**, Choudhury M., *Improving constraints on the reionization parameters using 21-cm bispectrum*, Submitted to **Journal of Cosmology and Astroparticle Physics**, Volume 2022, Issue 04, April 2022, id.045, 27 pp., DOI: https://iopscience.iop.org/article/10.1088/1475-7516/2022/04/045, arXiv:2108.07279

   Contribution: Helped with the simulations and analysis of the simulated data and their interpretation.

6. Mondal R., Mellema G., Shaw A. K., **Kamran M.**, Majumdar S., *The Epoch of Reionization 21-cm Bispectrum – I: The impact of light-cone effects and detectability*, accepted in **Monthly Notices of the Royal Astronomical Society**, Volume 508, Issue 3, December 2021, pp.3848-3859, DOI: https://doi.org/10.1093/mnras/stab2900, arXiv:2107.02668v2

   Contribution: Cross-checked the new algorithm presented in this paper to calculate the bispectrum and helped in the analysis and interpretation of the data, and wrote a section of the paper.

7. †**Kamran M.**, Ghara R., Majumdar S., Mondal R., Mellema G., Bharadwaj S., Pritchard J. R., Iliev I. T., *Redshifted 21-cm bispectrum – II. Impact of the spin temperature fluctuations and redshift space distortions on the signal from the Cosmic Dawn*, **Monthly Notices of the Royal Astronomical Society**, Volume 502, Issue 3, April 2021, p.3800–3813, DOI: 10.1093/mnras/stab216, arXiv:2012.11616

   Contribution: Contributed significantly in the formulation of the problem, helped in designing the simulations, analyzed all of the simulated data, developed the physical interpretation of the results, generated all of the plots and wrote most of the article.

8. †Majumdar S., **Kamran M.**, Pritchard J. R., Mondal R., Mazumdar A., Bharadwaj S., Mellema G. *Redshifted 21-cm bispectrum – I. Impact of the redshift space distortions on the signal from the Epoch of Reionization*, **Monthly Notices of the Royal Astronomical Society**, Volume 499, Issue 4, December 2020, p.5090–5106, DOI: 10.1093/mnras/staa3168, arXiv:2007.06584

   Contribution: Cross-checked the bispectrum estimation, derived an analytical model to predict the bispectrum behaviour, and wrote a significant portion of the paper.

9. Saxena A., Majumdar S., **Kamran M.**, Viel M., *Impact of dark matter models on the EoR 21-cm signal bispectrum*,**Monthly Notices of the Royal Astronomical**

Society, Volume 497, Issue 3, September 2020, p.2941–2953, DOI: 10.1093/mnras/staa1768 , arXiv:2004.04808

Contribution: Helped with the simulations and the data analysis.

Note: Publications 1, 4, 7 and 8 (marked with †) constitutes four main chapters of this thesis.

Table of Contents

List of Figures

List of Tables

List of abbreviations

HBB	Hot Big Bang
GUT	Grand Unification Theory
BBN	Big Bang Nucleosynthesis
CMB	Cosmic Microwave Background
CMBR	Cosmic Microwave Background Radiation
DA	Dark Age
CD	Cosmic Dawn
EoR	Epoch of Reionization
IGM	Intergalactic Medium
HI	Neutral Hydrogen
HII	Ionized Hydrogen
HeI	Neutral Helium
HeII	Singly Ionized Helium
LSS	Large Scale Structures
ISM	Interstellar Medium
C^2RAY	Conservative, Casual Ray – tracing
CC	Coeval Cube
LC	Light – cone
GMRT	Giant Metrewave Radio Telescope
LOFAR	Low Frequency Array
MWA	Murchison Widefield Array
HERA	Hydrogen Epoch of Reionization Array
PAPER	Precision Array for Probing Epoch of Reionization
SKA	Square Kilometre Array
EDGES	Experiment to Detect the Global EoR Signature
SARAS	Shaped Antenna measurement of the background RAdio Spectrum
RSD	Redshift Space Distortion
SFR	Star Formation Rate

Lyα	Lyman Alpha
QSO	Quasi – Stellar Object
HMXB	High Mass X – ray Binary
SED	Spectral Energy Density
NAOJ	National Astronomical Observatory of Japan
SNR	Signal to Noise Ratio
RT	Radiative Transfer
WMAP	Wilkinson Microwave Anisotropy Probe
Mpc	Megaparsecs
CDM	Cold Dark Matter
LoS	Line of Sight
AP	Alcock – Paczynski
HMF	Halo Mass Function
RFI	Radio Frequency Interference
FWHM	Full Width at Half Maximum
MAPS	Multi – frequency Angular Power Spectrum
PM	Particle – Mesh
FoF	Friends – of – Friend
UV	Ultraviolet

Chapter 1

Introduction

1.1 Brief history of our Universe

Cosmology is the study of the Universe as a whole, specifically the history of our Universe's origin and evolution. Humankind has always been curious about the constituents of our Universe and its history. In ancient times, humans theistically believed that some supernatural forces are responsible for the origin and the present state of the Universe as they could perceive it. Over the years, through gradual observations and refinement in modeling and interpreting the observations, it has been possible to arrive at the presently accepted understanding of our Universe [6]. During the last few decades, thanks to the availability of an enormous amount of observational data and sophisticated statistical tools, cosmology has entered into the era of precision cosmology. At present, it is possible to not only pin down the most favoured cosmological model based on various observations, but it is also possible to constrain the parameters of this model at the level of less than a percent, which was unthinkable only a few decades ago. Among the various models of the Universe's origin, the most prevailing and widely accepted one (that aligns well with the available observations till now) is the so-called "Hot Big Bang" (HBB) model.

According to the HBB model, ~ 13.6 billion years ago, the Universe around us today was in the form of a very hot ($T \approx 10^{32}$ K) and dense tiny ball of energy. Since the Big Bang, the Universe has been expanding and cooling till today. Figure 1.1 illustrates how our Universe has evolved from Big Bang to the present day. It is widely believed that the quantum fluctuations in energy fueled the birth of our Universe. These fluctuations grew

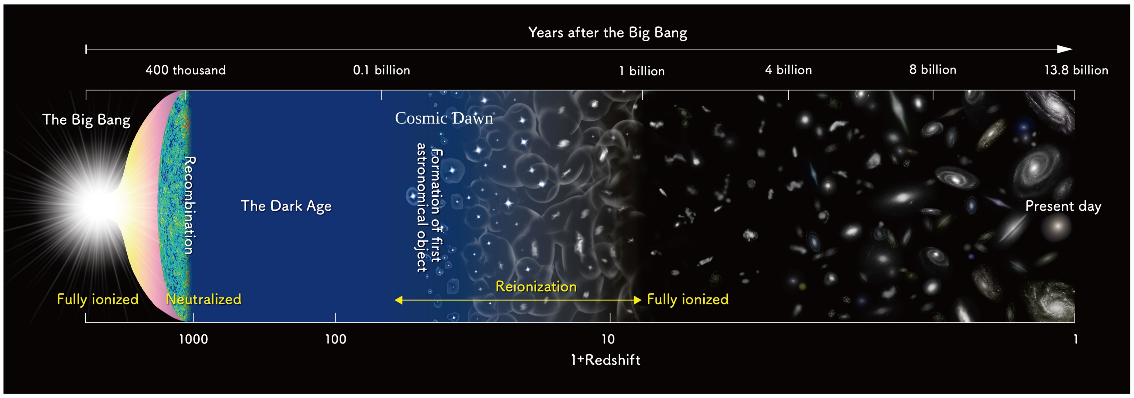

Figure 1.1: Artist impression of the evolutionary history of our Universe from Big Bang to present day. Image credit: NAOJ.

to form the Universe's present-day structures. The Universe, before reaching the current stage, has gone through several distinct eras. Many observations over the years have confirmed the presence of a few among these eras. The very first moment ($t_{\rm age} = 0$–10^{-43} seconds) was the Planck era, where all four known fundamental forces were united into a single force. This era could not be explained physically so far due to our limited current understanding of physics. Right after the Planck era, gravitational force decoupled, and space-time formed. The Universe entered into the GUT (Grand Unification Theory) era ($t_{\rm age} = 10^{-43}$–10^{-35} seconds), where the rest three forces were still united to a single Grand Unified force. Near the end of the GUT era, the Universe cooled enough that the strong nuclear force began to decouple. This transition produced a tremendous amount of energy that perhaps caused the space to undergo a rapid expansion, i.e., cosmic inflation [7]. Consequently, the Universe cooled off to a temperature $T \approx 10^{27}$ K. Right after the inflation, the Universe entered the electroweak era ($t_{\rm age} = 10^{-35}$–10^{-10} seconds), where electromagnetic and weak nuclear forces were still united. By the end of this era, the Universe cooled below the temperature $T \approx 10^{15}$ K, and the remaining two forces became distinct.

The decoupling of these four fundamental forces allowed the Universe to enter the era of elementary particle formation and "Big Bang Nucleosynthesis" (BBN). In these eras, the baryonic matters such as leptons, quarks and then the nuclei of the light elements began to form via nuclear fusion. The BBN era continued until the age of the Universe was $t_{\rm age} = 3$ Minutes [8]. From the beginning of BBN, the temperature of the Universe was so low ($T \approx 10^{12}$ K) that nucleosynthesis of only lightweight elements, such as hydrogen, helium, etc., could take place. The nucleosynthesis formed $\sim 75\%$ of hydrogen nucleus, i.e., proton, $\sim 25\%$ of the helium nucleus, and a tiny amount of heavier elements, mostly lithium. These nuclei could not collect the free electrons to form stable atoms during early times. The Universe, therefore, was fully ionized until the temperature of the Universe achieved a value $T \approx 3700$ K at the age of $t_{\rm age} \approx 0.25$ Myr. The electrons then began recombining with hydrogen and helium nuclei to form the neutral hydrogen (HI) and helium (HeI) atoms. The Universe consequently began to make a gradual phase transition from opaque to transparent. The recombination process continued with this phase transition until the last scattering ($t_{\rm age} \approx 0.4$ Myr) of the photons took place at temperature $T \approx 3000$ K, where these photons became completely decoupled from the matter to traverse the entire Universe. Due to the expansion of the Universe, the wavelength of this radiation is increased i.e. redshifted to a wavelength that falls in the microwave band of the electromagnetic spectrum. These are the photons we see today as the "Cosmic Microwave Background" (CMB) at a temperature $T_{\rm CMB} \approx 2.7$ K, which is today's average temperature of our Universe. The CMB is the first light in the Universe. One crucial point to keep in mind is that cosmologists deal with the redshift (z) of light rather than the time after the Big Bang ($t_{\rm age}$) at which this light was emitted, as we observe it today. One can directly relate z to $t_{\rm age}$ [9]. The higher the redshift of observation, the farther we will look back in time in cosmic history. From Big Bang to present day, the redshift decreases from infinity to zero.

After the last scattering (around $z \sim 1100$), the Universe became almost neutral and transparent to observations. However, the signals from this era are too feeble to observe via the current generation telescopes. The Universe, therefore, became dark and stayed in this state until the birth of the first luminous objects took place. This era is known as the "Dark Age" (DA: $1100 > z > 30$) [10, 11]. This is because no luminous sources were present in this era. We believe that the CMB, dark matter, dark energy, and baryonic matters in the form of atoms and electrons were the major components of the DA. Our present knowledge about dark matter and dark energy is significantly less. However, both components are essential in order to explain a number of events in our Universe. For example, one may ask if the structures we see today were formed at random locations? From the beginning of the DA, the distribution of the matter was non-uniform in the Universe. There were inhomogeneities in the matter density produced by the quantum fluctuations during the inflation, the imprints of which have been observed in the CMB maps. The baryonic matters fell into the gravitational potential wells formed by the over-dense regions of the dark matter. The regions with dark matter concentrations are known as the dark matter halos. The density fluctuations of the gas inside the dark matter halos due to the gravitational instability gradually grew to create collapsed objects (stars, galaxies, etc.). These collapsed objects thus are formed at biased locations. Several observations have confirmed that the galaxies are formed within dark matter halos [12,13].

The advent of the first luminous sources ended the DA and marked the onset of a new epoch, the so-called "Cosmic Dawn" (CD: $30 > z > 15$). These sources started emitting the radiations of different wavelengths that fall into the various bands of the electromagnetic spectrum such as X-ray and Ultra-Violet (UV) radiations [14, 15]. During CD, the X-ray caused a change in the thermal state of the entire intergalactic medium (IGM) from cold to uniformly heated one [16, 17]. When the whole IGM was about to be heated, the UV radiation with energies above 13.6 eV predominately began to ionize the HI surrounding the radiating sources [1, 10, 17]. The ionization process marked the onset of the new epoch, the so-called "Epoch of Reionization" (EoR). The EoR continued until the entire IGM got almost fully ionized from the completely neutral one. Various indirect observations suggest that the EoR spanned over a broad redshift range of $15 > z > 6$. As per findings of the low-redshift ($z < 6$) observations, in the post-EoR era, the amount of the HI is significantly less and has a very small value of the average fraction of HI ($\bar{x}_{\rm HI}$) in the IGM i.e. $\bar{x}_{\rm HI} \sim 10^{-4}$ [18]. During post-EoR, the HI is residing inside the galaxies or interstellar medium (ISM) in the form of a highly dense cloud that self-shields itself from the ionizing background. This thesis mainly focuses on the fundamental issues related to the formation and evolution of a variety of the first sources during Cosmic Dawn and Epoch of Reionization (CD-EoR) and on how the radiations from these sources impact the IGM through a number of astrophysical processes.

1.2 First sources during CD-EoR

The stars, galaxies, quasars, etc. are the very first sources during CD-EoR [19]. As stated in Section 1.1, the formation and evolution of these sources caused the changes in the thermal and ionization states of the IGM during this era [1, 20, 21]. It is widely accepted that the star-forming galaxies during CD-EoR are the primary source of HI ionization in the IGM (see e.g. [22, 23]). These galaxies are formed in the dark matter halos after the collapse of the gas inside these halos. The gas needs to cool down below a certain temperature known as the "virial temperature" ($T_{\rm vir}$), before it can collapse. For this cooling, the collapsing gas must have its mass above a specific cut-off known as the "Jeans mass". This is not possible in very low-mass halos ($M_{\rm halo} < 10^6 M_\odot$). Thus, only halos having mass above a certain threshold ($M_{\rm halo,min}$) are expected to host luminous sources as they attain a virial temperature $T_{\rm vir} \geq 10^4$ K required to cool and collapse the atomic hydrogen to form stars [24]. The corresponding cut-off mass satisfying the virial criterion is $M_{\rm halo,min} \sim 10^8\, M_\odot$. Additionally, the low mass halos ($10^6 M_\odot \lesssim M_{\rm halo} \lesssim 10^8 M_\odot$) can host stars formed via molecular hydrogen cooling, which requires $T_{\rm vir} \sim 300\,\mathrm{K}$. Thus, the stellar mass of a galaxy (M_*) is expected to have a relationship with the mass of the corresponding halo. This relationship is given by,

$$M_* = f_* \left(\frac{\Omega_{\rm B}}{\Omega_{\rm m}}\right) M_{\rm halo}\,, \tag{1.1}$$

where where f_* is the fraction of baryons within the stars in a galaxy. $\Omega_{\rm B}$ and $\Omega_{\rm m}$ respectively are the baryon density and matter density parameters.

Presence of metals in the ISM lead to faster cooling compared to the cooling mechanism via atomic or molecular line transitions in lighter elements. Metals, having a large number of energy states, can absorb the energy of the gas cloud to make transitions between these energy states that result in the cooling of the gas [25]. Thus, the collapse of metal-poor gas will be delayed compared to metal-rich gas. The stars in the first galaxies are expected to be metal deficient [26, 27]. They are only supposed to have light elements, which do not provide the effective cooling of the gas due to having a few energy states. However, these stars are believed to be short-lived [28] and eventually dies via supernova explosion. The supernova produces heavier elements in the ISM via nuclear fusion to make it metal-enriched. This subsequently catalyzes the star formation rate. It is widely believed that the stars in the galaxies produce UV photons. The mean free path ($R_{\rm mfp}$) of the UV photons decides the typical size of the ionized regions around the radiating sources. The UV photons have a small mean free path, which causes the photo-ionization of HI in the IGM. Note that these sources ionize only HI and HeI; however, they do not contribute significantly to HeII ionization and heating of the IGM.

The cooling rate thus directly controls the star formation rates (SFRs) and hence the rate of UV photon production. The production rate of the UV ionizing photons ($\dot{n}$) is given by

$$\dot{n} = f_{\rm esc} \rho_{\rm SFR} \xi_{\rm ion}\,, \tag{1.2}$$

where $f_{\rm esc}$ is the fraction of UV ionizing photons escaping into the IGM ([15]), $\rho_{\rm SFR}$ is the density of SFR, and $\xi_{\rm ion}$ represents the number of photons produced per unit time per unit SFR. The period of the EoR (aka reionization history) is constrained via the history of the SFRs of the early galaxies [29]. The precise estimation of the $f_{\rm esc}$ is required for a better constraint on the reionization history (e.g. [30]).

The first galaxies are also likely to have the supermassive or intermediate mass of accreting black holes at their centers, behaving as mini-quasars (mini-QSOs) [31–34]. The mini-QSOs majorly produce soft X-ray photons with a large mean free path. Due to this, the

X-ray photons interact with the IGM to heat and partially ionize the IGM gas. However, the mini-QSOs would have been less abundant in the early universe ($z > 7$) [35, 36]. The most distant quasars that could have been discovered are at $z = 7.642$ [37]. The quasars are thus believed to be abundant sufficiently at lower redshifts. The second ionization of the helium took place due to the high energy radiations from these quasars, which led to the helium reionization to be completed around redshift $z \sim 2.7$ [38–45]. Note that in this thesis, we consider the ionization of only HI atoms, which are diffused in the IGM.

Furthermore, the galaxies with a high star formation rate are likely towards the formation of binary systems such as the high mass X-ray binaries (HMXBs) [46, 47]. These binary sources also produce an ample amount of hard X-ray photons. These radiating sources interact with the IGM differently than the mini-QSOs, depending on the relative abundances and the energies of photons produced by them. The physical states of diffused HI in the IGM during CD-EoR thus will depend on source properties. These source properties strongly depend on the different types of sources and the parameter values related to each source. Among a number of different X-ray sources, the HMXBs would have been the most abundant X-ray sources during CD-EoR. The high-energy X-ray photons from these sources can easily escape from their host galaxies to travel large distances in the IGM. While traveling, it will be redshifted to the lower frequencies corresponding to the ionizing photons. Consequently, it will ionize the under-dense regions in the IGM partially [48]. In the meantime during their journey, these photons predominately heat the IGM. Thus, for the HI atoms in the IGM to be photo-ionized, the UV photons are more efficient than the X-ray photons. However, the X-ray photons are more effective in heating the gas throughout the IGM.

Here arises a question: Which among the two IGM processes, X-ray heating and UV photo-ionization, is expected to be dominant in the first phase of the CD-EoR? At high redshifts, the gas density in the IGM is very high to be able to be ionized via UV photons. In contrast, the X-ray photons with a large mean free path can easily pass through the IGM and gradually heat the IGM gas. The X-ray heating is thus believed to be dominated earlier than the UV photo-ionization.

In our models of the CD-EoR, the parameter related to the radiating sources directly controlling the intensity of X-ray photons from these sources is $f_{\rm X}$. It is known as the efficiency parameter of X-ray photon production. If the UV spectrum lies in the range $E^{\rm i}_{\rm UV}$ to $E^{\rm f}_{\rm UV}$ and the X-ray spectrum in the range $E^{\rm i}_{\rm X-ray}$ to $E^{\rm f}_{\rm X-ray}$, then the $f_{\rm X}$ can be defined as ratio of the X-ray luminosity to the UV luminosity from the radiating sources

$$f_{\rm X} = \frac{\int_{E^{\rm i}_{\rm X-ray}}^{E^{\rm f}_{\rm X-ray}} I(E)\, dE}{\int_{E^{\rm i}_{\rm UV}}^{E^{\rm f}_{\rm UV}} I(E)\, dE}\,, \tag{1.3}$$

where $I(E)$ is the spectral energy distribution (SED) of the galaxy. In this thesis we consider X-ray from the galaxies to follow the power law SED with a spectral index α:

$$I(E) = AE^{-\alpha}\,, \tag{1.4}$$

where A is the normalization constant that can be computed in terms $f_{\rm X}$ and spectral index α. The parameters $f_{\rm X}$ and α thus determine the X-ray properties of the sources.

A better constraint on the CD-EoR history requires the source models and related parameters to be tightly constrained. This further demands the precise measurements of the cosmological parameters related to our Universe.

1.3 Observational probes of the CD-EoR

Several observations have been performed so far in order to understand how our Universe evolved from the CMB formation to present-day large scale structures (LSS). The maps of the Universe formed by observations of the Cosmic Microwave Background (CMB) from redshift $z \sim 1100$ (see Figure 1.1) provide detailed pictures of the very early phase of our Universe [49–53]. On the other hand, the maps of the distribution of galaxies in the local Universe (at $z \sim 0$) via various galaxy redshift surveys provide information about the present state of our Universe [54–56]. Together they show clear pictures of the LSS in our Universe. However, we know very little about the evolution of the Universe from the CMB formation to the present-day structures. The middle phase, where the first luminous sources were formed and known as the CD-EoR, is little tested by the observations via present generation telescopes; thus we have very little knowledge about it.

A number of indirect observations, such as the Thompson scattering optical depth measurement from CMB [53, 57], high redshift quasar absorption spectra [18, 58, 59], and luminosity function of the Lyman α (Lyα) emitters [60–62], have shaped our knowledge about the CD-EoR up to an extent. However, these indirect observations are unable to resolve many fundamental issues related to the CD-EoR milestones, such as:

- information about the formation and evolution of first luminous sources (stars, galaxies, quasars, etc.) during this period,

- impact of these sources on the IGM,
- topology of the heated and ionized regions formed in the IGM by these sources,
- starting and termination points of this era in cosmic time.

Atomic hydrogen (HI) is the most abundant element in our Universe. The 21-cm radiation produced by the spin-flip transition of an electron-proton system in the 1s ground state of HI can be a direct tracer of these major milestones in the CD-EoR era. Due to the expansion of the Universe, this radiation which was emitted at frequency 1420 MHz will be cosmologically redshifted to the lower frequencies ($\nu_{\rm obs} = 1420 {\rm MHz}/(1+z)$) while traveling to the present-day observer from its point of emission in CD-EoR. It thus carries the information about the IGM when it was emitted. The present and next-generations of radio telescopes e.g. GMRT [63], LOFAR [64–67], MWA [68, 69], HERA [70–72], SKA [73, 74] are thus expected to capture the time evolution of this signal by utilizing this feature of the signal. We discuss the HI 21-cm radiation in detail in Section 1.4.

In this thesis, we focus on studying the CD-EoR era, during which the state of the IGM changed from cold and neutral to hot and ionized one, by the first population of the sources. Throughout this thesis we consider a scenario where the redshifted 21-cm radiation can be used as a tool to probe this era.

1.4 CD-EoR 21-cm signal

In the ground state, the HI atom has one electron in 1s orbital and one proton in the nucleus. The magnetic moments (arising due to the spin) of electron and proton interact with each other. This interaction causes the 1s state to split into two different energy levels separated by $\Delta E = 5.9\,\mu eV$ [75]. The high energy state corresponds to the parallel orientation of the electron and proton spin magnetic moments. Similarly, the low energy state corresponds to the anti-parallel direction of their spin magnetic moments. The spin-flip transition of the electron-proton system between these two spin states can be made by the emission or absorption of a photon of wavelength 21-cm or frequency of 1420 MHz in the rest frame of HI atom (e,g. see Figure 1.2).

The lifetime of the anti-parallel spin state of HI atom is $\sim$ 11 Myr. Thus the 21-cm line emission is a rare event. However, there are two privileges with the HI 21-cm signal as a tracer of the CD-EoR. First, most of the baryonic matter ($\sim 75\%$) is in the form

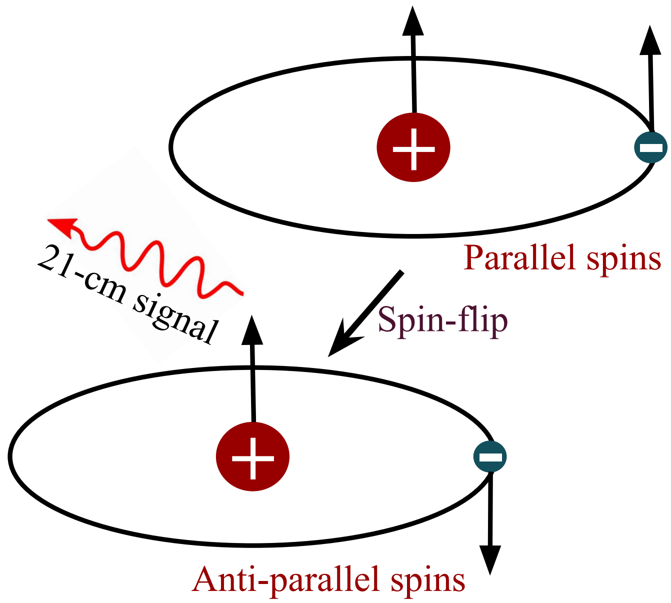

Figure 1.2: A cartoon that shows the spin-flip transition of an electron-proton system in the ground state of the neutral hydrogen atom from parallel (high energy) to anti-parallel (low energy) state. This transition emits a photon of frequency 1420 MHz (or wavelength 21-cm).

of HI. Therefore, the intensity of this signal is expected to be significant enough for the observations. Second, the IGM gas, which interacts with the 21-cm signal while this signal is traveling to the observer from its point of emission in the CD-EoR, is optically thin or transparent. The HI 21-cm signal thus can traverse the medium without being much absorbed. Together, these make the HI 21-cm signal a potential probe of our Universe.

We usually describe the relative population of HI in the two spin states in terms of the spin temperature (T_{S}). The ratio of the number density of HI in parallel (n_1) and anti-parallel (n_0) spin states is given as [76]:

$$\frac{n_1}{n_0} = 3 \exp\left(\frac{-0.068\,\mathrm{K}}{T_{\mathrm{S}}}\right). \tag{1.5}$$

This ratio controls the intensity of the 21-cm radiation from the HI cloud. The T_{S} thus corresponds to the intensity of this radiation. However, the T_{S} being a non-physical entity cannot be connected to the equivalent intensity via Planck's radiation law. Thus, dealing with different sorts of temperatures in radio-astronomy is very convenient than the equivalent intensities.

As the frequency of the 21-cm radiation is very low and additionally it is a part of the

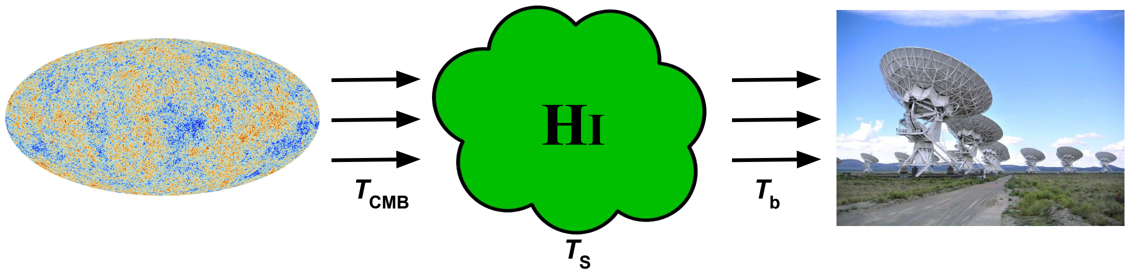

Figure 1.3: An illustration that shows the transfer of the CMB radiation that initially have temperature $T_{\rm CMB}$, entering into the diffused HI in the IGM with spin temperature $T_{\rm S}$, and emerging with a modulated temperature $T_{\rm b}$ that is measured by our telescopes.

CMB blackbody spectrum, the intensity of this radiation, therefore, can be connected to the equivalent temperature (aka brightness temperature: $T_{\rm b}$) via Planck's radiation law in the Rayleigh-Jeans limit [77] as

$$I(\nu) = \frac{2\nu^2}{c^2} k_{\rm B} T_{\rm b}(\nu)\,, \tag{1.6}$$

where ν is the observed frequency $\nu_{\rm obs} = 1420\,{\rm MHz}/(1+z)$, with z being the redshift of emitting HI cloud. $k_{\rm B}$ is the Boltzmann constant and c is the speed of light.

Since the intensity of the 21-cm radiation is controlled by the $T_{\rm S}$, the 21-cm brightness temperature, therefore, will be related to the $T_{\rm S}$. In the absence of background radiation, the $T_{\rm b}$ will be the same as $T_{\rm S}$ in the rest frame of the cloud. On the other hand, if either there is no gas in the IGM and only CMB is present, or there is a perfect balance between emission and absorption, then $T_{\rm b}$ will be the same as the CMB temperature ($T_{\rm CMB}$). The $T_{\rm CMB}$ can be assumed to be solely dependent on the redshift z following the relation $T_{\rm CMB}(z) = 2.73(1+z)\,{\rm K}$. In such a scenario, the observations will not provide anything exciting about the HI distribution in the IGM, which is the subject of our interest.

In the realistic scenario, the CMB acts as background radiation, and the diffused HI in the IGM acts as an intervening medium in the propagation of the CMB (e.g. see Figure 1.3). Since the frequency of the 21-cm photons lies in the low frequency end of the CMB blackbody spectrum known as the Rayleigh-Jeans tail of the CMB [78]. The CMB, therefore, will interact with the HI atoms and some photons will get absorbed. The CMB brightness temperature consequently will be reduced to $T_{\rm CMB} \times e^{-\tau(\mathbf{r},z)}$, where $\tau(\mathbf{r}, z)$ is the optical depth of intervening medium at redshift z and along the line of sight $\mathbf{r}$. The optical depth is a measure of "thickness" or "thinness" of a medium for a given wavelength to be traversed. Furthermore, there is also a probability of the 21-cm emissions to be contributed to the CMB by decreasing the HI spin temperature to a value $T_{\rm S}\times e^{-\tau(\mathbf{r},z)}$. Hence, the change in the spin temperature $T_{\rm S}(1-e^{-\tau(\mathbf{r},z)})$ will be contributed to the CMB. The CMB at redshift z eventually emerges along the line of sight $\mathbf{r}$ with the modulated brightness temperature,

$$T_{\rm b}(\mathbf{r},z) = T_{\rm S}(1-e^{-\tau(\mathbf{r},z)}) + T_{\rm CMB}(z)e^{-\tau(\mathbf{r},z)}\,. \tag{1.7}$$

This modulated CMB brightness temperature thus carries the imprints of the 21-cm signatures. This equation reveals that in order to estimate the brightness temperature ($T_{\rm b}$), one will require the precise estimation of the spin temperature ($T_{\rm S}$) and optical depth (τ) in the optically thin limit.

The optical depth of the HI cloud for the 21-cm signal is given as [77, 79]

$$\tau(\mathbf{r},z) = \frac{3h_{\rm p}c^3A_{10}\bar{n}_{\rm H}(z)}{32\pi k_{\rm B}\nu_{21}^2H(z)}\frac{x_{\rm HI}(\mathbf{r},z)[1+\delta_{\rm H}(\mathbf{r},z)]}{T_{\rm S}(\mathbf{r},z)}\Big[1-\frac{(1+z)}{H(z)}\frac{\partial v_r}{\partial r}\Big]\,, \tag{1.8}$$

where $h_{\rm p}$ is the Planck's constant, $A_{10}\approx 2.9\times 10^{-15}\,s^{-1}$ is the spontaneous decay rate of the spin-flip transition, $\bar{n}_{\rm H}$ is the average of total (neutral+ionized) hydrogen density, $\delta_{\rm H}$ is the matter overdensity/underdensity, $H(z)$ is the Hubble parameter, v_r is the local velocity of the gas (aka peculiar velocity) along the line of sight, and r is the comoving distance of the transitioning HI in the IGM.

The radio telescopes observe the contrast between signal emerging with temperature $T_{\rm b}$ from the HI in the IGM and its background radiation (i.e. CMB) at $T_{\rm CMB}$. This observable quantity is know as the differential brightness temperature or 21-cm fluctuations ($\delta T_{\rm b} = T_{\rm b}-T_{\rm CMB}$) and given as,

$$\delta T_{\rm b}(\mathbf{r},z) = \frac{T_{\rm b}(\mathbf{r},z)-T_{\rm CMB}(z)}{1+z} = \frac{T_{\rm S}(\mathbf{r},z)-T_{\rm CMB}(z)}{1+z}(1-e^{-\tau(\mathbf{r},z)})\,. \tag{1.9}$$

The factor $(1+z)$ in denominator comes due to the Hubble expansion of the Universe. In the optically thin regime $\tau(\mathbf{r},z)\ll 1$, the equation for $\delta T_{\rm b}(\mathbf{r},z)$ will become [79, 80]

$$\delta T_{\rm b}(\mathbf{r},z) \approx \frac{T_{\rm S}(\mathbf{r},z)-T_{\rm CMB}(z)}{1+z}\tau(\mathbf{r},z)\,. \tag{1.10}$$

A recent study [81] has shown that this linear approximation holds to be good during the EoR when the entire IGM is uniformly heated ($T_{\rm S}\gg T_{\rm CMB}$) and the ionization progresses significantly. However, during CD, the $T_{\rm S}$ is generally lower than $T_{\rm CMB}$. Then, an almost neutral IGM behaving like a partially opaque medium for the 21-cm signal will intervene in the propagation of this signal more than it does during EoR. Therefore, during CD, it is better to work with non-linear τ following the equation (1.9).

Using equations (1.8) and (1.10) we can write the the differential brightness temperature as,

$$\delta T_{\rm b}(\mathbf{r},z) = 27 x_{\rm HI}(\mathbf{r},z)\Big(1-\frac{T_{\rm CMB}(z)}{T_{\rm S}(\mathbf{r},z)}\Big)\big(1+\delta_{\rm H}(\mathbf{r},z)\big)\Big(\frac{\Omega_{\rm b}h^2}{0.023}\Big)\Big(\frac{0.15}{\Omega_{\rm m}h^2}\frac{1+z}{10}\Big)^{1/2} \times\Big[1-\frac{(1+z)}{H(z)}\frac{\partial v_r}{\partial r}\Big]\,\mathrm{mK}\,. \quad (1.11)$$

This equation reveals that the contrast between $T_{\rm S}$ and $T_{\rm CMB}$ will decide the nature of the 21-cm fluctuations. In the case with $T_{\rm S} = T_{\rm CMB}$, no signal will be observed. The signal will be observed in absorption or emission depending on whether $T_{\rm S}$ is smaller or larger than the $T_{\rm CMB}$.

1.4.1 21-cm signal in astrophysical context

The 21-cm signal in the context of astrophysics deals with fluctuations in this signal, given by equation (1.11), that arise due to the radiating astrophysical sources. This is the quantity of interest in an experiment using radio-interferometers. One crucial point evident from equation (1.11) is that at a particular redshift, the 21-cm fluctuations depend on the spatial variations in a number of factors such as $x_{\rm HI}$, $T_{\rm S}$ and $\delta_{\rm H}$ in this equation. These fluctuations are dictated by the spatial distribution of the first sources and how the radiations from these sources impact the IGM via different complex astrophysical processes. The 21-cm fluctuations thus carry information about these astrophysical sources. Additionally, the factors governing the different astrophysical processes evolve with redshift as these processes progress with time to change the physical state of the IGM; thereby, 21-cm fluctuations evolve with time. Thus in order to estimate $\delta T_{\rm b}$, proper knowledge about the $T_{\rm S}$ is necessary. The following three physical processes contribute in shaping the $T_{\rm S}$ [1, 16, 82]:

(1) CMB transition: The 21-cm part of the CMB blackbody spectrum can be absorbed by HI atom to be excited to upper energy spin-state, or HI can emit 21-cm radiation to the CMB. These transitions will change the populations of HI in the two different spin-states and hence $T_{\rm S}$.

(2) Collisional transition: The collisions of an HI atom with other HI atoms and residual free electrons after the recombination change the populations of HI spin-states via 21-cm transitions. The degree of collision solely depends on the density of the gas in the IGM. From the Dark Ages to subsequent epochs, the density goes down due to the Universe's expansion, which results in a gradual decrement in the effect of collisions.

(3) Transition due to Lyα scattering: The first luminous source also emits the Lyα photons right after its birth. These photons begin interacting with the HI atoms in the IGM. These photons with energy 10.2 eV excite the electrons of HI in the ground state ($n = 1$) to first excited state ($n = 2$). The average lifetime of $n = 2$ state is 10^{-8} s. This results in the HI atom de-exciting to its ground state. The de-excited electron may go into a spin-state that is different from the initial spin-state. Thus there are spin-flip transitions due to the Lyα photons. This is known as the Wouthuysen–Field effect [76, 83, 84].

These processes occur at a faster rate compared to the decay time of the 21-cm line. Therefore, the condition of the equilibrium between excitations and de-excitations of the spin-states due to the effect of these processes yields the T_{S} in terms of [76]:

$$T_{\mathrm{S}} = \frac{T_{\mathrm{CMB}} + x_\alpha T_\alpha + x_{\mathrm{c}} T_{\mathrm{g}}}{1 + x_\alpha + x_{\mathrm{c}}}\,, \tag{1.12}$$

where T_{g} is the kinetic temperature of the IGM gas, T_α is the color temperature of the Lyα radiation. x_α and x_{c} respectively are the Lyα coupling and collisional coupling coefficients. These coefficients tell how strongly the Lyα scattering and collisions take part in shaping the T_{S}. The repeated scattering of the Lyα photons with the HI establishes the local equilibrium between T_α and T_{g} and eventually makes these two temperatures almost equal ($T_\alpha \approx T_{\mathrm{g}}$). The equation 1.12 then can be written as:

$$T_{\mathrm{S}} = \frac{T_{\mathrm{CMB}} - T_{\mathrm{g}}}{1 + x_\alpha + x_{\mathrm{c}}} + T_{\mathrm{g}}\,. \tag{1.13}$$

From this equation it is clear that depending on the values of the coupling coefficients, the T_{S} couples with either T_{g} (when $x_\alpha + x_{\mathrm{c}} \gg 1$) or T_{CMB} (when $x_\alpha + x_{\mathrm{c}} \ll 1$) at a particular cosmic time. At a particular stage in the evolutionary history, one of the physical processes among the collisional coupling, Lyα coupling, X-ray heating, and UV photo-ionization dominates the 21-cm fluctuations. The collisional coupling is important during Dark Ages. However, during Cosmic Dawn, the Lyα coupling and X-ray heating are the dominant processes. These processes drive the T_{S} fluctuations, which in turn dictates the 21-cm fluctuations according to equation (1.11). Once the regions around the radiating sources are heated (i.e. $T_{\mathrm{S}} \gg T_{\mathrm{CMB}}$), then T_{S} becomes locally saturated in those regions, and UV photo-ionization begins to dictate the 21-cm fluctuations.

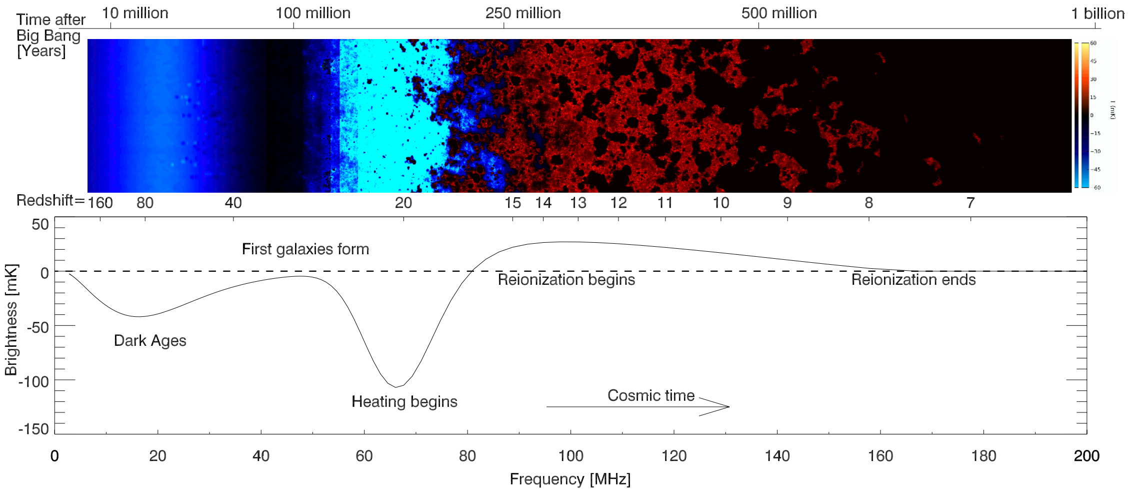

Figure 1.4: The redshift evolution of the 21-cm fluctuations (top panel) and global 21-cm signal (bottom panel) from the Dark Ages to the end of reionization era. This plot is taken from [1].

1.4.2 21-cm signal in cosmological context

The 21-cm signal in the context of cosmology deal with the all-sky average of the 21-cm differential brightness temperature (equation (1.11)) and given by,

$$\delta \bar{T}_{\rm b}(z) = 27\bar{x}_{\rm HI}(z)\Big(\frac{\Omega_{\rm b}h^2}{0.023}\Big)\Big(\frac{0.15}{\Omega_{\rm m}h^2}\frac{1+z}{10}\Big)^{1/2}\Big[1-\frac{T_{\rm CMB}(z)}{T_{\rm S}(z)}\Big]\,{\rm mK}\,. \tag{1.14}$$

This is the quantity of interest in an experiment using a single dish or dipole. Top panel in Figure 1.4 shows the redshift evolution of the 21-cm fluctuations (via equation 1.11) and the bottom panel shows redshift evolution of the all-sky averaged 21-cm signal (i.e. global 21-cm signal: equation 1.14). The various astrophysical processes that are relevant for shaping the $T_{\rm S}$, force the $T_{\rm S}$ to be coupled with either $T_{\rm g}$ or $T_{\rm CMB}$. This results in a contrast between $T_{\rm S}$ and $T_{\rm CMB}$. These processes thus leave their imprints on the global 21-cm signal, which allows us to divide the history of the Universe into the following broad classes (see Figure 1.5) [1]:

- During the late stages of the Dark Ages ($200 \lesssim z \lesssim 30$), the IGM gas temperature decreases adiabatically [$T_{\rm g} \propto (1+z)^2$] that lead $T_{\rm g} < T_{\rm CMB}$. During this time, the density of the Universe is so high that collisions force $T_{\rm S}$ to follow $T_{\rm g}$. These implies $T_{\rm S} < T_{\rm CMB}$ and hence $\delta\bar{T}_{\rm b} < 0$. Thus the 21-cm signal from this epoch is observed in absorption [80]. This signal gradually approaches zero. This is because of the further expansion of the Universe, which makes the IGM gas density too low for

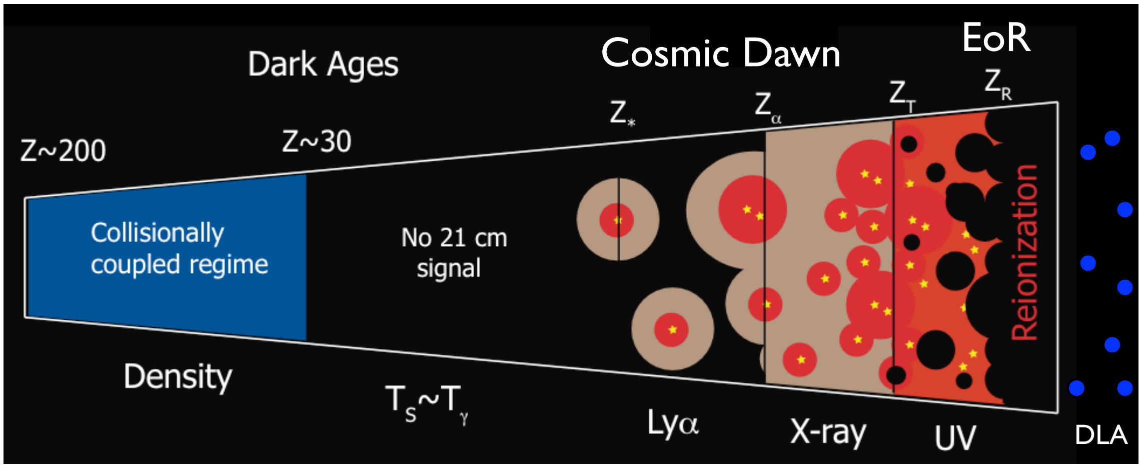

Figure 1.5: An illustration that shows the different phases of the Universe over the cosmic history from the Dark Ages to the end of end of reionization era. This is taken from [1].

effective collisions; thereby, T_{S} follows T_{CMB}. The 21-cm signal remains zero until the birth of the first sources takes place at redshift z_* (see Figure 1.5).

- These first luminous sources begin producing both Lyα and X-ray photons. The Lyα photons have a large scattering cross-section (and small mean free path) for HI cloud, while the X-ray photons have a large mean free path. These Lyα photons begin impacting the HI gas in IGM via the Wouthuysen–Field effect way earlier than X-ray photons start heating the IGM. This is because the IGM acts as the transparent medium for the X-ray photons until the Lyα coupling becomes saturated locally around the sources. The saturation here means the establishment of the local equilibrium between Lyα radiation and the gas surrounding the sources due to the repeated scattering of the Lyα photons. The Lyα coupling thus dominates before the X-ray heating, as illustrated in Figure 1.5. This process couples T_{S} to T_{g}. The cooling of the IGM is still adiabatic and remains in this state until the X-ray heating becomes dominant and, therefore, $T_{\mathrm{g}} < T_{\mathrm{CMB}}$. Together these establish $T_{\mathrm{S}} \sim T_{\mathrm{g}} < T_{\mathrm{CMB}}$. Thus the 21-cm signal is observed in absorption.

- Once the Lyα coupling saturates at z_α, the heating becomes vital in raising the T_{g} as well as T_{S} above T_{CMB}. Thus the 21-cm signal is seen in emission.

- When the IGM heating is completed at z_{T} ($T_{\mathrm{S}} \gg T_{\mathrm{CMB}}$), the 21-cm signal is no longer dependent on the T_{S} [16]. The UV photo-ionization then becomes important to dominate the 21-cm signal.

The theoretical models, simulations and observable statistics have been developing gradually during the last few decades in order to interpret the ongoing and upcoming future observations. In this thesis, we mainly focus on the modeling and simulation of the 21-cm fluctuations (equation 1.11) during CD-EoR with the proper modeling of the T_S (equation 1.12) as per requirement of different CD-EoR scenarios.

1.5 Observations of the CD-EoR 21-cm signal

While traveling to the observer, the CD-EoR 21-cm signal will redshift to a lower frequency that falls into the radio band. The detection of this signal, therefore, requires radio telescopes. Currently, two broad classes of experiments have been performing in order to detect the CD-EoR 21-cm signal. One of them aims to capture the global 21-cm signal using a single dish or dipole. Some of the famous global signal experiments are the Experiment to Detect the Global EoR Signature[1] (EDGES: [85, 86]), Shaped Antenna measurement of the background RAdio Spectrum[2] (SARAS:[87, 88]) etc. In the recent past, the EDGES experiment claimed the first detection of the 21-cm signal [86]. However, there are two major unpredicted/unexpected features in the observed signal i.e. the exceptionally high amplitude ($\sim$ 500 mK) and large width of the absorption profile. These two features have raised many doubts about this supposed signal detection. This is because the present theories suggest the amplitude to a value within the range 100–150 mK and no flatness in the profile. In support of this claimed detection, several theories have been proposed [89–91]. A number of further experiments are required to confirm the EDGES detection. Once confirmed, our current understanding of the CD-EoR will be revolutionized.

The other class of the experiments aims to capture the 21-cm fluctuations in the IGM using the present generation radio interferometers such as Giant Meterwave Radio Telescope[3] (GMRT:[63]), LOw Frequency ARray[4] (LOFAR:[65]), Hydrogen Epoch of Reionization Array[5] (HERA: [72]), Murchison Widefield Array[6] (MWA: [68, 69]), and Precision Array for Probing the Epoch of Reionization[7] (PAPER: [92]). Like the CMB brightness temperature map, imaging the 21-cm brightness temperature has not yet been possible by any

[1] http://loco.lab.asu.edu/edges/edges-science/
[2] http://www.rri.res.in/DISTORTION/saras.html
[3] http://www.gmrt.ncra.tifr.res.in
[4] http://www.lofar.org
[5] http://reionization.org
[6] http://www.haystack.mit.edu/ast/arrays/mwa
[7] http://eor.berkeley.edu

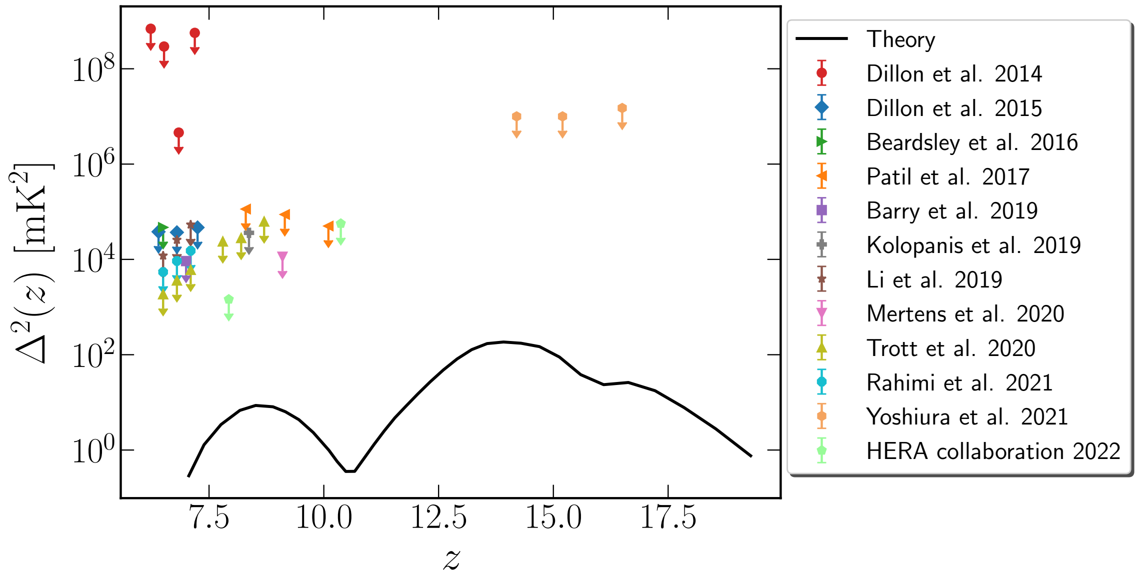

Figure 1.6: A summary plot of the power spectrum upper limits (represented by points) achieved by the various observations at $k = 0.1\,\mathrm{Mpc}^{-1}$. The solid line is the estimated power spectrum from the simulated signal using the GRIZZLY simulation. Credit: Abinash Kumar Shaw.

of these presently operational radio telescopes due to the following major reasons. First, this redshifted signal is very feeble. Second, this signal is significantly contaminated by various observational obstacles, such as

Foreground: Our own galaxy and the extra-galactic point sources in our local universe emit the radiations in the same frequency range as the expected signal. They are known as the "foreground". However, the foreground's intensity is $\sim 10^4$–10^5 times stronger than the expected 21-cm signal. These contaminate the 21-cm signal [93–98]. Proper foreground signal modeling is required in order to remove it from the contaminated CD-EoR 21-cm signal. A number of efforts have been performed in the direction of "foreground removal" [99–102], but the proper removal has not yet been possible. An alternative technique to mitigate the foreground considers a complete avoidance of the foreground while probing the CD-EoR using the 21-cm signal, hence known as 'foreground avoidance' [70,103–107].

System noise: The system noise is nothing but a kind of signal fluctuations other than the targeted signal that the telescopes capture in the absence of this targeted signal. This noise inevitably contaminates the 21-cm signal [108,109] and can be suppressed below the signal for a long integration time.

Ionospheric effects: Random fluctuations in the ionosphere refracts the redshifted 21-cm signal and distorts the apparent magnitude and location of the signal [110,111]. This,

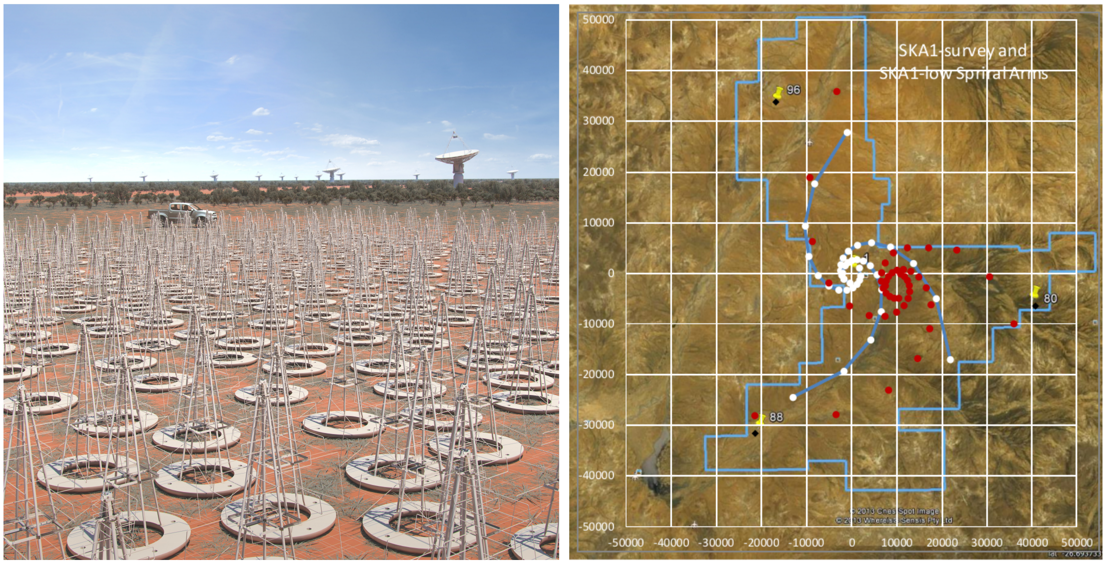

Figure 1.7: Left panel: A close up SKA-Low dipoles (Credit: SKAO). Right panel: Distribution of array of antenna on the ground (Credit: Dewdney and Braun 2016).

in principle, can be corrected for large baselines and a wide field of view. However, in practice, it is a challenging problem to solve.

Effect of radio frequency interference (RFI): The RFI is the artificial broadband and narrowband signals produced by humans through various sources such as cell phones, aircraft communications, FM radio transmissions, etc. This also contaminates the 21-cm signal [112–114].

Among all of these contaminants, the foreground is the most dominant contaminant of the 21-cm signal. Using the present generation telescopes as the test beds, mitigation techniques for many of the above mentioned hindrances in observing this signal are being developed [70, 99–107]. Once the proper removal of the contaminants from the polluted signal is achieved, the present generation radio interferometers will be able to detect the CD-EoR 21-cm signal statistically using different statistical measures such as variance [115–117], power spectrum [103, 118], and multifrequency angular power spectrum [119–121]. This is because the signal-to-noise ratio (SNR) for these statistics is high. Until the imaging of the CD-EoR 21-cm signal becomes possible, the present generation instruments are being employed to seek the prospects of detection of this signal via the power spectrum. However, the signal power spectrum has also not been detected yet by any of the presently operational radio telescopes due to the same reasons. As of now, due to the limited sensitivity, these radio interferometers are only able to estimate the maximum value (aka "upper limit") of the power spectrum [67, 98, 104, 118, 122–126]. This upper limit has been improving a lot toward the theoretical prediction of the power spectrum (see Figure 1.6). It is expected that by the time the next generation telescopes e.g. SKA become operational, solutions for most of the aforementioned observational obstacles will be produced. We, therefore, expect that the upcoming ratio interferometer SKA[8] [73, 74] will be sensitive enough to see the Universe not only during EoR but also during CD. Additionally, SKA-like telescopes will have a significantly higher signal-to-noise ratio to be able to probe higher-order Fourier statistics of the signal as well as to make tomographic images of the signal.

1.6 Simulations of the CD-EoR 21-cm signal

As discussed in Section 1.5, a number of observational obstacles do not allow us to detect the CD-EoR 21-cm signal via present-generation radio interferometers. Thus, until the interferometric detection of the CD-EoR 21-cm signal is possible, we require precise analytical modeling of the 21-cm signal and numerical simulations in order to predict the 21-cm observations beforehand. All the CD-EoR models developed so far are inspired by our current understanding of the present-day universe and various indirect observations of the CD-EoR. The simulations thus help in predicting the 21-cm observations and interpreting them correctly once the detection is made possible. Through detailed modeling of the 21-cm observable ($\delta T_{\rm b}$), we can draw information regarding the complex astrophysical processes during CD-EoR.

The CD-EoR simulations provide the distribution of heated, ionized, and neutral regions produced by the distribution of the radiating sources. These simulations do perform in three steps. First, they determine the dark matter distribution in the Universe. This distribution tells us about the HI distribution in the IGM as per the assumption that the hydrogen distribution follows the underlying dark matter distribution. Second, they identify the heating and ionizing sources in the IGM. Lastly, they generate the 21-cm images by simulating the heating and ionizing processes that are performed via the transport of the photons from these sources. These 21-cm images show the distribution of the heated and ionized regions in the IGM. In this section, we focus on two different ways to simulate the CD-EoR.

[8] http://www.skatelescope.org

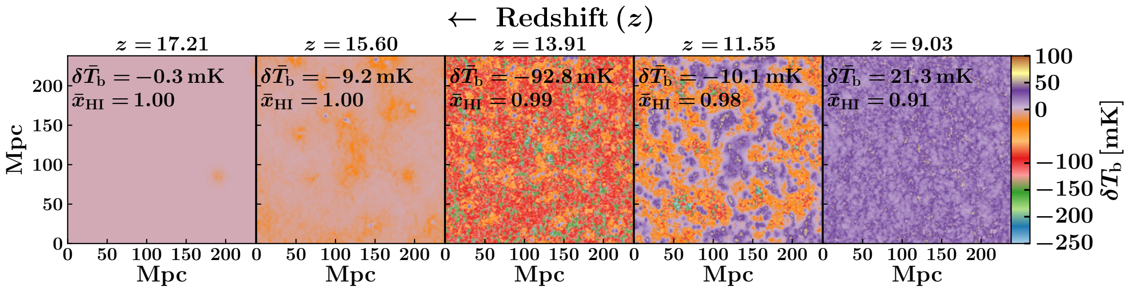

Figure 1.8: Zoomed in 2D slices (side length 238.09 Mpc) of the differential brightness temperature showing the redshift evolution (from left to right) of the fluctuations in the 21-cm signal from the CD. Each slice shows the special fluctuations in this signal. The full simulation volume is (714.29 Mpc^3) in size. This has been simulated using the GRIZZLY code.

1.6.1 Fully numerical simulations

The fully numerical simulations are based on solving the radiative transfer (RT) equations exactly on each grid point in the simulation box. These simulations, therefore, are computationally expensive. These codes first require the matter distribution in the Universe that can be generated via dark-matter N-body codes, such as PMFAST[127] and CUBEP^{3}M [128]. They further need the collapse of these dark matter to form gravitationally bound structures known as halos. The halo locations and properties can be found using a halo finder algorithm [129, 130]. The transfer of the radiations from the luminous sources that are formed inside these halos is the main concern of the fully numerical simulations in order to form heating and ionization maps. A few such codes are CRASH [131], C^2-RAY [132], and LICORICE [133]. These codes solve the RT equations in 3D.

1.6.2 Semi numerical simulations

The semi-numerical methods rely on a number of approximations in order to make the CD-EoR simulations faster. These approaches require the matter distribution in the Universe and the source population as required in fully numerical techniques. The matter distribution can be determined using the linear perturbation theory. One commonly used linear approximation approach that approximates the growth of structures is the Zel'dovich approximation [134]. Besides this, another approach exists based on the second-order Lagrangian perturbation theory [135, 136] for the same purpose. A thorough comparison of these two methods is given in [137]. These approximations are used in the N-body simulations [138].

Further, the number density of halos corresponding to different mass bins can be determined using the halo mass function (HMF) [139]. A widely accepted HMF in the astronomical community is the Press-Schechter formalism [140]. A number of fitting functions such as [141–143] provide the best matching with the HMF obtained from the N-body simulations [144].

Given the matter density fields and halo catalogs, one can construct the heating and ionization maps at different stages of the CD-EoR using the code based on the analytical formalism [145] such as excursion set theory [146]. Most of the semi-numerical codes are based on the excursion set formalism [21, 48, 145, 147, 148]. Even with some shortcomings, the results obtained from the semi-numerical simulations match those obtained using the fully numerical approaches [147, 149]. A few semi-numerical codes are 21cmFAST [150], SimFAST [151], ReionYuga [147, 148]

Another class of the semi-numerical approach exists that considers solving the RT equations in 1D. The BEARS [152] and GRIZZLY [153, 154] simulations use this approach. The results from the 1D RT simulations, matching those obtained from the fully numerical simulations, match much better than the simulations based on the excursion set formalism [154].

In this thesis, we use GRIZZLY code while simulating the signal from CD (see Section 3.3 for details) and ReionYuga code for EoR 21-cm signal simulations (see Section 2.4 for details). Figure 1.8 shows the 2D slices of the differential brightness temperature showing the redshift evolution of the fluctuations in the 21-cm signal from the CD corresponding to a fiducial CD scenario. Each slice shows the special fluctuations in this signal. This scenario has been simulated using the GRIZZLY code by assuming that the likely astrophysical processes dominant during CD, such as the Lyα coupling, X-ray heating and photo-ionization, are running simultaneously from the beginning of the CD in a self-consistent manner. At a very early stage of the CD, there are no heated and ionized regions (see left-most panel), but a few absorbing regions are present due to the Lyα coupling. As time passes, the Lyα coupling becomes stronger, resulting in the sizes of the absorbing regions increasing and eventually percolating. Once the Lyα coupling around the radiating sources tends to saturate, the X-ray heating around the same sources becomes active. The X-ray heating first reduces the strength of the absorption signal around the sources to make these regions less cold (or warm) and then gradually produces the heated regions around the sources. These heated regions grow and eventually percolate as the heating progresses with time. Then we reach a stage where the entire IGM has become uniformly heated. After the heating becomes saturated locally around the sources, UV photo-ionization becomes important.

It continues until the Hɪ in the IGM get fully ionized.

1.7 Simulated CD-EoR statistics

One of the most important characteristics of the CD-EoR is the fluctuations in the 21-cm field of Hɪ in the IGM majorly produced by heating and ionizing sources. These fluctuations are distributed throughout the IGM over different length scales. This spatial distribution of the fluctuations is majorly dependent on how these sources are distributed in the IGM and how strongly they radiate. We quantify the amplitude of fluctuations in the 21-cm signal using various statistics such as variance, power spectrum and bispectrum. The variance measures the amplitude of fluctuations at a single length scale. However, it is unable to tell anything about how the fluctuations are distributed at different length scales. The power spectrum, which is the target lower-order statistic for the detection of the signal being used by the presently operational telescopes, measures this scale dependence of the fluctuations in the 21-cm signal.

1.7.1 Power spectrum

The power spectrum, in principle, can be estimated through the product of the Fourier transform of the signal and its complex conjugate and given as,

$$\langle \Delta_{\rm b}(\mathbf{k}_1)\Delta^*_{\rm b}(\mathbf{k}_2)\rangle = V\delta^3_{\rm D}(\mathbf{k}_1-\mathbf{k}_2)\,P_{\rm b}(\mathbf{k})\,, \tag{1.15}$$

where $\Delta_{\rm b}(\mathbf{k})$ is the Fourier transform of $\delta T_{\rm b}(\mathbf{r})$, and $\delta^3_{\rm D}$ is the Dirac's delta function. From this equation it is evident that power spectrum ($P_{\rm b}(\mathbf{k})$) will be non-zero if and only if $\mathbf{k}_1-\mathbf{k}_2=0$ or $\mathbf{k}_1=\mathbf{k}_2(=\mathbf{k})$, where $\mathbf{k}$ is the wave number. The power spectrum thus provides the auto-correlation of the signal at a single Fourier mode. Hence, this statistic can provide a complete statistical description of a Gaussian random field. However, the spatial and temporal fluctuations of the CD-EoR 21-cm signal are highly non-Gaussian as they arise due to the non-random distribution of the heated and ionized regions in the IGM (for details, see Section 1.7.2). The power spectrum, being unable to capture this non-Gaussianity, cannot fully characterize the CD-EoR 21-cm signal. Despite this, the power spectrum has been adopted as the most conventional and primary observable of the CD-EoR observations. The bispectrum is the simplest higher-order statistic that can probe this non-Gaussianity and its scale dependence (for details, see Section 1.7.3).

From the simulated CD-EoR 21-cm data cube, we extract the power spectrum using the

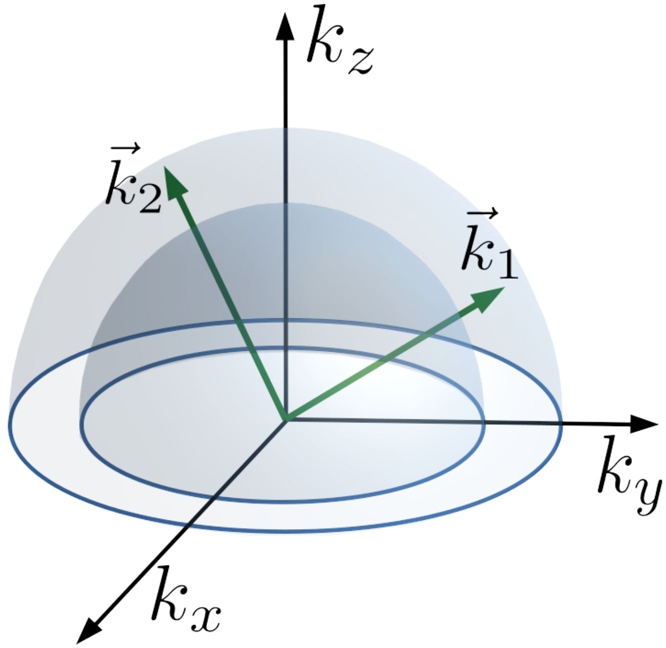

Figure 1.9: Illustrate the semi-spherical binning of the Fourier space. Credit: Abinash Kumar Shaw.

bin-averaged power spectrum estimator which is obtained by averaging $P_{\rm b}$ inside semi-spherical shells (bins) of radius k in Fourier space (see Figure 1.9). For an $i^{\rm th}$ bin it is given as (see [148] for further details)

$$\hat{P}_i(k) = \frac{1}{N_k V} \sum_{\mathbf{k} \in i} \Delta_{\rm b}(\mathbf{k}) \Delta_{\rm b}(-\mathbf{k}) \,, \tag{1.16}$$

where $N_{\rm k}$ is the number of k-modes the fall inside the $i^{\rm th}$ bin.

For convenience, we normalize the power spectrum with the Fourier volume to make it the dimensionless [139] and given as,

$$\Delta^2(k) = \frac{k^3}{(2\pi^2)} P(k) \,. \tag{1.17}$$

Here, for simplicity, we have dropped the subscript "i" and hat from $\hat{P}_i(k)$. The Δ^2 is a crucial statistical measure of the 21-cm signal as it encapsulates the information about the fluctuations in the matter density δ, the time evolution of the neutral hydrogen fraction $x_{\rm HI}$ and spin temperature $T_{\rm S}$. A number of studies have shown that the evolution of Δ^2 probes several crucial features of the CD-EoR 21-cm signal. [3, 14, 16, 48, 79, 119, 155–160]. In the left panel of Figure 1.10, we show the redshift evolution of the Δ^2 estimated from

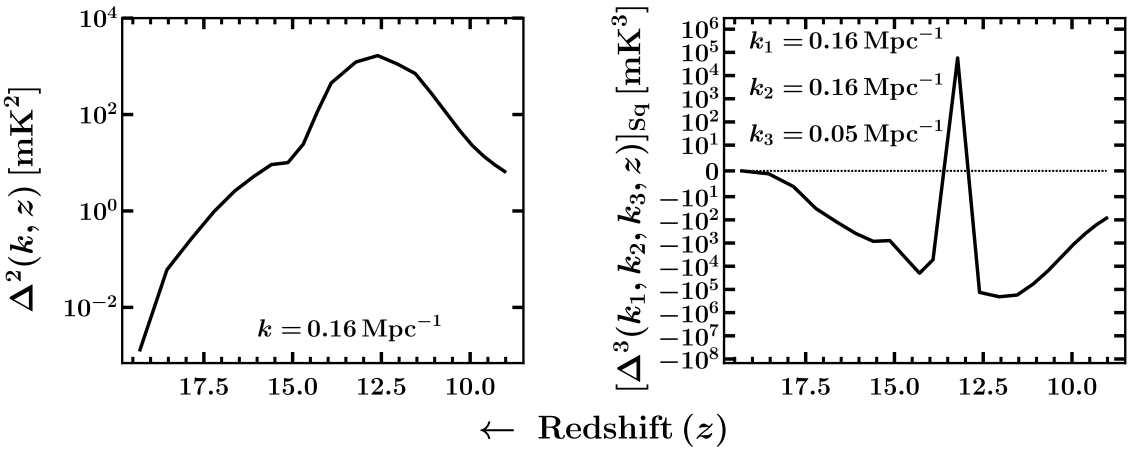

Figure 1.10: Left panel: The redshift evolution of the spherically averaged power spectrum at $k = 0.16\,\mathrm{Mpc}^{-1}$. Right panel: The redshift evolution of the spherically average bispectrum at $k_1 = 0.16\,\mathrm{Mpc}^{-1}$.

the simulated 21-cm signal from the CD, the maps of which are shown in Figure 1.8. We see the features of the Δ^2 arising due to the Lyα coupling and X-ray heating processes.

1.7.2 The non-Gaussianity

The Gaussian distributions correspond to the stochastic or random processes. It is widely accepted that the fluctuations in the HI distribution in the neutral and cold IGM (i.e. during Dark Ages) follow the fluctuations in the dark matter with some bias. This is because the dark matter particles are concentrated at the locations where the matter density is high i.e. at biased locations and where the first sources form later. The matter distribution (dark matter + baryonic matter) thus itself encapsulate a kind of non-Gaussianity. Additionally, the heating and ionizing radiations from these CD-EoR sources interact with the IGM in order to produce heated and ionized regions. These regions further introduce a high level of non-Gaussianity in the 21-cm field. These together make the CD-EoR 21-cm signal highly non-Gaussian. The non-Gaussianity thus is the inherent characteristics of the CD-EoR 21-cm fluctuations. Furthermore, the growth and percolation of the heated and ionized regions causes this intrinsic non-Gaussianity to evolve (increased/decreased) with time [161]. In this thesis we quantify this intrinsic and time-evolving non-Gaussianity in the CD-EoR 21-cm fluctuations using the bispectrum.

Apart from these, there is an additional primordial non-Gaussianity that comes from the non-Gaussian fluctuations during inflation [162]. However, capturing this non-Gaussianity during CD-EoR in the presence of complex astrophysical processes is difficult. One can

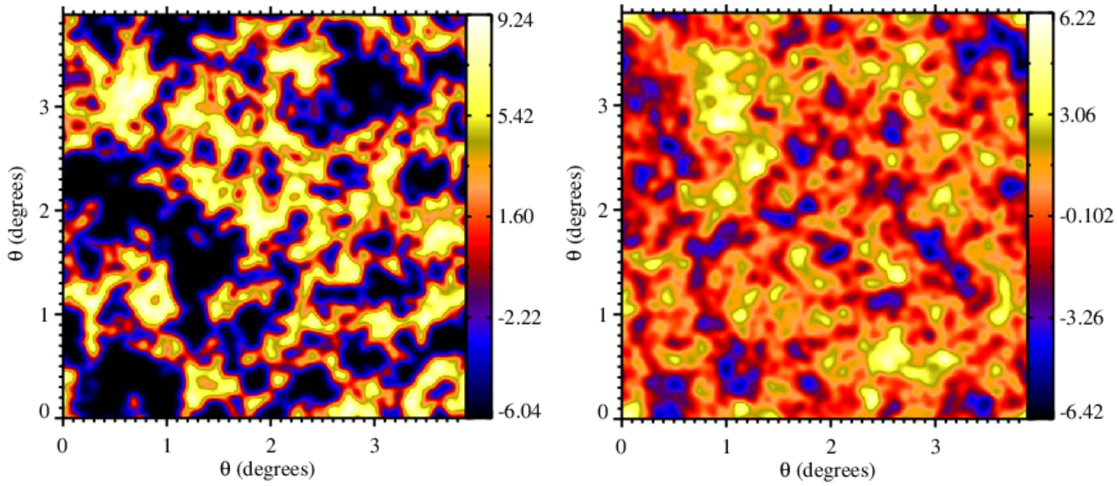

Figure 1.11: Left panel: 21-cm differential brightness temperature map at $z = 7.02$. This has been simulated using a fully numerical reionization simulation that is convolved with a 5 arcminute FWHM Gaussian beam and 0.8 MHz bandwidth. Right panel: Gaussian fluctuations, having the same power spectrum as the fluctuations in the left panel. These two maps are very different but cannot be distinguished by the power spectrum. These maps are taken from [2].

probe this non-Gaussianity either during the Dark ages or during post-EoR.

As stated in Section 1.7.1, the power spectrum is able to describe only the Gaussian random field. However, the non-Gaussianity affects the error in the power spectrum estimation (viz cosmic variance) [148,163–166]. In Figure 1.11, the left panel shows the 21-cm image at a particular stage of the EoR ($z = 7.02$), using a full numerical simulation. This image, therefore, is non-Gaussian distribution of the ionized regions. The right panel in this figure show a constructed Gaussian 21-cm image which appears different from the left panel. This Gaussian 21-cm image was constructed in a way that its power spectrum matches with the power spectrum of the non-Gaussian image. This clearly demonstrates that the power spectrum cannot probe the non-Gaussianity present in the 21-cm images.

In order to deal with the non-Gaussianity, one need to head towards other statistics which are sensitive to the non-Gaussianity. One point statistics such as the skewness and kurtosis are capable to probe the non-Gaussianity in the 21-cm signal [116,117,167–169]. However, these statistics can capture the non-Gaussianity at a single length scale and hence unable to correlate the signal at different length scales. To probe this scale dependence of the non-Gaussianity we need the higher order statistics such as the bispectrum (three point). The bispectrum being the first higher order statistic has potential to correlate the signal at different Fourier modes and thus can capture the non-Gaussianity at different length

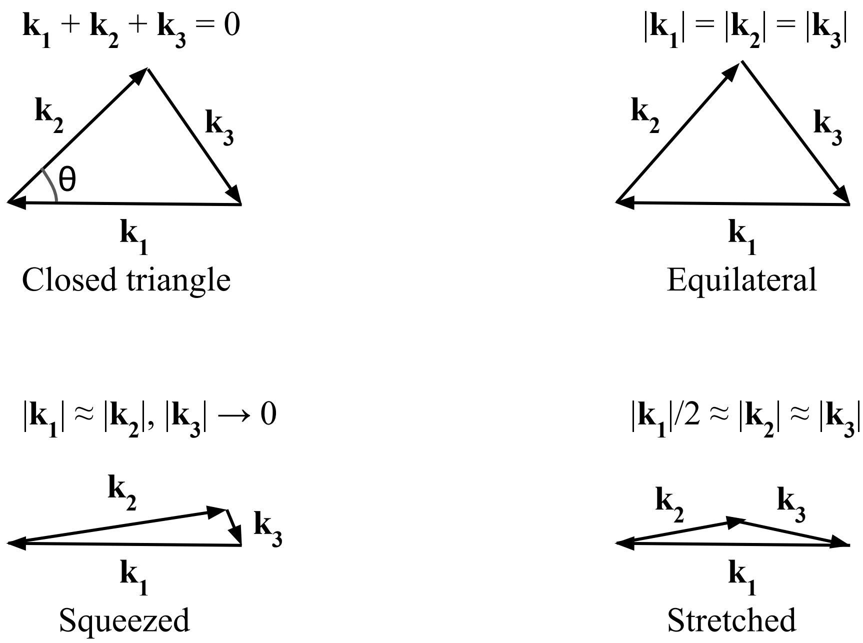

Figure 1.12: An illustration of the triangle configurations formed by three wave numbers $\mathbf{k_1}$, $\mathbf{k_2}$ and $\mathbf{k_3}$ in the Fourier space. The bispectrum is estimated via constructing a closed triangle configuration with these three wave numbers in the k-space shown in the top left panel. The triangles in the other panels are the few special k-triangle configurations such as equilateral, squeezed and stretched.

scales.

The primary aim of this thesis is to study the non-Gaussianity in the simulated CD-EoR 21-cm signal using the bispectrum.

1.7.3 Bispectrum

The bispectrum is the simplest higher order Fourier statistic that can probe the time-evolving non-Gaussianity and its scale dependence. It, in principle, can be estimated through the product of the Fourier transform of the signal for groups of three different wave numbers in the Fourier space which form closed triangles (aka k-triangle: see a triangle in Figure 1.12) and given as,

$$\langle \Delta_{\rm b}(\mathbf{k}_1)\Delta_{\rm b}(\mathbf{k}_2)\Delta_{\rm b}(\mathbf{k}_3)\rangle = V\delta^{\rm K}_{\mathbf{k}_1+\mathbf{k}_2+\mathbf{k}_3,0}\, B_{\rm b}(\mathbf{k}_1,\mathbf{k}_2,\mathbf{k}_3)\,, \tag{1.18}$$

where $\Delta_{\rm b}(\mathbf{k})$ is the Fourier transform of $\delta T_{\rm b}(\mathbf{r})$, $\delta^{\rm K}_{\mathbf{k}_1+\mathbf{k}_2+\mathbf{k}_3,0}$ is the Kronecker's delta function which will be non-zero when $\mathbf{k}_1+\mathbf{k}_2+\mathbf{k}_3 = 0$, and V is the of the simulation/observation volume. The behaviour of the bispectra solely depend on the configurations of the k-triangles as well as the length scale of the observation for which the bispectra are being estimated. The configurations of the k-triangles can be defined in term of shapes of the k-triangle which are determined by the ratio $|\mathbf{k_2}|/|\mathbf{k_1}|$ and cosine of angle between $\mathbf{k_1}$ and $-\mathbf{k_2}$ ($\cos\theta = -(\mathbf{k}_1 \cdot \mathbf{k}_2)/(k_1 k_2)$). The size of the k-triangle is represented by $|\mathbf{k_1}|$, which determine the length scale of observation.

From the binned data cube, we extract the bispectrum using the bin-averaged bispectrum estimator which is obtained by averaging $B_{\rm b}$ inside a semi-spherical bin corresponding to $i^{\rm th}$ triangle configuration. It is given as

$$\hat{B}_i(k_1, k_2, k_3) = \frac{1}{N_{\rm tri} V} \sum_{[\mathbf{k}_1+\mathbf{k}_2+\mathbf{k}_3=0]\in i} \Delta_{\rm b}(\mathbf{k}_1)\Delta_{\rm b}(\mathbf{k}_2)\Delta_{\rm b}(\mathbf{k}_3)\,, \tag{1.19}$$

where $N_{\rm tri}$ is the number of samples of closed triangles associated with the $i^{\rm th}$ triangle configuration bin. Estimating the bispectrum for a particular k-triangle configuration from a data set is computationally expensive due to the rigorous sampling of all possible orientations of the k-triangle.

For convenience, we normalize the bispectrum with the Fourier volumes corresponding to two independent wave numbers in the definition of the bispectrum to make it the dimensionless,

$$\Delta^3(k_1, k_2, k_3) = \frac{k_1^3 k_2^3}{(2\pi^2)^2} B(k_1, k_2, k_3)\,. \tag{1.20}$$

In the right panel of Figure 1.10, we show the redshift evolution of Δ^3 estimated from the same simulated CD 21-cm signal data used while estimating the power spectrum. We see the features of the Δ^3 arising due to the Lyα coupling and X-ray heating processes. The bispectrum has an additional feature compared to the power spectrum, its sign, which can be both positive and negative. The magnitude, sign, and their evolution with redshift can probe the fundamental features associated with the non-Gaussianity of the redshifted CD-EoR 21-cm signal.

Since the bispectrum estimation requires a three-point correlation, the observations of the CD-EoR 21-cm bispectrum will require more sensitivity than needed for power spectrum detection. As SKA-like telescopes are expected to have enough sensitivity required for detection of the CD-EoR 21-cm bispectrum [170–172], thus it is imperative to develop a framework for the physical interpretation of this signal statistic. The discussion about the bispectrum in details is given in Section 2.2.

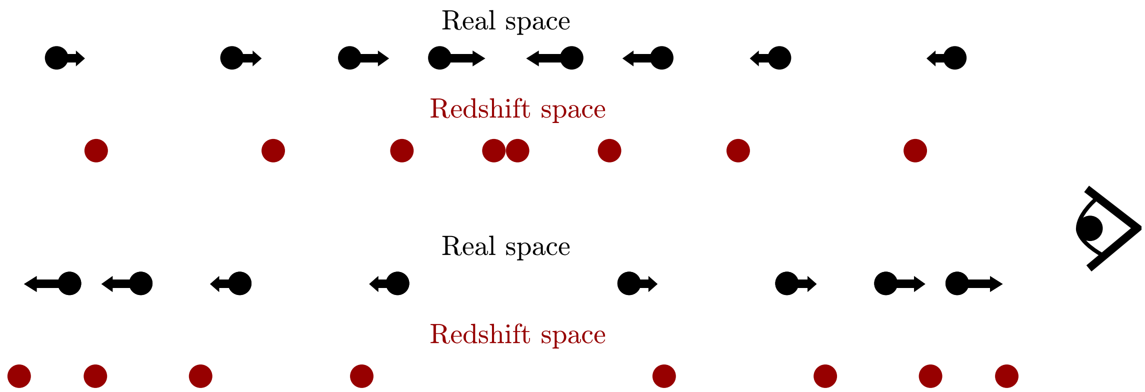

Figure 1.13: An illustration showing the Kaiser effect. To an observer, the dense regions will appear even denser along the line of sight and the under-dense regions will appear more under-dense. This is taken from [3].

1.8 Line of sight anisotropies

The information related to the different unique local effects, such as peculiar velocities of the HI gas, are imprinted in the redshifted CD-EoR 21-cm signal along a particular LoS direction. Furthermore, the information regarding how the signal evolves along this LoS direction is also imprinted in the redshifted 21-cm signal. The cosmological principle assumes that the Universe is statistically homogeneous and isotropic at sufficiently large length scales of observations. However, the signal along a particular LoS direction appears to be anisotropic due to a number of LoS effects. The major LoS effects are the redshift space distortion (RSD) [173, 174], light-cone (LC) [175, 176], and Alcock-Paczynski (AP) [177] effects. The RSD belongs to the non-linear peculiar velocities of the HI gas in the IGM. These peculiar velocities result in the gas being clustered in the high-density regions and dispersed from the low-density regions. The signal from the high-density regions will be boosted in the redshift space and the signal from low-density regions will be reduced. This is known as the Kaiser effect [173] (see Figure 1.13 for illustration of the Kaiser effect). The Kaiser effect results in an additional redshift or blueshift on top of the redshift due to the expansion of the Universe. This effect, therefore, is known as redshift space distortion (RSD). The RSD thus modulates the signal along the LoS direction. An illustration of the RSD effect on the 21-cm signal is shown in the top panels of Figure 1.14. This figure clearly demonstrates that the brightness of the pixels in the 21-cm maps is modulated by the RSD effect. The bottom panels show the impact of the RSD on the 21-cm power spectrum (right panel) when compared with the 21-cm power spectrum when no RSD has been considered (left panel). It is visible that the RSD stretches the power spectrum along the LoS.

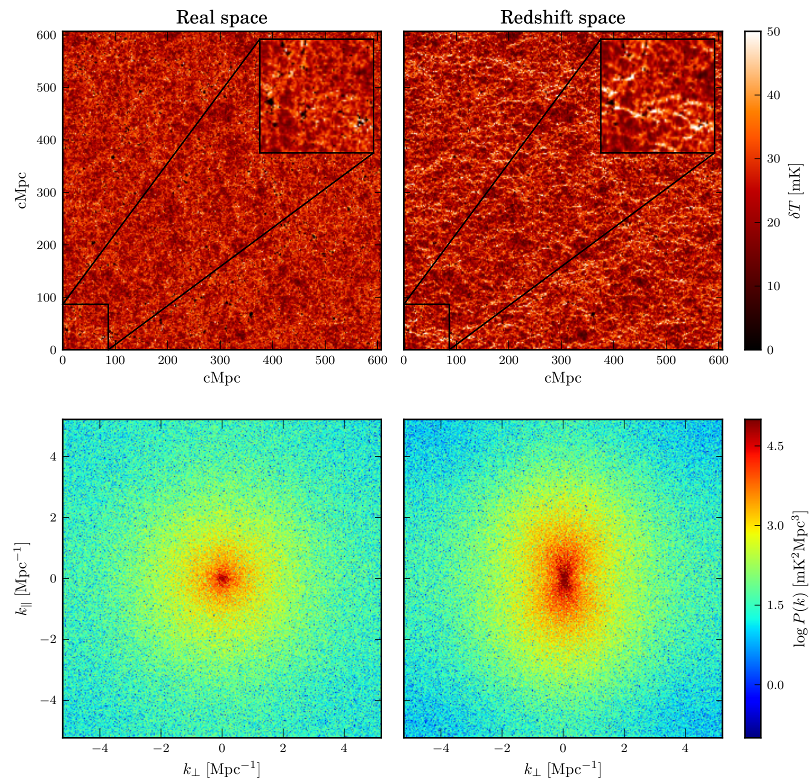

Figure 1.14: Visual illustration showing the impact of the RSD on the 21-cm map (top panels) and on the power spectrum (bottom panels). The left panels considers that no RSD is present. The right panels clearly show the impact of the RSD along the line of sight direction on both the 21-cm signal and its power spectrum. The RSD increases the contrast of the pixels in the 21-cm map and stretches the power spectrum along the line of sight. This is taken from [3].

The CD-EoR simulations assume that the signal from each part of the simulation volume is at the same frequency i.e. at the same redshift. This volume is known as the coeval-cube (CC). However, in practice, each 2D slices in the simulation volume that are perpendicular to the LoS directions are at a different redshift. The signal thus evolves along the LoS direction. This is known as the LC effect. In Figure 1.15, we show a comparison between 2D slices of the 21-cm maps of the coeval cube (left panel) and the corresponding LC cube (right panel). We can see that ionized regions in the slice of the LC cube are modulated due to the LC effect. The AP effect is completely different from these two effects as it is genuinely related to the geometry of space-time, which is non-Euclidean.

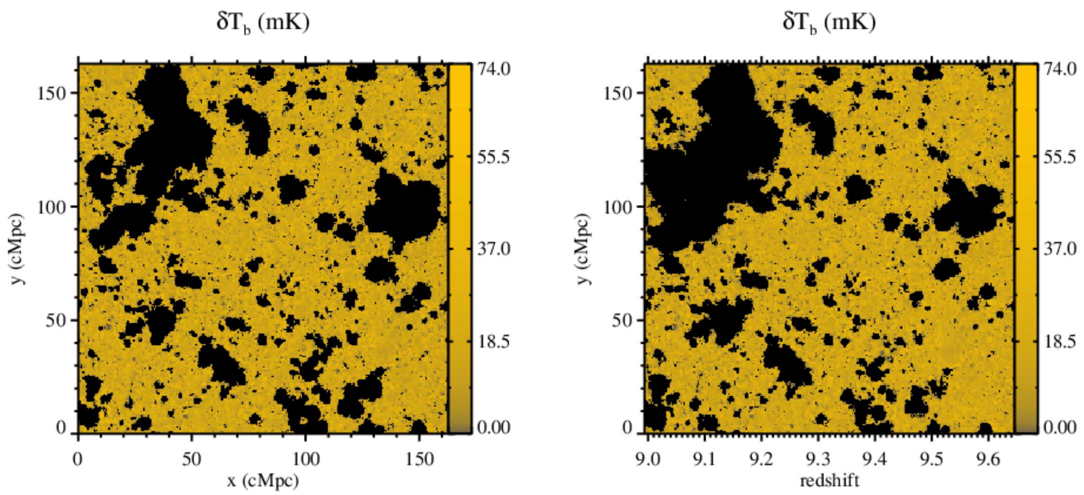

Figure 1.15: Left panel: 2D slice of the 21-cm map from a coeval cube at $z = 9.31$. Right panel: same 2D slice but from the light cone cube at central redshift $z_{\rm c} = 9.31$. The sizes of the ionized (HII) regions are changed along the line of sight direction (y-axis) due to the light cone effect. This is taken from [4].

These LoS effects imprint their signature on the statistical estimates of the 21-cm signal by making the signal anisotropic along the LoS axis. In view of the future SKA-Low interferometric observations of the CD-EoR, it is important to understand the impacts of these possible effects on the signal for its accurate detection and correct interpretation. Therefore, one needs to consider these effects while estimating the CD-EoR parameters using various statistical estimates such as the power spectrum and bispectrum, etc.

Previously, [79,178], for the first time, analytically studied the effect of RSD in the context of the CD-EoR 21-cm signal. Their study pointed out that the redshift space anisotropy significantly changes the shape and magnitude of the 21-cm power spectrum. Further, [156,179] used this inherent anisotropy in the 21-cm power spectrum and showed that the matter power spectrum can be extracted during CD-EoR. An earlier study of [180], for the first time, properly implemented the effect of peculiar velocity in the simulations of the EoR 21-cm signal. They have quantified the effect of RSD by estimating the monopole and quadrupole moments of the power spectrum. The evolution in the quadrupole moment of the power spectrum with the mean neutral fraction $\bar{x}_{\rm HI}$ at large length-scales ($k \sim 0.12\,{\rm Mpc}^{-1}$) can be used to constrain the reionization history to a great degree [160]. Further, [153] quantified the effect of RSD on 21-cm power spectrum during CD, when the fluctuations in the $T_{\rm S}$ controls the 21-cm fluctuations. They have reported that the effect of RSD on the CD 21-cm power spectrum is not too high compared to its effect on EoR 21-cm power spectrum. One of the major goals of this thesis is to quantify the anisotropy due to the peculiar velocity of the HI gas in the IGM using the bispectrum. For the first time, we study the RSD's impact on the CD-EoR 21-cm bispectrum. In this thesis, among a number of LoS anisotropies, we only consider the RSD while simulating the 21-cm signal from the CD-EoR.

1.9 Thesis Motivation and Objectives

This doctoral thesis aims at building a physical interpretation of the expected HI 21-cm bispectrum from the CD-EoR era using state-of-the-art large-scale simulations of the signal. The physical interpretation of this higher-order signal statistic developed in this thesis will be crucial for providing better constraints to the CD-EoR model parameters using future SKA observations of this era. The previous studies of the signal bispectrum have been fairly limited in their scope to develop such physical interpretation of the signal, which this thesis attempts. The first studies of the EoR bispectrum by [161] and [181] attempted to characterize it via a simple analytical toy model. One of the crucial features of the bispectrum predicted in their studies was its sign, which can be both positive and negative.

The predictions on bispectrum sign made by [161] and [181] were independently confirmed by [182–185] using detailed simulations of the signal. These studies were limited to the analysis of bispectrum for a few special shapes of the k-triangles e.g. equilateral, isosceles, squeezed, etc. However, to obtain a comprehensive understanding of the signal non-Gaussianity, one needs to consider all possible unique triangle shapes and sizes in the Fourier space while estimating the bispectrum. Fairly recently, [5] proposed a method to parameterize the bispectrum for triangles of all possible unique shapes in the Fourier space. Further, these earlier studies of the CD-EoR 21-cm bispectrum had not considered some of the intrinsic line of sight (LoS) anisotropies present in the signal e.g. redshift space distortion (RSD) [173,174], light-cone effect [175,176], etc., while analyzing its bispectrum. These effects are expected to have a significant impact on almost any Fourier statistic of the signal [3, 79, 159, 178, 180, 186–189].

This thesis presents a comprehensive study of the CD-EoR 21-cm bispectrum for all possible unique k-triangles shapes using a large suite of simulated signals. In this study, we focus on the signal from Cosmic Dawn, where the spin temperature (T_{S}) dominates the 21-cm brightness temperature fluctuations, as well as the Epoch of Reionization, where T_{S} does not play a significant role (as $T_{\mathrm{S}} \gg T_{\mathrm{CMB}}$). We also quantify the impact of RSD on the CD-EoR 21-cm bispectrum.

For a given CD-EoR model, we first demonstrate how the bispectrum for all unique k-triangles behave at different stages of the CD-EoR and for different length scales of observation (i.e. different k_1 modes). For the first time, we quantify the impact of RSD on the spherically averaged CD-EoR 21-cm bispectrum in the entire unique k-triangle space [190, 191]. We also quantify the effect of the $T_{\rm S}$ fluctuations on the bispectrum during the CD [191]. The nature of radiating sources dictates how they impact various ongoing IGM physical processes during CD-EoR. We further demonstrate how the various X-ray sources, such as mini-QSOs and high mass X-ray binaries (HMXBs), affect the IGM physics and thus the magnitude and sign of the signal bispectrum in the all unique k-triangle space.

Next, we present an extensive analysis to connect the redshift evolution of the large-scale ($k_1 \sim 0.16\,{\rm Mpc}^{-1}$) 21-cm bispectrum (which is expected to be detectable via future SKA observations) with two dominant IGM physical processes during the CD, which are, Lyα coupling and X-ray heating. This is possible as these two processes are the dominant contributors to the highly non-Gaussian spatial and temporal fluctuations in the signal. The bispectrum being the potential probe of this non-Gaussianity is therefore expected to probe these IGM processes. Using a suite of signal simulations, for the first time, we show how these two major IGM processes affecting the 21-cm signal during CD impact the magnitude, sign and the sequence of sign changes of the large-scale 21-cm bispectrum. Further, the impact of these processes on the 21-cm signal and its non-Gaussianity vary depending on the properties of the first sources of light. The source properties are mainly determined via two major source parameters i.e. the minimum halo mass $M_{\rm h,min}$ and X-ray photon production efficiency $f_{\rm X}$. We additionally study the impact of variation in these source parameters on the large-scale 21-cm bispectrum for all possible unique k-triangles in the Fourier domain. This study is essential in order to check the robustness of the features observed in the large-scale 21-cm bispectrum with the various radiating sources during CD, having different source properties (parameters).

1.10 Thesis Organization and Contribution

This thesis consists of six chapters. Chapter one presents the introduction and motivation of the thesis, chapters two to five describe its original contributions to the field, and chapter six presents the summary and future scope of this thesis. The brief chapter-wise contributions of this thesis are described as follows:

1.10.1 Chapter 2: The EoR 21-cm bispectrum and the impact of redshift space distortions on this signal statistic

In this chapter, we present a comprehensive study of the spherically averaged EoR 21-cm signal bispectra using an ensemble of simulated signals. This work is the first of its kind, as it quantifies for the first time, the EoR (where $T_{\rm S} \gg T_{\rm CMB}$) 21-cm bispectra for all possible unique k-triangles in the triangle parameter space. All of the earlier works in this sub-domain have considered only a few specific types of k-triangles. We find that the 21-cm bispectra are non-zero for most of the triangle parameter space and during almost the entire period of the reionization. This firmly establishes that the EoR 21-cm signal is highly non-Gaussian and this non-Gaussianity also evolves with time. Furthermore, for the first time, we quantify the impact of the redshift space distortions (RSD) on the spherically averaged EoR 21-cm bispectrum in the entire unique triangle space. Our analysis indicates that the effect of the RSD anisotropies is significant on the bispectrum magnitude ($> 50\%$) and sign. We thus conclude in this chapter that one would need to properly consider the impact of the RSD on the EoR 21-cm bispectra to achieve a correct interpretation of this signal statistics obtained from future observation. For more details, please refer to chapter 2 of the thesis or our journal article [190].

1.10.2 Chapter 3: The CD 21-cm bispectrum and the impact of spin temperature fluctuations and the redshift space distortions on this signal statistic

This chapter presents a comprehensive view of the non-Gaussianity in the simulated 21-cm signal originating from the CD, where $T_{\rm S}$ fluctuations are important, through the signal bispectra estimated for all unique k-triangles. Additionally, for the first time, we quantify the impact of the spin temperature fluctuations and that of the redshift space distortions on this signal statistic by estimating it for all unique k-triangle shapes. We find that the impact of RSD on the CD 21-cm bispectra is significant ($> 20\%$), and the level of this impact depends on the specific stage of the CD and the k-triangle shape and size for which the bispectra are being estimated. We also find that $T_{\rm S}$ fluctuations have maximum impact on the bispectra magnitude for small k-triangles and at the stage when Lyα coupling reaches its saturation. Further, we study the impact of different heating sources, such as mini-QSOs and HMXBs, in order to investigate whether the redshift evolution of the bispectrum features (magnitude, sign and sequence of sign changes) can distinguish these sources more accurately than the power spectrum. We observe that the redshift evolution of the bispectra magnitude and sign follow a generic trend for both source models. However, the redshifts at which the bispectra magnitude reach their maximum and minimum values and the redshifts where the bispectra go through their sign changes depend on the source model. For more details, please refer to chapter 3 of the thesis or our journal article [191].

1.10.3 Chapter 4: Probing IGM physics during Cosmic Dawn using the redshifted 21-cm bispectrum

In this chapter, we demonstrate, for the first time, how the two major IGM processes, namely Lyα coupling and X-ray heating, affecting the 21-cm signal during the CD impact the magnitude and the sign of the large-scale squeezed limit 21-cm bispectrum. For this, we consider four different simulated scenarios for the evolution of the signal from the CD. The first three are simplistic and extreme scenarios in which only a single physical process dominates the fluctuations in the 21-cm signal. The fourth scenario includes all three physical processes in a self-consistent manner and therefore is the most realistic CD scenario. We demonstrate that the redshift evolution of the sign and the magnitude of the 21-cm bispectrum can disentangle the dominating contributions from Lyα coupling and X-ray heating of the IGM in a far more distinctive manner than the evolution of the global signal or the power spectrum. This opens up a new avenue probing the first luminous sources and their impact on the IGM physics during the CD. For more details, please refer to chapter 4 of the thesis or our article [192].

1.10.4 Chapter 5: Impact of the source properties on the CD 21-cm bispectrum

This chapter discusses a follow-up in depth investigation of the features of the CD 21-cm bispectrum that has been observed in the Chapter 4 by considering a wide range of properties (parameters) of the first light sources during the CD. The source properties considered here are mainly determined via two major source parameters i.e. the minimum halo mass $M_{\rm h,\,min}$ and X-ray photon production efficiency $f_{\rm X}$. In this work, for the first time, we study the impact of variation in these source parameters on the large-scale 21-cm bispectrum for all possible unique triangles in the Fourier space. Our detailed and comparative analysis of the power spectrum and bispectrum shows that the shape, sign and magnitude of the bispectrum combinedly provide a better measure of the signal fluctuations and its non-Gaussianity compared to the power spectrum. This study also firmly establishes that it is important to study the sequence of sign changes along with the variations in the shape and magnitude of the bispectrum throughout the CD history to arrive at a robust conclusion about the dominant IGM processes at different cosmic times. For more details, please refer to chapter 5 of the thesis or our article [193].

1.10.5 Chapter 6: Summary and future scopes

In this chapter, we conclude the major findings of this thesis and also discuss some of the future scopes of this work.

Chapter 2

The EoR 21-cm bispectrum and the impact of redshift space distortions on this signal statistic

---

This chapter is adapted from: Majumdar S., **Kamran M.**, Pritchard J. R., Mondal R., Mazumdar A., Bharadwaj S., Mellema G.; *Redshifted 21-cm bispectrum – I. Impact of the redshift space distortions on the signal from the Epoch of Reionization*; **Monthly Notices of the Royal Astronomical Society**; Volume 499, Issue 4, December 2020, p.5090–5106; DOI: https://doi.org/10.1093/mnras/staa3168 [arXiv:2007.06584].

2.1 Introduction

After the Big Bang the Universe gradually cooled down and once it reached a temperature of about 3000 K most of the hydrogen in the Universe went through a phase change from ionized (HII) to neutral (HI) during the so-called epoch of recombination. After this it stayed neutral until the first sources of light formed. These sources are thought to have generated enough radiation in the X-ray and ionizing UV bands (see e.g. [14, 15] for properties of the sources of reionization) to gradually heat and "re"-ionize most of the neutral hydrogen (see e.g. [1,21,48,82] for reviews). This final phase transition of hydrogen marks one of the least understood periods in the history of our universe: the Epoch of Reionization (EoR). Only a few indirect observations guide our present understanding of this epoch. These are the cosmic microwave background radiation (CMB) (see e.g. [51, 57]), the absorption spectra of high redshift quasars (see e.g. [18, 58, 59, 194]) and the luminosity function and clustering properties of Lyα emitters (see e.g. [60, 195–199]). They jointly suggest that this phase transition of hydrogen spans a wide redshift range, $6 \lesssim z \lesssim 15$ (see e.g. [23, 200–202]). However, these observations do not provide the precise duration and timing of reionization and they do not put strong constraints either on the properties of the main sources of ionization and heating nor on the typical size distribution of the ionized regions at different stages of reionization.

The redshifted 21-cm line, originating from spin-flip transitions in HI atoms, is the most promising tool for the direct observation of the EoR and can potentially answer many of its fundamental puzzles, as mentioned above. The brightness temperature of the redshifted 21-cm line directly probes the HI density at the epoch where the radiation originated. One can, in principle, track the evolution of HI during the entire reionization period by observing this line at different redshifts.

Motivated by this prospect a number of low frequency radio interferometers, such as the GMRT [97], LOFAR [67], MWA [122, 124], PAPER [123] and 21CMA [203] are competing to achieve the first statistical detection of the redshifted 21-cm signal from the EoR. However, as yet none of these has produced a successful detection of the signal, largely due to the complications of separating the signal from the $\sim 4-5$ orders of magnitude stronger foreground emission (see e.g. [93, 94, 96, 100], and system noise [108, 109]. Only weak upper limits on the expected 21-cm signal have been obtained [67, 97, 122–125].

Once an optimal method of separating the signal from the foreground contaminated data is achieved, the first generation interferometers will probably detect the signal via statistical quantities such as the variance (e.g. [115–117]), the multi-frequency angular power spectrum (e.g. [119, 120, 204, 205]) and the power spectrum (e.g. [103, 118]), as these lead to the high signal-to-noise ratios (SNR). The power spectrum has been shown to probe many important features of the signal (see e.g. [3, 79, 119, 156–159, 187, 206]) and thus can be used for the EoR parameter estimation [74, 207–210].

However, only for a Gaussian random field does the power spectrum provide a complete statistical description. The fluctuations in the EoR 21-cm signal are dictated by the interplay between the underlying matter density and the evolving distributions of the ionized regions[1]. These make the signal highly non-Gaussian. The power spectrum is incapable of capturing this non-Gaussianity in the signal, however the error in the power

[1]When the spin temperature T_{S} has saturated over the CMB temperature T_{CMB} i.e. $T_{\mathrm{S}} \gg T_{\mathrm{CMB}}$.

spectrum estimation (cosmic covariance) will be significantly affected by it [148, 163, 164]. The position dependent power spectrum, estimated by dividing a large survey volume into several smaller sub-volumes and then calculating the power spectra of those sub-volumes, can however quantify to some degree the signal correlation (mode coupling) between small and large length scales which is caused by the signal's non-Gaussianity [211].

Quantifying the non-Gaussianity of the signal requires the use of higher order statistics. One-point statistics such as the skewness and kurtosis provide a straightforward means to achieve this (see e.g. [116,117,167–169]). They capture the general level of non-Gaussianity integrated over the range of scales from which they are measured. However, as one-point statistics, they are incapable of quantifying the correlation of the signal between different length scales.

The bispectrum, which is estimated through the product of the Fourier transform of the signal for a set of three wave numbers ($\mathbf{k}$) that form a closed triangle in Fourier space, is on the other hand capable of quantifying the correlations of the signal between different Fourier modes. It is apparent that a successful detection of the signal bispectrum, the Fourier equivalent of the three point correlation function, will require more sensitivity than needed for the signal power spectrum. [212] tried to put an upper limit on the signal bispectrum using the observations with the MWA Phase II array. Measurement of the bispectrum not only characterise the non-Gaussianity of the signal but will also constitute an important confirmative detection of the EoR 21-cm signal, as any claimed measurement of the power spectrum could contain contributions from residual foregrounds or noise.

Understanding the characteristics of the EoR 21-cm bispectrum is more relevant now in view of the construction of the more sensitive next generation radio interferometers HERA [71, 103] and the SKA1-LOW [74]. SKA1-LOW is expected to see first light in around 2026. The detection and characterization of EoR 21-cm signal is one of its key science goals. As argued above, a measurement of the 21-cm bispectrum should be an integral part of this both as a confirmation of any claimed power spectrum measurement and as a quantification of the non-Gaussianity of the signal.

Theoretical efforts to characterize the EoR 21-cm bispectrum started with analytical models [161, 181] which were followed by more detailed radiative transfer and semi-numerical simulations of the signal [183–185, 213–215]. In a previous paper (hereafter Paper I [183]), we quantified the EoR 21-cm bispectrum using an ensemble of semi-numerically simulated 21-cm signals and for a variety of k-triangles (e.g. equilateral, isosceles, etc.). Through an analytical model for the 21-cm signal fluctuations, we showed that there are two competing components of the signal driving the non-Gaussianity in the signal: fluctuations in the neutral fraction ($x_{\rm HI}$) field and fluctuations in the matter density field. We further showed that the sign of the bispectrum works as a unique marker to identify which of these two components is driving the non-Gaussianity: the bispectrum will have a negative sign when the non-Gaussianity is driven by the distribution of the ionized regions and it will be positive when the non-Gaussianity is driven by the matter density fluctuations. We also proposed that this sign change in the bispectrum when viewed as a function of triangle configuration and reionization history can be used as a confirmative test for the detection of the EoR 21-cm signal. [184], using a set of semi-numerical simulations of the EoR, independently arrived at similar conclusions. [215] have studied the impact of different dark matter models on the EoR 21-cm bispectrum and have shown that the differences in the signal bispectrum is more prominent for different dark matter models compared to the differences in the signal power spectrum. Analysing a set of radiative transfer simulations of the Cosmic Dawn (CD), when X-ray heating played a crucial role in determining the brightness temperature fluctuations, [185] showed that amplitude and sign of the CD 21-cm bispectrum depends on the distribution and size of the heated regions. In a follow up work, [216] investigated how the signal bispectrum is affected by the presence of foreground signals and whether foreground mitigation through subtraction or avoidance would be better for detecting it. It should be pointed out that due to the specific definition of the bispectrum estimator used by [213, 214], these authors were unable to capture the sign of the bispectrum, which [183], [184] and [185] found to be an important feature of this statistic.

The coherent inflows and outflows of matter into overdense and underdense regions respectively, produce an additional red– or blueshift in the 21-cm signal on top of the cosmological redshift, changing the contrast of the 21-cm signal, and making it anisotropic along the LoS. This apparent LoS anisotropy in the signal is known as redshift space distortions (RSD) and was first highlighted by [79, 178] and [186] in the context of the 21-cm signal from the CD/EoR. Using analytical models for the signal they showed that the peculiar velocities will significantly change the amplitude and the shape of the 21-cm power spectrum. Their analytical predictions were later independently tested and validated through both radiative transfer and semi-numerical simulations by [3, 147, 153, 159, 160, 180, 189]. All of these studies independently report a significant change in the shape and amplitude of signal power spectrum, sometimes by a factor of ~ 3 or more depending on the k mode and stage of reionization. This implies that if the effect of RSD is not taken into account, it may lead to an incorrect interpretation of the signal.

All of the previous CD/EoR 21-cm bispectrum studies have been performed for the real space signal i.e. without taking into account redshift space distortions. In this chapter we aim to quantify the impact of RSD on the shape, amplitude and sign of the EoR 21-cm signal bispectrum at different stages of reionization using an ensemble of simulated 21-cm signals. Additionally, we present the first comprehensive view of the signal's non-Gaussianity by calculating the bispectrum for all possible unique k-triangles in Fourier space. The earlier EoR 21-cm bispectrum studies mentioned above only considered a few specific k-triangle configurations when estimating the bispectrum. We first identify all possible unique k-triangles in terms of the triangle parameters, following the formalism of [5] and then estimate the spherically averaged real and redshift space bispectra to quantify the impact of the redshift space distortions. Lastly, we provide a physical interpretation of our results based on the quasi-linear model of brightness temperature fluctuations proposed by [159].

The structure of this chapter is as follows. In Section 2.2, we briefly describe the algorithm that we adopt to estimate the bispectrum from the simulated signal. We also define the unique triangle configurations (Section 2.2.2) that we consider for our bispectra estimation. Section 2.4 briefly describes our method to generate mock 21-cm data sets. In Section 2.5, we discuss and interpret our estimated bispectra for all unique triangle configurations as well as a quasi-linear model to understand the results (Section 2.3). Finally, in Section 2.6 we summarise our findings.

Throughout this chapter, we have used the Planck+WP best fit values of cosmological parameters $h = 0.6704$, $\Omega_{\rm m} = 0.3183$, $\Omega_\Lambda = 0.6817$, $\Omega_{\rm b}h^2 = 0.022032$, $\sigma_8 = 0.8347$ and $n_s = 0.9619$ [52].

2.2 Bispectrum estimation for all unique triangle configurations

2.2.1 Bispectrum estimator for the simulated 21-cm signal

The bispectrum $B_{\rm b}(\mathbf{k}_1, \mathbf{k}_2, \mathbf{k}_3)$ of the 21-cm brightness temperature fluctuations $\delta T_{\rm b}(\mathbf{x})$ can be defined as

$$\langle \Delta_{\rm b}(\mathbf{k}_1)\Delta_{\rm b}(\mathbf{k}_2)\Delta_{\rm b}(\mathbf{k}_3)\rangle = V\delta^{\rm K}_{\mathbf{k}_1+\mathbf{k}_2+\mathbf{k}_3,0}\, B_{\rm b}(\mathbf{k}_1, \mathbf{k}_2, \mathbf{k}_3)\,, \tag{2.1}$$

where $\Delta_{\rm b}(\mathbf{k})$ is the Fourier transform of $\delta T_{\rm b}(\mathbf{x})$ and $\delta^{\rm K}_{\mathbf{k}_1+\mathbf{k}_2+\mathbf{k}_3,0}$ is the Kronecker delta function, equal to 1 when $\mathbf{k}_1 + \mathbf{k}_2 + \mathbf{k}_3 = 0$ and 0 otherwise. The $\delta^{\rm K}_{\mathbf{k}_1+\mathbf{k}_2+\mathbf{k}_3,0}$ ensures that only those $\mathbf{k}$ triplets contribute to the bispectrum which form a closed triangle (see left

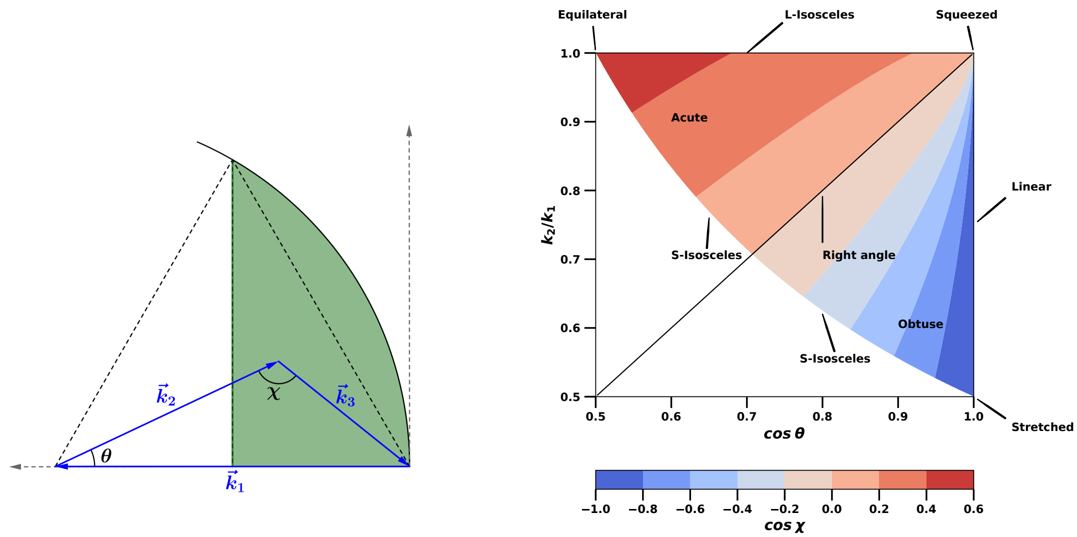

Figure 2.1: The left panel shows the definition of unique triangles in **k**-space. The right panel shows the variation of $\cos\chi$ with k_2/k_1 and $\cos\theta$ in unique triangles. The unique triangle parameter space is defined following [5].

panel of Figure 2.1). The angular brackets denote ensemble average of the target statistic. For brevity we drop the subscript "b" when describing the brightness temperature from this point on-wards.

The estimator, that one can use to compute the bispectrum from the observed or simulated data, can be defined for the $m^{\rm th}$ triangle configuration bin as

$$\hat{B}_m(\mathbf{k}_1, \mathbf{k}_2, \mathbf{k}_3) = \frac{1}{N_{\rm tri} V} \sum_{[\mathbf{k}_1+\mathbf{k}_2+\mathbf{k}_3=0]\in m} \Delta(\mathbf{k}_1)\Delta(\mathbf{k}_2)\Delta(\mathbf{k}_3)\,, \tag{2.2}$$

where $N_{\rm tri}$ is the number of closed triangles contributing to the $m^{\rm th}$ triangle bin for which one estimates the bispectrum. As discussed in detail in section 2 of Paper I, the bispectrum of a real field such as the 21-cm signal, also is a real quantity.

To estimate the bispectra from the simulated signal cubes we adopt the method described in Paper I. This method is a direct implementation of Equation (2.2) along with the following two equations of constraints:

$$k_2/k_1 = n\,, \tag{2.3}$$

and

$$\frac{\mathbf{k}_1.\mathbf{k}_2}{k_1 k_2} = -\cos\theta\,. \tag{2.4}$$

The angle θ (between $\mathbf{k_1}$ and $\mathbf{k_2}$) is defined in Figure 2.1. Using the above equations one can parametrize the triangle configurations in terms of the values of k_1, n and $\cos\theta$, which jointly determine the size and shape of the triangle. Another way of interpreting the shape of the triangle is through the angle χ, the angle between arms k_2 and k_3 of the k-triangle, which is dependent on n and $\cos\theta$ via

$$\cos\chi = \frac{n^2 + [1 + n^2 - 2n\cos\theta] - 1}{2n\sqrt{1 + n^2 - 2n\cos\theta}}\,. \tag{2.5}$$

The computationally intensive part of the bispectrum estimation algorithm is the search for closed $\mathbf{k}$-triangles in a gridded Fourier space. Equations (2.3) and (2.4) effectively eliminate two nested *for* loops from the triangle search algorithm. This makes the calculation of bispectra from gridded data much more efficient. For a more detailed discussion of this method of bispectrum estimation we refer the reader to section 2 of Paper I.

2.2.2 Unique k_1-triangle configurations

In Paper I, our analysis of 21-cm bispectrum was limited to only a few types of $\mathbf{k}$-triangles, namely equilateral, isosceles and triangles with $n = 2$, 5, and 10. A comprehensive view of the signal non-Gaussianity as captured by the bispectrum requires the calculation of the bispectrum for all possible $\mathbf{k}$-triangles. However, not all $\mathbf{k}$-triangles will be unique in their shape and size. To identify unique $\mathbf{k}$-triangles in the Fourier space we follow the definition of [5] and impose the following additional conditions:

$$k_1 \geq k_2 \geq k_3 \tag{2.6}$$

$$0.5 \leq \cos\theta \leq 1.0 \tag{2.7}$$

$$0.5 \leq n \leq 1.0\,. \tag{2.8}$$

The triangles that satisfy these conditions are confined to the region of the $n - \cos\theta$ parameter space where $n\cos\theta \geq 0.5$. This effectively means that the location of the tip which connects $\mathbf{k_2}$ and $\mathbf{k_3}$, as we vary $\cos\theta$ and n, will be restricted to the shaded region shown in the left panel of Fig. 2.1. Any triangle that falls outside of this region, can be transformed into one that does by relabelling its sides. Note that Equation (2.6) ensures that in this parameterization of unique k-triangles, $\mathbf{k_1}$ remains the largest side under all circumstances. This point is important as we bin our bispectra estimates based on the value of k_1.

For ease of identification of k-triangles of different shapes in $n - \cos\theta$ parameter space we indicate them in the right panel of Fig. 2.1 and also list them here:

- L-isosceles are triangles with $n = 1.0$ and $0.5 \lesssim \cos\theta \lesssim 1.0$ i.e. $0 \lesssim \cos\chi \lesssim 0.5$. These triangles have $k_1 = k_2$.
- The $n\cos\theta = 0.5$ arc in the parameter space defines S-isosceles triangles. These triangles have $k_2 = k_3$.
- The junction of the L and S isosceles triangles represents equilateral triangle i.e. $\cos\theta = 0.5$ and $n = 1.0$ (i.e. $\cos\chi = 0.5$).
- Triangles with $\cos\theta \to 1.0$ and $0.5 \lesssim n \lesssim 1.0$ are linear triangles. At these limits all three ks become collinear (i.e. $\cos\chi \to -1.0$).
- Triangles with $\cos\theta = n$ are right angle triangles (i.e. $\cos\chi = 0$).
- The junction of L-isosceles, linear and right angle triangles represents squeezed triangles where $\cos\theta = n = 1.0$ (i.e. $\cos\chi = 0$). For squeezed triangles the smallest arm $k_3 \to 0$.
- The junction of S-isosceles and linear triangles defines stretched triangles where $\cos\theta = 1.0$ and $n = 0.5$ (i.e. $\cos\chi = -1.0$).
- Triangles with $\cos\theta < n$ are acute angle triangles (i.e. $\cos\chi > 0$).
- Triangles with $\cos\theta > n$ are obtuse angle triangles (i.e. $\cos\chi < 0$).

To estimate bispectra from the simulated signal cubes we have divided the region $n\cos\theta \geq 0.5$ in the triangle parameter space into a grid of resolution $\Delta\cos\theta = 0.01$, $\Delta n = 0.05$. Additionally, we have divided the entire k_1 range (defined by $k_{\rm min} = 2\pi/[\text{box size}]$ and $k_{\rm max} = 2\pi/2[\text{grid spacing}]$) into 15 logarithmic bins. For our simulation data (see Section 2.4) $k_{\rm min} = 0.03\ {\rm Mpc}^{-1}$ and $k_{\rm max} = 5.61\ {\rm Mpc}^{-1}$. The estimated bispectra are averaged over these k_1 bins.

2.3 Quasi-linear model for the redshift space EoR 21-cm bispectrum

The main aim of this chapter is to quantify the impact of the redshift space distortions on the EoR 21-cm bispectrum, an effect which has not been considered in any of the previous studies. However, it would be easier to interpret this impact if we can analyze it with the help of an analytical model (e.g. [158,159,178]). In this section we use the prescription of [159] to construct such a model for the redshift space 21-cm bispectrum.

The redshift space bispectrum depends on how the three vectors $\mathbf{k_1}$, $\mathbf{k_2}$ and $\mathbf{k_3}$, that form a closed triangle in the Fourier space, are oriented with respect to the LoS. We use μ_1, μ_2 and μ_3 respectively to denote the cosine of the angles that $\mathbf{k_1}$, $\mathbf{k_2}$ and $\mathbf{k_3}$ make with the LoS. However, as pointed out by [5], μ_1, μ_2 and μ_3 are not independent of each other, in fact they refer to a particular triangle whose shape and size are fixed for a fixed set of values of k_1, n and $\cos\theta$. These authors also showed that all possible orientations of a triangle of fixed shape and size with respect to the LoS can be obtained by performing rigid body rotations of the triangle (see sections 2 and 3 of [5] for more details). This is a crucial point that should be kept in mind while interpreting the redshift space spherically averaged signal bispectrum.

Adopting the quasi-linear model of [159], the redshift space 21-cm bispectrum for a fixed $\mathbf{k}$-triangle can be written as the sum of different auto and cross bispectra between two fields, namely the total hydrogen density ($\rho_{\rm H}$) and the neutral hydrogen density ($\rho_{\rm HI}$):

$$
\begin{aligned}
B^{\rm s,qlin}(\mathbf{k_1}, \mathbf{k_2}, \mathbf{k_3}) = \left(\widehat{\delta T_{\rm b}}\right)^3 \Big[& B^r_{\Delta_{\rho_{\rm HI}}, \Delta_{\rho_{\rm HI}}, \Delta_{\rho_{\rm HI}}} + \\
& \left(\mu_3^2 B^r_{\Delta_{\rho_{\rm HI}}, \Delta_{\rho_{\rm HI}}, \Delta_{\rho_{\rm H}}} + \mu_2^2 B^r_{\Delta_{\rho_{\rm HI}}, \Delta_{\rho_{\rm H}}, \Delta_{\rho_{\rm HI}}} + \mu_1^2 B^r_{\Delta_{\rho_{\rm H}}, \Delta_{\rho_{\rm HI}}, \Delta_{\rho_{\rm HI}}}\right) \\
& + \left(\mu_1^2\mu_2^2 B^r_{\Delta_{\rho_{\rm H}}, \Delta_{\rho_{\rm H}}, \Delta_{\rho_{\rm HI}}} + \mu_1^2\mu_3^2 B^r_{\Delta_{\rho_{\rm H}}, \Delta_{\rho_{\rm HI}}, \Delta_{\rho_{\rm H}}} + \mu_2^2\mu_3^2 B^r_{\Delta_{\rho_{\rm HI}}, \Delta_{\rho_{\rm H}}, \Delta_{\rho_{\rm H}}}\right) \\
& + \mu_1^2\mu_2^2\mu_3^2 B^r_{\Delta_{\rho_{\rm H}}, \Delta_{\rho_{\rm H}}, \Delta_{\rho_{\rm H}}} \Big],
\end{aligned} \tag{2.9}
$$

where

$$
\widehat{\delta T_{\rm b}}(z_{\rm cos}) = 27\bar{x}_{HI}(z_{\rm cos}) \left(\frac{\Omega_{\rm b}h^2}{0.023}\right) \left(\frac{0.15}{\Omega_{\rm m}h^2} \frac{1+z_{\rm cos}}{10}\right)^{1/2} {\rm mK} \tag{2.10}
$$

and the superscripts s and r represent terms in redshift and real space, respectively. It is convenient to represent the anisotropy in the signal bispectrum by decomposing it in the orthonormal basis of spherical harmonics Y_ℓ^m. The different angular multipole moments of the RSD bispectrum thus can be expressed as:

$$\begin{aligned}\bar{B}^m_\ell(k_1, n, \cos\theta) = \left(\widehat{\delta T_{\rm b}}\right)^3 \Big[&\delta_{\ell,0} B^r_{\Delta_{\rho_{\rm HI}},\Delta_{\rho_{\rm HI}},\Delta_{\rho_{\rm HI}}} \\ &+ \Big([\overline{\mu_3^2}]^m_\ell B^r_{\Delta_{\rho_{\rm HI}},\Delta_{\rho_{\rm HI}},\Delta_{\rho_{\rm H}}} + [\overline{\mu_2^2}]^m_\ell B^r_{\Delta_{\rho_{\rm HI}},\Delta_{\rho_{\rm H}},\Delta_{\rho_{\rm HI}}} \\ &\quad + [\overline{\mu_1^2}]^m_\ell B^r_{\Delta_{\rho_{\rm H}},\Delta_{\rho_{\rm HI}},\Delta_{\rho_{\rm HI}}} \Big) \\ &+ \Big([\overline{\mu_1^2\mu_2^2}]^m_\ell B^r_{\Delta_{\rho_{\rm H}},\Delta_{\rho_{\rm H}},\Delta_{\rho_{\rm HI}}} + [\overline{\mu_1^2\mu_3^2}]^m_\ell B^r_{\Delta_{\rho_{\rm H}},\Delta_{\rho_{\rm HI}},\Delta_{\rho_{\rm H}}} \\ &\quad + [\overline{\mu_2^2\mu_3^2}]^m_\ell B^r_{\Delta_{\rho_{\rm HI}},\Delta_{\rho_{\rm H}},\Delta_{\rho_{\rm H}}} \Big) \\ &+ [\overline{\mu_1^2\mu_2^2\mu_3^2}]^m_\ell B^r_{\Delta_{\rho_{\rm H}},\Delta_{\rho_{\rm H}},\Delta_{\rho_{\rm H}}} \Big] . \end{aligned} \tag{2.11}$$

The $\bar{B}^m_\ell$ here represents the value of a specific multipole averaged over all possible orientations of a fixed triangle. In this chapter we are interested in the spherically averaged redshift space signal bispectrum, which is nothing but the monopole moment of the Equation (2.9), i.e. Equation (2.11) for $m = 0$ and $\ell = 0$. For the monopole moment[2], different coefficients in Equation (2.11) will take the form

$$\delta_{0,0} = 1\,, \tag{2.12}$$

$$[\overline{\mu_1^2}]^0_0 = [\overline{\mu_2^2}]^0_0 = [\overline{\mu_3^2}]^0_0 = \frac{1}{3}\,, \tag{2.13}$$

$$[\overline{\mu_1^2\mu_2^2}]^0_0 = \frac{1}{15}\left(2\cos^2\theta + 1\right)\,, \tag{2.14}$$

$$[\overline{\mu_2^2\mu_3^2}]^0_0 = \frac{2\cos^2\theta + 3n^2 - 6n\cos\theta + 1}{15s^2}\,, \tag{2.15}$$

$$[\overline{\mu_3^2\mu_1^2}]^0_0 = \frac{\left(2\cos^2\theta + 1\right)n^2 - 6n\cos\theta + 3}{15s^2}\,, \tag{2.16}$$

$$[\overline{\mu_1^2\mu_2^2\mu_3^2}]^0_0 = \frac{4\left(n^2+1\right)\cos^2\theta + n^2 - 4n\cos^3\theta - 6n\cos\theta + 1}{35s^2}\,, \tag{2.17}$$

where $s = \sqrt{1 - 2n\cos\theta + n^2}$.

The above equations demonstrate that out of the eight coefficients of the monopole moment, four are dependent on the shape of the triangle (Equations (2.14)- (2.17)). These

[2]To quantify the impact of the RSD precisely one in principle would need to estimate all non-zero angular multipole moments of Equation (2.9), the direction dependent bispectrum (see e.g. [217]). However, our aim here is to quantify the impact of RSD on the spherically averaged bispectrum. This is why we concentrate only on the monopole moment of the RSD bispectrum in this chapter.

shape dependent coefficients vary in the range[3] $0.01 - 0.20$. Equation (2.11) also shows that in the absence of any redshift space distortions, the observed spherically averaged 21-cm bispectrum i.e. the monopole of Equation (2.11) will reduce to $\left(\widehat{\delta T_{\rm b}}\right)^3 B^r_{\Delta_{\rho_{\rm HI}}\Delta_{\rho_{\rm HI}},\Delta_{\rho_{\rm HI}}}$ (first term in the R.H.S.). We thus identify all R.H.S. terms apart from the first one as the redshift space correction (RC) terms to the real space spherically averaged bispectrum ($m = 0$, and $\ell = 0$). Among the seven RC terms we label the sum of the first three terms as $B_{\mu^2-\rm RC}$, the sum of the next three as $B_{\mu^4-\rm RC}$ and the last as $B_{\mu^6-\rm RC}$. We will use Equation (2.11) together with these notations as a tool to provide some physical interpretation of the simulated redshift space 21-cm bispectra below in Section 2.5.2.2.

2.4 Simulating the redshifted 21-cm signal from the EoR

For our study we use the redshifted EoR 21-cm brightness temperature maps from the simulations of [164] at the seven different redshifts 13, 11, 10, 9, 8, 7.5 and 7. In this section we briefly summarize the semi-numerical technique used to generate the redshifted signal. A detailed description of these simulations can be found in [120, 164]. Our simulation method for the 21-cm signal is divided into three main steps. In the first step, we generate dark matter distributions at the desired redshifts using a publicly available parallelized particle mesh (PM) N-body code[4]. In the second step, we identify collapsed dark matter halos using a publicly available Friends-of-Friend (FoF) code[5]. The final step is to generate ionization fields using a publicly available semi-numerical reionization code[6] which is based on the excursion set formalism of [145]. The third step closely follows the inside-out reionization model of [206]. Here the assumptions are that the hydrogen follows the underlying matter distribution and that luminous sources form within the halos. Finally, the resulting neutral hydrogen fields are mapped to redshift space to generate the redshifted 21-cm signal following [180].

The N-body simulation was run for a comoving volume $V = [215.04\,{\rm Mpc}]^3$ (using a 3072^3 grid) with a spatial resolution of 70 kpc and a mass resolution $1.09\times10^8\,M_\odot$. We use the N-body particle positions to generate the HI density field, and particle velocities to generate the velocities of HI particles. Halos were identified using a linking length of 0.2 times

[3]The detailed k-triangle shape dependence of these four coefficients are shown in Figure A.1 in the Appendix A.1.

[4]https://github.com/rajeshmondal18/N-body

[5]https://github.com/rajeshmondal18/FoF-Halo-finder

[6]https://github.com/rajeshmondal18/ReionYuga

the mean inter-particle separation. We also require a halo to have a minimum of 10 dark matter particles which corresponds to a minimum halo mass $M_{\rm halo,\,min} = 1.09 \times 10^9\, M_\odot$ (see e.g. [206] for a detailed justification for this halo and particle mass threshold). The number of ionizing photons emitted by a source is assumed to be proportional to the mass of its host halo with a dimensionless proportionality constant $N_{\rm ion}$. The reionization process was simulated on a coarser 384^3 grid with spacing 0.56 Mpc using the density fields and the ionizing photon fields. We determine whether a grid point is completely ionized or not by smoothing the hydrogen density fields and the ionizing photon fields using spheres of different radii starting from the grid spacing to $R_{\rm mfp}$. Here, $R_{\rm mfp}$ is a free parameter in the simulations, and analogous to the mean free path of the ionizing photons. A grid point is considered to be completely ionized if for any smoothing radius, the smoothed photon density exceeds the smoothed hydrogen density at that grid point.

For our fiducial model, we assume that the universe is 50% ionized (the mass averaged neutral fraction $\bar{x}_{\rm HI} \approx 0.5$) by $z = 8$, $R_{\rm mfp} = 20\,{\rm Mpc}$ [218] and $N_{\rm ion} = 23.2$. We also ensure that reionization ends by $z \sim 6$ and that the Thomson scattering optical depth is consistent with [57].

2.5 Results

There are various ways in which one could normalize the bispectrum. One popular normalization method, mostly used in the analysis of the large scale structures of the Universe, is to use the reduced bispectrum Q defined as $Q(k_1, k_2, k_3) = B(k_1, k_2, k_3)/\big[P(k_1)P(k_2) + P(k_2)P(k_3) + P(k_3)P(k_1)\big]$. This particular normalization approach is motivated by the linear perturbation theory of the density fluctuations. In the scenarios where the target field has weak non-Gaussianity, the linear perturbation theory can provide a very good approximation of the field bispectrum using different combinations of the products of the field power spectrum ([219, 220]). However, the EoR 21-cm field is expected to be highly non-Gaussian (with a significant evolution with cosmic time) in nature. Thus, this approach (i.e. via $Q(k_1, k_2, k_3)$) of normalizing the bispectrum would not be ideal. The second approach of normalizing the bispectrum could be via $b(k_1, k_2, k_3) = B(k_1, k_2, k_3)/\sqrt{(k_1, k_2, k_3)^{-1} P(k_1)P(k_2)P(k_3)}$. There is an widespread use of this approach in the domain of signal processing and it was introduced by [221]. This has also been used for the analysis of 21-cm bispectrum from the cosmic dawn by [185]. As argued by [185] and others this particular normalization of bispectrum (via $b(k_1, k_2, k_3)$) will effectively wash out the magnitude of the bispectrum and will retain only the phase coupling between different k modes. However, in this chapter we are interested in exploring all possible features (both magnitude and sign) and their evolution (across cosmic time and size and shape of k triangles) of the bispectrum statistic. Additionally, if one plans to use 21-cm bispectrum as the target statistic to constrain the parameters of EoR, it will be imperative to use both the magnitude as well as the phase coupling information contained within the bispectrum to put a tighter constrain on the inferred parameter values (e.g. in case of the parameter estimation using power spectrum both the magnitude as well as the shape of the statistic is used). Therefore, throughout this chapter we choose to normalize the spherically averaged bispectrum via $\left[k_1^3 k_2^3 B(k_1, k_2, k_3)/(2\pi^2)^2\right]$, unless otherwise specified.

Following the discussion in Section 2.2 we parameterize all of the estimated bispectra from simulations with three parameters: n, $\cos\theta$ and k_1. As discussed in Section 2.2, we only consider the bispectra from k-triangles that satisfy the uniqueness condition, $n\cos\theta \geq 0.5$. In discussing the results below, we focus on bispectra with $k_1 = 0.20, 0.58, 1.18, 2.37\,\mathrm{Mpc}^{-1}$ and designate these triangles as *small*, *intermediate*, *large* and *largest*.[7] Furthermore, we analyze the 21-cm bispectra at four different stages of reionization corresponding to mass averaged neutral fractions $\bar{x}_{\mathrm{HI}} = 0.93, 0.73, 0.49, 0.32$, labelled as *very early*, *early*, *middle* and *late* stages of reionization respectively.

2.5.1 EoR 21-cm bispectrum in real space

As they have not before been presented in this representation, we first show the real space EoR 21-cm bispectra for all unique triangles in the n-$\cos\theta$ space (Figure 2.2). The first important point to note from this figure is that for almost the entire unique triangle parameter space and for all phases of reionization, the 21-cm bispectra are non-zero. This is direct evidence that the signal is highly non-Gaussian. We also notice that the magnitudes and signs of the bispectra depend on three factors, the k-triangle shape, the value of the k_1 mode and the stage of reionization. To better understand the relation of the magnitude and sign of the bispectra to these three factors, we show in Figure 2.3 the bispectra for the limiting values of k-triangle parameters in the n-$\cos\theta$ space (linear and L-isosceles limits for *small* and *large* k_1-triangles at all four stages of the EoR).

A careful analysis of Figures 2.2 and 2.3 reveals that for *small* k_1-triangles bispectra are

[7] Note that due to our limited simulation volume, the triangle bins with $k_1 < 0.20\,\mathrm{Mpc}^{-1}$ are severally affected by the sample variance. For a given k_1 mode, the number of closed triangles in a triangle bin for bispectrum calculation are minimum at the linear and the squeezed limit. For example for $k_1 = 0.20\,\mathrm{Mpc}^{-1}$ bin the minimum number of triangles at the squeezed limit is ~ 100 and at the linear limit it is $\sim 100 - 1000$, whereas for other triangle shapes it varies between $\sim 1000 - 50000$.

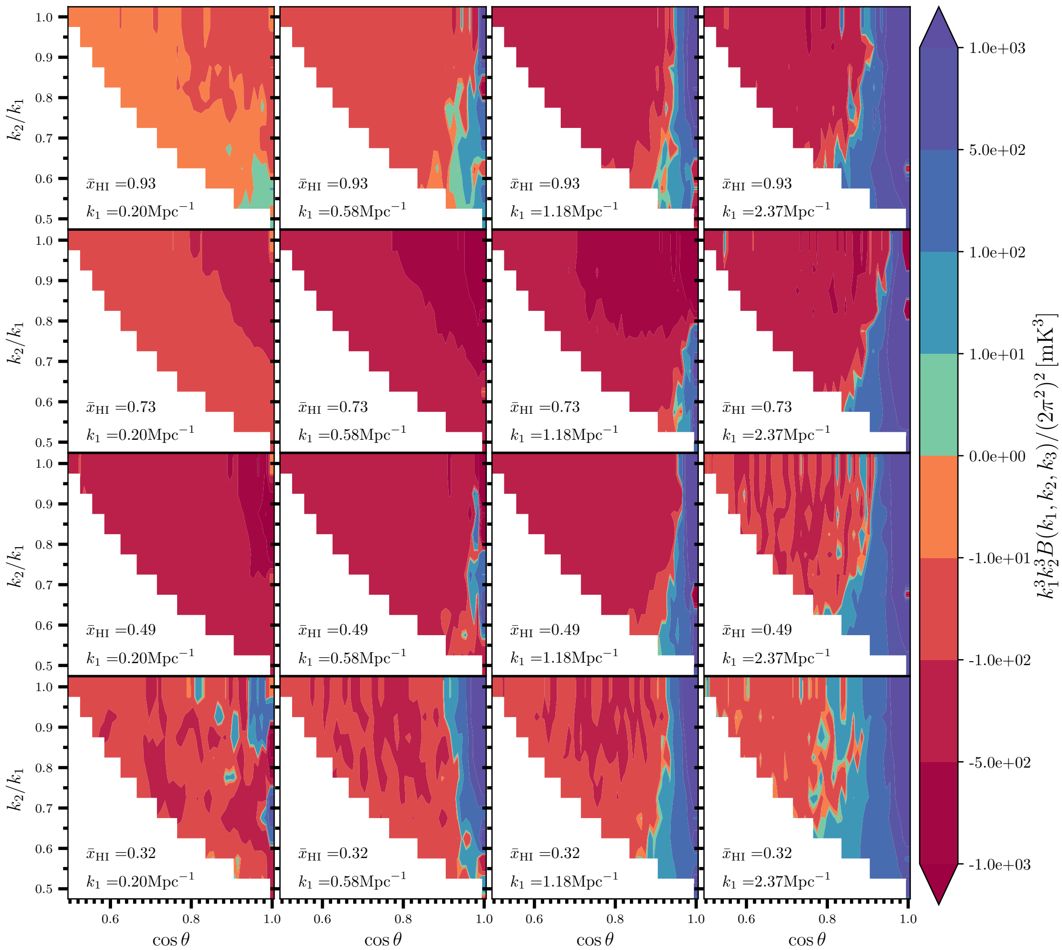

Figure 2.2: The real space bispectra for all unique triangle configurations at four different stages of the EoR and for four different k_1 modes.

negative in most of the unique n-$\cos\theta$ space during the entire period of the reionization. The magnitude of the bispectra initially increases with decreasing $\bar{x}_{\rm HI}$ and reaches its maximum value around the *middle* stages of the EoR, after which the magnitude decreases with decreasing $\bar{x}_{\rm HI}$. For a fixed $\bar{x}_{\rm HI}$, the magnitude of the bispectra increases along the L-isosceles line with increasing $\cos\theta$ and for linear triangles the magnitude increases with increasing n. The largest magnitudes are obtained for bispectra from the squeezed limit triangles. This is true for almost all stages of reionization.

For the *intermediate* k_1-triangles the bispectra show a similar trend as for the *small* k_1-triangles. A notable exception is that the former become positive at the linear limit of triangles during the *late* stages of the EoR. The overall magnitude of the bispectra for almost all shapes of k-triangles are larger for *intermediate* k_1-triangles than for *small*

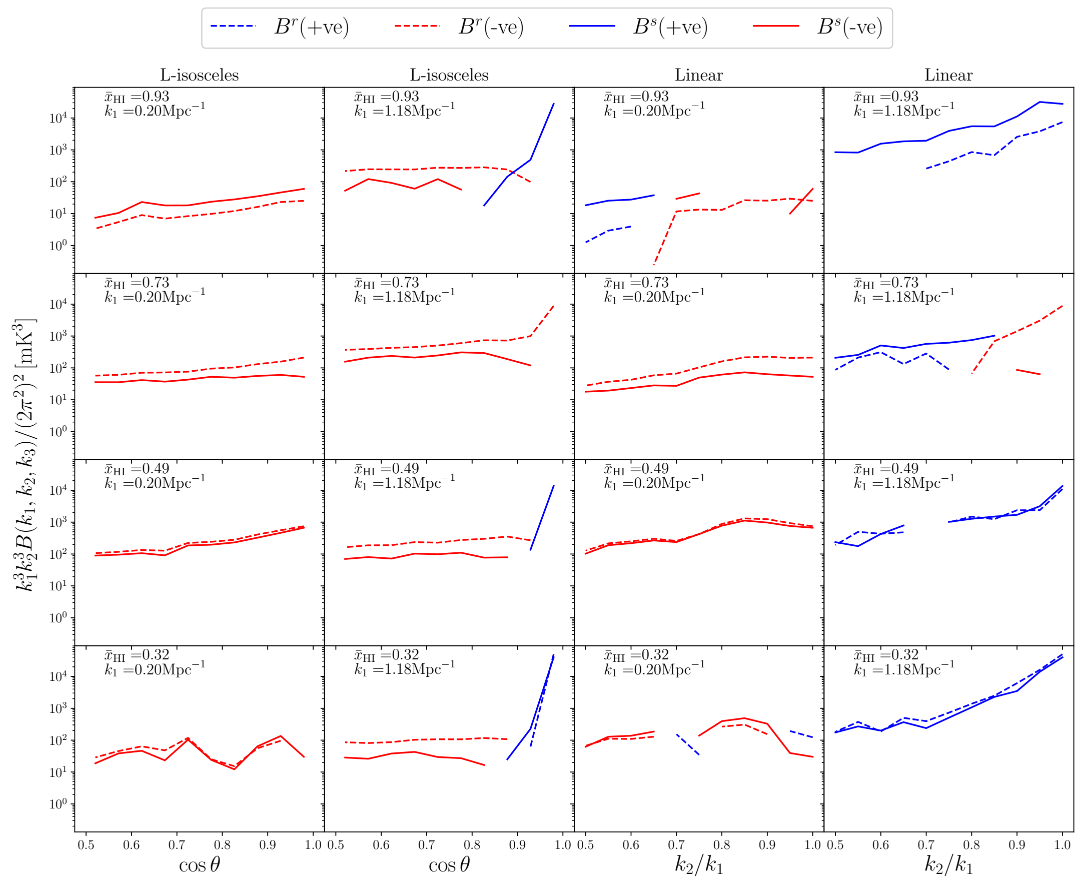

Figure 2.3: The bispectra in real (B^r) and redshift space (B^s) for the limiting values of k-triangle parameters. The solid lines and dashed lines represent bispectra in redshift and real space respectively. The red and blue colours represent negative and positive values of the bispectra respectively. The bispectra are shown at four different stages of the EoR and for two different k_1 modes (small and large).

k_1-triangles.

The bispectra for the *large* k_1-triangles show even larger magnitudes. This increase is more prominent around linear triangles. In addition, these bispectra become positive in an increasingly larger area of the n-$\cos\theta$ space, around the linear triangles, for decreasing $\bar{x}_{\rm HI}$.

This trend of increase in the area of the n-$\cos\theta$ space where bispectra is positive with the increase in k_1 magnitude is seen to continue for the *largest* k_1-triangles as well. The area of the n-$\cos\theta$ space around the linear triangles where the bispectra become positive, is even larger for this case. However, the magnitude of the bispectra for the *largest* k_1-triangles monotonically decreases with the progress of the reionization. This is a feature that is opposite of the trend seen for the *small*, *intermediate* and *large* k_1-triangles.

The k_1 value, triangle shape and $\bar{x}_{\mathrm{HI}}$ dependence of the bispectra magnitude observed in Figure 2.2 and 2.3 and discussed above can be interpreted in the following manner: the signal's non-Gaussianity is relatively small at large scales during the *very early* stages of the EoR. This can be understood from the fact that although the fluctuations in the 21-cm signal during these early stages are dominated by the fluctuations introduced by the HII regions, the HII regions are still very small in size. Thus the overall amplitude of fluctuations in the signal is relatively low in magnitude compared to the signal from the later stages of the EoR. When we probe bispectra for triangles with *intermediate, large* and *largest* k_1 modes, the magnitude of the bispectra increases as they become increasingly sensitive to the small HII regions (left to right, top two rows of the Figure 2.2). Furthermore, the gradual increase in bispectra magnitude with decreasing $\bar{x}_{\mathrm{HI}}$ and peaking around $\bar{x}_{\mathrm{HI}} \sim 0.5$ is directly related to the gradual increase in the signal fluctuations (and non-Gaussianity) due to the progress of reionization until we reach a significant amount of percolation among the HII regions. Furthermore, progress in reionization changes the topology of the 21-cm signal and for $\bar{x}_{\mathrm{HI}} \lesssim 0.5$ it is dictated by the size and distribution of the neutral regions rather than of the ionized regions. The bispectra for triangles with the *largest* k_1 modes see a decrease in magnitude with the decreasing $\bar{x}_{\mathrm{HI}}$. This is caused by the fact that as reionization progresses the sizes and number density of the HII regions gradually increase which leads to a decrease of the signal fluctuations at smaller length scales [222].

The sign reversal of the bispectra discussed above is an important phenomenon, which has been reported earlier in the context of the 21-cm signal from the EoR in [183] and [184] and in the context of the 21-cm signal from the CD in [185]. However, all of these previous studies have reported this sign change for a few specific types of triangles. Here we demonstrate the evolution in bispectra sign across all unique triangle types, k_1 modes and stages of reionization.

2.5.2 EoR 21-cm bispectrum in redshift space

2.5.2.1 Impact of the RSD on the 21-cm bispectra

Next, we quantify the impact of the RSD on the monopole moment of the 21-cm bispectra. Figure 2.4 shows the spherically averaged redshift space bispectra for all unique k-triangles in the n-$\cos\theta$ space. Similar to the case of the real space bispectra, in Figure 2.3 we also

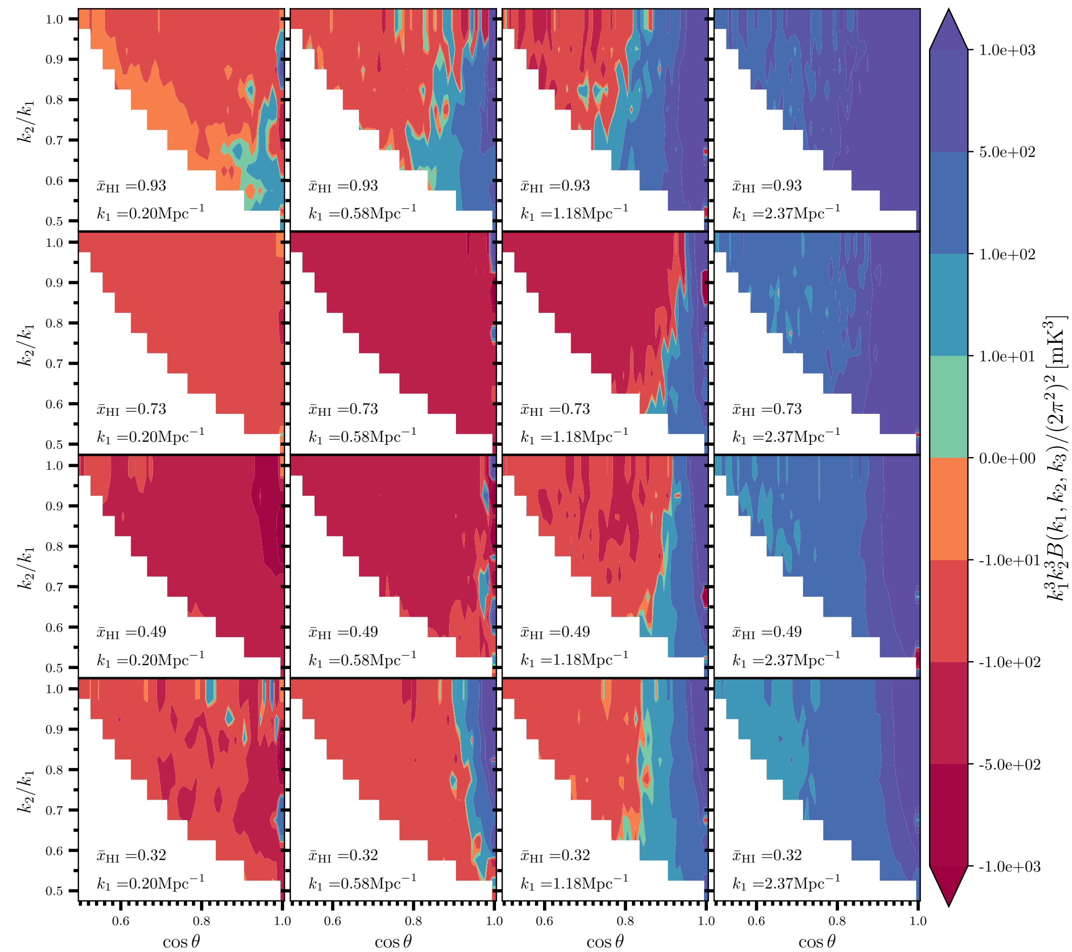

Figure 2.4: The redshift space bispectra for all unique triangle configurations at four different stages of the EoR and for four different k_1 modes.

show the redshift space bispectra for the limiting values of k-triangle parameters in the n-$\cos\theta$ space (linear and L-isosceles limits for *small* and *large* k_1-triangles at all four stages of the EoR).

A quick qualitative visual comparison of Figures 2.2, 2.4 and 2.3 reveals many of the important effects RSD has on the signal bispectra. The first is that both the magnitude and the sign of the bispectra are affected. For *small* k_1-triangles and at *very early* stages of the EoR, RSD manifests itself through a large boost in the magnitude values. Similarly, the magnitude of the bispectra for *large* k_1-triangles also get boosted at this stage and in addition they also show a sign change. As reionization progresses, we see an opposite effect on the magnitudes, as they are smaller for the RSD case for both *small* and *large* k_1-triangles. It is further clearly visible from Figure 2.4 that the area in the n-$\cos\theta$ space

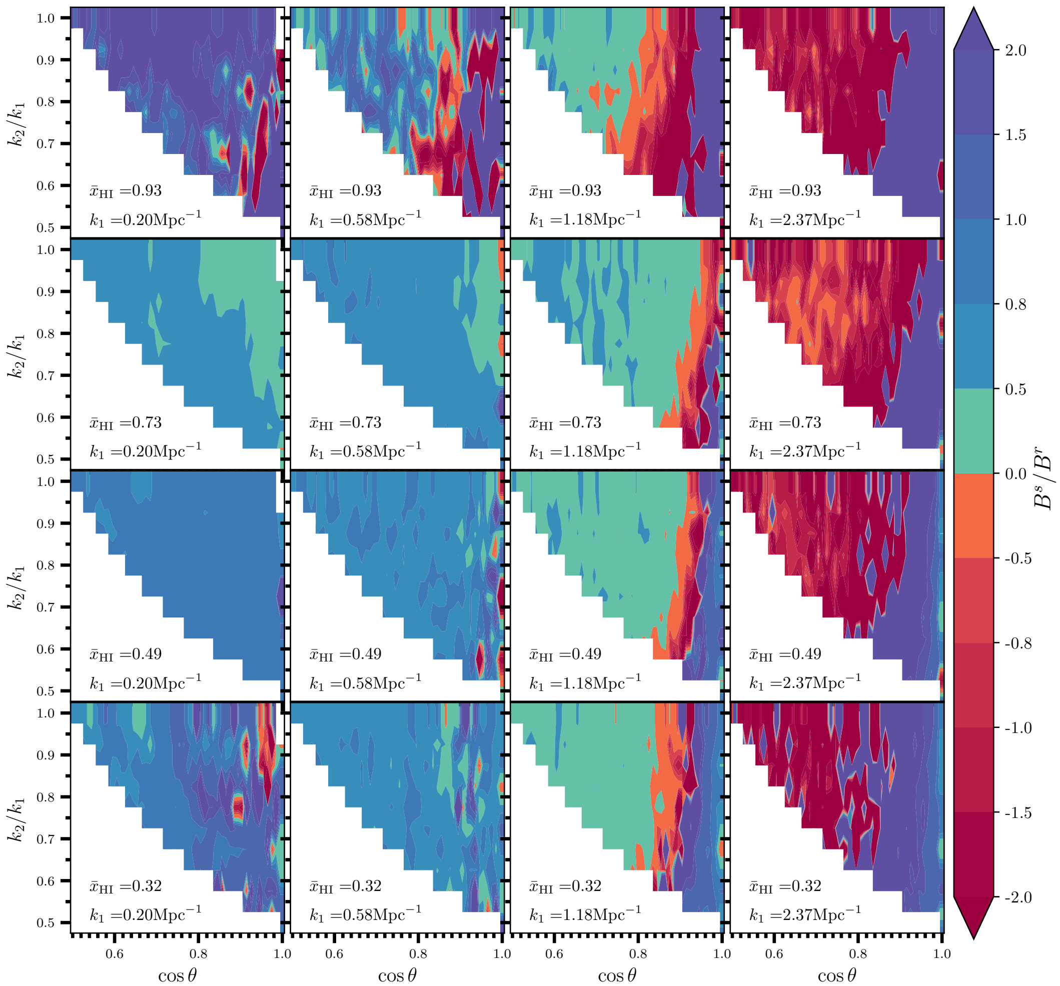

Figure 2.5: The ratio between the redshift space and real space bispectra for all unique triangle configurations at four different stages of the EoR and for four different k_1 modes.

where the bispectra become positive for *large* k_1-triangles, is larger when RSD is applied. For the *largest* k_1-triangles, RSD makes the bispectra positive for the entire unique n-$\cos\theta$ space at all stages of the EoR.

To quantify the impact of the RSD in detail, we show the ratio of spherically averaged bispectra in redshift and real space, i.e. B^s/B^r in Figure 2.5. We discuss this ratio in order of increasing k_1 values. Starting with the *small* k_1-triangles we notice that during the *very early* stages of the EoR, RSD enhances the magnitude of the bispectra by more than 50% in almost the entire unique k-triangle space. However, as reionization progresses (*early* stages), RSD reduces the amplitudes of the bispectra, by $\sim 50\%$ around the squeezed and

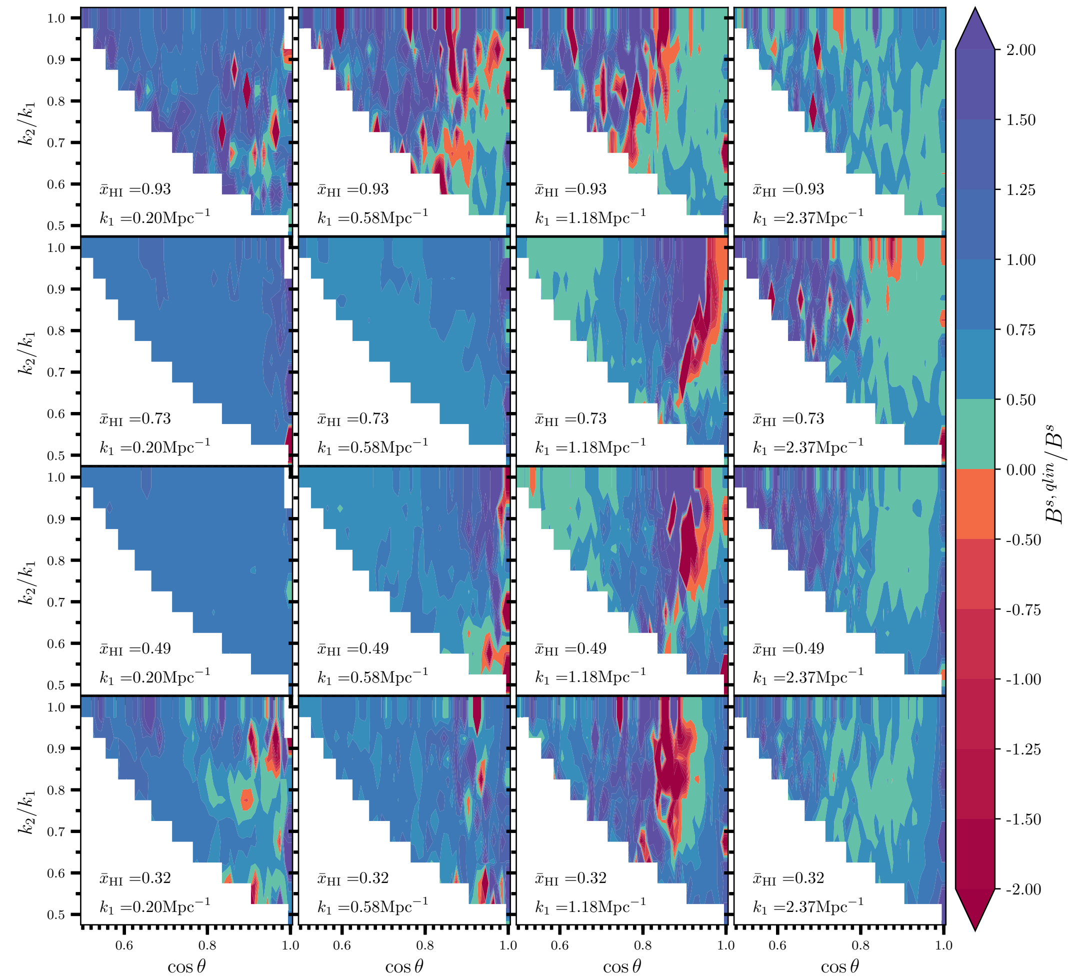

Figure 2.6: This figure shows $B^{\rm s,\,qlin}/B^{\rm s}$ for all unique triangle configurations at four different stages of the EoR and for four different k_1 modes.

linear limit and by $\sim 20-50\%$ for the other k_1-triangles. During the *middle* and *late* stages of the reionization, RSD continues to reduce the amplitude of the bispectra but to a smaller degree ($\lesssim 20\%$).

For *intermediate* k_1-triangles the bispectra witness a stronger impact (both in magnitude and sign) of the RSD. At the *very early* stages of the EoR, the B^s has a different sign than B^r for the $\cos\theta$ range $0.8 \lesssim \cos\theta \lesssim 0.9$. At these scales the magnitude of B^s is enhanced by $\sim 50-100\%$ for the linear k-triangles for $0.9 \lesssim \cos\theta \lesssim 1.0$ for the entire range of n. As reionization progresses (*early* stages) the magnitude of B^s reduces with respect to B^r by more than $\sim 50\%$ in the vicinity of linear k-triangles with $0.6 \lesssim n \lesssim 1.0$ and $0.9 \lesssim \cos\theta \lesssim 1.0$. During the *middle* and *late* stages of the EoR the reduction in bisepctra

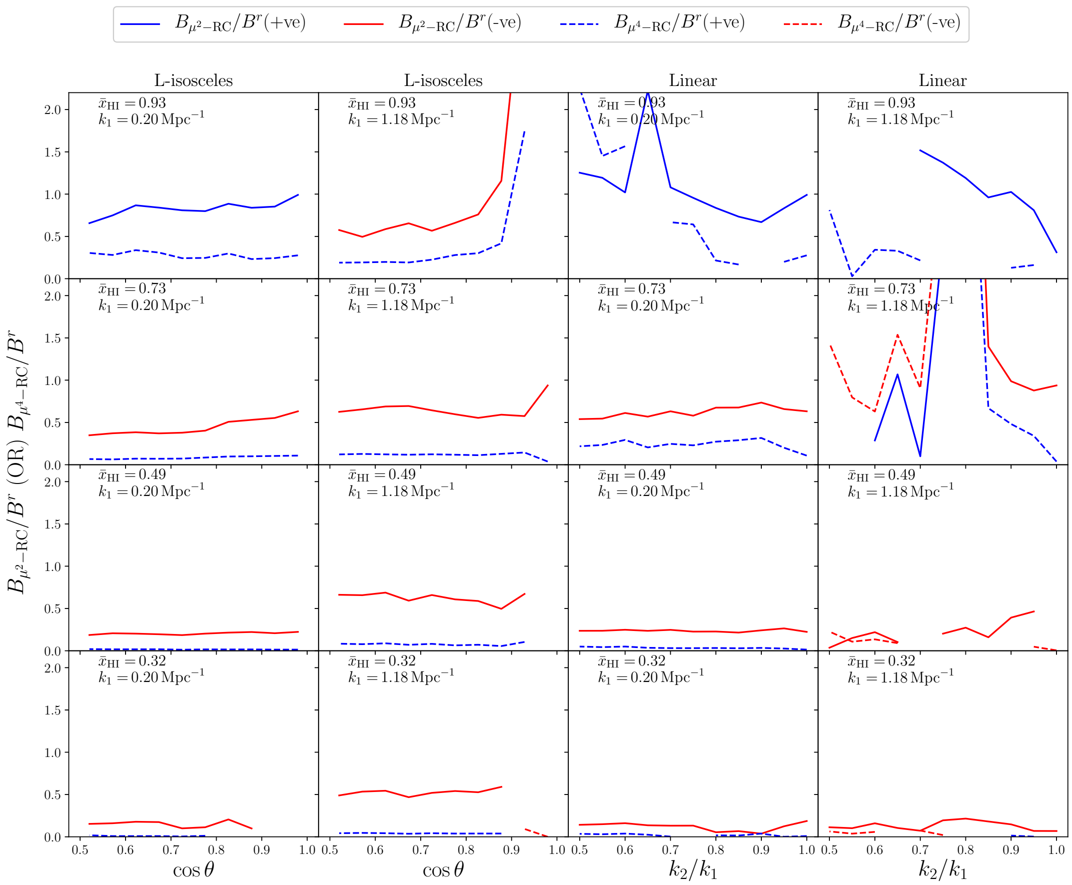

Figure 2.7: The ratios $B_{\mu^2-\mathrm{RC}}/B^r$ and $B_{\mu^4-\mathrm{RC}}/B^r$ for the limiting values of k-triangle parameters in the n-$\cos\theta$ space. The solid lines and dashed lines show the ratios $B_{\mu^2-\mathrm{RC}}/B^r$ and $B_{\mu^4-\mathrm{RC}}/B^r$ respectively. The red and blue colours represent negative and positive values of the ratios respectively. The ratios are shown at four different stages of the EoR and for two different k_1 modes (*small* and *large*).

amplitude due to RSD remains within $\leq 20\%$ in almost the entire unique n-$\cos\theta$ space.

The *large* k_1-triangle bispectra are even more sensitive to the effect of redshift space distortions. This is maybe due to the fact that non-linear features of the signal are more prominent at small length scales. The sign of the B^s is the opposite of that of the B^r for triangles with $0.7 \lesssim \cos\theta \lesssim 0.9$ during the *very early* stages of the EoR. This range of $\cos\theta$, for which a sign difference is observed shifts to higher values of $\cos\theta$ (i.e. $0.9 \lesssim \cos\theta \lesssim 1.0$) as the reionization transitions from the *very early* to the *early* stages. As reionization progresses further (i.e. *middle* and *late* stages) this $\cos\theta$ range (where the sign difference is observed) again shifts towards smaller values (i.e. $0.8 \lesssim \cos\theta \lesssim 0.9$). The magnitude of the bispectra are also affected by the RSD for *large* k_1-triangles. At the *very*

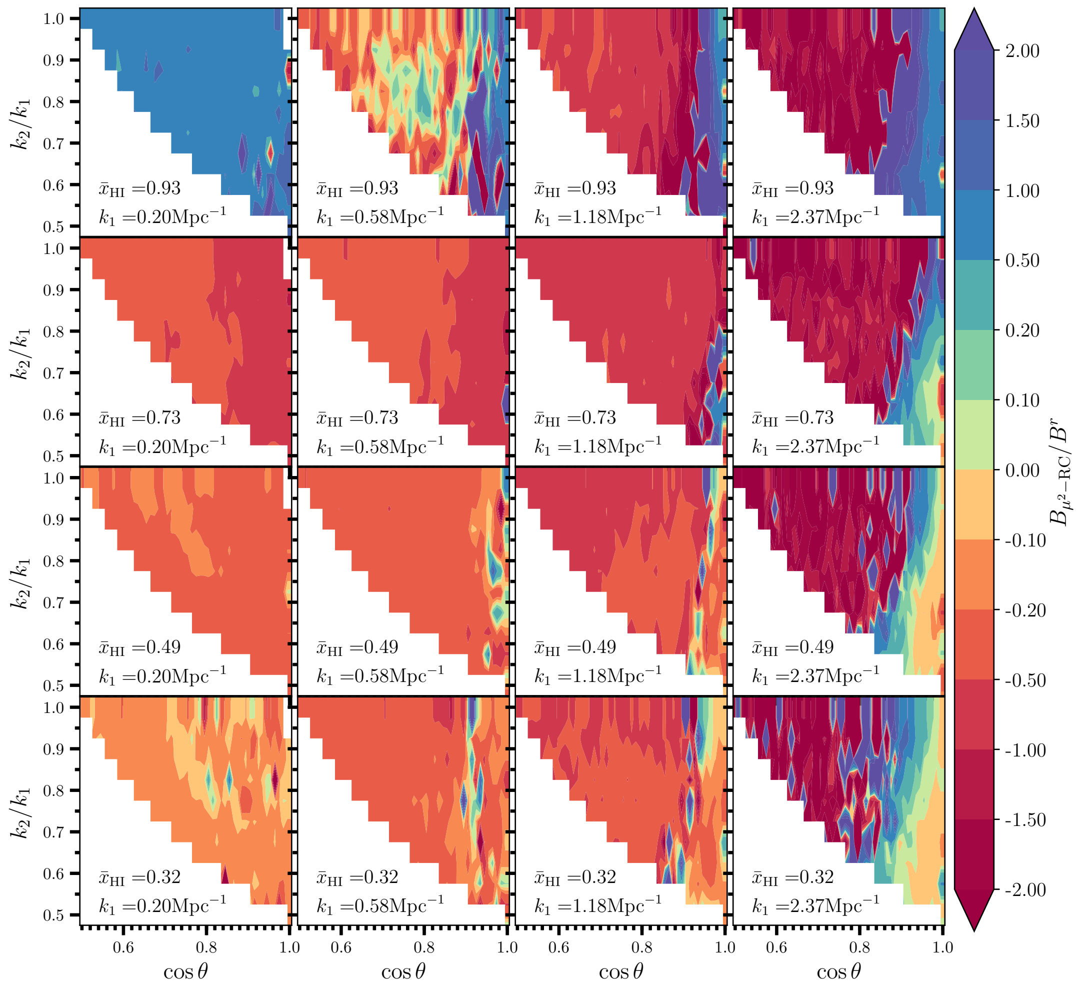

Figure 2.8: The ratio between the $B_{\mu^2-\mathrm{RC}}$ and B^r for all unique triangle configurations at four different stages of the EoR and for four different k_1 modes.

early stages of the EoR and for $0.5 \lesssim \cos\theta \lesssim 0.8$ the RSD decreases the magnitude by more than $\sim 50\%$ and for $0.8 \lesssim \cos\theta \lesssim 1.0$ the RSD increases the magnitude by more than $\sim 50\%$. During the later stages (*early, middle* and *late* stages of the EoR) the magnitude of B^s decreases by more than $\sim 50\%$, except for the region in the n-$\cos\theta$ space where the ratio B^s/B^r changes sign.

The RSD has its maximum impact both in terms of sign and magnitude on the bispectra for the *largest* k_1-triangles. As already noted above, for these triangles B^s is positive for the entire unique n-$\cos\theta$ space during the entire period of reionization. Therefore the sign of the B^s is the opposite of that of B^r for $0.5 \lesssim \cos\theta \lesssim 0.85$ (Figure 2.5). The magnitude also changes by roughly $\sim 50\%$ in this region of parameter space. Furthermore, for $0.85 \lesssim \cos\theta \lesssim 1.0$ the magnitude of B^s enhances by more than $\sim 50\%$.

Overall it can be concluded that, the impact of RSD on the magnitude of the bispectrum (for any type of k-triangle and for any k_1-mode) is minimum when reionization is roughly half way through.

2.5.2.2 Interpretation of the redshift space bispectra using the quasi-linear model

Several toy models for the size and distribution of the ionized regions have been used to interpret and explain the real space EoR 21-cm bispectrum [161, 183]. However, building such a toy model for the redshift space 21-cm bispectrum is difficult as the redshift space distortions changes the signal in a very complex manner. A matter density field, when subject to the redshift space distortions, changes in the following way: a spherical over-density region will attract more matter radially from its surroundings, which will make it appear squashed along the LoS of the observer. Whereas a spherical low density region will radially loose matter to its neighbours and thus will appear elongated along the LoS of the observer. If we consider an inside-out model for reionization (which is the case for our simulated 21-cm signal), there the highest matter overdensity regions will ionize first and after which the lower matter density regions will follow suit. Due to the redshift space distortions these early ionized regions (which are located on highest matter overdensity regions) will appear squashed along the LoS and the early neutral regions will appear stretched along the LoS in the 21-cm maps. However, this simplistic picture is somewhat valid at the very early stages of the EoR and for spherical ionized regions. As reionization progresses, more and more lower matter density regions get ionized and the ionized regions themselves also start merging together then this simplistic picture can no longer describe the 21-cm fluctuations and the impact of the redshift space distortions on it.

To interpret the features observed in the redshift space bispectra we therefore turn to the quasi-linear model for B^s expressed by Equation (2.11). However, before interpreting the results using this model we first check in which regions of the n-$\cos\theta$ space, for what k_1-values and for what stages of the EoR it provides a good approximation to B^s. Figure 2.6 shows the ratio of the bispectra estimated from Equation (2.11) (using the simulated $\rho_{\rm H}$ and $\rho_{\rm HI}$ fields) and the bispectra estimated from the simulated redshift space 21-cm brightness temperature fields, i.e. $B^{\rm s,\,qlin}/B^{\rm s}$. We observe that the quasi-linear model provides a very good estimate (with deviations of less than 10 percent from the actual B^s) in almost the entire n-$\cos\theta$ space and for the entire period of reionization for *small* and *intermediate* k_1-triangles. The quasi-linear predictions for bispectra for *large* and *largest*

k_1-triangles show somewhat higher deviations ($\sim$ 10–50 percent). However, even for this group of triangles in most of the scenarios, the quasi-linear model is able to predict the magnitude and the sign of the B^s reasonably well.

As discussed in Section 2.3, the R.H.S. of Equation (2.11) introduces seven correction (RC) terms to the real space bispectra as a model for the redshift space bispectra. We divide these seven RC terms into three groups - $B_{\mu^2-\mathrm{RC}}$, $B_{\mu^4-\mathrm{RC}}$ and $B_{\mu^6-\mathrm{RC}}$ (see Section 2.3 for details). Next, we try to identify which one among these three groups of RC terms is the dominant one. To this end we plot in Figure 2.7 the ratios $B_{\mu^2-\mathrm{RC}}/B^r$ and $B_{\mu^4-\mathrm{RC}}/B^r$ for the limiting values of k-triangle parameters in the n-$\cos\theta$ space (linear and L-isosceles) for *small* and *large* k_1-triangles. The advantage of plotting this ratio is that apart from quantifying the relative magnitudes of the RC terms, the sign of the ratio will tell us whether a given RC term is contributing with the same sign (positive ratio) or with the opposite sign (negative ratio) of the real space bispectra. We do not plot the ratio $B_{\mu^6-\mathrm{RC}}/B^r$ as its magnitude is negligible compared to the ratios $B_{\mu^2-\mathrm{RC}}/B^r$ and $B_{\mu^4-\mathrm{RC}}/B^r$ at almost all stages of the EoR and for almost all of the studied triangle types.

The figure clearly shows that for these limiting triangle shapes the dominant RC term is $B_{\mu^2-\mathrm{RC}}$ among $B_{\mu^2-\mathrm{RC}}$ and $B_{\mu^4-\mathrm{RC}}$. At the *very early* stages of the EoR and for *small* k_1-triangles $B_{\mu^2-\mathrm{RC}}/B^r$ is positive and its magnitude varies in the range $0.6 - 2.0$, whereas in the same regime $B_{\mu^4-\mathrm{RC}}/B^r$ is also positive and its magnitude varies in the range $0.1 - 0.6$ for most the triangle shapes. This explains why we see a boost in the bispectra due to the RSD during the *very early* stages of the EoR and for *small* k_1-triangles (see Figure 2.3). During all the later stages of the EoR (i.e. *early, middle* and *late* stages) for the *small* k_1-triangles $B_{\mu^2-\mathrm{RC}}/B^r$ is negative and its magnitude reduces as reionization progresses. However, $B_{\mu^4-\mathrm{RC}}/B^r$ is positive for the same triangles but has a much smaller magnitude compared to $B_{\mu^2-\mathrm{RC}}/B^r$ at the *early* stages of the EoR. During the *middle* and *late* stages of the EoR $B_{\mu^4-\mathrm{RC}}/B^r$ for same triangles is negligible. This explains why we see a reduction in the magnitude of the redshift space bispectra (with respect to the real space bispectra) for *small* k_1-triangles with the progress of reionization. This is also the reason why during the *late* stages of the EoR eventually $B^s \sim B^r$. A somewhat similar behaviour of $B_{\mu^2-\mathrm{RC}}/B^r$ and $B_{\mu^4-\mathrm{RC}}/B^r$ is observed for *large* k_1-triangles as well.

Next, to understand how the $B_{\mu^2-\mathrm{RC}}$ term shapes the redshift space bispectra for all types of triangles and for the entire period of the reionization, we show in Figure 2.8 the ratio $B_{\mu^2-\mathrm{RC}}/B^r$ for the entire unique n-$\cos\theta$ space following the convention of Figure 2.2. In line with what we have observed for the limiting shapes of the triangles in Figure 2.7, Figure 2.8 shows that for the *small* k_1-triangles during the *very early* stages of the EoR

$B_{\mu^2-\mathrm{RC}}/B^r \sim 1.0$ and also has a positive sign. The $B_{\mu^4-\mathrm{RC}}/B^r$ and $B_{\mu^6-\mathrm{RC}}/B^r$ ratio for the same triangles (shown in Figures A.2 and A.3) have a magnitude in the range $0.0-0.1$ with opposite signs with respect to each other. This explains why we observe a boost in the magnitude of redshift space bispectra in the entire unique n-$\cos\theta$ space at this stage. For the later stages of the EoR the $B_{\mu^2-\mathrm{RC}}/B^r$ becomes negative and also shows a decrease in magnitude with decreasing $\bar{x}_{\mathrm{HI}}$. However, it still remains the dominant RC term and can explain the decrease in amplitude of the redshift space bispectra (compared to real space bispectra) during the *early* and *middle* stages of the EoR until $B^s \sim B^r$ at the *late* stages of the EoR.

For the *intermediate* k_1-triangles at the *very early* stages of the EoR the magnitude of $B_{\mu^2-\mathrm{RC}}/B^r$ falls roughly in the range 0.2–1.0 and has a negative sign (Figure 2.8). $B_{\mu^4-\mathrm{RC}}/B^r$ ranges from 0.5 to 1.0 with mostly a positive sign (Figure A.2) and $B_{\mu^6-\mathrm{RC}}/B^r$ varies from 0.1 to 1.0 with mostly a negative sign (Figure A.3). Hence in this regime the contribution of $B_{\mu^2-\mathrm{RC}}$ is comparable with the other two RC terms. Further, as the two RC terms with higher powers of μ have competing signs, the RSD bispectra show a fluctuating sign when compared with the real space bispectra (see Figure 2.5) for this regime. As reionization progresses (i.e. *early, middle* and *late* stages) all three correction terms - $B_{\mu^2-\mathrm{RC}}/B^r$, $B_{\mu^4-\mathrm{RC}}/B^r$ and $B_{\mu^6-\mathrm{RC}}/B^r$ follow a somewhat similar behaviour as for the *small* k_1-triangles case described above and thus the redshift space bispectra also follow the suit.

At the *very early* stages of the EoR the $B_{\mu^2-\mathrm{RC}}/B^r$ for *large* k_1-triangles shows a variation in magnitude with triangle shape. The magnitude varies in the range 1.0–2.0 and it gradually increases as we approach the linear regime of triangles along the $\cos\theta$ axis. It also changes sign from negative to positive around $\cos\theta \sim 0.9$. The $B_{\mu^4-\mathrm{RC}}/B^r$ ratio shows a similar variation in magnitude ranging from 0.2 to 1.0 and the sign changes from positive to negative around $\cos\theta \sim 0.9$. Similarly, the magnitude of $B_{\mu^6-\mathrm{RC}}/B^r$ ranges from 0.1 to 1.5 and its sign changes from negative to positive around $\cos\theta \sim 0.9$. This boosts the magnitude of the redshift bispectra significantly around the linear regime of triangles and also ensures it is positive in the same region of the n-$\cos\theta$ space. The overall magnitude of all three RC terms decreases as reionization progresses. However, the trend in the variation of magnitude with the triangle shape remains more or less the same. This results in a overall decrease in the magnitude of the redshift space bispectra with the values around the linear regime of triangles and a sign change in the redshift space bispectra around $\cos\theta \sim 0.9$.

For the *largest* k_1-triangles the magnitude of $B_{\mu^2-\mathrm{RC}}/B^r$ varies in the range 0.5–2.0 and changes its sign from negative to positive around $\cos\theta \sim 0.8$ at almost all stages of the EoR. Similarly, the magnitude of $B_{\mu^4-\mathrm{RC}}/B^r$ range from 0.1 to 0.5 with a sign change from positive to negative around the same $\cos\theta$ value as above. The relative magnitude of $B_{\mu^6-\mathrm{RC}}/B^r$ with respect to the other two RC terms is somewhat negligible in this regime (≤ 0.1). This effectively ensures that the redshift space bispectra are positive at all stages of the EoR. The magnitude of the bispectra increases with increasing values of $\cos\theta$ and reaches a maximum around the linear limit of triangles (Figure 2.4).

2.6 Chapter Summary and Conclusions

In this chapter we have presented a comprehensive study of the spherically averaged EoR 21-cm signal bispectra, which are a probe of the non-Gaussianity present in the signal. This work is the first of its kind, as it quantifies the EoR 21-cm bispectra for all possible unique k-triangles in the triangle parameter (n-$\cos\theta$) space using an ensemble of simulated signals. All previous efforts in estimating the EoR 21-cm bispectra were less complete as they were limited to a few specific kind of k-triangles. The article corresponding to this chapter is also the first to quantify the impact of redshift space distortions on the signal bispectra.

We find that the 21-cm bispectra are non-zero for most of the triangle parameter space and during almost the entire period of the reionization. This strongly establishes that the EoR 21-cm signal is highly non-Gaussian. Our findings can be further summarized as below:

- The magnitude of both the real and redshift space signal bispectra (in the entire triangle parameter space) initially increases with decreasing $\bar{x}_{\mathrm{HI}}$ for all k_1-triangles having values $k_1 \lesssim 1.0\,\mathrm{Mpc}^{-1}$. They achieve their maximum approximately for $\bar{x}_{\mathrm{HI}} \sim 0.5$ after which they decrease with decreasing $\bar{x}_{\mathrm{HI}}$. This is due to the fact that the signal fluctuations increase gradually with the increasing sizes of the HII regions and peak at the mid-point of reionization.

- The 21-cm bispectra in both real and redshift space show a gradual increment in the magnitude as we go from smaller to larger k_1 values (the largest arm in the k-triangle) with $k_1 \lesssim 1.0\,\mathrm{Mpc}^{-1}$ and for a fixed $\bar{x}_{\mathrm{HI}}$. This seems to be a signature of the impact of the HII region size distribution at a given stage of the EoR.

- The sign of the EoR 21-cm bispectra, an important feature of this statistic, is negative for most of the n-$\cos\theta$ space for the real space signal (across all k_1-triangles and for almost all $\bar{x}_{\rm HI}$ values). It is positive only in the limit and vicinity of squeezed ($n \sim 1.0$ and $\cos\theta \sim 1.0$) and linear (i.e. $n \sim 0.5 - 1.0$ and $\cos\theta \sim 1.0$) k_1-triangles. The region of positive bispectra in the n-$\cos\theta$ space increases in area as we move from smaller to larger k_1-triangles. Another important point to note is that the magnitude of the bispectra reaches its maximum for the squeezed and linear triangles.

- The redshift space distortions affect the bispectra for all unique k-triangles significantly, both in terms of magnitude and sign, during the entire period of the reionization. The impact due to RSD on the bispectra magnitude is larger (as large as $\sim 100\%$) during the early stages of the EoR ($\bar{x}_{\rm HI} \gtrsim 0.7$) for triangles with small and intermediate k_1 modes ($k_1 \lesssim 0.6\,{\rm Mpc}^{-1}$). The RSD have a smaller impact (at most $\sim 50\%$) on the bispectra magnitude during the later stages of the EoR ($\bar{x}_{\rm HI} \lesssim 0.7$) for the same k_1-triangles.

- The gradual change in the sign of the bispectra is most prominent when one analyses the bispectra across small to large k_1-triangles for any given stage of reionization. The signal bispectra in redshift space are mostly negative for all unique triangles with $k_1 \sim 0.2\,{\rm Mpc}^{-1}$ (small) all stages of the EoR. As we move from smaller to larger k_1 triangles at any give stage of reionization, an area with positive bispectra starts to appear close to the $\cos\theta \sim 1$ line which increases in size the larger k_1 becomes. In case of the largest k_1-triangles discussed here ($k_1 \sim 2.4\,{\rm Mpc}^{-1}$), the bispectra have positive sign for the entire n-$\cos\theta$ parameter space. A similar trend in the evolution of the sign is observed for the real space signal as well. However, the area in the n-$\cos\theta$ space where bispectra are positive is much smaller in real space than in redshift space. This is true for all stages of reionization and for all k_1-triangles.

- The RSD have their maximum impact on the larger k_1-triangle bispectra ($k_1 \gtrsim 0.6\,{\rm Mpc}^{-1}$). It enhances the magnitude of the signal bispectra for $k_1 \sim 1.0\,{\rm Mpc}^{-1}$ triangles by $\sim 100\%$, in the region of the n-$\cos\theta$ space where B^s and B^r have opposite signs. The bispectra for other unique triangles in the n-$\cos\theta$ (for the same k_1 values) space experience a decrease in magnitude, sometimes as low as ~ 80 percent, due to the RSD. For $k_1 \sim 2.4\,{\rm Mpc}^{-1}$ triangles, the RSD change the magnitudes by at least $\sim 100\%$ in most of the unique n-$\cos\theta$ space. Additionally, it also changes the signs within $\cos\theta$ range $0.5 \lesssim \cos\theta \lesssim 0.85$.

- The quasi-linear model (Equation (2.11)) provides a very good prediction and physical interpretation for the redshift space EoR 21-cm bispectra (with $\leq 10\%$ uncertainties) in the entire unique n-$\cos\theta$ space for $k_1 \leq 0.6\,{\rm Mpc}^{-1}$ triangles during the early stages of the EoR ($\bar{x}_{\rm HI} \geq 0.5$). These predictions deviate more (≥ 20 percent) from the simulated B^s as we move towards triangles with larger k_1 modes ($k_1 \geq 0.6\,{\rm Mpc}^{-1}$) and to the later stages of the EoR. We have further established that among the three groups of the RC terms shown in Equation (2.11), mainly the group $B_{\mu^2-{\rm RC}}$ dominates in shaping the redshift space 21-cm bispectra. This group contains three cross-bispectra which are $[\overline{\mu_1^2}]^0_0 B_{\Delta_{\rho_{\rm H}},\Delta_{\rho_{\rm HI}},\Delta_{\rho_{\rm HI}}}$, $[\overline{\mu_2^2}]^0_0 B_{\Delta_{\rho_{\rm HI}},\Delta_{\rho_{\rm H}},\Delta_{\rho_{\rm HI}}}$ and $[\overline{\mu_3^2}]^0_0 B_{\Delta_{\rho_{\rm HI}},\Delta_{\rho_{\rm HI}},\Delta_{\rho_{\rm H}}}$. The other RC terms do not have a similar impact in shaping the redshift space signal bispectra.

The analysis of the simulated EoR 21-cm signal bispectra presented here is quite comprehensive in nature. It establishes that the impact of redshift space distortions on the signal bispectrum is significant, both in terms of bispectra magnitude and sign. Thus it is important to take into account the effect of the RSD for any interpretation of the signal bispectra.

The analysis in this chapter does not consider the period of cosmic history when the effect of spin temperature fluctuations on the signal is significant i.e. CD. We present a detailed analysis of the redshifted 21-cm bispectrum from the CD in Chapter 2.

Chapter 3

The CD 21-cm bispectrum and the impact of spin temperature fluctuations and the redshift space distortions on this signal statistic

This chapter is adapted from: **Kamran M.**, Ghara R., Majumdar S., Mondal R., Mellema G., Bharadwaj S., Pritchard J. R., Iliev I. T.; *Redshifted 21-cm bispectrum – II. Impact of the spin temperature fluctuations and redshift space distortions on the signal from the Cosmic Dawn*; **Monthly Notices of the Royal Astronomical Society**; Volume 502, Issue 3, April 2021, p.3800–3813; DOI: https://doi.org/10.1093/mnras/stab216 [arXiv:2012.11616].

3.1 Introduction

The appearance of the first stars and galaxies in the Universe is often referred to as the Cosmic Dawn (CD). In the subsequent epoch, known as Epoch of Reionization (EoR), the neutral hydrogen (HI) in the Inter-Galactic Medium (IGM) was ionized by the radiation from those early sources. The CD-EoR epoch is one of the least understood chapters from the evolutionary history of our Universe. Observations of the redshifted HI 21-cm signal produced by the spin-flip transition of the electron in the ground state of hydrogen, will provide a wealth of information about the thermal and ionization states of the IGM during the CD/EoR as well as about the properties of the first sources in the early Universe (see e.g. [1, 10, 21]).

A number of radio interferometers such as the GMRT[1] [97], LOFAR[2] [67], MWA[3] [122], PAPER [123] and HERA[4] [72] have dedicated considerable amounts of observing time to detect the CD-EoR 21-cm signal. Due to their limited sensitivity, these interferometers can only hope to detect the redshifted 21-cm signal statistically using the spherically averaged power spectrum as an estimator. The future Square Kilometre Array (SKA)[5] will however have sufficient sensitivity to also produce tomographic images of the 21-cm signal [2, 74, 223].

There is a considerable observational effort underway to detect the 21-cm power spectrum (see e.g. [67, 94, 96] etc.). So far, only weak upper limits on the expected EoR 21-cm power spectrum have been obtained [67, 122–125]. Apart from power spectrum, several authors have proposed other statistics to detect the 21-cm signal such as variance (e.g. [115–117, 224]), multi-frequency angular power spectrum (e.g. [119, 120, 204, 205]) etc.

The power spectrum is nothing but the variance at different length scales and therefore, is able to capture many crucial features of the signal (see e.g., [3, 79, 119, 147, 156–160, 178, 180, 206, 225, 226]). It can capture the complete statistical properties of a Gaussian random field, for which all higher-order statistics do not contain any additional information. However, the 21-cm signal is highly non-Gaussian in nature [132, 148, 161]. The non-Gaussianity in the EoR 21-cm signal evolves as reionization proceeds [163–166]. Thus power spectrum will not be able to characterize this signal completely. Some of the one-point statistics such as skewness and kurtosis can capture this non-Gaussianity (see e.g., [116, 117, 167–169, 227] etc). However, these can only probe the non-Gaussian features at a single length scale. To probe the non-Gaussian features at different length scales, one requires some robust higher-order statistics such as the bispectrum.

The bispectrum, the Fourier transform of the three point correlation function, can capture the non-Gaussian component of the signal in different Fourier modes. The non-Gaussian features in the EoR 21-cm signal were first studied using the bispectrum by [178] who employed an analytical model of spherically ionized regions. They reported that the sign of the bispectrum can have negative values. [183] estimated the EoR 21-cm bispectrum using

[1]http://www.gmrt.ncra.tifr.res.in
[2]http://www.lofar.org/
[3]http://www.mwatelescope.org/
[4]https://reionization.org/
[5]http://www.skatelescope.org/

a suite of semi-numerical simulations, focusing on some specific k-triangles (equilateral, isosceles etc.). They confirmed that the bispectrum displays sign changes and showed that the interplay between neutral fraction and matter density fluctuations decides the sign of the bispectrum. A negative bispectrum indicates that the non-Gaussianity is arising due to fluctuations in the neutral fraction whereas a positive bispectrum occurs when the non-Gaussianity is arising due to the matter density fluctuations. [184] independently produced similar results. Furthermore, in the context of the CD, [185] have calculated the bispectrum (with a different normalization) for some specific k-triangles by using a fully-numerical simulation. They showed that bispectrum is driven by the interplay between the size and shape of the heated regions and their distributions. They also found that irrespective of the type of the X-ray heating sources, the bispectrum magnitude is largest for equilateral k-triangle configurations. [214] presented another independent study of the CD-EoR 21-cm bispectrum for some specific types of k-triangles. However, their estimator was unable to capture the sign of the bispectrum.

The peculiar velocity of the gas modifies the cosmological redshift of the 21-cm signal and makes it anisotropic along the LoS. This LoS anisotropy in the signal is known as redshift space distortions (RSD). In the context of the CD-EoR 21-cm signal, their effect was first calculated by [79] using analytical models for the 21-cm observable. They showed that the RSD has a large impact on the amplitude and shape of the 21-cm power spectrum. Subsequent works studied the RSD using semi-numerical and fully-numerical simulations [3, 120, 147, 153, 159, 160, 180, 189].

All previous studies of the CD-EoR 21-cm bispectrum were restricted to certain specific triangle configurations and neglected the RSD effect. For a comprehensive description of the non-Gaussianity of a field through bispectrum, all possible closed unique k-triangles should be considered. In a recent study, [5] have shown a way to parametrize the real and redshift space bispectrum for all unique k-triangles. Further, [190, 215] have studied the bispectrum for all unique k-triangles using simulations of the EoR 21-cm signal. [215] demonstrated how different dark matter models impact the EoR bispectrum through their impact on the structure formation. In [190] (which is chapter 2 in this thesis), we have also considered the impact of the RSD on the EoR 21-cm signal bispectrum. We showed that all possible unique k-triangles capture the non-Gaussianity arising due to two competing sources i.e., matter density fluctuations and the neutral hydrogen fluctuations. We have also shown that the squeezed and linear k-triangles capture the largest magnitude of the bispectrum, and they are highly sensitive to the non-Gaussianity arising due to the matter density fluctuations at small scales. We further showed that the RSD impacts both the magnitude and the sign of the bispectrum irrespective of the stages of the EoR and size and shape of the k-triangles.

This chapter aims to quantify the non-Gaussianity in the CD 21-cm signal through the bispectrum while considering all possible unique k-triangles. We do not include the reionization part (discussed in details in Chapter 2) of the cosmic history here. This is the first study of the redshift space 21-cm bispectrum from the CD considering all the possible unique k-triangles.

The structure of the chapter is as follows: In Section 3.2 we present the formalism for estimating the bispectrum from the simulated signal. Section 3.3 describes the simulations used to generate the 21-cm maps. The Section 3.4 we discuss our analysis of the bispectra for different source models. Finally in Section 3.5 we summarise our results.

In this chapter, we have used the cosmological parameters $h = 0.7$, $\Omega_{\rm m} = 0.27$, $\Omega_\Lambda = 0.73$, $\Omega_{\rm b} = 0.044$ consistent with the *WMAP* results [228] and within the error bars consistent with the *Planck* results [52].

3.2 Bispectrum estimation

We adopt the bispectrum estimator defined in [183] to compute the bispectrum from the simulated data for the $i^{\rm th}$ triangle configuration bin as

$$\hat{B}_i(\mathbf{k}_1, \mathbf{k}_2, \mathbf{k}_3) = \frac{1}{N_{\rm tri} V} \sum_{[\mathbf{k}_1+\mathbf{k}_2+\mathbf{k}_3=0]\in i} \Delta_{\rm b}(\mathbf{k}_1)\Delta_{\rm b}(\mathbf{k}_2)\Delta_{\rm b}(\mathbf{k}_3)\,, \tag{3.1}$$

where $\Delta_{\rm b}(\mathbf{k})$ is the Fourier transform of the differential brightness temperature of the 21-cm field, $N_{\rm tri}$ is the number of statistically independent samples of closed triangles associated with the $i^{\rm th}$ triangle configuration bin, V is the simulation volume. The actual calculation of the bispectrum is performed using the algorithm of [183] and [190].

In this chapter, we consider the bispectrum estimation for all unique triangles in Fourier space, the details of which have been described in section 2.2.

3.3 Simulating the 21-cm signal from cosmic dawn

We produce 21-cm differential brightness temperature ($\delta T_{\rm b}$) maps using the GRIZZLY [153] simulations. This simulation approximates the impact of each source using spherically symmetric solutions of the radiative transfer equation. It is an independent implementation of the BEARS algorithm [152,229,230]. We refer the interested readers to [153,154,231]

Source Models and Scenarios	Model-A	Model-B
Source type	mini-QSO	HMXB
Spectral index (α)	1.5	0.2
Spin Temperature ($T_{\rm S}$)	Self consistent	Self consistent

Table 3.1: Different scenarios considered in this study. We choose the star formation efficiency $f_\star = 0.03$, minimum mass of dark matter halos that contain sources $M_{\rm halo,min} = 2 \times 10^9$ M$_\odot$, escape fraction of UV photons $f_{\rm esc} = 0.1$ and the rate of emission of the X-ray photons per stellar mass $\dot{N}_X = 4 \times 10^{42}$ s^{-1} M$_\odot^{-1}$ for both the scenarios.

for further details.

3.3.1 Cosmological simulations

GRIZZLY uses gridded versions of cosmological density and velocity fields and halo catalogues at different redshift as inputs to produce $\delta T_{\rm b}$ maps at those redshifts. The density and velocity fields used in this study were obtained as part of the PRACE[6] project PRACE4LOFAR. This dark-matter only N-body simulation was performed using the CUBEP^{3}M code [128]. The details of this simulation are as follows: (i) simulation volume: $(500\,h^{-1})^3$ comoving Mpc^3. (ii) number of particles: 6912^3, (iii) mass of each particle: 4.05×10^7 M$_\odot$. We use gridded versions of the density and velocity fields with a resolution of 600^3. The minimum mass of the halos resolved in this simulation is $\approx 10^9$ M$_\odot$ which means that these halos consist of at least ≈ 25 particles.

3.3.2 Source properties

In this simulation we assume that all the dark matter halos with mass larger than the cut-off mass $M_{\rm halo,min}$ host star forming galaxies, sources of hard X-ray spectra such as high-mass X-ray binaries (HMXBs) and sources of soft X-ray spectra such as mini-quasars (mini-QSOs) etc. We further assume that most HI ionizing photons are produced by the stars in galaxies. The stellar content of a galaxy is assumed to be proportional to the mass of the dark matter halo that hosts the galaxy. Thus, the stellar mass inside a halo of mass $M_{\rm halo}$ is $M_\star = f_\star \left(\frac{\Omega_{\rm b}}{\Omega_{\rm m}}\right) M_{\rm halo}$ where $f_\star$ is the star formation efficiency. We choose

[6]Partnership for Advanced Computing in Europe: http://www.prace-ri.eu/

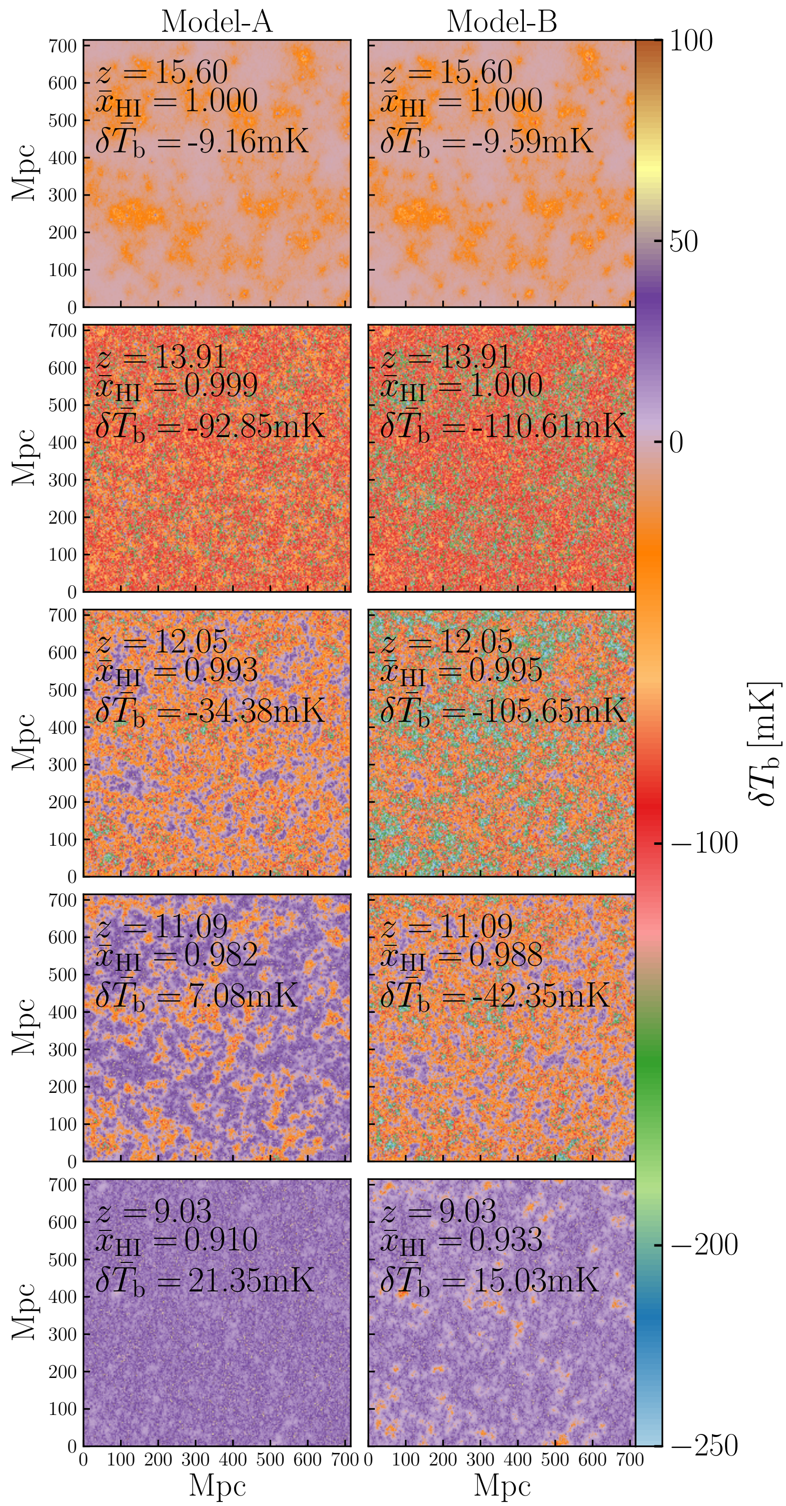

Figure 3.1: Slices of the brightness temperature showing the redshift evolution of the 21-cm signals for Model-A (Left panels) and Model-B (right panels).

$f_\star = 0.03$ [232, 233] throughout this paper.

We use the publicly available stellar population synthesis code PEGASE2[7] [234] to generate the SED of the galaxies assuming a stellar metallicity of 0.01, a mass range of 1 to 100 $\mathrm{M}_\odot$ and a Salpeter initial stellar mass function. The stellar luminosity in this source model scales with the stellar mass of the galaxies.

In addition to the star formation efficiency and the stellar luminosity, the actual number of HI ionizing photons that enter the IGM from the galaxies also depends on the escape fraction ($f_{\rm esc}$) of those ionizing photons. We assume $f_{\rm esc} = 0.1$ for the ionizing photons produced inside the galaxies.

Apart from the ionizing photons produced by the stellar sources, we also consider contributions from the X-ray sources such as mini-QSO and HMXBs. Unlike the stellar UV photons, X-rays can travel over long distances through the neutral IGM before they are absorbed. We model the X-ray part of the SED as a power-low of energy $I_X(E) \propto E^{-\alpha}$, where α is the spectral index of the X-ray source. In our study, we consider two different α values 1.5 and 0.2 which roughly represents mini-QSOs [235–237] and HMXBs [238, 239]. The former we refer to as Model-A, the latter as Model-B. We assume that the rate of emission of the X-ray photons per stellar mass is $\dot{N}_X = 4 \times 10^{42}\ \mathrm{s}^{-1}\ \mathrm{M}_\odot^{-1}$ for both types of X-ray sources. This is consistent with the observations of HMXBs in local star forming galaxies in the 0.5-8 keV band (see e.g. [238]). Our X-ray band spans from 100 eV to 10 keV, while the UV band spans between 13.6-100 eV. The normalization of the X-ray band used in the 1D radiative transfer is done using the X-ray band spanning to 10 keV. Note that the hard X-ray photons with energy $\gtrsim 2$ keV will remain unabsorbed in our simulation volume due to their long mean free path.

3.3.3 21-cm signal simulation

Given the SED of a source, GRIZZLY first generates a large number of one-dimensional profiles of the ionization fraction ($x_{\rm HII}$) and gas temperature ($T_{\rm K}$) for various combinations of the source parameter values at different redshifts. The appropriate 1D profiles are then applied to each dark matter halo in the 3D simulation volume to generate the $x_{\rm HII}$ and $T_{\rm K}$ cubes at the redshifts of interest. The algorithm applies a photon/energy conserving correction to overlapping regions. Although this method is based on several approximations such as isotropic radiative transfer, overlap correction, etc., it still perform well when compared to a full radiative transfer simulation with the C^2-RAY code [132] (see

[7] http://www2.iap.fr/pegase/

the details in [154]).

GRIZZLY also takes into account an inhomogeneous Lyα background assuming that the Lyα flux scales as $1/r^2$ with radial distance r from the source. The Lyα photon number density determines the strength of coupling between the spin-temperature and the gas temperature (Wouthuysen-Field effect, [240, 241]). Although Lyα photons can also heat the gas in the IGM [242,243], their impact is usually much less than the X-rays and thus we do not include Lyα heating in this paper. We also do not include the systematic sources of uncertainties in models of thermal histories of the IGM (e.g. underlying cosmology, the choice of halo mass function etc.), which significantly affects the Thomson scattering optical depth and global 21-cm signal amplitude [244]). An important point to note here is that in these simulations we have considered the Lyα coupling and the X-ray heating of the IGM to be running simultaneously (i.e. $T_{\rm S}$ is calculated in a self consistent manner) from very early stages of the CD.

The redshift space distortions are implemented in our simulation using the following principle. If the redshift z is caused only due to the Hubble expansion, then the redshift space position $\boldsymbol{s}$ of the source of the signal will be same as its comoving real space position $\boldsymbol{r}$. However, due to the gas peculiar velocities along the LoS ($v_{||}$), the signal coming from the location $\boldsymbol{r}$ will appear to be coming from a location $\boldsymbol{s}$, to the present day observer, following

$$\boldsymbol{s} = \boldsymbol{r} + \frac{1+z}{H(z)} v_{||} \hat{r} \tag{3.2}$$

where, $\hat{r}$ is the unit vector along the LoS.

We generate $\delta T_{\rm b}$ cubes at 22 redshift values in the range 9 to 20 using the $x_{\rm HII}$, $T_{\rm K}$ and the Lyα coupling coefficient cubes. Next we apply the effect of the RSD [3, 153, 159, 160, 180, 245] to these $\delta T_{\rm b}$ cubes. For this we use the cell movement method (or Mesh-to-Mesh (MM)-RRM scheme) of [159].

3.3.4 Scenarios

We consider two different source scenarios in this study. These two scenarios only differ in the spectral index of the X-ray sources. In Model-A we use $\alpha = 1.5$, the value typical for mini-QSOs. In Model-B we use $\alpha = 0.2$, typical for HMXBs. All other parameters such as the minimum mass of halos used $M_{\rm halo,min}$, the escape fraction for UV photons $f_{\rm esc}$, etc., are identical. Table 3.1 lists all relevant source and simulation parameter values used here.

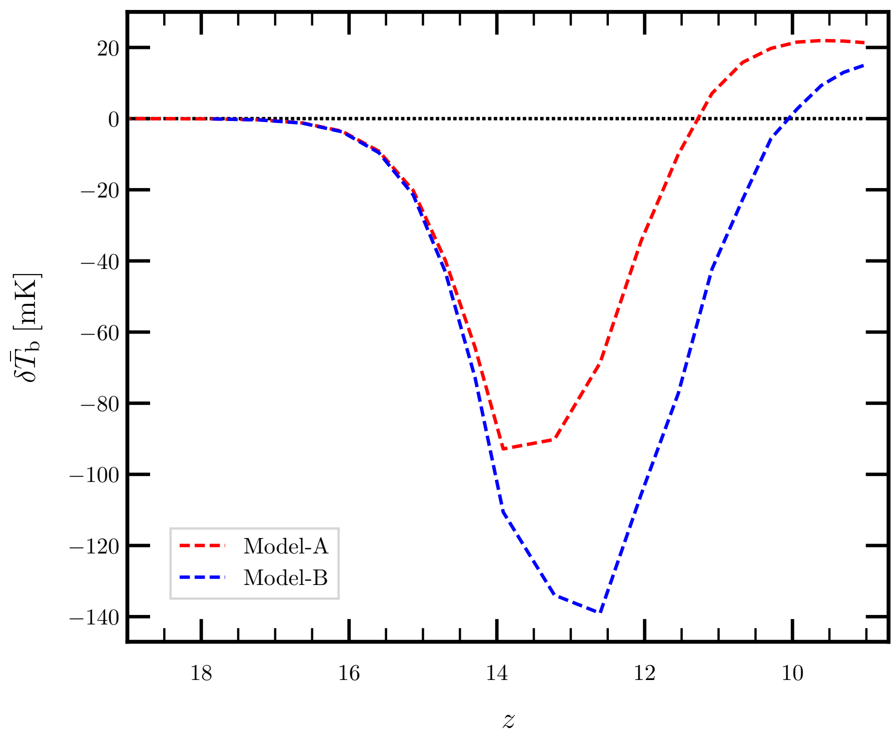

Figure 3.2: Evolution of global 21-cm signal with redshift for mimi-QSO (red curve) and HMXB (blue curve) sources.

3.4 Results

In this section, we present the analysis of the 21-cm bispectrum from the Cosmic Dawn for the two different Lyα coupling and X-ray heating scenarios we have introduced in Section 3.3.2. Figure 3.1 shows the slices of $\delta T_{\rm b}$ maps for Model-A and Model-B, while the evolution of the 21-cm mean brightness temperature for two cases are shown in Figure 3.2. In this paper, we are interested in the impact of the spin temperature fluctuations on the signal statistics of these two models, for which they show significant variation in the mean brightness temperature evolution (Figure 3.2). The effects of Lyα coupling are the same for both models. However, the effects of X-ray heating are different. The heating of the gas happens at a later time in Model-B as compared to Model-A. This is because the source spectrum used in Model-B contains less number of soft X-ray photons as compared to a steeper source spectrum used in Model-A. The soft X-ray photons get absorbed easily due to their smaller mean free path as compared to the hard X-ray photons.

Among the two source models that we have simulated, we choose Model-A (i.e. mini-QSOs with halo mass $\geq 2 \times 10^9\,{\rm M}_{\odot}$, see Table 3.1 for more details) to be our fiducial source

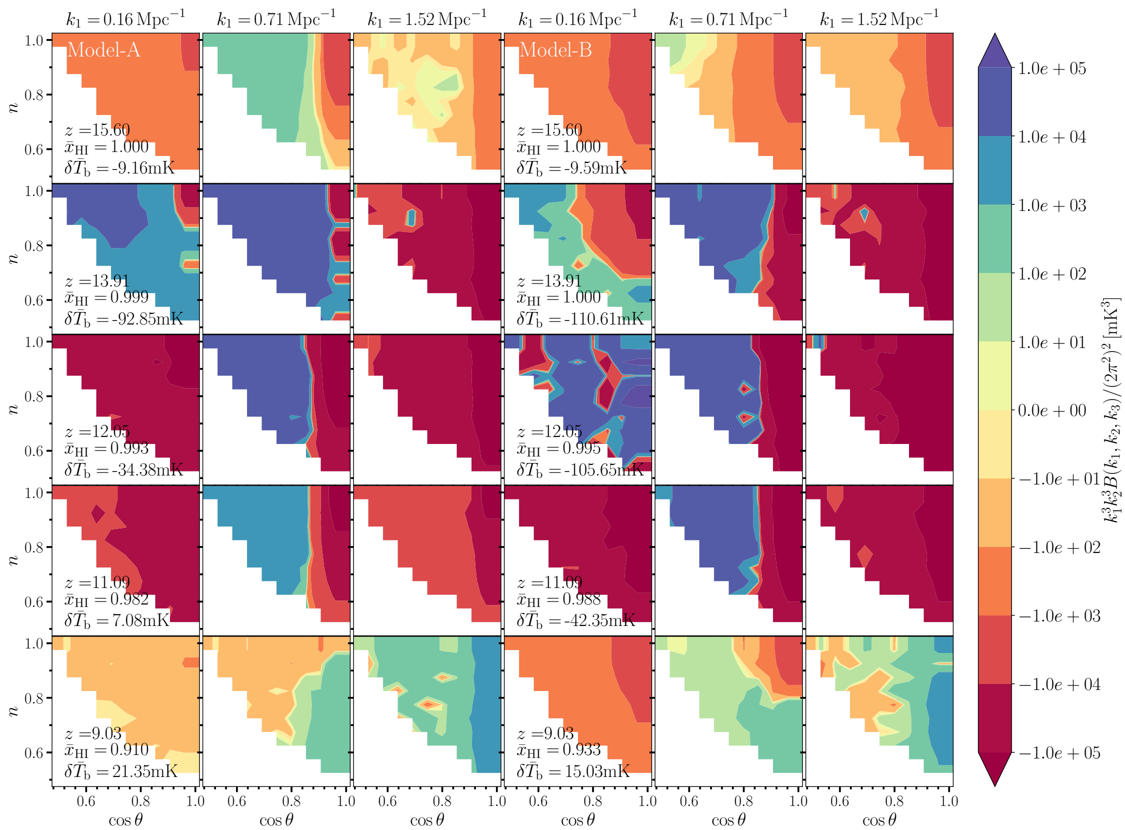

Figure 3.3: The redshift space bispectra for all unique triangle configurations for Model-A (left three columns) and Model-B (right three columns) at five different stages of the CD and for three different k_1 modes.

model. Following the convention of [190] and [215], we demonstrate our results in terms of the spherically averaged normalized bispectrum defined as $\left[k_1^3 k_2^3 B(k_1, k_2, k_3)/(2\pi^2)^2\right]$. Throughout this paper we show the 21-cm bispectra estimated from the redshift space data, unless otherwise stated. To designate different stages of the CD we use the following convention: *very early* ($z \sim 16$), *early* ($z \sim 14$), *middle* ($z \sim 12$), *late* ($z \sim 11$) and *very late* ($z \sim 9$). Further, we label the triangles with k_1 modes $\approx 0.2, 0.7$ and $1.5\,\mathrm{Mpc}^{-1}$ as *small*, *intermediate* and *large* k_1-triangles respectively[8]. The δT_b slices as shown in Figure 3.1 represent those five different stages of the IGM in this study.

[8]Due to our limited simulation volume, the triangle bins having k_1 smaller than $0.16\,\mathrm{Mpc}^{-1}$ will be affected significantly by the sample variance.

3.4.1 Bispectrum for the fiducial source model

Here we first try to understand the general trends in the bispectra magnitude and sign for the fiducial model as a function of redshift and magnitude of the k_1 mode. Below we divide our discussion for the fiducial model into two segments: evolution of the bispectrum magnitude and evolution of the bispectrum sign.

3.4.1.1 Evolution of the bispectrum magnitude

The first three columns in Figure 3.3 show the normalized spherically averaged bispectra for our fiducial model at the five different stages of the CD (varying from top to bottom) and for the three different k_1 modes (varying from left to right) as defined in Section 3.4. A quick inspection of Figure 3.2 (red dashed curve for the fiducial model) reveals that the mean 21-cm signal is in absorption during most of the CD and it turns into an emission signal around $z \approx 11.5$. This implies that for our fiducial model the first three rows of Figure 3.3 show the bispectrum when the signal is in absorption and the bottom two rows show the bispectrum when the signal is in emission.

We first discuss the variation of the magnitude of the bispectra with z. For ease of understanding, in addition to Figure 3.3, we plot the bispectra for equilateral and squeezed triangles as a function of redshift in Figure 3.4. A visual inspection of the Figures 3.3 and 3.4 reveals that the magnitude of the bispectrum is lowest during the *very early* and the *very late* stages of the CD. This magnitude is much larger (more than ~ 2 orders of magnitude) during the *early middle* and *late* stages of the CD compared to the beginning and the end of the CD. This is due to the fact that during the intermediate stage of the CD the fluctuations in the signal becomes maximum. The reason for the low magnitude of the bispectrum at the *very early* and *very late* stages of the CD can be understood in the following manner. The fluctuations in the 21-cm signal during the CD can potentially have many constituents. Among them are the fluctuations in the matter density field, fluctuations in the hydrogen neutral fractions and the fluctuations in the spin temperature. Among these three, the fluctuations in the neutral fraction stays relatively low in amplitude during the entire duration of the CD as only up to $\sim 10\%$ of neutral hydrogen ionizes by the end of the CD (around the *very late* stage). The magnitude of the fluctuations in the matter density is even lower during this period when compared to the other constituents of the signal fluctuations. Additionally, the fluctuations in the T_S field is relatively small during the *very early* stages because there are very few absorption and emission regions around this time and they are also very small in their sizes. This leads to a relatively small magnitude of bispectrum at the *very early* stages of the CD.

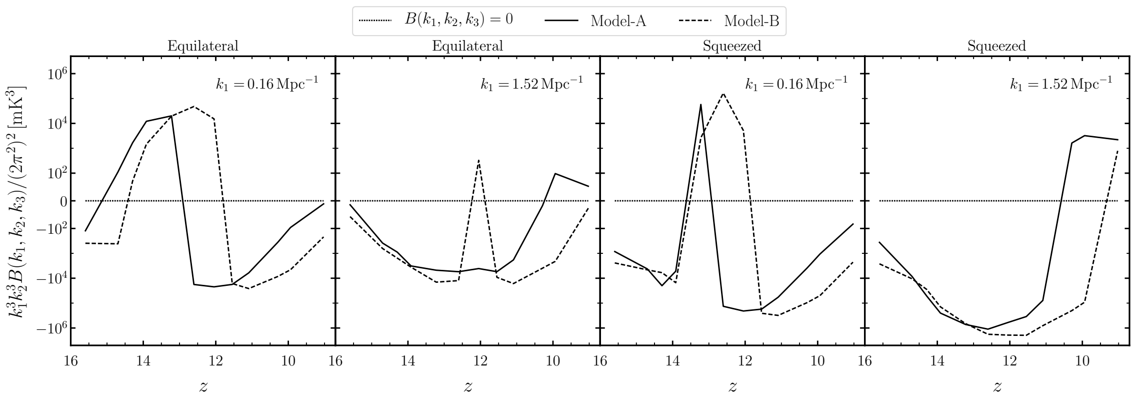

Figure 3.4: Variation of the bispectrum with redshift for different source models for two types of triangles and two different k_1 modes.

Around the *very late* stages T_{S} becomes much larger compared to the CMB temperature (T_γ), and the signal enters into the EoR era with a significant ionization (less than 10%). At this stage, the components responsible for 21-cm signal fluctuations are the matter density and hydrogen neutral fraction fluctuations. The fluctuations in these components around *very late* stages are also relatively small. This makes the bispectrum magnitude smaller during the *very late* stages. This is a direct evidence of the fact that the CD 21-cm signal non-Gaussianity quantified by the bispectrum is relatively higher than the EoR 21-cm signal non-Gaussianity.

An important point to note here is regarding the magnitude of the bispectra during the *late* stages. Around this stage, although the global signal is of emission in nature with a relatively small mean brightness temperature (i.e., $\delta\bar{T}_{\mathrm{b}} \sim 7\,\mathrm{mK}$), the bispectrum magnitude is still relatively large. This is due to the additional high fluctuations introduced in the field by some left over absorption regions (see panels in the fourth row of Figure 3.1).

Next, we discuss the variation of the bispectrum magnitude with k_1. Around *very early* stage, the magnitude of the bispectrum is maximum at the limit and vicinity of squeezed ($n = 1, \cos\theta = 1$) k_1-triangles. This largest magnitude patch in the n–$\cos\theta$ space expands its area around the linear k-triangles with increasing values of k_1. The bispectrum magnitude for the rest of k_1-triangles at this stage is smaller by $\sim$ 1–2 orders of magnitude. Around *early* stage and for *small* k_1 mode, the maximum bispectrum magnitude is observed for the equilateral, squeezed, and similar class of k-triangles. For these k-triangles with larger k_1 values, the bispectrum magnitude more or less remains the same, but for the rest of the k-triangles in this class, it increases with an increase in k_1 magnitude. Further, the bispectrum magnitude around *middle* stage does not show a significant variation with k_1. Next, around the *late* stage, the bispectrum magnitude decreases with increase

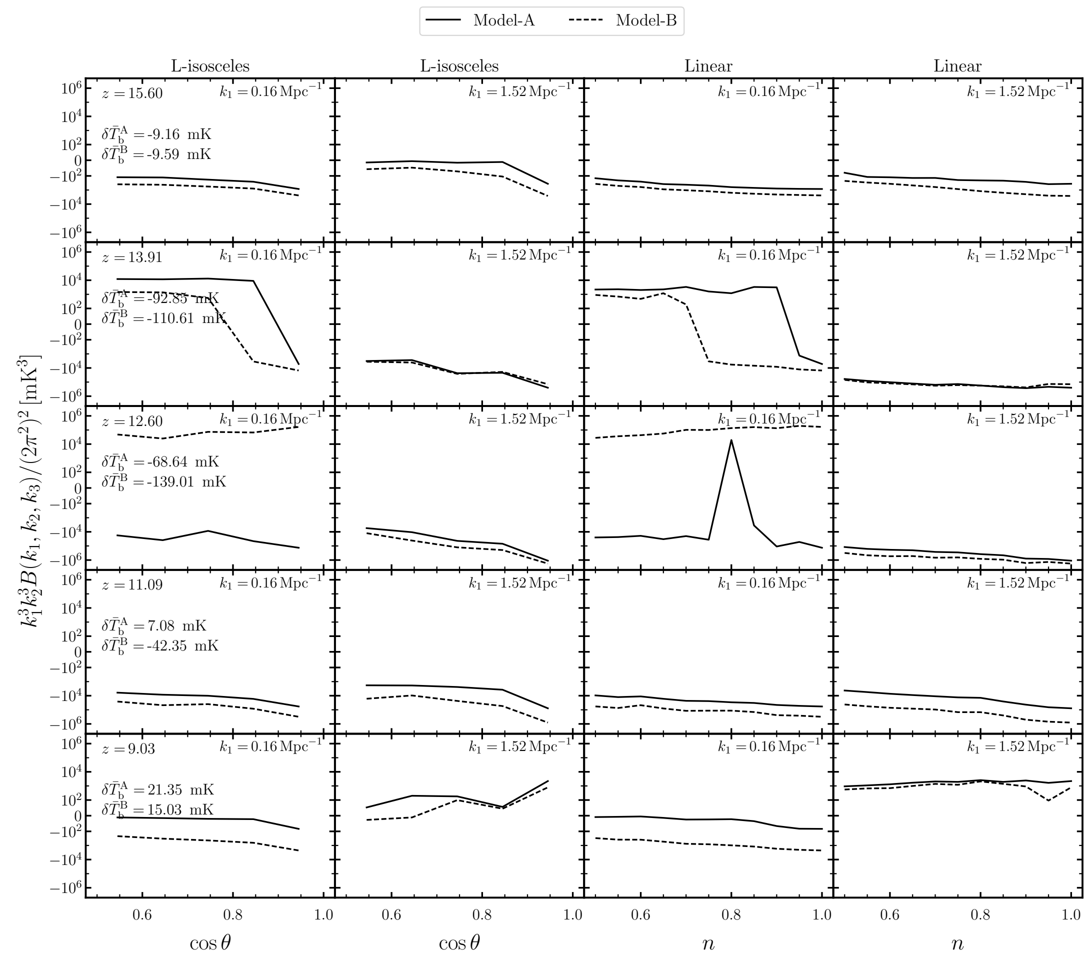

Figure 3.5: The redshift space bispectra for L-isosceles ($\cos\theta$, $n = 1$) and linear (n, $\cos\theta = 1$) k-triangles for Model-A (solid lines) and Model-B (dashed line) at five different stages of CD and for *small* and *large* k_1 modes.

in k_1 values except for the squeezed and the linear k-triangles. Lastly, around *very late* stage, the bispectrum magnitude increases with k_1, and its largest variations are seen for the linear k-triangles. Hence, for most of the time during the CD, bispectrum will have maximum magnitude in the limit and the vicinity of squeezed and linear k-triangles.

3.4.1.2 Evolution of the bispectrum sign

We next focus on the sign of the bispectrum which has been identified as an important feature of this statistic along with its magnitude in several earlier works [183–185, 190]. In Figure 3.3 for Model-A we observe that around *very early* stage $B(k_1 \approx 0.2\,\mathrm{Mpc}^{-1})$ is

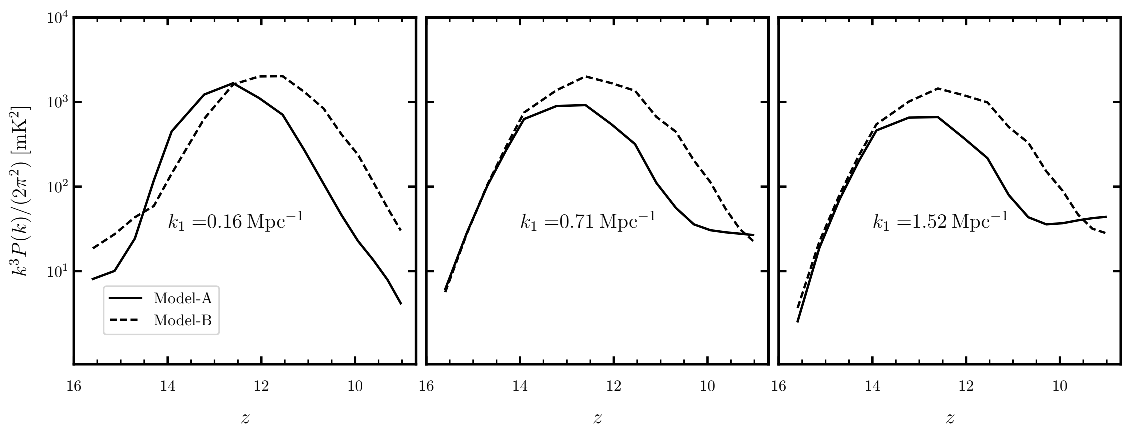

Figure 3.6: Variation of the power spectrum with redshift for different source models for three different k_1 modes.

negative for the entire $n - \cos\theta$ space. This is due to the fact that at *very early* stage the size and number density of Lyα coupled regions are very large. Whereas, the size and number density of the heated regions are comparatively very low (see the top left panel of Figure 3.1). The bispectrum can have a negative sign due to either of the following two reasons: if $\Delta_{\rm b}$s for all three k-modes have negative sign or the $\Delta_{\rm b}$ for only one k mode has negative sign. Due to the dominance of the absorption regions during this period (Figure 3.1), it is most likely that the first cause is satisfied in this case. For the *large* k_1-triangles in the entire n–$\cos\theta$ space the bispectra remain negative until the *late* stage. This behaviour is observed for the period when $T_{\rm S}$ fluctuations dominate over the other two constituent fields. A detailed discussion on this behaviour is further given in Section 3.4.3.

We also observe that there are certain regions in the $n - \cos\theta$ space where the bispectra are positive. The bispectrum can have a positive sign if either all three $\Delta_{\rm b}$ are positive or only one $\Delta_{\rm b}$ is positive. $B(k_1 \sim 0.2\,{\rm Mpc}^{-1})$ is positive only at the *early* stage for almost entire $n-\cos\theta$ space, except in the limit and vicinity of the squeezed k-triangles. Further, the $B(k_1 \approx 0.7\,{\rm Mpc}^{-1})$ is positive within the $\cos\theta$ range $0.5 \lesssim \cos\theta \lesssim 0.85$ for the entire CD except the *very late* stage. The bispectra become positive at the *very late* stage for $k_1 \gtrsim 1\,{\rm Mpc}^{-1}$ in the entire $n - \cos\theta$ space. This is the stage when signal is in emission regime and the matter density fluctuations dominate over the other two constituents of the signal. This results is also in good agreement with the findings of [190] for the early stages of reionization.

Next, we discuss the sign reversal (change) of the bispectra due to the cosmic evolution of the signal as well as due to the variations in the k_1 mode. In the earlier studies [183–

185, 190], this phenomenon has been associated with the nature of the non-Gaussianity in the 21-cm signal. We first discuss this as a function of k_1 mode for a fixed stage of the CD. Figure 3.3 shows that for our fiducial model at the *very early* stage as we move from *small* to *intermediate* k_1 modes, a sign change of the bispectra (from negative to positive) is observed within $\cos\theta$ range $0.5 \lesssim \cos\theta \lesssim 0.9$. As one further moves towards *large* k_1 modes the sign again gets reversed within the same $\cos\theta$ range. A similar feature is also observed for the *middle* and the *late* stages of CD. At the *early* and the *very late* stages the scenario is different compared to the other stages. During the *early* stage, as one moves from *small* to *large* k_1 mode the sign of the bispectra change first for the linear k-triangles and then for the entire $n - \cos\theta$ space (except at the limit and the vicinity of the squeezed k-triangles). Further, at the *very late* stage as we go towards the *large* k_1 mode, the bispectra change its sign first for linear k-triangles and then for all k-triangles. This is due to the fact that as we go towards larger k_1 modes at this stage, the matter density fluctuations dominates. This has been identified as the source of the positive sign of the bispectrum.

We next focus on the sign reversal of the bispectra with redshift (i.e. stages of the CD, see Figures 3.3 and 3.4 for Model-A). During a major portion (i.e., from *very early* to *late* stages) of the CD when the $T_{\rm S}$ fluctuations dominate over the matter density and the neutral fraction fluctuations, the sign reversal of the bispectra with z is observed only for *small* k_1-triangles. For this k_1-triangles the sign change takes place twice, first in the transition from the *very early* (panel at first column and first row in Figure 3.3) to the *early* (panel at first column and second row) stage and next in the transition from the *early* to the *middle* (panel at first column and third row) stage. This happens in almost entire n–$\cos\theta$ space. The reason behind these sign reversals can be understood via a close investigation of the brightness temperature maps (see first column of Figure 3.1). At the *early* stage the Lyα coupling is still dominant over the X-ray heating. However, we see that the heated regions are more numerous (but very small in size) at this stage (compared to the *very early* stage) and are distributed following the source locations (i.e. collapsed halos, purple in colour in these maps). As we know that the bispectrum can be positive if either all three $\Delta_{\rm b}$ are positive or only one $\Delta_{\rm b}$ is positive. The maps in Figure 3.1 suggests that the second reason is most probable during this period, i.e. in most of the cases two length scales (corresponding k modes) belongs to the Lyα coupled regions (giving rise to two negative $\Delta_{\rm b}$s) and one length scale falls in the heated regions (corresponding to one positive $\Delta_{\rm b}$) resulting in the observed positive sign of the bispectra. By the *middle* stage the Lyα coupled regions still dominate the brightness temperature fluctuations but heated regions are larger in size now. Following same argument now in most of the cases two $\Delta_{\rm b}$s are positive (as they belong to the heated regions) and one $\Delta_{\rm b}$ is negative (belonging the Lyα coupled regions) in their contribution to the bispectrum estimator, resulting in a negative bispectrum.

Finally, we observe one more sign reversal of the bispectra in *intermediate* and *large* k_1-triangles and for almost the entire n–$\cos\theta$ space, during the transition from the *late* to the *very late* stages. This sign reversal can be understood as follows: At the *late* stage the distribution of the heated regions dominates the brightness temperature fluctuations, however there are still a significant amount of Lyα coupled absorption regions present in the IGM (see the panel corresponding to $z = 11.09$ for Model-A in Figure 3.1). This makes the bispectrum negative at this stage. By the *very late* stage most of the IGM is heated (i.e. $T_{\rm S}$ approaches its saturation limits) and there are some ionized regions present in the IGM (following the distribution of the sources, see the bottom panel for Model-A in Figure 3.1). This effectively constitutes the very early stages of the EoR, when the bispectrum is expected to be positive [183, 184, 190]. This particular sign reversal of the bispectrum in *intermediate* and *large* k_1 modes can be used as a confirmative test of the saturation of the heating of the IGM and the starting point of a significant global reionization.

Note that in Figure 3.4 the bispectrum for equilateral k triangle for Model-B shows a sudden change in sign around $z \sim 12$ for large k_1 triangles. A similar sign change of this kind is not observed in Model-A in the same or any earlier or later redshifts. Other than this feature, the redshift evolution of the equilateral k triangle bispectrum is quite consistent in both models. Presently, we do not have any obvious interpretation for this feature. In future, we would like to study this in detail by generating many statistically independent realizations of the signal. It will help us to identify if this is caused due to the sample variance or not.

To draw a comparison between the redshift evolution of the bispectrum and the popular spherically averaged 21-cm power spectrum, we show this power spectrum for three representative k modes in Figure 3.6. A comparison between Figure 3.4 and 3.6 shows that at the *very early* stage, both the power spectra and bispectra start with a small magnitude irrespective of the k mode, for both source models. The magnitude of both of these statistics then increases with decreasing redshift and reach their respective maximum value in the redshift range $z \sim 12 - 13$. Both of them then gradually decrease their magnitude during the later stages of the cosmic dawn. This is consistent with the evolution of the fluctuations in the 21-cm field that we have discussed earlier. However, apart from the magnitude evolution the bispectrum also shows significant evolution in the sign the details of which depend on the shape of the k-triangle and the magnitude of the k_1 mode involved.

The evolution of the bispectrum thus has the potential to provide us with more insight about the IGM physics compared to what can be derived from the power spectrum.

3.4.2 Effect of the source models on the bispectrum

In this section, we compare the redshift space 21-cm bispectrum for two different source models. The details of these two models are tabulated in Table 3.1. We first compare the source models through their 21-cm bispectra for a few specific k-triangle shapes, e.g., equilateral, squeezed, L-isosceles and linear k-triangles, and then generalize this comparison for all unique triangle shapes in the n–$\cos\theta$ space.

First we check the impact of source models on the shape of the bispectra. A visual inspection of of the evolution of bispectra for equilateral and squeezed k-triangles as a function of z, shown in Figure 3.4, reveals that for a specific k_1 mode for both the models the shapes of the bispectra are same. The main features of the shapes of the bispectra in two models only differ by the redshift values at which they appear. Therefore, in Figure 3.4 the bispectra from two models appear to be just shifted with respect to each other. A similar feature can also be seen in the power spectra (see Figure 3.6).

Next, we compare the bispectra of both the models for L-isosceles and linear k-triangles. Figure 3.5 shows the bispectra for Models A and B at five different stages of the CD and for *small* and *large* k_1 modes. The first two and the last two columns represent bispectra for the L-isosceles and linear k-triangles, respectively. We first compare the magnitude and sign of the bispectra for both source models at different stages of the CD. An important observation from this figure is that the shape of the bispectra does not depend on the source model, rather it only depends on the stage of evolution of the CD and the specific k_1-triangle under consideration. Further, at the *very early* stage the magnitude of the bispectra are slightly larger for Model-B than that for Model-A irrespective of the k_1 modes and the triangle shapes. Additionally, at this stage the sign of the bispectra are negative in the entire n (for the linear k-triangles) and $\cos\theta$ (for the L-isosceles k-triangles) range.

At the *early* stages and for small k_1 mode for both the L-isosceles and the linear k-triangles the magnitude of the bispectra for Model-A are larger than Model-B only when the sign of the bispectra are positive. A reverse phenomenon is observed when the sign of the bispectra are negative. Furthermore, at the *early* stage although the shape of the bispectra for both models are same, the sign of the bispectra for small k_1 triangles get reverse for small values of $\cos\theta$ in Model-B. On the other hand, at this stage for *large* k_1

triangles the magnitude, the sign and the shape of the bispectra for both the models are same.

We next observe that at the *middle* stage of the CD for the *small* L-isosceles and the linear k_1-triangles the sign of the bispectra for Model-A are negative and for Model-B are positive while their magnitudes are same. Further, at this stage for *large* L-isosceles and linear k_1-triangles the magnitude of the bispectra are larger in Model-B, but, they have same signs and the shapes as Model-A.

At the *late* stage of the CD the magnitude of the bispectra for Model-B are larger than that for Model-A irrespective of the k_1 mode and k-triangle shapes. The sign of the bispectra are same for both models irrespective of the k_1 mode k-triangle shapes.

Finally, at *very late* stage we observe a large difference between magnitude of the bispectra for Model-A and B at *small* k_1 mode. It is large by ~ 2 orders of magnitude for Model-B as compared to Model-A. This is due to the fact that for Model-A, by the *very late* stage most of the IGM is heated (i.e. $T_{\rm S}$ approaches its saturation limits) however, for Model-B there are still some leftover unheated Lyα coupled regions (see bottom panel of Figure 3.1). This causes a larger fluctuation in the signal for Model-B compared to Model-A at these redshifts, leading to a higher magnitude of the bispectra. This feature implies that due to the presence of only HMXB type sources (i.e. Model-B) the IGM will get heated completely at a later time as compared to the scenario when there are only mini-QSO (Model-A) type sources. Further, at this stage for small k_1 triangles the sign and the shape of the bispectra are same in both models. Lastly, for large k_1-triangles the sign of the bispectra are positive in both models and the magnitude of the bispectra in Model-A is slightly higher than that in Model-B. Hence we can conclude that the different source models do not significantly affect the shape of the bispectra but, they change its magnitude (significantly) and sign depending on the stages of the CD and k-triangle shape for which the bispectra are being estimated.

Next, we generalize our discussion for all unique k-triangles in the n–$\cos\theta$ space. In the last three columns of Figure 3.3 we show the bispectra for all unique k-triangles for Model-B at five different stages (at the same redshifts as for Model-A shown in Figure 3.3) of the CD and at three different k_1 modes. We now discuss the impact of the different sources on the evolution of the bispectra through a comparison between Model-A and Model-B. We first compare their redshift evolution at *small* k_1 mode. For triangles with *small* k_1 mode, as one make transition from the *very early* stage to the *early* stage, the sign reversal of the bispectra for Model-B is observed only in the limit and the vicinity of the S-isosceles k-triangles. On the other hand for Model-A it is observed almost in the entire n–$\cos\theta$

space. For Model-B a further transition from *early* to *middle* stage at *small* k_1 mode makes the bispectra sign positive almost in the entire n–$\cos\theta$ space. However, during the same transition in Model-A the bispectra sign changes from positive to negative in for all triangle shapes. In the next obvious transition, from *middle* to *late* stage, for Model-B we observe a complete sign change (positive to negative) of the bispectra for in the entire n–$\cos\theta$ space. On the contrary, for Model-A no further sign change is observed. Lastly, in the transition from *late* to *very late* stage, for Model-B no sign reversal is observed (similar to Model-A), rather, a decrease in the magnitude of the bispectra is observed in the entire n–$\cos\theta$ space. This decrements in the magnitude for Model-B is small as compared to what is observed for Model-A in this regime. In fact around *very late* stage, for Model-B, in the entire n–$\cos\theta$ space, the magnitude of the bispectra is larger by ~ 2 orders of magnitude compared the same for Model-A. This is due to the same physical reason as discussed earlier in this section for L-isosceles and linear k-triangles. Hence triangles of all shapes, in the entire n–$\cos\theta$ space, carries the signature of the late time saturation of IGM heating by the HMXB type sources as compared to the scenario for mini-QSO type sources.

We observe that the two source models have similar impact on the sign of the bispectra (and its change with redshift) from the *very early* to the *very late* stages of the CD for the *intermediate* and *large* k_1 modes. The only difference in their impact shows up through the magnitude of the bispectra for these k_1 modes (similar to the discussion earlier in this section for L-isosceles and linear k-triangles for the large k_1 mode).

3.4.3 Impact of the spin temperature fluctuations on the bispectrum

The spin temperature fluctuation is the component (the other two components being the matter density and the neutral fraction) that has maximum contribution in determining the nature and magnitude of the 21-cm brightness temperature fluctuations during the CD. Consequently one would expect that it will have a significant impact on the bispectrum of the signal as well. One of the main aim of this chapter is to study the impact of the spin temperature fluctuations on the bispectrum statistic. To quantify this impact, we compute the quantity $\mathfrak{D} = [||B_{\mathrm{Low\,T_S}}| - |B_{\mathrm{High\,T_S}}||]/|B_{\mathrm{High\,T_S}}|$ (see Figure 3.7) where, $B_{\mathrm{Low\,T_S}}$ is the bispectrum values when fluctuations in the T_{S} has been taken under consideration. On the other hand, $B_{\mathrm{High\,T_S}}$ is the bispectrum values at the limit when T_{S} reaches saturation i.e., $T_{\mathrm{S}} = T_{\mathrm{K}} \gg T_\gamma$. Thus this quantity $\mathfrak{D}$ will also be a function of k_1, n, $\cos\theta$, just as the bispectrum itself. A high value of $\mathfrak{D}$ corresponds to a large impact of the spin

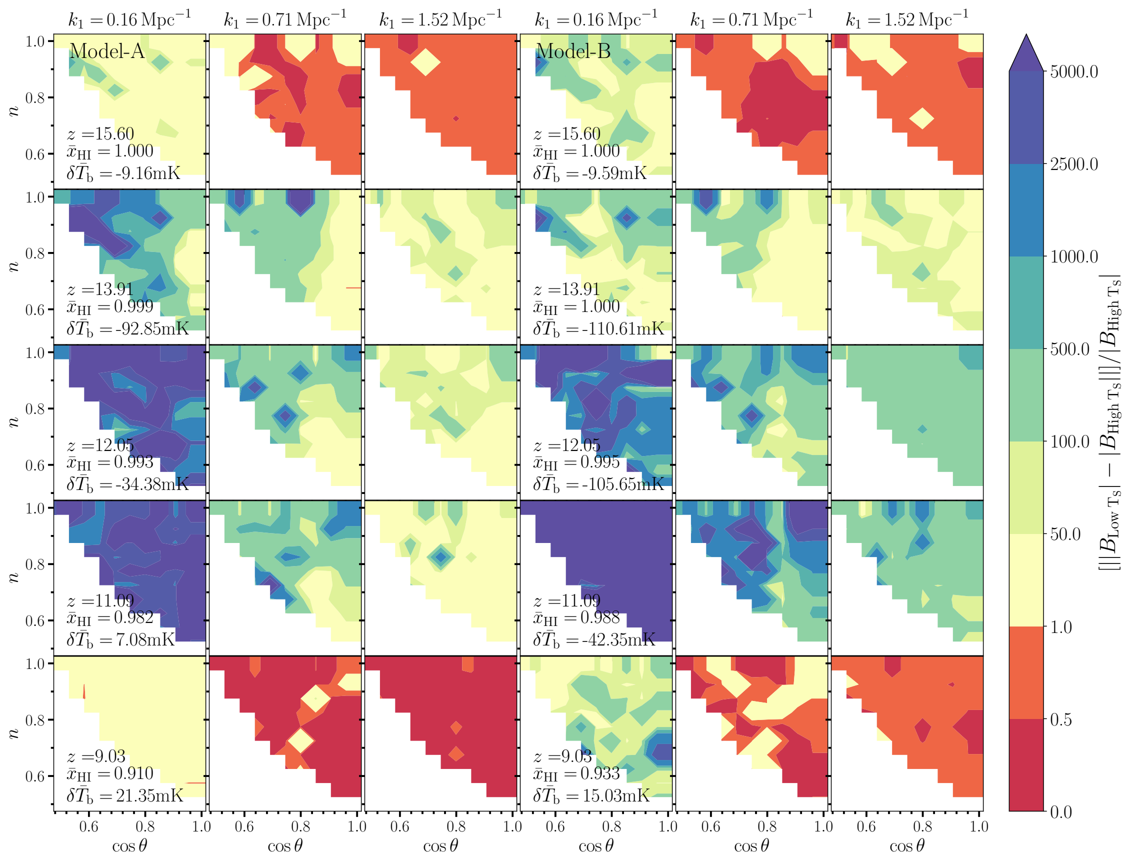

Figure 3.7: The quantity $\mathfrak{D}(k_1,\, n,\, \cos\theta) = [||B_{\mathrm{Low\ T_S}}| - |B_{\mathrm{High\ T_S}}||]/|B_{\mathrm{High\ T_S}}|$, estimating the effect of the spin temperature fluctuations on the bispectrum magnitude for Model-A (left three columns) and Model-B (right three columns) at five different stages of the CD and for three different k_1 modes.

temperature fluctuations on the bispectra and vice versa. Figure 3.7 shows $\mathfrak{D}(k_1,\, n,\, \cos\theta)$ for both Models A and B, at three different k_1 modes and five different stages of the CD.

We first note the k_1 dependence of $\mathfrak{D}$ from Figure 3.7. We find that irrespective of the source models and stage of the CD and for almost all unique triangle shapes, $\mathfrak{D}$ decreases monotonically as one varies k_1 modes from *small* to *large*. $\mathfrak{D}$ has largest magnitude for *small* k_1-triangles and smallest magnitude for *large* k_1-triangles. The reason for this behaviour of $\mathfrak{D}$ can be understood in the following manner: the smaller k-modes will be sensitive to the signal coming from the larger length scales. The signal fluctuations at large scales (i.e. smaller k-modes) is significantly influenced by the presence of large number of absorption and emission regions (having sizes smaller than the large length scale under consideration). Thus one would expect the magnitude of bispectra to decline monotonically from *small* to *large* k_1-triangles.

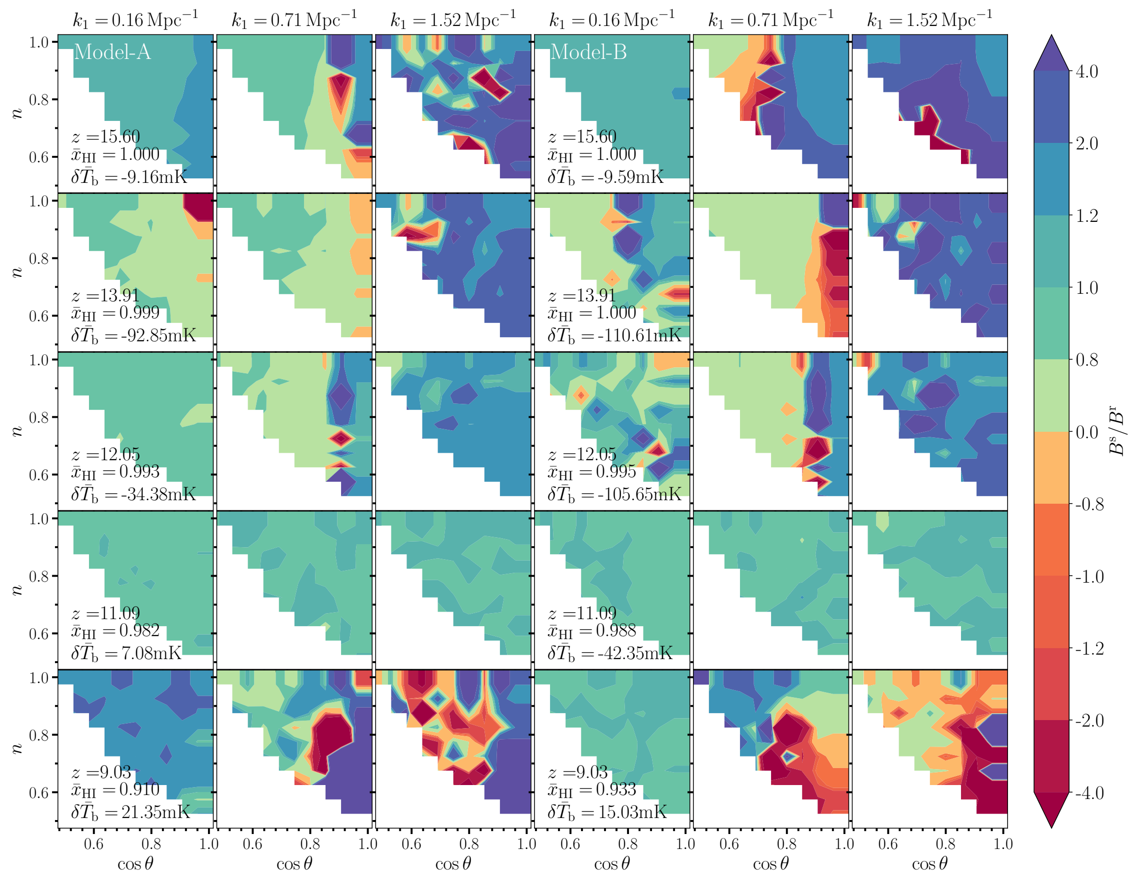

Figure 3.8: The ratio $B^{\rm s}/B^{\rm r}$, quantifying the impact of the RSD on the CD 21-cm bispectra for all unique triangle configurations of Model-A and Model-B at five different stages of the CD and for three different k_1 modes.

We next discuss the redshift evolution of $\mathfrak{D}$. Irrespective of the source model and k_1 mode, one can clearly see a general trend in the evolution of $\mathfrak{D}$. The $\mathfrak{D}$ is small at the *very early* stage. It then gradually increases and reaches a maxima around the *middle* stage for Model-A and around the *late* stage for Model-B. After the *middle* stage it gradually decreases until the *very late* stage. One can see a clear one-to-one correspondence between the evolution of $\mathfrak{D}$ with redshift and the evolution of the amplitude of fluctuations in the signal with redshift (see Figure 3.1).

3.4.4 Impact of the RSD on the CD bispectrum

We next focus on quantifying the impact of RSD on the 21-cm bispectrum from the CD. As per our knowledge this is the first attempt to quantify the effect of RSD on the CD 21-cm bispectrum using simulated signals. To quantify the impact of RSD, we show the ratio of the spherically averaged bispectrum in redshift space (B^{s}) to its real space counterpart (B^{r}), i.e., $B^{\mathrm{s}}/B^{\mathrm{r}}$ in Figure 3.8. The figure shows redshift evolution of the $B^{\mathrm{s}}/B^{\mathrm{r}}$ for both models and for three different k_1 modes. The RSD affects both magnitude and sign of the bispectra. The values of the $B^{\mathrm{s}}/B^{\mathrm{r}}$ in this figure can be divide into three groups: $B^{\mathrm{s}}/B^{\mathrm{r}} \approx 1$, implying that the impact of the RSD is negligible, $B^{\mathrm{s}}/B^{\mathrm{r}} > 1$ implying that the RSD enhances the magnitude of the bispectra and $0 < B^{\mathrm{s}}/B^{\mathrm{r}} < 1$, implying that RSD reduces the magnitude of the bispectra. Additionally, if $B^{\mathrm{s}}/B^{\mathrm{r}} < 0$, it implies that the RSD changes the sign of the bispectra. We label this sign change as *sign difference* between the real and redshift space bispectrum.

Starting at the *very early* stage, we observe that the RSD enhances the magnitude of the bispectra (by $\lesssim 100\%$ for Model-A and $\lesssim 10\%$ for Model-B) for *small* k_1 modes, in the entire n–$\cos\theta$ space. For *intermediate* and *large* k_1 modes the impact is even larger. The RSD either changes (increases or decreases) the magnitude of the bispectra by more than 20% or/and introduces *sign difference* for these k-triangles. As the Lyα coupling and X-ray heating of the IGM progresses further, for different source models RSD impacts differently depending on the stages of the CD and k_1 modes involved.

In the *early* stages for *small* k_1 mode, the *sign difference* arises in the limit and vicinity of the squeezed k-triangles in Model-A, however, for Model-B no such *sign difference* is observed. Furthermore, for other k-triangles n–$\cos\theta$ space (for both models), the RSD decreases the bispectrum magnitude by more than 20%. For *intermediate* and *large* k_1-triangles in the entire n–$\cos\theta$ space, RSD has the largest impact on both magnitude (changes as high as $\sim 400\%$) and sign, irrespective of the source models.

While transitioning form the *early* to the *middle* stage, the impact of RSD decreases until the *late* stage is reached (irrespective of k_1 modes and source types). Hence, the RSD has minimum impact around the *late* stages for both source models and for all k_1-triangles. A further transition from the *late* to the *very late* stage allows the impact of RSD on the bispectra to increase.

Finally, we discuss the impact of the RSD around the *very late* stage. For *small* k_1 mode, it affects only the magnitude of the bispectra for Model-A, enhancing it by more than $\sim 20\%$. On the other hand, for *intermediate* and *large* k_1 modes, the RSD changes both the magnitude and the sign of the bispectra irrespective of source model.

3.4.5 Interpretation of the CD redshift space bispectra using the linear theory of the RSD

To interpret the features observed in the spherically averaged redshift space bispectra, we opt for the linear model for the differential brightness temperature in redshift space while considering the effect of the $T_{\rm S}$ fluctuations [79, 82, 178]. Under this linear model one can express the spherically averaged CD redshift space bispectra as a correction to the real space bispectra as shown in Section 2.3 of Chapter 2. In Chapter 2 (Section 2.5.2.2 and Appendix A.1) we have demonstrated that the correction term that has maximum impact on the redshift space bispectra is the $B_{\mu^2-{\rm RC}}$. In case of the CD 21-cm signal bispectra that we consider here, we find the same to be true (demonstrative figures not shown here and we request the interested readers to refer to Chapter 2).

3.5 Chapter Summary and Discussions

In this chapter, we have presented a comprehensive view of the non-Gaussianity in the 21-cm signal from the Cosmic Dawn (CD) through the signal bispectra estimated for all unique k-triangles. All of the earlier works in this line have considered only a few specific types of k-triangles. We explore the k-triangles, $\mathbf{k}_1 + \mathbf{k}_2 + \mathbf{k}_3 = 0$, using k_1, $n = k_2/k_1$ and $\cos\theta = -(\mathbf{k}_1 \cdot \mathbf{k}_2)/(k_1 k_2)$ quantities. Additionally, for the first time, we also quantify the impact the redshift space distortions as well as the impact of the spin temperature fluctuations on the CD 21-cm bispectra for all unique k-triangles. The characteristics of the heating and ionizing sources in the early universe may have a significant impact on the signal bispectrum. To understand the impact of the source models on the bispectra, we have considered two different types of sources in this work, they are mini-QSOs (Model-A) and HMXBs (Model-B). Note that the entire analysis presented in this chapter is based on the redshift space 21-cm signal from the cosmic dawn. The findings of our analysis can be summarized as follows:

- The magnitude of the CD 21-cm bispectra in the entire n–$\cos\theta$ space initially increases with decreasing redshift irrespective of the k_1 modes and source model. This is due to the increasing amplitude of fluctuations in the signal due to the simultaneous Lyα coupling and X-ray heating of the IGM. The bispectrum reaches its maxima around the stage when the signal fluctuations are also at their maximum (and the Lyα coupling reaches its saturation). After that the bispectrum magnitude decreases with decreasing redshift as further heating of the IGM decreases the amplitude of fluctuations in the signal. Finally, the magnitude of the bispectrum is minimum when most of the IGM is heated.

- The redshift evolution of the magnitude of the bispectra for both source models show similar trends, however the redshifts at which the maxima and minima of the amplitude appears depend on the nature of the sources of heating and ionization. For mini-QSO type sources maxima and minima of the bispectra magnitude appear around $z \sim 12$ and $z \sim 9$, respectively. Whereas for HMXB type sources they appear around $z \sim 11$ and $z \lesssim 9$. Bispectra for triangles of almost all unique shapes show this behaviour. This is a signature of the rather late saturation of IGM heating in case of the HMXB type sources as compared to the mini-QSO type sources.

- The sign of the CD 21-cm bispectra is an important feature of this statistic. For a given stage of the CD and a specific length scale, the sign of the bispectra effectively probes which among the three physical processes, namely heating, Lyα coupling and reionization, is the major cause of non-Gaussianity in the signal.

- The sign reversal of the bispectra is an important phenomenon associated with the nature of the non-Gaussianity in the signal. In scenarios when both Lyα coupling and X-ray heating are underway simultaneously (in a competitive manner), we observe two sign reversals in bispectra for *small* k_1-triangles (irrespective of the source models). The first one is from negative to positive and the second one from positive to negative (see first and fourth columns in Figure 3.3 for Model-A and Model-B respectively). Via a visual inspection of the simulated 21-cm maps we associate the first sign reversal with the emergence of the numerous but very small sized heated regions in the IGM while the Lyα coupling still have dominating contribution to the signal fluctuations and thus to its non-Gaussianity. The second sign reversal is associated with the phase when the Lyα coupling in the entire IGM is complete. Such distinct signature of these two unique phases of the CD is not visible in any other signal statistics e.g. the redshift evolution of the mean global signal or the power spectrum. Thus the sign reversals of bispectrum have the possibility of providing us a unique and independent way of constraining the CD history. To check the robustness of this phenomenon we need to study it for a variety of source models and cosmic dawn scenarios. We have studied about these issues in details in our recent works [192] and [193] which we have presented in this thesis as Chapter 4 and 5 respectively.

- The spin temperature fluctuations have significant impact on the signal bispectra. Independent of the source models, the impact is maximum on the bispectra for triangles with *small* k_1 modes. Further, for a specific k-triangle the impact of $T_{\rm S}$

fluctuations on the signal bispectra initially increases with decreasing z due to the simultaneous Lyα coupling and X-ray heating of the IGM. The impact T_{S} fluctuations is largest around the stage when the Lyα coupling reaches saturation. After this the impact of the T_{S} fluctuations gradually decreases as X-ray heating takes up the dominant role in shaping the signal and overall amplitude of fluctuations in the signal brightness temperature also goes down.

- The redshift space distortions have a significant impact on both the magnitude and the sign of the bispectra. The level of this impact depends on the specific stage of the CD and k-triangle shape and size. At any given stage of the CD, its maximum impact is observed at bispectra for the large k_1-triangles. For most of scenarios RSD changes the magnitude of the bispectra by more than $\sim 20\%$.

- We find that a model bispectra based on the linear theory of the RSD provides a good interpretation the simulated bispectra observed for triangles with small k_1 modes. Further, among the three groups of correction terms that contributes in the model bispectra, the $B_{\mu^2-\mathrm{RC}}$ dominates in shaping the CD 21-cm redshift space bispectra amplitude and sign.

The CD scenarios considered here (for both source models) have both the Lyα coupling and the X-ray heating of the IGM running in parallel from the *very early* stages of the CD. As discussed before, this may have a significant impact on the bispectra amplitude, sign and sign reversal. In order to connect the redshift evolution of the 21-cm bispectrum with these IGM processes, we also need to study the scenarios where first the Lyα coupling of the IGM reaches saturation and then X-ray heating starts to contribute significantly. We have studied this recently in our work [192] and presented it here in Chapter 4.

The analysis of the CD 21-cm redshift space bispectra in this chapter though of very comprehensive in nature but is limited to only two source models, both having same model parameters like $M_{\mathrm{halo,\,min}}$, f_{X}. To properly understand the impact of the source models on the signal bispectra, we will need to study it for a much wider variety of sources, which we have studied in our recent work [193] and presented in this thesis as a chapter (Chapter 5).

Chapter 4

Probing IGM physics during Cosmic Dawn using the redshifted 21-cm bispectrum

---

This chapter is adapted from: **Kamran M.**, Majumdar S., Ghara R., Mellema G., Bharadwaj S., Pritchard J. R., Mondal R., Iliev I. T.; *Probing IGM Physics during Cosmic Dawn using the Redshifted 21-cm Bispectrum*; submitted to **Physical Review Letters** [arXiv:2108.08201v2].

4.1 Introduction

The Cosmic Dawn (CD) and Epoch of Reionization (EoR) are the periods in the history of the Universe during which the formation of the first sources of radiation caused major changes in the thermal and ionization states of the Inter-Galactic Medium (IGM). Various complex astrophysical processes dictate the state of the IGM during CD [1, 82].

The redshifted 21-cm line, originating from the hyperfine spin-flip transition of the electron in the ground state of neutral hydrogen atoms (HI), can trace the cosmological and astrophysical evolution of the IGM during CD in the most direct manner. Ongoing and upcoming radio interferometric experiments e.g. GMRT [97], LOFAR [67], MWA [122], PAPER [123], HERA [72] and SKA [74] are expected to be sensitive enough to probe this signal from the CD through various statistics such as the variance [117, 224], power spectrum [3], etc.

The power spectrum measures the amplitude of fluctuations in a signal at different length scales and can fully quantify the statistical properties of a pure Gaussian random field. However, the CD 21-cm signal is highly non-Gaussian due to the joint effects of the non-random distribution of first light sources in the IGM, the nature of the radiation emitted by these sources, as well as the interaction of this radiation with the HI gas in the IGM [132, 148, 161]. The nature and strength of fluctuations of this signal at any location in the IGM are determined by the relative population densities of the two different spin states of the 1s ground state of the HI atom. This ratio is commonly expressed as $n_1/n_0 = 3\exp(-0.068\,\mathrm{K}/T_\mathrm{S})$, where T_S is the so-called spin temperature, n_1 and n_0 are the population densities of the parallel and anti-parallel spin states respectively. Different IGM processes, determined by the nature of the different types of radiation coming from the first sources, affect this ratio. Thus, the fluctuations in the HI 21-cm signal are expected to carry the signatures of these IGM processes [82]. In other words, the nature of the fluctuations in the signal and therefore its inherent non-Gaussianity is determined by which IGM process dominates at what cosmic time [161, 183–185, 190, 192]. The power spectrum is not sensitive to this non-Gaussianity in the signal, hence one cannot probe the IGM physics solely based on this statistic. Higher-order statistics such as the bispectrum are required to describe how the 21-cm signal's non-Gaussianity evolves at different length scales [183–185, 190, 192, 211, 246].

Compared to the power spectrum, which is always positive by definition, the CD 21-cm bispectrum can be either positive or negative [183–185, 190, 192]. We thus expect the sign and magnitude of the bispectrum to be dependent on the dominant IGM processes, as these processes dictate the nature of non-Gaussianity in the signal. It is therefore imperative to ask whether the sign and magnitude evolution of the 21-cm bispectrum can identify which IGM processes dominate at which stage of the CD.

In this chapter, we demonstrate for the first time that it is possible to probe the CD IGM physics through the evolution of the sign and magnitude of the 21-cm bispectrum.

4.2 Simulating the HI 21-cm signal from the Cosmic Dawn

This work is based on an N-body simulation using the CUBEP^{3}M code [128] in a volume $(500\,h^{-1})^3$ comoving Mpc^3 using 6912^3 dark matter particles. The resolved halos have been identified with having at least 25 particles, resulting in minimum halo mass $\approx 10^9$ $\mathrm{M}_\odot$. The dark matter density and velocity fields were interpolated on a 600^3 grid. We then use these ingredient fields in the 1D radiative transfer code GRIZZLY [153, 154] to simulate the 21-cm differential brightness temperature (δT_b) maps at 22 redshift snapshots in the range $z = 9$ to 20 following the equations in [82]:

$$\delta T_\mathrm{b}(\mathbf{r}, z) = 27 x_\mathrm{HI}(\mathbf{r}, z)\big(1 + \delta_\mathrm{b}(\mathbf{r}, z)\big)\left(1 - \frac{T_\mathrm{CMB}(z)}{T_\mathrm{S}(\mathbf{r}, z)}\right)\left(\frac{\Omega_\mathrm{b} h^2}{0.023}\right)\left(\frac{0.15}{\Omega_\mathrm{m} h^2}\frac{1+z}{10}\right)^{1/2} \mathrm{mK}, \quad (4.1)$$

where $\mathbf{r}$ is the comoving distance to the source of emission, z is the redshift at which the signal was emitted, $x_\mathrm{HI}(\mathbf{r}, z)$ is the hydrogen neutral fraction, $\delta_\mathrm{b}(\mathbf{r}, z)$ is the fluctuations in the underlying baryon density and $T_\mathrm{CMB}(z)$ is the Cosmic Microwave Background (CMB) radiation temperature. The spin temperature is connected to the IGM processes via the equation

$$T_\mathrm{S}(\mathbf{r}, z) = \frac{T_\mathrm{CMB}(z) + x_\alpha(\mathbf{r}, z) T_\mathrm{g}(\mathbf{r}, z)}{1 + x_\alpha(\mathbf{r}, z)} \quad (4.2)$$

Hence the value of T_S will be determined by the strength of the Lyα coupling process x_α and the temperature of the IGM, T_g. T_g is determined by the adiabatic cooling due to cosmological expansion and the heating due to X-ray sources. Here we do not consider the impact of collisions on T_S as our redshift range ($20 > z > 9$) is well below the regime where collisions are important ($z \gtrsim 30$) [82]. Hence, the evolution of the fluctuations in the 21-cm signal depends on the changes in the Lyα coupling, X-ray heating and photo-ionization of the IGM gas and below we will focus on the impact of these three processes on the bispectrum. The 21-cm signal will be observed in either absorption or emission depending on whether the factor $(1 - T_\mathrm{CMB}/T_\mathrm{S})$ is negative or positive, respectively. However, once heating has raised T_g substantially above T_CMB at late stages of the CD, the 21-cm emission becomes insensitive to the value of T_S, a regime known as spin temperature saturation, and then photo-ionization becomes important.

Further, the X-ray sources in our simulations have a spectral energy density $I_X(E) \propto E^{-\alpha}$ with $\alpha = 1.5$ which roughly represents mini-QSOs [247, 248]. These are expected to be the major sources of the soft X-ray photons during the CD. Apart from the X-ray photons produced by mini-QSOs, we also consider the contributions from star forming galaxies which produce ionizing photons. We further assume the stellar content of a galaxy to be proportional to the mass of the dark matter halo that hosts the galaxy. Thus, the stellar mass inside a halo of mass M_halo is $M_\star = f_\star\left(\frac{\Omega_\mathrm{b}}{\Omega_\mathrm{m}}\right) M_\mathrm{halo}$ where $f_\star$ is the star formation efficiency. We choose $f_\star = 0.03$ [249, 250] throughout this chapter. More details about these simulations can be found in [192].

Processes \ Scenarios	Model-a_0	Model-a	Model-b	Model-c
Lyα-coupling	Yes	Yes	Saturated	Yes
X-ray heating	No	No	Yes	Yes
Ionization	No	Yes	Yes	Yes

Table 4.1: All simulated CD scenarios considered in this study.

We have applied the effect of the redshift space distortions (RSD) to these simulated $\delta T_{\rm b}$ cubes by using the MM-RRM scheme of [159]. The cosmological parameters used in the simulations are $h = 0.7$, $\Omega_{\rm m} = 0.27$, $\Omega_\Lambda = 0.73$, $\Omega_{\rm b} = 0.044$, which are consistent with *WMAP* [228] and *Planck* results [52].

In this chapter we consider four different scenarios for the evolution of the signal from the Cosmic Dawn as listed in Table 4.1. The first three are simplistic and extreme scenarios in which only a single physical process dominates the fluctuations in the 21-cm signal. The fourth scenario includes all three physical processes and therefore is the most realistic CD scenario. We use the first three scenarios to demonstrate the unique signatures of each of the three physical processes on the 21-cm bispectrum, which eventually helps us in explaining the bispectrum from Model-c, the most realistic scenario. The details of these scenarios are as follows: In Model-a_0, we only consider the evolution of Lyα coupling in a cold and neutral IGM. Model-a is a modified version of Model-a_0 where we also include the effect of photo-ionization of HI in the IGM. In Model-b, we consider the processes of X-ray heating and ionization but assume that a very strong Lyα background fully couples $T_{\rm S}$ to $T_{\rm g}$. Finally, in Model-c, we include all of these processes in a self-consistent manner. Figure 4.1 shows the slices through the $\delta T_{\rm b}$ cube from very early to very late stages of the CD (left to right) for Model-a (top panels), Model-b (middle panels), and Model-c (bottom panels). The redshift evolution of the $\delta \bar{T}_{\rm b}$ (global signal) for all of these models are shown in the left panel of Figure 4.2.

Note that in this chapter we are specifically interested to explore the impact of IGM physics on the bispectrum during CD, specifically when Lyα coupling and X-ray heating are the most dominant processes. However, we also wanted to include the later stages of the CD in our analysis, when it gradually transitions to the EoR, thus up to $\sim 10\%$ of HI ionization has been considered in our models.

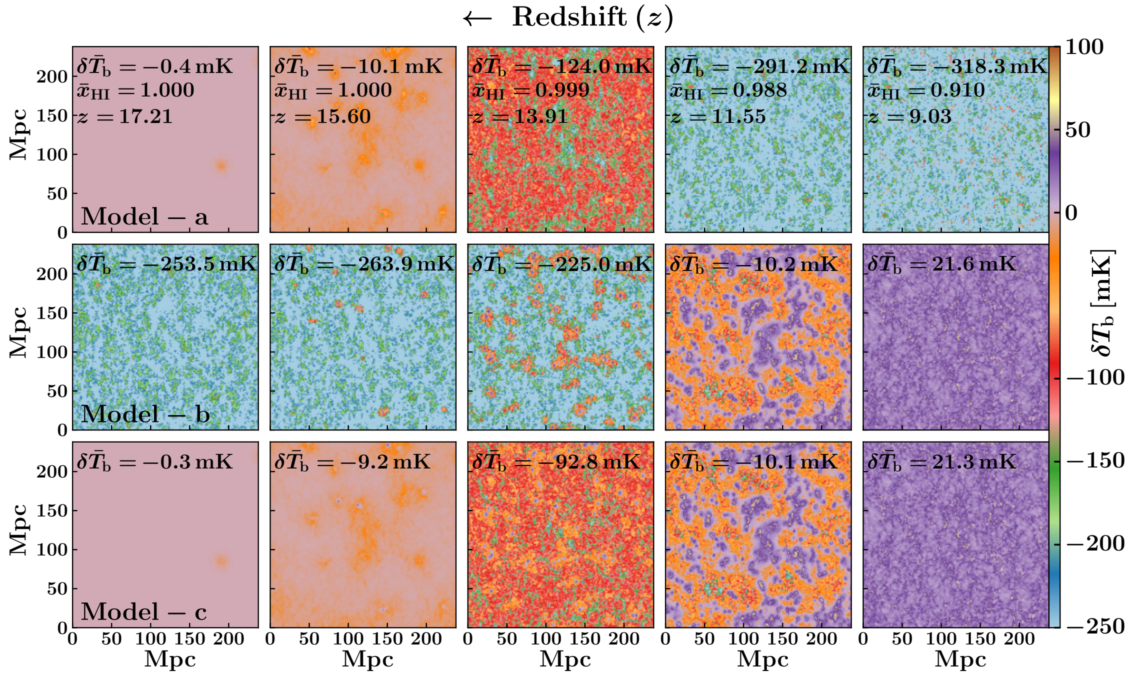

Figure 4.1: Zoomed in slices (side length 238.09 Mpc) of the brightness temperature showing the redshift evolution of the 21-cm signal for scenarios Model-a (Top panels), Model-b (Middle panels), Model-c (Bottom panels). The full simulation volume is $(714.29\,\text{Mpc})^3$ in size.

4.3 Bispectrum estimation

We adopt the bispectrum estimator and associated algorithm discussed in 2 to compute the bispectrum from the simulated data as

$$\hat{B}_i(\mathbf{k}_1, \mathbf{k}_2, \mathbf{k}_3) = \frac{1}{N_{\rm tri} V} \sum_{[\mathbf{k}_1+\mathbf{k}_2+\mathbf{k}_3=0]\in i} \Delta_{\rm b}(\mathbf{k}_1)\Delta_{\rm b}(\mathbf{k}_2)\Delta_{\rm b}(\mathbf{k}_3)\,, \tag{4.3}$$

where $\Delta_{\rm b}(\mathbf{k})$ is the Fourier transform of $\delta T_{\rm b}(\mathbf{r})$, V is the observation or simulation volume and $N_{\rm tri}$ is the number of closed triangles associated with the $i^{\rm th}$ triangle configuration bin while satisfying the condition $\mathbf{k}_1 + \mathbf{k}_2 + \mathbf{k}_3 = 0$. Throughout this chapter, we discuss spherically averaged bispectrum estimates obtained from our simulations.

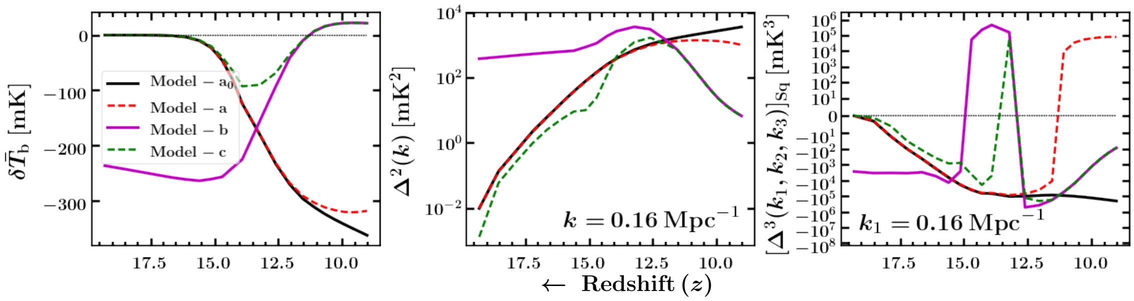

Figure 4.2: Redshift evolution of the global 21-cm signal (left panel), the spherically averaged power spectrum at $k \sim 0.16\,\mathrm{Mpc}^{-1}$ (middle panel), and the bispectrum for squeezed limit k-triangles with $k_1 \sim 0.16\,\mathrm{Mpc}^{-1}$ (right panel). Different colours represent different CD scenarios as shown in Table 4.1.

4.4 Results

We estimate the power spectrum $[P(k)]$ and bispectrum $[B(k_1, k_2, k_3)]$ for all CD scenarios of Table 4.1 for $k_1 = 0.16\,\mathrm{Mpc}^{-1}$, which represents large length scales that can be potentially probed by telescopes e.g. SKA. For the sake of convenience, we designate $k_1 \leq 0.16\,\mathrm{Mpc}^{-1}$ as 'large-scale'. We normalize these statistics as $\Delta^2(k) = k_1^3 P(k)/2\pi^2$ and $\Delta^3(k_1, k_2, k_3) = k_1^3 k_2^3 B(k_1, k_2, k_3)/(2\pi^2)^2$. Recent studies [183, 190, 192] suggest that among all k-triangles, the magnitude of the bispectrum is maximum for the squeezed limit k-triangles. One would therefore expect the bispectrum for this shape of k-triangle to have the maximum signal-to-noise ratio [170, 172] and thus to have the highest probability of detection in future SKA observations. In addition to this, the squeezed limit bispectrum for $k_1 = k_2 = 0.16\,\mathrm{Mpc}^{-1} > k_3 \to 0$, provides the correlation between the signal fluctuations at large and very large length scales. Motivated by this we only consider the large-scale squeezed limit bispectrum i.e. $[\Delta^3(k_1, k_2, k_3)]_{\rm Sq}$ and investigate how they are affected by various IGM processes. The right panel in Figure 4.2 shows the redshift evolution of $[\Delta^3(k_1, k_2, k_3)]_{\rm Sq}$. Note that we consider the k_1 bin width, $\Delta k_1 \sim 0.17\,\mathrm{Mpc}^{-1}$, in such a manner that the centre of the bin corresponds to $k_1 \approx 0.16\,\mathrm{Mpc}^{-1}$.

Before describing our results, we discuss the nature of the expected signal using simple analytical models. These will help us to interpret the basic nature of the results obtained from our simulations. Let us assume an IGM with uniform properties, and therefore uniform 21-cm signal (a 'background') in which one physical process locally changes the 21-cm signal around a source. For convenience, we also assume that the region with the changed 21-cm signal has a spherical shape. Such a description was used by [161, 183] for the case of a neutral, spin temperature saturated ($T_{\rm S} \gg T_{\rm CMB}$) background, which therefore has 21-cm in emission, in which photo-ionizing sources produce ionized regions with a zero 21-cm signal. They showed that the sign of the signal fluctuations of such a field in Fourier domain is negative and of the form: $\Delta_{\rm b} \propto -W(kR)\sum \exp i\mathbf{k}\cdot\mathbf{r}$, where $W(kR)$ is the spherical top-hat window function, R is the comoving radius of the ionized spheres and the summation is performed over all such spheres with centres at $\mathbf{r}$. The negative sign is due to the regions having a lower signal than the background. The same approach can be used for other processes and backgrounds, for example, a neutral heated (emission) region in a cold and neutral (absorption) background, which by analogy yields positive fluctuations.

Following this line of argument, one can predict the sign of the signal fluctuations on large-scales in scenarios when one of the three IGM processes is dominant. Note that we only consider the sign here, so the exact shape of the regions is irrelevant. The four relevant cases during CD are:

1. A Lyα coupled region in a neutral, cold and approximately uncoupled ($T_{\rm S} \approx T_{\rm CMB}$) background. The region will have a strong negative 21-cm signal in a very weak negative background. Consequently, the large-scale $\Delta_{\rm b}$ will be negative.

2. An X-ray heated region ($T_{\rm S} > T_{\rm CMB}$) in a neutral, cold and fully Lyα coupled background ($T_{\rm S} < T_{\rm CMB}$). The region will have a positive 21-cm signal in a negative background. Consequently, the large-scale $\Delta_{\rm b}$ will be positive.

3. An ionized region in a neutral, heated and fully Lyα coupled background ($T_{\rm S} > T_{\rm CMB}$). The region will have zero 21-cm signal in a positive background. Consequently, the large-scale $\Delta_{\rm b}$ will be negative.

4. An ionized region in a neutral, cold and fully Lyα coupled background ($T_{\rm S} < T_{\rm CMB}$). The region will have zero 21-cm signal in a negative background. Consequently, the large-scale $\Delta_{\rm b}$ will be positive.

5. A Lyα coupled region in a neutral and heated background ($T_{\rm S} > T_{\rm CMB}$). The region will have a negative 21-cm signal in a positive background. Consequently, the large-scale $\Delta_{\rm b}$ will be negative.

4.4.1 Bispectrum magnitude and sign

As stated earlier, the large-scale squeezed limit bispectrum $[\Delta^3]_{\rm Sq}$ probes the correlation between three large-scale $\Delta_{\rm b}$ corresponding to the three k-modes of the squeezed limit k-triangle. Hence, one would expect the magnitude of $[\Delta^3]_{\rm Sq}$ to depend on the magnitudes of these three $\Delta_{\rm b}$. Furthermore, the sign of $[\Delta^3]_{\rm Sq}$ is given by the sign of the product of three $\Delta_{\rm b}$s averaged over the bin corresponding to the k-triangle. Hence, if the $\Delta_{\rm b}$s are positive, then $[\Delta^3]_{\rm Sq}$ will be positive. Similarly, if the $\Delta_{\rm b}$s are negative, then $[\Delta^3]_{\rm Sq}$ will be negative. We use this analogy only when we connect the simulated results to the simple analytical models.

4.4.2 Model-a$_0$ and Model-a

The redshift evolution of the average or global signal $\delta\bar{T}_{\rm b}$, the spherically averaged power spectrum Δ^2 and squeezed limit bispectrum $[\Delta^3]_{\rm Sq}$ for Model-a$_0$ are shown by solid black lines in the left, middle and right panels of Figure 4.2. This CD scenario involves only the Lyα coupling process. This process starts with a negligible contribution to the global 21-cm signal during very early stages and gradually grows the 21-cm fluctuations with decreasing redshift (left panel of Figure 4.2). Due to this, the magnitude of the $\Delta_{\rm b}$ gradually enhances and consequently causes the magnitude of $[\Delta^3]_{\rm Sq}$ to increase with decreasing redshift. As expected from the analytical model 1, the sign of $[\Delta^3]_{\rm Sq}$ is indeed negative.

For Model-a, $[\Delta^3]_{\rm Sq}$ agrees with that for Model-a$_0$ until $z \sim 12$, as shown by the dashed red line in right panel of Figure 4.2. This is because the ionization process, which is included in Model-a but not in Model-a$_0$, does not play a significant role until this redshift ($\bar{x}_{\rm HI} \sim 0.99$). As ionization gains importance for $z \lesssim 12$, it causes a sign reversal in $[\Delta^3]_{\rm Sq}$ from negative to positive. This is consistent with the expectation from the analytical model 4.

4.4.3 Model-b and Model-c

Model-b, shown by magenta lines in Figure 4.2, considers X-ray heating in an IGM with fully saturated Lyα coupling ($T_{\rm S} = T_{\rm g}$). Hence, in this model, the 21-cm signal transitions from a state of global absorption to a state of global emission. During the early stages ($19 \gtrsim z \gtrsim 15.5$), only a few X-ray sources are active. The heating they cause cannot compete with the adiabatic cooling due to the expansion of the Universe. The net effect is a gradual cooling of the IGM that further decreases the $T_{\rm S}$, at a faster rate than the CMB temperature does (as $T_{\rm CMB} \propto (1+z)$). This implies a gradual enhancement in $\left|1 - T_{\rm CMB}/T_{\rm S}\right|$ with time during these early stages, and with a negative sign as $T_{\rm S} < T_{\rm CMB}$. This results in the negative $\delta\bar{T}_{\rm b}$ with a slowly evolving magnitude seen in the left panel of Figure 4.2. In this redshift range $\Delta_{\rm b}$ cannot be predicted analytically but seems to follow a similar trend as the global signal as $[\Delta^3]_{\rm Sq}$ is found to be negative with a slowly evolving magnitude.

IGM heating in Model-b becomes important at $z \sim 15.5$ and reduces the magnitude of the absorption signal around the sources by producing warm (or less cold) regions (second panel from left in the middle row of Figure 4.1). Additionally, it also produces small heated regions (where 21-cm signal is in emission) around the same sources. This effect continues as heating progresses and results in an overall reduction in the magnitude of $\Delta_{\rm b}$ until $z \sim 15$. The magnitude of the bispectrum also follows this trend for $15.5 \gtrsim z \gtrsim 15$. As heating progresses further by $z \sim 14.5$, the heated regions grow in number and size. The 21-cm signal fluctuations thus can be thought of as being due to a few emission regions embedded in an absorption background. This is the case as predicted in analytical model 2. Hence, the large-scale $\Delta_{\rm b}$ will be positive. This will result in a positive $[\Delta^3]_{\rm Sq}$ (i.e. a sign reversal in $[\Delta^3]_{\rm Sq}$). In the redshift range $14.5 \gtrsim z \gtrsim 13$, heated regions grow substantially and percolate. Thus, in this redshift range although the signal fluctuations and its bispectrum cannot be predicted analytically, the simulated $[\Delta^3]_{\rm Sq}$ remains positive by $z \sim 13$.

As heating progresses the regions grow in number and size and this percolation process leads to more and more heated regions overlapping, ultimately resulting in a single large connected cluster of heated regions. This will also result towards a situation where the heated emission regions occupy a larger volume in the IGM than the cold absorption ones. Hence, we gradually move towards the scenario where a few isolated cold absorbing regions are embedded in a hot emitting background. The $\Delta_{\rm b}$s thus follow the trend predicted by model 5. This results in a negative $[\Delta^3]_{\rm Sq}$, another sign reversal in $[\Delta^3]_{\rm Sq}$, which is indeed seen at $z \sim 12.5$. Due to the continued X-ray heating, the leftover absorption regions disappear (see the two right most panels in the second row of Figure 4.1) and hence the magnitude of $\Delta_{\rm b}$ also goes down, which in turn gradually reduces the $[\Delta^3]_{\rm Sq}$ magnitude towards the end of the CD.

The physical insights obtained from Models-$\rm a_0$, a and b can now be used to understand the evolution of $[\Delta^3]_{\rm Sq}$ for the realistic CD scenario, Model-c. In the redshift range $19 \gtrsim z \gtrsim 14$ $[\Delta^3]_{\rm Sq}$ for Model-c, shown by the dashed green line in the right panel of Figure 4.2, shows similar trends in shape and sign as that of Models-$\rm a_0$ and a. We see that initially Model-c follows Models-$\rm a_0$ and a, implying that Lyα coupling to cold gas is the dominant process during these stages. The sign reversal seen around $z \approx 14$ is due to X-ray heating becoming the dominant process, which remains the case until the end of the simulation at $z = 9$, as we see that Model-c follows Model-b. One important point to note here is that during $19 \gtrsim z \gtrsim 11.5$, the magnitude of $[\Delta^3]_{\rm Sq}$ for Model-c is smaller than that of the Models-$\rm a_0$, a and b, simply because the Lyα coupling has not yet saturated in Model-c.

4.4.4 Bispectrum a better probe of IGM physics

We compare the evolution of the signal bispectrum with that of the power spectrum (middle panel of Figure 4.2) in their ability to identify the dominant IGM processes during the CD. We have demonstrated that the bispectrum via its sign and sign changes can conclusively tell us which IGM process dominates $\Delta_{\rm b}$ at what cosmic time. The redshift evolution of the power spectrum does show certain subtle features at the time of transition from the dominance of one physical process to the other. However, as this statistic is always positive, it is difficult to unequivocally identify these transitions on the basis of the power spectrum alone.

4.4.5 Detectability of the CD 21-cm bispectrum

Recently, [170] have studied the detectability of the 21-cm bispectrum from the EoR. They have shown that even in the presence of system noise and cosmic variance, a $\geq 5\sigma$ detection of the squeezed limit bispectrum is possible with SKA for $k_1 \lesssim 0.8\,{\rm Mpc}^{-1}$. Since the maximum amplitude of the large-scale squeezed limit 21-cm bispectrum from the CD is ~ 2 orders of magnitude larger than that from the EoR [192] we therefore expect that the large-scale squeezed limit 21-cm bispectrum from the CD would be detectable with the SKA observations. The full detectability prediction is beyond the scope of this thesis. We plan to explore it in future.

4.5 Chapter Summary and conclusions

In this chapter we show for the first time how the two major IGM processes affecting the 21-cm signal during the CD, namely Lyα coupling and X-ray heating, impact the magnitude and sign of large scale ($k_1 \sim 0.16\,{\rm Mpc}^{-1}$) squeezed limit 21-cm bispectrum. We demonstrate that the sign of the $[\Delta^3]_{\rm Sq}$ is negative as long as Lyα coupling is the dominant IGM process. We show that this conclusion holds even in the presence of X-ray heating. The $[\Delta^3]_{\rm Sq}$ goes through a double sign change, around the time when X-ray heating becomes the most dominant IGM process. We have further demonstrated that these transitions cannot be conclusively probed by the power spectrum.

Our analysis suggests that $[\Delta^3]_{\rm Sq}$ is a better statistic to put constraints on the dominating IGM processes during CD. This will become important in the context of the future 21-cm observations of CD with the SKA. Our analysis here is restricted only to the CD, when ionization never becomes the dominant process for the 21-cm fluctuations. In future, we plan to explore the connection of the sign of $[\Delta^3]_{\mathrm{Sq}}$ with the IGM physics during the EoR.

In this chapter, we have not studied how the various radiating sources during CD, having different source properties (parameters), impact the 21-cm signal and its bispectrum through the possible astrophysical processes. This is essential in order to check the robustness of the features in the large-scale 21-cm bispectrum. We have extensively studied this in the Chapter 5.

Chapter 5

Impact of the source properties on the CD 21-cm bispectrum

This chapter is adapted from: **Kamran M.**, Ghara R., Majumdar S., Mellema G., Bharadwaj S., Pritchard J. R., Mondal R., Iliev I. T.; *Redshifted 21-cm bispectrum: Impact of the source models on the signal and IGM physics from the Cosmic Dawn*; submitted to **Journal of Cosmology and Astroparticle Physics** [arXiv:2207.09128].

5.1 Introduction

The Cosmic Dawn and Epoch of Reionization (CD-EoR) is the period in the Universe's cosmic history during which the first glimpse of luminous sources such as stars, galaxies, quasars, etc. appeared. The radiations from these sources affected the physical states of the Universe by changing the thermal and ionization states of the intergalactic medium (IGM) during this period. A significant theoretical understanding of this epoch has been developed so far but has been little tested by the observations yet. The interferometric observations of the redshifted 21-cm signal, produced by the spin-flip transition of the electron-proton system in the 1s ground state of the neutral hydrogen (HI), are the direct tracer of HI distribution in the IGM. This signal also carries the information about the first sources, which have different properties and that drive the fluctuations in the 21-cm signal. This opens up a possibility to understand how these sources perturbed the physical states of the IGM through various underlying astrophysical processes [1,10,21]. The likely astrophysical processes dominant during the CD-EoR are the Lyα coupling, X-ray heating, and photo-ionization of IGM gas. It is widely accepted that the stars in the galaxies are the major sources of UV photons that ionize most of the HI in the IGM. The other sources, such as quasars and the X-ray binaries (XRBs), are believed to be the primary sources of the X-ray photons that drive the IGM heating. The dominant astrophysical processes decide the nature and amplitude of the 21-cm signal fluctuations around the sources and their evolution with time during the CD-EoR.

In order to detect the CD-EoR 21-cm signal, a number of observational efforts have been made by the present generation of radio interferometers such as the GMRT[1] [97], LOFAR[2] [67], MWA[3] [122], PAPER [123] and HERA[4] [72,126]. However, a number of observational obstacles such as foregrounds [251,252], systematics [253,254], etc introduce difficulties in the way of its detection, thereby these instruments are unable to image the CD-EoR maps and hope to have potential to detect the expected signal statistically. They are only able to achieve the weak upper limits of the signal fluctuations so far using the power spectrum statistic [67,122–126]. The upcoming Square Kilometre Array (SKA)[5] [2,74,223] will be able to go ahead and might make detailed tomographic images of the CD-EoR.

Until the imaging of the CD-EoR 21-cm signal becomes possible, the present generation instruments are being employed to seek the prospects of detection of this signal using different statistical measures such as variance [115,117,224], power spectrum [67,94,96] etc. The power spectrum can capture the amplitude of fluctuations present in the CD-EoR 21-cm maps at different length scales. The spherically averaged power spectrum as an estimator characterizes a signal and fully describes the statistical properties of a Gaussian random field [3, 79, 119, 147, 148, 156–160, 163, 164, 178, 180, 206, 225]. The cumulative effect of the biased distribution of radiation sources, non-uniform heating, and ionization of the IGM gas by these sources introduce a high level of non-Gaussianity in the CD-EoR 21-cm maps [132,148,161,170,191,192]. This non-Gaussianity evolves together with the progress in ongoing astrophysical processes [163–166, 183, 190, 191]. By definition, the power spectrum provides the auto-correlation between the signal at a single Fourier mode and thus cannot capture this non-Gaussianity. The fundamental statistics which can capture this non-Gaussianity are skewness and kurtosis [116, 117, 167–169, 227, 255]. However, these statistics can only probe the non-Gaussian features at a single length scale.

[1] http://www.gmrt.ncra.tifr.res.in
[2] http://www.lofar.org/
[3] http://www.mwatelescope.org/
[4] https://reionization.org/
[5] http://www.skatelescope.org/

One requires some robust higher-order statistics such as the bispectrum to study how the non-Gaussian features at different length scales evolve [170, 183, 190–192].

The bispectrum, by definition, correlates the signal fluctuations in the Fourier space at three wave numbers (k modes) when forming a closed triangle. This statistic thus can capture the non-Gaussianity present in the 21-cm maps. The bispectrum has an additional feature which is its sign, compared to the power spectrum, which always attains positive values [161, 182, 183, 190]. These features make the bispectrum a robust statistical probe of all those additional fundamental characteristics of the signal that are genuinely immersed in the signal's non-Gaussianity. For instance, the astrophysical processes, which are the primary source of the non-Gaussianity during the CD-EoR, are directly connected with the source properties. One, therefore, expects the bispectrum to be a potential probe of this IGM physics [192]. Further, the nature and level of the non-Gaussianity are expected to depend on the following factors. First is the variety of sources of radiation. Second is the rate at which a particular source emits radiation that is intimately linked with the source parameters. Thus, it is expected that the bispectrum can identify and distinguish the various kinds of CD-EoR sources [185, 191, 246]. Furthermore, assuming the bispectrum to be highly sensitive to the source parameters, expected to put a tighter constraint on the CD-EoR parameters than that the power spectrum does [171, 172].

In one of our earlier works [191], we have considered various sources of light during the CD, such as the star-forming galaxies, mini quasars (mini-QSOs), and high mass X-ray binaries (HMXBs). We have shown in [191] that the evolution of the 21-cm bispectrum magnitude and the sign can distinguish these sources better than the 21-cm power spectrum. In another previous work [192], we have shown how the 21-cm signal bispectrum probes the impact of all possible astrophysical processes on the signal fluctuations by capturing the intrinsic non-Gaussianity in the signal during CD. However, in [192], we have not studied how the different X-ray sources, from fainter to brighter, impact the 21-cm signal and its bispectrum through the possible astrophysical processes. We have also not studied the effect of different $M_{\rm h,\,min}$ (minimum mass of source hosting halos) values on the 21-cm signal and its bispectrum. These CD scenarios impact the IGM with the different Lyα coupling, X-ray heating, and photo-ionization processes. This article studies how varying source parameter values impact the CD signal bispectrum. In this work, therefore, we have considered several simulated CD scenarios corresponding to all possible combinations of the values of the related source parameters within a certain range that directly control the physical processes going on in the IGM. We focus on how these different CD scenarios that affect the 21-cm signal via the different astrophysical processes will impact the large-scale 21-cm bispectrum. In addition to these, we are also interested in investigating what additional information the bispectrum for a variety of triangles in the Fourier space can draw than that the bispectrum of a special k-triangle does.

The structure of the chapter is as follows: In Section 5.2 we present the simulations used to generate the 21-cm maps. Section 5.3 describes the formalism for estimating the bispectrum from the simulated signal. Section 5.4 discusses our analysis of the bispectra for different source models. Finally in Section 5.5 we summarise our results.

In this chapter, we have used the cosmological parameters $h = 0.7$, $\Omega_\mathrm{m} = 0.27$, $\Omega_\Lambda = 0.73$, $\Omega_\mathrm{b} = 0.044$ consistent with the *WMAP* results [228] and within the error bars consistent with the *Planck* results [52].

5.2 Simulation of the Cosmic Dawn 21-cm signal

The redshifted 21-cm signal from the CD is measured against the Cosmic Microwave Background Radiation (CMBR). The strength of this radio signal is often described by the differential brightness temperature (δT_b), which can be expressed as [82]

$$\delta T_\mathrm{b}(\mathbf{r}, z) = 27 x_\mathrm{HI}(\mathbf{r}, z)\big(1 + \delta_\mathrm{b}(\mathbf{r}, z)\big)\left(1 - \frac{T_\mathrm{CMB}(z)}{T_\mathrm{S}(\mathbf{r}, z)}\right)\left(\frac{\Omega_\mathrm{b} h^2}{0.023}\right)\left(\frac{0.15}{\Omega_\mathrm{m} h^2}\frac{1+z}{10}\right)^{1/2} \mathrm{mK} \quad (5.1)$$

where $\mathbf{r}$ and z denote the position and redshift of the 21-cm signal emitting region. The quantities δ_b and $T_\mathrm{CMB}(z)$ denote the baryonic density contrast, and the CMBR temperature, respectively. In addition to the dependence on the density field and cosmological parameters (as shown in Equ.5.1), $\delta T_\mathrm{b}(\mathbf{r}, z)$ also depends on the redshift-space distortion effect due to the velocity of the gas in the IGM. The astrophysical imprints on $\delta T_\mathrm{b}(\mathbf{r}, z)$ comes from the neutral fraction $x_\mathrm{HI}(\mathbf{r}, z)$ and the spin temperature T_S terms. The H I spin temperature T_S during CD can be expressed as [76]

$$T_\mathrm{S}(\mathbf{r}, z) = \frac{T_\mathrm{CMB}(z) + x_\alpha(\mathbf{r}, z) T_\mathrm{g}(\mathbf{r}, z)}{1 + x_\alpha(\mathbf{r}, z)} \quad (5.2)$$

where $x_\alpha(\mathbf{r}, z)$ is the Lyα coupling coefficient and $T_\mathrm{g}(\mathbf{r}, z)$ is the IGM gas temperature. We ignore the effect of the collision of hydrogen with other hydrogen atoms and electrons in Equ.5.2 as the contribution of that process is expected to be negligible at the redshifts of our interest. Note that we do not consider any excess radio background (see e.g., [256–258]) to the CMBR.

We use GRIZZLY [259] code to simulate δT_b maps at 23 redshift snapshots for different astrophysical source models in the redshift range between 10 and 18. The algorithm uses

$f_{\rm X}$	0.1	2.15	46.4	1000
$M_{\rm h,Min}$ $(10^9\, M_\odot)$	1.0	2.15	4.64	10.0

Table 5.1: Different values of the X-ray heating efficiency parameter $f_{\rm X}$ and the minimum mass of halo with radiating sources $M_{\rm h,\,min}$ as considered in this study. We consider all possible pairs of the two source parameter ($f_{\rm X}$, $M_{\rm h,\,min}$) values and explore sixteen simulated CD scenarios in this study.

a one-dimensional radiative transfer scheme which approximates that the photon transfer from individual sources is isotropic. We refer the reader to [154, 259] for the details of the algorithm. This algorithm requires dark matter halo catalogs, gridded cosmological density, and velocity fields as input. The density and velocity fields used in this study are taken from results of the PRACE[6] project PRACE4LOFAR. The dark-matter only N-body simulation was performed in a volume $(500h^{-1})^3$ comoving Mpc^3 (for details, see e.g.,[260]) using CUBEP^{3}M code [128]. The outputs density and velocity fields were gridded on 600^3 grids. The dark-matter halos were resolved by an on-the-fly spherical overdensity halo finder, which identified halos with masses higher than $\approx 10^9$ M$_\odot$.

The source model used in the GRIZZLY algorithm assumes the stellar mass (M_*) of a galaxy formed in a dark matter halo of mass $M_{\rm h}$ is $M_* = f_*\left(\frac{\Omega_{\rm B}}{\Omega_{\rm m}}\right)M_{\rm h}$ where we fix the value of the star formation efficiency f_* to 0.03 [249, 250] in this study. The algorithm also requires the spectral energy distribution (SED) per stellar mass of a galaxy as input for the 1D radiative transfer. The SED per stellar mass of a galaxy used in the code is generated using a publicly available population synthesis code PEGASE2 [234]. This set the emission rate of ionizing photons per unit stellar mass as $2.85 \times 10^{45}\ s^{-1}M_\odot^{-1}$. In addition to the stellar contribution, we also consider an X-ray spectrum as a power-law of the energy with a spectral index fixed to 1.2. The emission rate of the X-ray photons per unit stellar mass is set as $f_{\rm X} \times 10^{42}\ s^{-1}M_\odot^{-1}$ where we vary the X-ray heating efficiency $f_{\rm X}$. We define the UV band as an energy range of 13.6 eV to 100 eV, while the X-ray band span from 100 eV to 10 keV. Such SEDs are also used in our previous studies, such as [209, 239, 259]. The source model used in this paper also assumes that only those dark matter halos with masses larger than $M_{\rm h,\,min}$ emit Lyα, UV and X-ray photons. We also vary $M_{\rm h,\,min}$ in this study. Table 5.1 shows the four different values of each parameters $f_{\rm X}$ and $M_{\rm h,\,min}$ as considered in this study. We consider 16 different Cosmic Dawn scenarios, which correspond to different combinations of $f_{\rm X}$ and $M_{\rm h,\,min}$.

Note that our large simulation volume does not consider low mass halos ($M_{\rm h,\,min} < 10^9 M_\odot$)

[6] Partnership for Advanced Computing in Europe: http://www.prace-ri.eu/

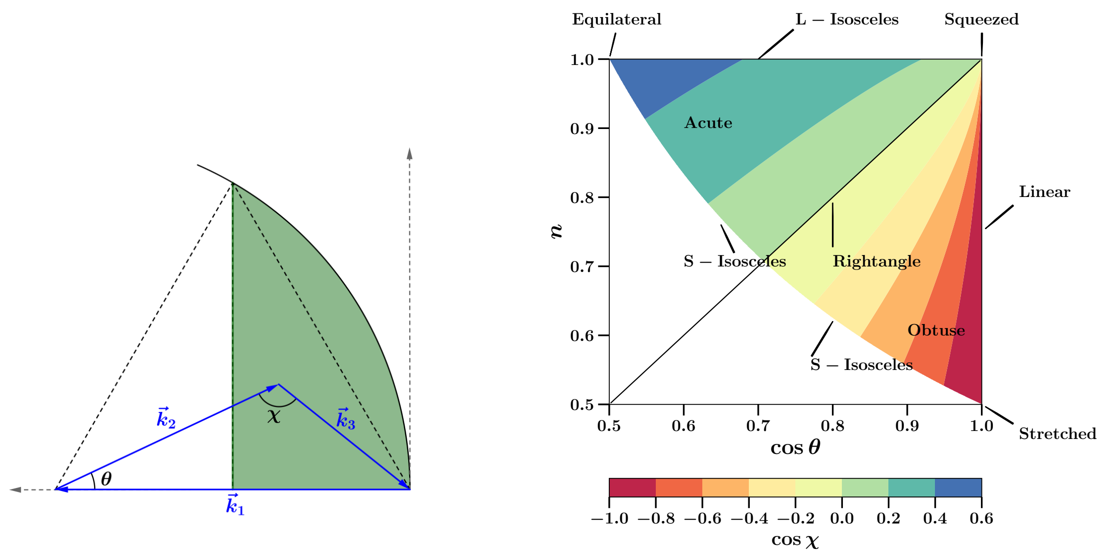

Figure 5.1: **Left panel:** Shows the definition of unique triangles in Fourier space. The shaded region is formed by all possible point of intersection between $\mathbf{k}_2$ and $\mathbf{k}_3$ vectors while equations (5.6), (5.7) and (5.8) are satisfied. **Right panel:** Shows the variation of $\cos\chi$ with n and $\cos\theta$ for all unique k-triangles. The region $n\cos\theta \geq 0.5$ is bounded by the S-isosceles, L-isosceles and linear k-triangles. The corner points represent equilateral, squeezed and stretched limit of k-triangles.

because resolving these halos in this large volume requires simulations of a very high dynamic range which are beyond the computing power that we have allowed to access. Even if we include the mini-halos using an approximation technique, e.g., the subgrid model [153, 261], the broad conclusion regarding the bispectrum is expected to remain the same (for details, see section 3.2 of [153], which shows the importance of mini-halos in the context of the power spectrum).

5.3 Bispectrum estimation

In this section, we discuss the formalism for estimating the bispectra for all possible unique triangles in Fourier space.

5.3.1 The bispectrum and the different triangle configurations

We use the definition of the bispectrum estimator given in [183] to estimate the bispectra from the simulated data. The bispectrum estimator for the i^{th} triangle configuration bin is given as

$$\hat{B}_i(\mathbf{k}_1, \mathbf{k}_2, \mathbf{k}_3) = \frac{1}{N_{\rm tri} V} \sum_{[\mathbf{k}_1+\mathbf{k}_2+\mathbf{k}_3=0]\in i} \Delta_{\rm b}(\mathbf{k}_1)\Delta_{\rm b}(\mathbf{k}_2)\Delta_{\rm b}(\mathbf{k}_3)\,, \tag{5.3}$$

where $\Delta_{\rm b}(\mathbf{k})$ is the Fourier transform of the differential brightness temperature of the 21-cm field, $N_{\rm tri}$ is the number of samples of closed triangles associated with the $i^{\rm th}$ triangle configuration bin, V is the simulation volume. The actual calculation of the bispectrum has been performed using the algorithm of [183] and [190]. This algorithm has introduced two following constraints in order to define the shapes of the k-triangles, which additionally reduces the computation time for bispectrum estimation,

$$n = \frac{k_2}{k_1} \tag{5.4}$$

$$\cos\theta = -\frac{\mathbf{k}_1 \cdot \mathbf{k}_2}{k_1 k_2}, \tag{5.5}$$

where k_1 and k_2 are the magnitudes of the vectors $\mathbf{k}_1$ and $\mathbf{k}_2$ respectively.

5.3.2 The unique triangle configurations in the triangle parameter space

For a given size of k-triangle, which is determined by the magnitude of the k modes involved; its shape can be uniquely specified in the $n-\cos\theta$ space by imposing the conditions prescribed in [5], i.e.,

$$k_1 \geq k_2 \geq k_3 \tag{5.6}$$

$$0.5 \leq n \leq 1.0 \tag{5.7}$$

$$0.5 \leq \cos\theta \leq 1.0. \tag{5.8}$$

The unique triangles are only presented by the shaded region in the $n - \cos\theta$ space where $n\cos\theta \geq 0.5$ as shown in the right panel of Figure 5.1. The shaded region in the left panel of this figure is formed by all possible point of intersection between $\mathbf{k}_2$ and $\mathbf{k}_3$ vectors while equations (5.6), (5.7) and (5.8) are satisfied. The left panel of this figure also shows all possible unique k-triangles represented by the cosine of the angle χ subtended by the vertex of triangle facing the k_1 arm. For a detailed classification of unique k-triangles we refer the reader to Section 2.2 in Chapter 2.

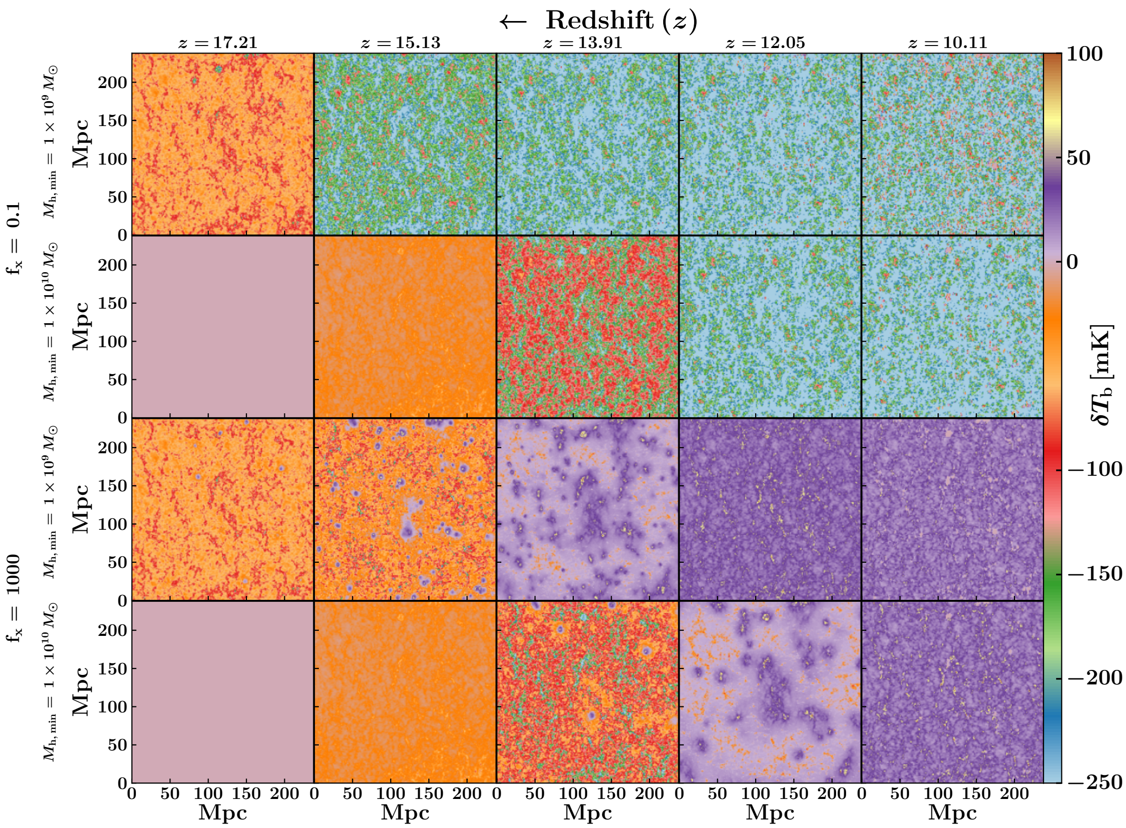

Figure 5.2: Zoomed in slices (side length 238.09 Mpc) of the differential brightness temperature (δT_{b}) for four different CD scenarios showing the redshift evolution of the 21-cm signal. The upper two panels show the redshift evolution of δT_{b}, where $f_{\mathrm{X}} = 0.1$ (smallest), and $M_{\mathrm{h,\,min}}$ attains two extreme values of the considered range. The lower two panels have $f_{\mathrm{X}} = 1000$ (largest) with the same $M_{\mathrm{h,\,min}}$ values as the upper panels. The full simulation volume is $(714.29\,\mathrm{Mpc})^3$ in size.

We estimate and analyze the spherically averaged bispectra extracted from the data cubes simulated at required redshifts during CD. For this, we divide the entire n as well as $\cos\theta$ range with step sizes $\Delta n = 0.05$ and $\Delta\cos\theta = 0.01$. We further bin the entire k_1-range ($k_{\mathrm{min}} = 2\pi/[\text{box size}] \approx 0.01\,\mathrm{Mpc}^{-1}$, $k_{\mathrm{max}} = 2\pi/2[\text{grid spacing}] \approx 2.64\,\mathrm{Mpc}^{-1}$) into 15 logarithmic bins. We label each bin by the value of k_1 as the magnitude of the k_1 bin determines the size of the k-triangle in our formalism.

5.4 Results

In this section, we present the analysis of the 21-cm bispectrum from the CD for several scenarios corresponding to all possible combinations of the source parameters, listed in

Table 5.1. Fig. 5.2 shows the slices of δT_{b} maps for four different scenarios with different ($M_{\mathrm{h,\,min}}$, f_{X}) pairs formed by the combinations of two extreme values of these parameters. Here panels in each row show the redshift evolution of a specific CD scenario with decreasing redshifts from left to right. The panels in two top rows show the redshift evolution of δT_{b}, where $f_{\mathrm{X}} = 0.1$ (smallest) and $M_{\mathrm{h,\,min}}$ is kept fixed at the two extreme values of its range listed in Table 5.1. Similarly, the bottom two panels have $f_{\mathrm{X}} = 1000$ (largest) with the same $M_{\mathrm{h,\,min}}$ values as the two top panels. Figure 5.2 shows that signal strength is low at $z \sim 17$ due to inefficient Lyα coupling in any CD scenario. At $z \sim 14$ the maps for $f_{\mathrm{X}} = 0.1$ and 1000 are different as emissions regions go very fast for $f_{\mathrm{X}} = 1000$ scenarios. Further, the scenarios with $f_{\mathrm{X}} = 0.1$ remain absorption signal dominated throughout the redshift range considered in this study. However, the signal for $f_{\mathrm{X}} = 1000$ scenarios becomes emission dominated at the late stages of the CD.

In Fig. 5.3, the left-most panel (designated as the first panel) shows the redshift evolution of the global 21-cm brightness temperature ($\delta \bar{T}_{\mathrm{b}}$) for all CD scenarios considered here. One can see that the amplitude of the absorption trough remains small for larger values of f_{X}. The transition from absorption signal to emission happens earlier for larger f_{X} values. The second and third panels demonstrate the redshift evolutions of the mean Lyα coupling coefficient ($\bar{x}_{\alpha}$) and the fraction of the simulation volume heated above the CMB temperature ($\bar{f}_{\mathrm{Heated}}$), i.e., $T_{\mathrm{g}} > T_{\mathrm{CMB}}$, respectively. The Ly$\alpha$ coupling coefficient is independent of the f_{X} values and varies only with the $M_{\mathrm{h,\,min}}$ values. The $\bar{x}_{\alpha}$, therefore, for smaller $M_{\mathrm{h,\,min}}$ are larger. The $\bar{f}_{\mathrm{Heated}}$ will depends on both f_{X} and $M_{\mathrm{h,\,min}}$ values. For example, the heating for scenarios with higher f_{X} and lower $M_{\mathrm{h,\,min}}$ values will begin and saturate earlier. The right-most panel in Figure 5.3 shows the redshift evolution of the global ionization fraction ($\bar{x}_{\mathrm{HII}}$) for all CD scenarios. In this study, we assume that X-ray photons will also engage in a small amount of photo-ionization via their X-ray photons on top of the usual dominant UV photo-ionization. Therefore, photo-ionization will depend on both $M_{\mathrm{h,\,min}}$ and f_{X} values. The ionization will be faster in the scenarios with smaller $M_{\mathrm{h,\,min}}$ and higher f_{X} values. Thus it is clear that the Lyα coupling, thermal, and ionization histories of the IGM are different in the different CD scenarios due to their strong dependence on the CD source properties and thus result in different CD histories ($\delta \bar{T}_{\mathrm{b}}$ vs z) in different scenarios.

The primary aim of this article is to study the impact of the CD source models on the 21-cm bispectrum. In one of our earlier works [191], we have considered various sources of light during the CD, such as the star-forming galaxies, mini quasars (mini-QSOs), and high mass X-ray binaries (HMXBs). Among these source models, the mini-QSOs and HMXBs are the sources of soft and hard X-ray photons, respectively. These sources were hosted in

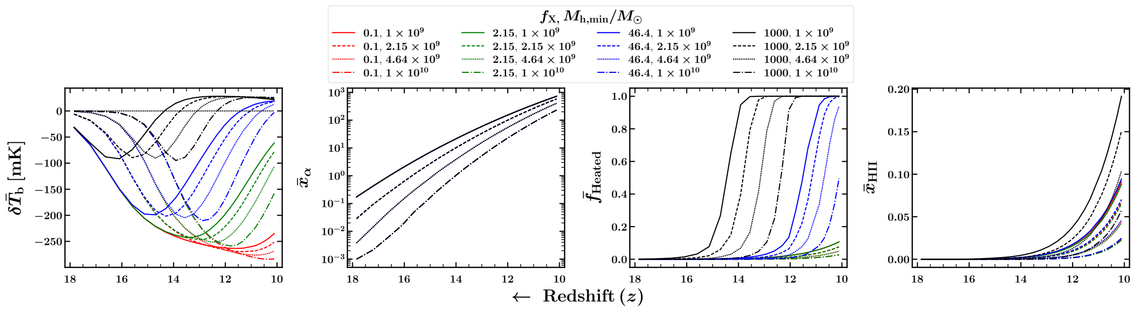

Figure 5.3: **First panel:** It shows the redshift evolution of the global 21-cm differential brightness temperature ($\delta\bar{T}_b$) for all CD scenarios. **Second panel:** It demonstrates the redshift evolution of the mean Lyα coupling coefficient. **Third panel** It shows the evolving fraction of the simulation volume heated above the CMB temperature (i.e. $T_g > T_{CMB}$). **Fourth panel** It represents the evolution of the global ionization fraction ($\bar{x}_{HII}$).

the halos with the same minimum halo mass ($M_{h,\,min}$) and were assumed to interact with the IGM through the same Lyα coupling process. Additionally, we have considered the same X-ray efficiency parameter (f_X) for these source models. Hence, the X-ray photon production rate was the same for both types of sources. These sources only differ in their ability to heat the IGM, as the energy of photons of one source model was different from the other. We have shown in [191] that the evolution of the 21-cm bispectrum magnitude and the sign can distinguish these sources better than the 21-cm power spectrum. Following this line of argument, we would like to go one step further and ask, does the variation in source parameters ($M_{h,\,min}$ and f_X) impact the signal bispectrum? In this article, we mainly focus on this specific point.

In this work, we assume that the star-forming galaxies are the dominant sources of ultraviolet (UV) photons, and mini-QSOs are the only sources of X-ray photons. Both of these sources are hosted by the halos above a minimum mass. This implies that all the astrophysical processes, such as the Lyα coupling, X-ray heating, and UV ionization, vary with $M_{h,\,min}$ (see Figure 5.3). We further consider different f_X values for each $M_{h,\,min}$. The f_X values will determine the X-ray photon production rate. The sources with the smallest f_X values thus belong to the faintest X-ray sources, while the largest f_X values belong to the brightest X-ray sources. These sources will have different IGM heating signatures (see the third panel of Figure 5.3). One important point to note here is that for each CD scenario considered here, all of the possible astrophysical processes are running simultaneously (in a competitive manner with each other) from the beginning of the CD. For a particular CD scenario, which astrophysical process dominates over the rest at a specific stage of the

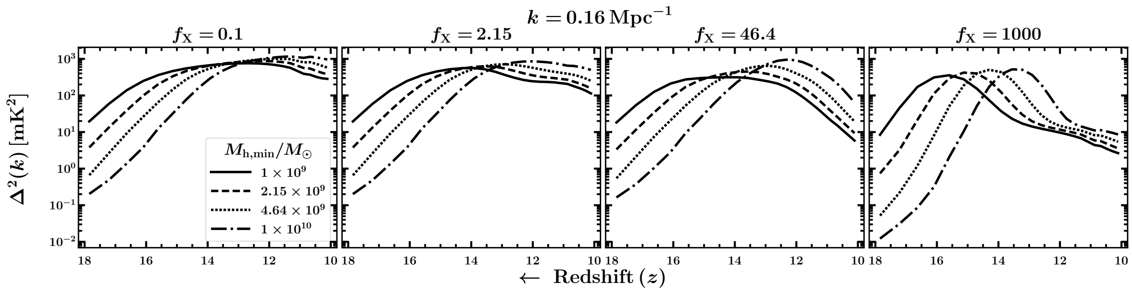

Figure 5.4: The redshift evolution of the power spectra at $k = 0.16\,\mathrm{Mpc}^{-1}$. Each panel represents the evolution of the same at a fixed f_X, but for all $M_{\rm h,\,min}$ values.

CD compared to other scenarios, is solely dependent on the combination of the f_X and $M_{\rm h,\,min}$ values considered for that scenario.

For all the simulated CD scenarios, generated using all possible combinations of parameter values listed in Table 5.1, we have estimated the 21-cm power spectrum $[P(k)]$ and bispectrum $[B(k_1, k_2, k_3)]$. To estimate the bispectrum we use the method prescribed in [183]. Further, we follow the convention of [191] and [190] to demonstrate our result in terms of spherically averaged normalized power spectrum and bispectrum that are respectively defined as $\Delta^2(k) = \left[k^3 P(k)/(2\pi^2)\right]$ and $\Delta^3(k_1, n, \cos\theta) = \left[k_1^3 k_2^3 B(k_1, k_2, k_3)/(2\pi^2)^2\right]$. To get the better insights of the signature of the sources with different properties on the IGM, we first discuss the evolution of $\Delta^2(k)$ with redshifts and then see how the $\Delta^3(k_1, n, \cos\theta)$ is able to account for these different signatures from various sources.

5.4.1 The redshift evolution of the power spectrum

Before discussing whether the power spectrum can distinguish the different CD source models, it is imperative to ask if the 21-cm signal is highly non-Gaussian due to the distribution and characteristics of various radiating sources, then how will a Gaussian statistics such as power spectrum distinguish between these sources? The power spectrum, which measures the amplitude of fluctuations in the signal as a function of Fourier modes or inverse of length scales, will be able to distinguish the signature of the sources only up to a certain extent. It will be sensitive only to the amplitude variation in the signal arising due to the variation in the parameter values of the sources. However, it will not be sensitive to the correlation present in the signal between different length scales. Thus the next higher order statistic that can capture this Non-Gaussian correlation present in the signal between different length scales is the bispectrum. Therefore bispectrum is expected to be more sensitive to the variations in the source properties. By definition, this statistic has more features than the power spectrum, i.e. its sign and magnitude. The magnitude of the bispectrum itself can provide additional information about the signal that the power spectrum cannot. In this section, we discuss the extent to which power spectrum can distinguish different source models.

Figure 5.4 shows the redshift evolution of the power spectra $[\Delta^2(k)]$ at $k = 0.16\,\mathrm{Mpc}^{-1}$. Each panel represents the evolution of the same for a fixed f_X and all possible $M_{\mathrm{h,\,min}}$ values. It is apparent that $\Delta^2(k)$ at a particular f_X strongly depends on the value of $M_{\mathrm{h,\,min}}$. At the early stages of the CD, the power spectra for the low $M_{\mathrm{h,\,min}}$ sources have a higher magnitude than that for high $M_{\mathrm{h,\,min}}$ sources. This is because, in the case of the low $M_{\mathrm{h,\,min}}$ sources, very low mass halos ($M_h = 10^9$–$10^{10}\,M_\odot$), which are numerous in number compared to the high mass halos, are also contributing. Hence, these sources will produce a relatively larger amplitude of fluctuations in the signal via a comparatively stronger Lyα coupling process compared to the case when these low mass sources are ignored (see two left panels of Figure 5.2 or second panel of Figure 5.3). During the late stages of the CD, the heating becomes more prominent for low $M_{\mathrm{h,\,min}}$ sources together with the photo-ionization. Therefore they start to lower the amplitude of fluctuations in the 21-cm signal during the late stages of the CD. This results in the low $\Delta^2(k)$ for the low $M_{\mathrm{h,\,min}}$ sources scenario. Thus, at the late stages of the CD, $\Delta^2(k)$ becomes smaller for low $M_{\mathrm{h,\,min}}$ sources than for relatively high $M_{\mathrm{h,\,min}}$. For the sources at a fixed f_X and $M_{\mathrm{h,\,min}}$, $\Delta^2(k)$ first increases, reaches the maxima, and then decreases. The steepness with which the $\Delta^2(k)$ decreases solely depends on how prominent the IGM heating is by that time. Thus, the larger the rate of heating, the larger will be the steepness of decrement (see this in Figure 5.4 as we move from left to right panels). One can pose the question, what determines the redshift at which $\Delta^2(k)$ starts to decline? This decline in $\Delta^2(k)$ happens when the heating dominates over the Lyα coupling. This, in principle, occurs at the time when the emission (heated) regions in the IGM grow to diminish the absorption background. However, this does not mean the heating was inefficient before this redshift. Heating actually became important at a somewhat higher redshift than this. This phenomenon, in principle, makes the IGM warm (or less cold) by decreasing the amplitude of the absorption signal around the sources before producing the heated regions around the same sources. The power spectrum cannot capture this duration which also depends strongly on the source parameters. However, the bispectrum is expected to probe this characteristic in the signal. In the following sections, we explore to what extent bispectrum can robustly distinguish various source models.

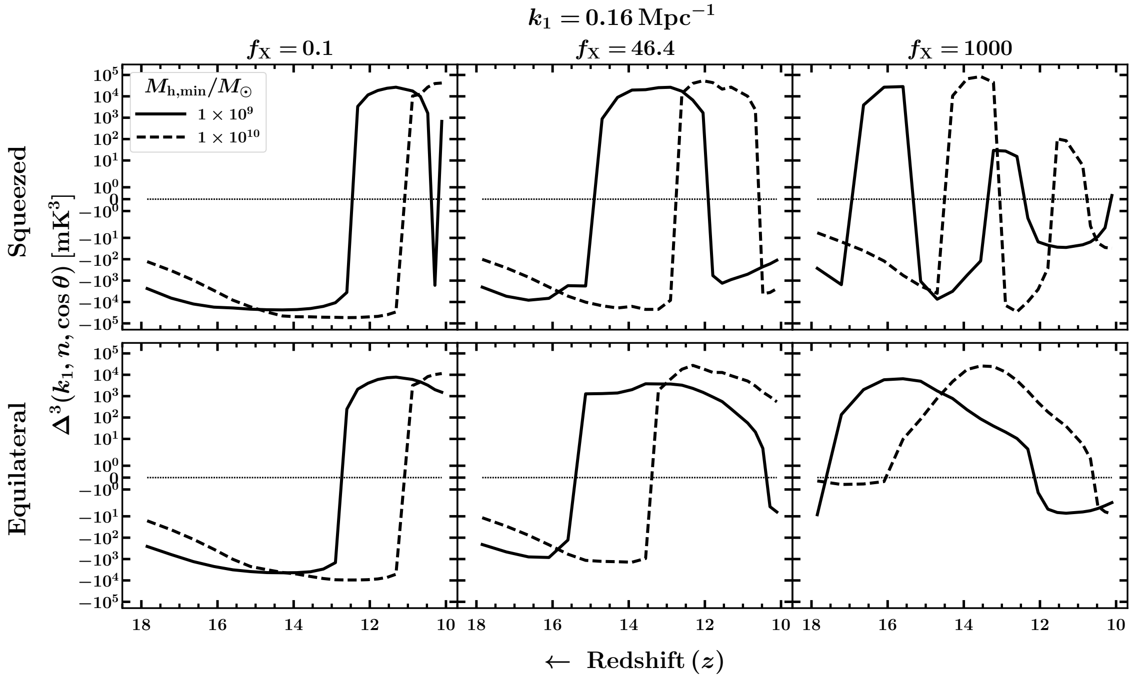

Figure 5.5: **Top panels:** It show the redshift evolution of the bispectra for squeezed limit at $k_1 = 0.16\,\mathrm{Mpc}^{-1}$. **Bottom panels:** It show the same for equilateral k-triangles, and at the same k_1 mode. For each panel the bispectra are demonstrated at a fixed f_X, but with two extreme values of $M_{h,\,min}$.

5.4.2 The redshift evolution of the bispectrum

5.4.2.1 Squeezed-limit and equilateral bispectrum

Fig. 5.5 shows the redshift evolution of the bispectra for squeezed limit (top panels) and equilateral (bottom panels) k-triangles for $k_1 = 0.16\,\mathrm{Mpc}^{-1}$. In each panel, we demonstrate the bispectra at a fixed f_X, but with two extreme values of $M_{h,\,min}$. At first glance, one can see that irrespective of the triangle configurations, the shapes of the bispectra for a fixed value of f_X appear to be the same for both $M_{h,\,min}$ values. The difference between the features of the bispectra in these two scenarios is that they appear at the different redshifts. Thus, the feature in the signal bispectrum for low $M_{h,\,min}$ sources is shifted towards higher redshifts compared to high $M_{h,\,min}$ sources. We also observe similar features in the shapes of the power spectra. The physical reason behind it is that the sources with low mass halos ($< 10^{10}\,M_\odot$) are activated way earlier in time for low $M_{h,\,min}$ scenarios. They begin to impact the IGM through the aforementioned astrophysical processes earlier than that for the high $M_{h,\,min}$ scenarios. The dominant IGM processes are common for both of these low and high $M_{h,\,min}$ scenarios. Therefore, the 21-cm signal coming from the IGM in these CD scenarios attain the same sort of topological distributions at different cosmic times. This will result in similar shapes or features in any of the statistical measures of the 21-cm signal, only shifted by the redshifts at which these features appear. This then raises the question, if different $M_{\mathrm{h,\,min}}$ scenarios result only in shifting of the features in the bispectra with redshift, which is similar to the behaviour observed in the power spectra as well, then how the bispectrum can be treated as a better statistic for distinguishing these source models? This is because these source models, depending on their respective source parameter values, invoke different levels of the non-Gaussianity in the signal, the time evolution of which can be tracked through the evolution of both bispectrum magnitude and sign. The sign of the bispectrum and its time evolution is a unique tracer of all the dominant physical processes in the IGM, which are determined by the source parameter values (for details, we refer the interested reader to [192]).

We next discuss how the bispectrum evolves with redshift while keeping f_{X} and $M_{\mathrm{h,\,min}}$ values fixed (see Figure 5.5). We first focus on the evolution of the bispectrum for squeezed limit k-triangles and then compare it with the same for equilateral k-triangles to see if one of the triangle shapes is a more suitable probe to distinguish between different source models. For $f_{\mathrm{X}} = 0.1$, from the very early stages of the CD, the magnitude of bispectrum for squeezed limit k-triangle increases. This increment happens until the redshift up to which a particular $M_{\mathrm{h,\,min}}$ source model dictates the 21-cm signal fluctuations via the Lyα coupling process. For instance, this redshift for $M_{\mathrm{h,\,min}} = 1 \times 10^9\, M_{\odot}$ sources is $z \sim 13.5$. Although the heating is too slow for $f_{\mathrm{X}} = 0.1$, the bispectrum is highly sensitive to the heating process. Thus when eventually heating becomes dominant over Lyα coupling, the increase in bispectrum magnitude stops. These processes impact the large-scale fluctuations in the 21-cm signal; thus, the small k squeezed-limit signal bispectrum is more sensitive to them. The heating first reduces the amplitude of the absorption signal around the sources by producing warm (or less cold) regions and then produces the heated (emission) regions around the same sources. The reduction in the magnitude of the bispectrum in the redshift range $13.5 \gtrsim z \gtrsim 12.5$ is the signature of this phenomenon. Once a significant amount of heated regions are formed, they will cause the bispectrum to become positive (i.e. a sign change in the bispectrum). The bispectrum remains positive until another physical process (i.e. photo-ionization) becomes dominant over the heating. As ionization becomes important, there will be a race between the heating and ionization processes at late CD stages for $f_{\mathrm{X}} = 0.1$ sources. The ionized regions will form in the already heated regions. The heated regions, by this time, start to act as a large-scale background for the ionized regions. Previously, [161] has shown that the Fourier equivalent of the 21-cm fluctuations (i.e. Δ_{b}) at a large length scale due to the ionization in the heated background will be negative. This will result in a negative bispectrum at late CD stages (i.e. another sign change). However, even at late stages for $f_{\rm X} = 0.1$ scenarios, all of the heated regions have not merged together to form a uniformly heated background. Further, by this time, the ionization rate is higher than the heating rate (see third and fourth panels of Figure 5.3), which eventually results in the ionization front overcoming the heating front. Once this transition happens, the ionized regions now appear in a Lyα coupled background (see the last panel of Figure 5.2 for $f_{\rm X} = 0.1$, $M_{\rm h,\,min} = 1 \times 10^9\, M_\odot$). In [192], we have shown that the large scale $\Delta_{\rm b}$ dominated by the ionized regions in a Lyα coupled IGM will be positive. This will correspond to the positive bispectrum at the very late stage of the CD (another sign change).

Next, we discuss how the squeezed-limit bispectra evolve with redshifts for different $f_{\rm X}$ values, irrespective of the value of $M_{\rm h,\,min}$. As we move from left to right panels in Figure 5.5, the $f_{\rm X}$ values increases logarithmically. The feature of the sign change of the squeezed limit bispectra that we discussed earlier for $f_{\rm X} = 0.1$ also remains consistent for higher $f_{\rm X}$ values. The only difference is that this feature appears at earlier redshifts for higher values of $f_{\rm X}$. In addition to this, we observe a follow-up sign change from positive to negative. This second sign reversal is a signature that all the heated regions are being connected to form a heated background. On this background, a few leftover cold absorbing regions are embedded, and their fluctuations dictate the 21-cm fluctuations. This results in a negative squeezed-limit bispectrum. Due to further heating, the leftover absorbing regions also diminish in volume to make the entire IGM uniformly hot. This causes the magnitude of the negative bispectra to decrease with the decreasing redshifts. To see the connection of bispectrum with the IGM physics in detail, we refer the reader to our recent work [192].

Furthermore, for $f_{\rm X} = 1000$, we observe very important features in the evolution of the squeezed-limit bispectra at late stages, irrespective of $M_{\rm h,\,min}$ values. These features are two additional sign changes in the bispectra (designated as third and fourth sign changes, respectively). We first interpret the third sign change by considering the source model with $M_{\rm h,\,min} = 1 \times 10^9\, M_\odot$ for instance, the bispectrum of which is shown via a solid black line. Since, for $f_{\rm X} = 1000$, heating of the IGM is faster, due to which the entire IGM gets heated way earlier compared to the case where the heating is slow (see the third panel from left in Figure 5.3). Further heating thus will not contribute to the 21-cm fluctuations. The photo-ionization in this scenario is also not dominant by the redshift $z \sim 13.5$ (see the solid black line in the right-most panel of Figure 5.3) at which the sign change is being observed. Thus the fluctuations in the IGM 21-cm signal can be dominated by the matter density fluctuations alone. It has been well established that the bispectrum sign will be positive if the matter density fluctuations dictate the 21-cm fluctuations in heated IGM ([183, 190]). That is why we observe a positive bispectrum in the redshift range $13.5 \gtrsim z \gtrsim 12.5$. Around $z \sim 12.5$, the photo-ionization becomes the dominant process in an already heated IGM. Previously, [183, 190] have also shown that the bispectrum sign due to the neutral fraction fluctuations in a heated IGM will be negative. For $z \lesssim 12.5$, therefore, we observe a negative bispectrum (the fourth sign change of the bispectrum).

We next compare the evolution of the bispectra for equilateral k-triangle with the same for squeezed-limit k-triangle. In Figure 5.5, the bottom panels show the redshift evolution of the bispectra for the equilateral k-triangle. The features in the shapes of the equilateral bispectra for $f_{\rm X} = 0.1$ and 46.6 match with that of the squeezed one. This implies that the equilateral bispectra are able to probe the same signal characteristics that the squeezed-limit bispectra are probing. The bispectra for these two triangle shapes only differ by the redshift values at which their respective features appear. The reason for this is the following: for $k_1 = 0.16\,{\rm Mpc}^{-1}$ (designated as the "large scale"), the squeezed-limit triangle satisfies the condition $k_1 = k_2 = 0.16\,{\rm Mpc}^{-1} > k_3 \to 0$. The bispectrum for this triangle shape provides the correlation between the signal fluctuations at two different length scales i.e. large and very large scales. On the other hand, the equilateral bispectrum for $k_1 = k_2 = k_3 = 0.16\,{\rm Mpc}^{-1}$ provide the correlation between signal fluctuations at the same length scales i.e. large scale. Thus, the ways in which the bispectra for these two triangle shapes behave in order to characterize the signal are different. For the same reason, the features of the equilateral bispectra for $f_{\rm X} = 1000$ significantly differ from that of the squeezed one. Unlike the squeezed limit bispectra, where its evolution features a total of four sign changes during the entirety of the CD, the equilateral bispectra show only two sign changes. These two sign changes are far apart in redshifts compared to the first two sign changes in the squeezed-limit bispectra. The first sign change from negative to positive appears at a very early stage, whereas the second one from positive to negative appears at a very late stage of the CD. The equilateral bispectra thus remain positive for most of the time during the CD. Hence, the equilateral bispectrum is able to follow the evolution of the heated regions in the IGM for a long duration compared to the squeezed-limit bispectrum.

5.4.2.2 L-Isosceles bispectrum

The squeezed and equilateral triangle shapes are special cases of a more generic triangle shape i.e. L-isosceles (L refers to 'Large') triangles. It is therefore imperative to ask how well the L-isosceles bispectra retain the features of the signal as probed by the squeezed and

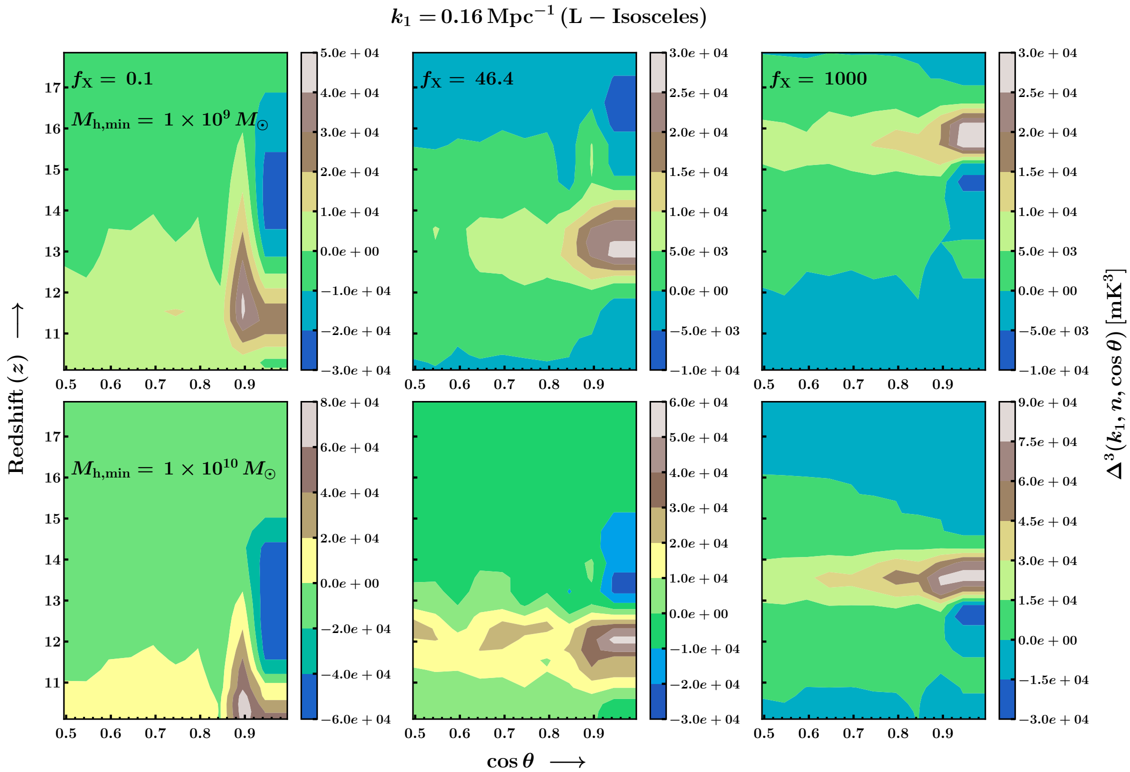

Figure 5.6: **Top panels:** It show the redshift evolution of the L-Isosceles bispectra at three different f_X values at a fixed $M_{h,\,min} = 1 \times 10^9\,M_\odot$. **Bottom panels** It show the same at $M_{h,\,min} = 1 \times 10^{10}\,M_\odot$.

equilateral bispectra. In the n–$\cos\theta$ space (shaded region in the right panel of Figure 5.1), the horizontal line with $n = 1$ and $\cos\theta \in [0.5, 1]$ is the representation of the L-isosceles k-triangles. The letter L refers to 'Large', as L-Isosceles are those isosceles k-triangles that satisfy the condition $k_1 = k_2 \geq k_3$, i.e. two large arms of each triangle are equal. The two endpoints on the L-Isosceles line are the equilateral ($\cos\theta = 0.5$) and squeezed ($\cos\theta = 1.0$) k-triangles. In order to get an understanding of about up to what extent the observed features of the squeezed-limit and equilateral signal bispectra from CD could be generalized, we estimate the bispectra for L-Isosceles k-triangles at $k_1 = 0.16\,\mathrm{Mpc}^{-1}$. In Figure 5.6 top panels show the redshift evolution of the L-Isosceles bispectra for three different f_X values while keeping $M_{h,\,min}$ fixed ($1 \times 10^9\,M_\odot$). The bottom panels show the same at $M_{h,\,min} = 1 \times 10^{10}\,M_\odot$. For a fixed f_X, the effect of $M_{h,\,min}$ on the L-isosceles bispectra is the same as it is on the squeezed-limit and equilateral bispectra. For instance, the shapes of the bispectra for different $M_{h,\,min}$ are the same. They only differ by the redshift values at which their features appear. However, the magnitude of the bispectra might get altered with changing $M_{h,\,min}$. This depends on how these different $M_{h,\,min}$

sources impact the IGM. Further, for a fixed $M_{\mathrm{h,\,min}}$, the effect of varying f_{X} that we have observed already in the case of the squeezed-limit bispectrum redshift evolution, extends to the L-isosceles which are in the vicinity of squeezed k-triangle bispectra i.e. with $\cos\theta \in (0.8, 1)$. Under the same conditions, the features in the equilateral bispectrum evolution can also be seen to be propagating to L-isosceles bispectra which are within its vicinity i.e. $\cos\theta \in (0.5, 0.8)$. This can be clearly understood through the following example: for sources with $M_{\mathrm{h,\,min}} = 1\times10^{9}\,M_{\odot}$, the effect of X-ray heating with $f_{\mathrm{X}} = 1000$ causes the bispectra for squeezed limit and triangle shapes in its vicinity to change its sign four times. Similarly, the bispectra for equilateral and triangle shapes in its vicinity change their sign only twice.

5.4.3 Evolution of the bispectrum in the source parameter space

In this section, we present a comparative study of the power spectrum and bispectrum evolution in the parameter space of f_{X} and $M_{\mathrm{h,\,min}}$. Figure 5.7 shows the evolution of the power spectrum (top panels) and bispectrum for squeezed (middle panels) and equilateral k-triangles (bottom panels) for $k_1 = 0.16\,\mathrm{Mpc}^{-1}$. Each of them is demonstrated at three different stages of the CD (varying from left to right). The left panels are from the *early* stages of the CD, where the Lyα coupling process dictates the 21-cm fluctuations in the cold IGM. The middle panels are from an *intermediate* stage where the X-ray heating competes with the Lyα coupling. Depending on the CD scenarios, this competition can be weaker or stronger. The right panels are from the *late* stages of the CD, where the Lyα process for all CD scenarios and X-ray heating for the scenarios with the highest f_{X} values are saturated. The ionization thus becomes important after heating in the case of this highest f_{X} scenario. The number on each pixel is an estimate of the respective signal statistic (power spectrum or bispectrum) corresponding to that pixel. A visual inspection of this figure reveals that the evolution of the power spectrum magnitude is very slow compared to the variation in magnitude of the bispectrum. On top of this, an additional privilege with the bispectrum is its sign and sign change with the varying source parameter values. The magnitude and sign evolution of the bispectrum in this parameter space makes it a more robust probe of the different source models.

Next, we explore how the bispectrum changes its shape, magnitude and sign with varying source parameters and thus potentially provides a unique and robust probe of the source models. For this, we focus on how the features in the bispectrum capture the changes in the IGM physical processes arising due to the variations in the source parameters. At

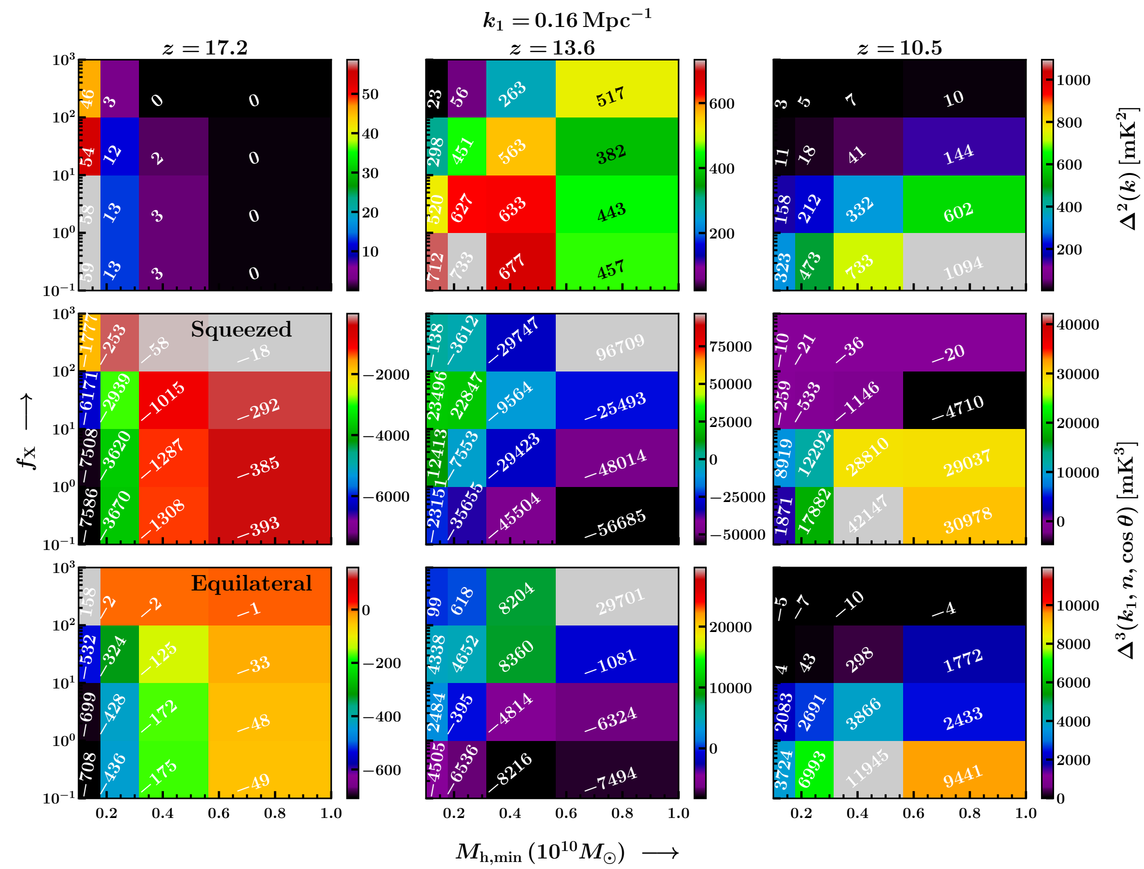

Figure 5.7: **Top panels:** It show the evolution of the power spectrum in the phase space formed by $M_{\mathrm{h,\,min}}$ and f_{X} values for $k_1 = 0.16\,\mathrm{Mpc}^{-1}$. Each panels are at three different redshifts designated as *early*, *intermediate*, and *late* CD stages respectively from left to right. **Middle panels:** It show the bispectrum evolution for squeezed-limit k-triangle in the same phase space. **Bottom panels:** It show the same for equilateral k-triangle.

the *early* stage of the CD, the squeezed-limit bispectra are negative in the entire phase space. In our earlier work [192], we have shown that during the *early* stages of the CD, the bispectrum will be negative when the Lyα coupling dictates the 21-cm signal fluctuations in the uniformly cold/heated background IGM. It is, therefore, evident that whatever be the source models, if the dominant process is the Lyα coupling in the uniformly cold/heated IGM, then the bispectrum will be negative. The equilateral bispectra are also negative for most of the parameter space except for the scenario having the lowest $M_{\mathrm{h,\,min}}$ and highest f_{X} values, in which the bispectrum is positive. Previously, [192] has also established that during the CD, the bispectrum will be positive when the signal is coming from the emitting (heated) regions placed in the cold or less warm background. This positive equilateral bispectrum is the signature that the fluctuations induced by the heated regions generated for this specific source model are being probed. This comparative analysis confirms that the equilateral bispectrum can probe even smaller heated regions formed at the beginning of the CD compared to the squeezed-limit bispectrum. This is because the squeezed-limit bispectrum probes the comparatively larger-scale features than the equilateral bispectrum.

Further, at the *early* stage, the region in the parameter space, where the magnitude of the negative bispectrum is maximum, is the representation of strong Lyα coupling. The magnitude of this negative bispectrum decreases with increasing $f_{\rm X}$ (from bottom to top) while $M_{\rm h,\,min}$ stays constant. We explain this phenomenon as follows. The increasing $f_{\rm X}$ values result in an increased rate of heating. The heating around the sources, as it progresses with time, has two significant effects. The first effect is that heating decreases the contrast between the already existing absorbing regions and their background. These absorbing regions were produced by the Lyα coupling around the same sources. The sources continue to heat their surrounding IGM further and eventually convert these absorbing regions around them into heated regions. The brighter the X-ray sources are, the quicker this transition to generated heated regions around them happens. This implies that if the $f_{\rm X}$ value is large enough, one might observe this transition happening even during the *early* stage of the CD, compared to the comparatively fainter X-ray sources. This results either in a decrease in the magnitude of the negative bispectrum or the appearance of a positive bispectrum with increasing $f_{\rm X}$. At the *early* stages, we also observe the decreasing bispectrum magnitude with increasing $M_{\rm h,\,min}$ for a fixed $f_{\rm X}$. This is because, when we move from lower to higher $M_{\rm h,\,min}$ values, the low mass halos, which are numerous compared to high mass halos, are no longer taking part in shaping the state of the IGM. Because of the absence of participation from low mass halos, as we go from lower to higher $M_{\rm h,\,min}$ values, the strength of the Lyα coupling also decreases (see the second panel in Figure 5.3), resulting in a decrement in the magnitude of the negative bispectrum.

At the *intermediate* stages, we observe very drastic changes in the magnitude and sign of both squeezed-limit and equilateral bispectra in the $f_{\rm X} - M_{\rm h,\,min}$ parameter space, compared to variation in the bispectra during the *early* stages. This is because, by the *intermediate* stage, the heating of the IGM has become a prominent physical process in almost all source models. The Lyα coupling, which has been the dominant IGM process so far, now competes with X-ray heating as the major contributor to the 21-cm fluctuations. The regions in the $f_{\rm X} - M_{\rm h,\,min}$ parameter space, where the bispectra for a particular triangle shape are negative, imply that this triangle shape probes the signal fluctuations dominated by the absorption regions. On the other hand, the positive bispectra imply that the signal fluctuations are dominated by the heated regions.

The evolution of the bispectrum in the parameter space can be connected to the dominant IGM physical processes in the following manner. For instance, at the *intermediate* stages, the squeezed-limit bispectrum for the lowest $M_{\rm h,\,min}$ value shows a sign change, from negative to positive, as one changes the $f_{\rm X}$ value slightly from its lowest value to a higher one. The magnitude of this positive bispectrum increases with increasing $f_{\rm X}$ until the highest $f_{\rm X}$ value is reached, where the bispectrum again becomes negative (i.e., there is a second sign change). This can be explained in the following way. The increase in $f_{\rm X}$ increases the rate of heating by all the sources. In addition to this, for scenarios with low $M_{\rm h,\,min}$ values, the low mass halos, which are numerous compared to the high mass halos, also contribute to the heating. These two effects together increase the overall heating rate. Hence, by the *intermediate* stages, the heated regions have been created in the Lyα coupled background in scenarios with higher $f_{\rm X}$ values. Therefore, the bispectrum in these scenarios will be positive until one reaches the highest $f_{\rm X}$ value. The heating rate for the highest $f_{\rm X}$ value is high enough such that the heated regions start to overlap to form a single large connected heated cluster by the *intermediate* stage. Hence, the signal fluctuations at this stage can be thought of coming from the leftover absorption regions in a uniformly heated background (see the third panel from left in Figure 5.2 at $f_{\rm X} = 1000$, and $M_{\rm h,\,min} = 1 \times 10^9\, M_\odot$). The $\Delta_{\rm b}$, thus, will be negative, which results in a negative bispectrum. Further, for the highest $M_{\rm h,\,min}$ values, the evolution trend of the squeezed-limit bispectrum with varying $f_{\rm X}$ is quite different. The bispectrum magnitude first decreases with increasing $f_{\rm X}$ until the largest $f_{\rm X}$ value is reached, where it turns positive. This is because due to having the highest $M_{\rm h,\,min}$ value in this scenario, the low-mass halos do not contribute at all to the heating process. Hence, the IGM heating is slow for $f_{\rm X} = 0.1$, and the Lyα coupling is the sole major contributor to the signal fluctuations. Hence we get a large negative bispectrum in this scenario. As $f_{\rm X}$ increases, the heated regions grow and gradually diminish the sizes of the absorption regions, hence their impact on the 21-cm fluctuations. This effectively explains the trend of the bispectrum discussed above.

During the *intermediate* stages, another interesting evolutionary feature of the bispectrum is observed with the variation in the $M_{\rm h,\,min}$ for sources with the lowest values of $f_{\rm X}$. This is the increasing magnitude of the negative bispectrum as one moves from the lowest values of $M_{\rm h,\,min}$ towards its higher values. The physical interpretation of this feature is the following. The scenarios when the $f_{\rm X}$ has a rather low value, even in them, the faint X-ray sources will start their contribution towards IGM heating by the *intermediate* stages of the CD. In such scenarios, in the cases with the lowest $M_{\rm h,\,min}$, the sources will contribute significantly towards heating on top of the usual Lyα coupling. The heating will be faster for the lower $M_{\mathrm{h,\,min}}$ values compared to the higher ones. Hence, the level of fluctuations introduced by the Lyα coupling to the 21-cm signal will decrease significantly by the *intermediate* stage. On the other hand, in scenarios with the highest $M_{\mathrm{h,\,min}}$ values, the 21-cm signal fluctuation level will be the highest due to the predomination of Lyα coupling. Hence, we observe the maximum negative bispectrum in these scenarios. The evolution of the bispectrum in the parameter space during the *late* stages of the CD can be similarly connected to the IGM physics.

The bispectrum of the equilateral triangle in the parameter space during the different CD stages are shown in the bottom panels of Figure 5.7. The evolution of the bispectrum for an equilateral triangle in the parameter space at a particular CD stage is more or less similar to the squeezed-limit bispectrum, with some differences. These differences are solely dependent on the shape of the k-triangle that probes a specific feature of the 21-cm field. For instance, at the *early* stage of the CD, the equilateral bispectrum for the sources with the lowest $M_{\mathrm{h,\,min}}$ values and with increasing values of f_{X} eventually show a sign change when one reaches the highest f_{X} value. On the other hand, the squeezed-limit bispectrum does not show any such sign change for the same variations in the parameters. This is because the equilateral triangle can probe the fluctuations introduced by the heated region even at the very early stages of the CD.

5.4.4 Evolution of the bispectrum in the triangle parameter space

In this section, we discuss the bispectrum for all unique triangle shapes. In our discussion, we specifically focus on two points. Among them, the first one is to what extent the features of the bispectrum observed for squeezed-limit and equilateral k-triangles can be extended to their neighbouring triangle shapes in the n–$\cos\theta$ space. Our second point of focus is to understand what additional information about the signal and the source models can be drawn by studying the bispectrum for all unique triangles. Figure 5.8 shows the bispectra for all unique k-triangles with $k_1 = 0.16\,\mathrm{Mpc}^{-1}$. The first two columns in this figure show the bispectra for $M_{\mathrm{h,\,min}} = 1\times10^{9}\,M_{\odot}$, at seven different stages of the CD and for two different f_{X} values. The last two columns show the same for $M_{\mathrm{h,\,min}} = 1\times10^{10}\,M_{\odot}$. During the very early stages of the CD, for any value of $M_{\mathrm{h,\,min}}$ and f_{X}, the bispectra are negative in the entire unique n–$\cos\theta$ space (see the top panels in Figure 5.8). This is because, for any CD scenario, the heating of the IGM is negligible at this stage, and the Lyα coupling dictates 21-cm fluctuations. Thus any of the unique k-triangles probes the fluctuations introduced by the absorbing regions.

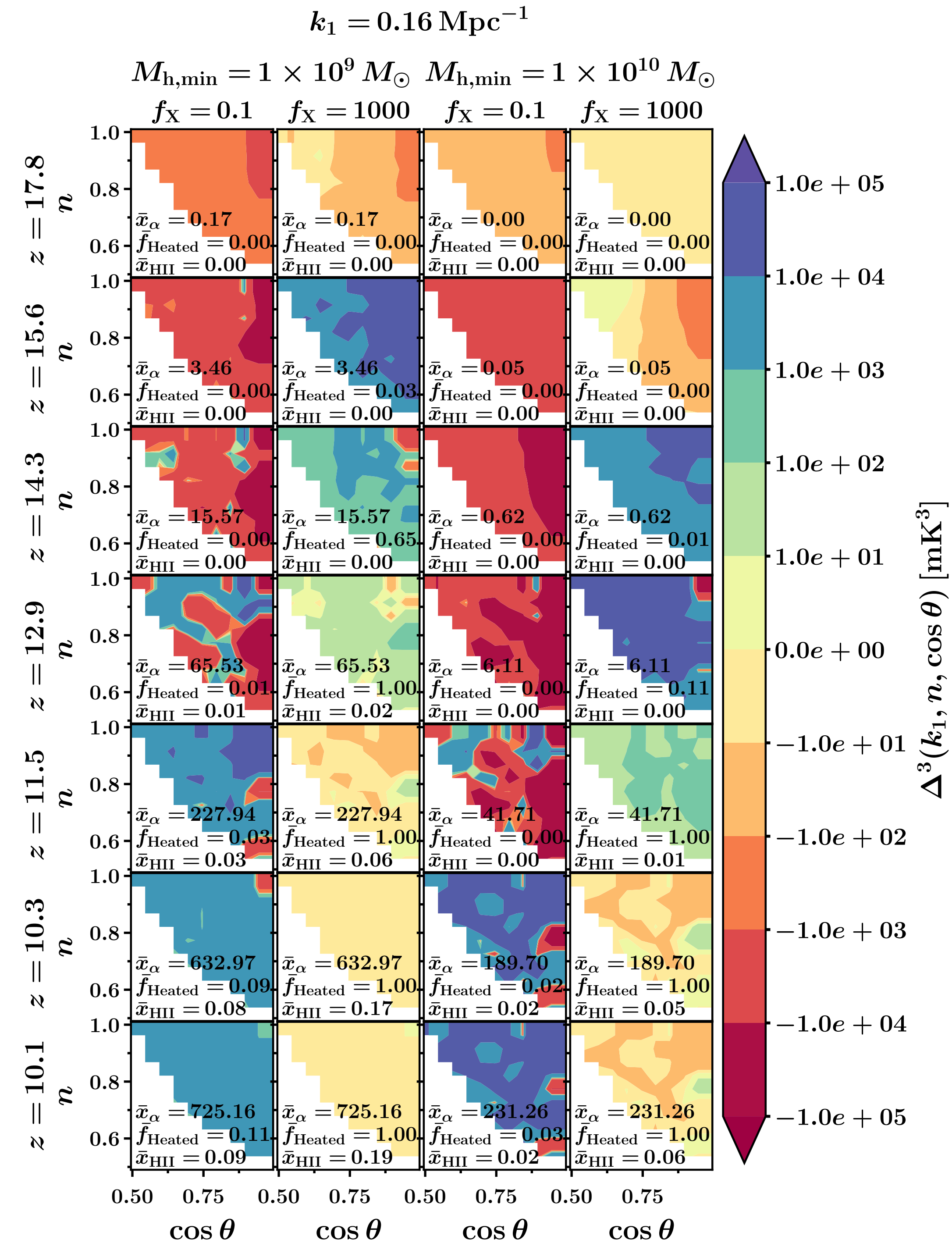

Figure 5.8: It shows the 21-cm bispectra for all unique k-triangle configurations for $k_1 = 0.16\,\mathrm{Mpc}^{-1}$, for $M_{\mathrm{h,\,min}} = 1\times10^{9}\,M_{\odot}$ (left two columns), and $M_{\mathrm{h,\,min}} = 1\times10^{10}\,M_{\odot}$ (right two columns) at seven different stages of the CD and for two different f_{X} values.

In Section 5.4.2.1 we have reported, for scenario with $M_{\mathrm{h,\,min}} = 1 \times 10^9\, M_\odot$ and $f_{\mathrm{X}} = 0.1$, the redshift evolution of the squeezed-limit bispectrum show a total of three sign changes (see solid black line in the top-left panel of Figure 5.5). In the unique n–$\cos\theta$ space, we observe the same features for a set of k-triangles that are in the vicinity of the squeezed k-triangle (see the left-most column of Figure 5.8). Further, for the same $M_{\mathrm{h,\,min}}$ and f_{X} values, we have also reported the single sign change in the equilateral bispectrum (see solid black line in the bottom-left panel of Figure 5.5). Most of the k-triangles in the unique n–$\cos\theta$ space show this feature, except the ones in the vicinity of the squeezed-limit triangles. A further interesting observation that one can have from this analysis is that the redshift of appearance of these sign change features of the signal bispectrum depends on the triangle shapes. For a few triangles that do not belong to the L-isosceles group, these sign changes happen at an earlier redshift compared to the squeezed-limit and equilateral triangles. This is because the bispectrum estimation for these triangles involves signal fluctuations coming from multiple length scales; thus, they may be able to pick up the impact of heating even earlier than the squeezed-limit bispectrum. Further, as we increase the value of $M_{\mathrm{h,\,min}}$ to $1 \times 10^{10}\, M_\odot$ and keep f_{X} fixed at 0.1, we observe that the same sign change features appear in the bispectrum. The only difference is that in this case, because of the lack of source hosting halos early on, these features appear at later redshifts during the CD.

Earlier in Section 5.4.2.1 we have also reported, for the scenarios with $f_{\mathrm{X}} = 1000$ and for any value of $M_{\mathrm{h,\,min}}$, the redshift evolution of the squeezed-limit bispectrum show a total of four sign changes (see the top-right panel of Figure 5.5). We observe the same features in the 21-cm bispectra for a set of k-triangles that are in the vicinity of the squeezed k-triangle in the unique n–$\cos\theta$ space (see panels in second and fourth columns from the left of Figure 5.8). Further, the equilateral bispectrum has shown a double sign change (see the bottom-right panel of Figure 5.5). Most of the k-triangles in the unique n–$\cos\theta$ space show this same feature of the 21-cm bispectra, except the ones in the vicinity of squeezed-limit triangles. When we compare all of these features obtained for scenarios with two extreme values of $M_{\mathrm{h,\,min}}$, the features observed for the largest $M_{\mathrm{h,\,min}}$ value appear to be delayed compared to the same for the smallest $M_{\mathrm{h,\,min}}$ value.

5.5 Chapter summary and discussions

This article is a follow-up to our previous work [192]. In [192], we have shown how the 21-cm signal bispectrum probes the impact of all possible astrophysical processes on the signal fluctuations by capturing the intrinsic non-Gaussianity in the signal during Cosmic

Dawn (CD). The Lyα coupling and X-ray heating are the two dominant astrophysical processes during CD. The third process, photo-ionization, becomes important during the late stages of the CD. In [192], we have considered that the radiating sources reside inside the halos whose masses are above a certain minimum threshold ($M_{\rm h,\,min}$). To probe the signature of the aforementioned physical processes in the IGM induced by these radiating sources, we considered several CD scenarios. In a few of these scenarios, there were no X-ray emissions from the sources (i.e., $f_{\rm X} = 0$). On the other hand, the sources corresponding to the rest of the scenarios emit ample amounts of X-ray photons (i.e. for which the $f_{\rm X}$ values are high). However, in [192], we have not studied how the different X-ray sources, from fainter to brighter, impact the 21-cm signal and its bispectrum through the possible astrophysical processes. We have also not studied the effect of different $M_{\rm h,\,min}$ values on the 21-cm signal and its bispectrum. These CD scenarios impact the IGM with the different Lyα coupling, X-ray heating, and photo-ionization processes. Besides these, we studied only the squeezed-limit bispectrum in the earlier work.

This follow-up article is focused on addressing the following key questions. The first among them is to what extent and how varying source parameter values impact the CD signal bispectrum. The second question that this work tries to address is to what extent the results for squeezed and equilateral bispectrum can be extended to bispectrum obtained for triangles of other unique shapes. Further, it also tries to explore what additional information may be extracted using the bispectrum of various unique triangle shapes. In this work, therefore, we have considered several simulated CD scenarios corresponding to all possible combinations of the values of the source parameters within a certain range (see Table 5.1), such as $f_{\rm X}$ and $M_{\rm h,\,min}$. We focus on how these different CD scenarios that affect the 21-cm signal via the different astrophysical processes will impact the large-scale ($k_1 = 0.16\,{\rm Mpc}^{-1}$) 21-cm bispectrum. The findings of our analysis are summarized as follows:

- The different astrophysical source parameters during CD, such as $M_{\rm h,\,min}$ and $f_{\rm X}$, directly control the physical processes going on in the IGM. These processes determine the nature of fluctuations in the 21-cm signal emerging from the IGM. One can relate the fluctuations in the signal to the IGM processes and thus to the source parameters to some extent via the signal power spectrum. However, the signal bispectrum provides a far better and more robust connection between the signal fluctuations and the source parameters. This is because compared to the power spectrum, which is always positive by definition, the bispectrum can have both positive and negative signs. Further, the shape of the bispectrum is also more sensitive to the variation in these source parameters. This is due to the simple fact that the bispectrum is capable of quantifying the intrinsic non-Gaussianity in the signal to which the power spectrum is not sensitive. Therefore both the sign and shape of the bispectrum work as a more sensitive smoking gun for the ongoing dominant physical processes in the IGM induced by the specific source properties (or parameters).

- The nature and the level of non-Gaussianity in the 21-cm signal emerging from the IGM depend on the nature of the sources (defined by their parameter values). The nature of the sources determines which physical process in the IGM is dominant at what cosmic time. For example, we observed in our analysis that, if we consider two different CD scenarios, both having the same values of $M_{\rm h,\,min}$ but different values of $f_{\rm X}$, then the one with lower $f_{\rm X}$ (i.e. having fainter X-ray photon producing sources) will be able to heat up the entire IGM at a far later stage compared to the scenario which has higher $f_{\rm X}$ values. These two scenarios can be conclusively distinguished by the shape and sign (and their variation with cosmic time) of the bispectra estimated using small k (i.e. large length scale) squeezed limit triangles or triangle shapes that are close to it in the n–$\cos\theta$ space.

- Next, let us consider two CD scenarios with the same $f_{\rm X}$ values but different $M_{\rm h,\,min}$ values. In this case, sources of equal masses in both scenarios produce an equal amount of X-ray photons. However, the scenario where $M_{\rm h,\,min}$ is lower will have a larger number of low mass sources. This results in a faster IGM heating in the scenario with lower $M_{\rm h,\,min}$ values. Therefore, the features in the bispectrum connected to the dominance of X-ray heating will appear at an earlier redshift in the scenario with lower $M_{\rm h,\,min}$ compared to the other one. Thus the evolution of the bispectra with cosmic time will appear to be shifted with respect to each other in these two CD scenarios while keeping the nature and its prominent features almost the same. Similar to the discussion in the previous point, here also we find that bispectrum for small k (i.e. large length scale) squeezed limit triangles and the triangle shapes in its vicinity are able to optimally probe the impact of X-ray heating even in this case.

- The analysis presented in this paper, both in terms of the simulations of the signal and our physical interpretation of the bispectra of the simulated signal, is based on the assumption that the first dominant IGM physical process when the first sources of lights were formed was Lyα coupling. These sources started to impact the IGM via X-ray heating at a later time, depending on their corresponding $f_{\rm X}$ and $M_{\rm h,\,min}$ values. Thus after analyzing the signal bispectra for a large number of $f_{\rm X}$ and

$M_{\mathrm{h,\,min}}$ values, we arrive at the following generic conclusion: The sign of the 21-cm bispectrum for a particular triangle configuration can tell us the relative contrast of the fluctuations in the 21-cm signal with respect to its background. For example, a negative bispectrum can arise under two conditions in the IGM. First, when the fluctuations in the signal are dominated by the distribution of cold absorbing regions in a relatively warm or hot background. Second, when the signal fluctuations are determined by the distribution of heated regions in a relatively cold or less warm background. Therefore, just by looking at the sign of the bispectrum, it would be difficult to say which among the two conditions mentioned above is resulting in the negative bispectrum. In this paper, we demonstrate using the suit of signal simulations at our disposal, that it is important to study the sequence of sign changes along with the variations in the shape and magnitude of the bispectrum throughout the CD history to arrive at a robust conclusion about the dominant IGM process at different cosmic times.

Chapter 6

Summary and Future Scopes

6.1 Summary and conclusions

The advent of the first luminous sources led the Universe into an era where the light from these sources transitioned the state of the intergalactic medium (IGM) gas, consisting of mostly atomic neutral hydrogen (HI), from cold and neutral to hot and ionized one. This period in cosmic history is known as the Cosmic Dawn and the Epoch of reionization (CD-EoR) (see e.g. 1, 14, 15, 21, 82 for reviews). This particular phase of our Universe is largely untested by the observations via the present generation telescopes; thus, we have very little knowledge about it. The redshifted 21-cm radiation, produced by the spin-flip transition of an electron-proton system in the 1s ground state of HI, can map the Universe by directly tracing the HI distribution diffused in the IGM. The fluctuations in the 21-cm signal arise due to various astrophysical processes in the IGM during this period. The radio telescopes mainly target to detect spatial and temporal fluctuations of the signal in Fourier space. Fourier statistics like power spectrum can be directly employed with a higher signal-to-noise ratio (SNR) [103, 118]. The power spectrum measures only the amplitude of fluctuations in the signal at different length scales [3,79,156,157,160]. It can provide a complete statistical description of a pure Gaussian random field. However, the spatial and temporal fluctuations of the CD-EoR 21-cm signal are highly non-Gaussian as they arise due to the non-random distribution of the heated and ionized regions in the IGM [132,148,161]. The power spectrum, being unable to capture this non-Gaussianity, cannot fully characterize the CD-EoR 21-cm signal. The bispectrum is the simplest higher-order statistic that can probe this non-Gaussianity and its scale dependence [161,183–185,190–

192, 262]. In principle, it can be estimated through the product of the Fourier transform of the signal, for groups of three different wave numbers in the Fourier space which form closed triangles (aka k-triangle). The behaviour of the bispectrum solely depends on the shape and size of the k-triangles. As SKA-like telescopes (expected to be operational in the near future) are expected to detect the CD-EoR 21-cm bispectrum [170–172], it is imperative to develop a framework for the physical interpretation of this signal statistic.

The bispectrum for different k-triangle shapes can uniquely probe different distinct features of the expected signal [5]. **Motivated by this, for the first time, we have estimated the CD-EoR 21-cm bispectrum, considering all possible unique triangle shapes to get a comprehensive view of the non-Gaussianity in this signal [183,191,192].** All the earlier works in this sub-domain considered only a few specific types k-triangles. We find that the 21-cm bispectra are non-zero for most of the triangle parameter space and during the entire period of the CD-EoR. This strongly establishes that the CD-EoR 21-cm signal is highly non-Gaussian. The earlier studies also have not considered any line of sight (LoS) anisotropies such as redshift space distortion (RSD), light-cone effect, etc., while analyzing the bispectrum. In this thesis, for the first time, we quantify the anisotropy due to the peculiar velocity of the HI gas to quantify the impact of the RSD on the CD-EoR 21-cm bispectrum magnitude and sign [190, 191]. Our analysis indicates that the effect of the RSD anisotropies is significant on the bispectrum magnitude ($> 50\%$ in EoR and $> 20\%$ in CD) and sign. We thus conclude that one would need to take into consideration correctly the impact of the RSD on the CD-EoR 21-cm bispectra to provide a correct interpretation of this signal statistics obtained from future observation. This impact is tightly correlated to the nature of radiation emitted by the first sources. Additionally, for the first time, we also quantify the effect of spin temperature ($T_{\rm S}$) fluctuations during CD. We find that $T_{\rm S}$ fluctuations have maximum impact on the CD 21-cm bispectra magnitude for small k-triangles and at the stage when Lyα coupling reaches saturation.

Furthermore, we have studied the impact of the different heating source models on the CD 21-cm bispectrum in [191]. For this, we have considered two different types of sources in this work, they are mini-QSOs and HMXBs. We observe that the redshift evolution of the bispectrum magnitude and sign follow a generic trend for both source models. However, the redshifts at which the bispectra magnitude reach their maximum and minimum values and show their sign reversal depends on the source model. When the Lyα coupling and the X-ray heating of the IGM occur simultaneously, we observe two consecutive sign reversals in the bispectra for small k-triangles ($k_1 \sim 0.16\,{\rm Mpc}^{-1}$), irrespective of the source models. One arising at the beginning of the IGM heating and the other at the end of Lyα coupling saturation. This feature can be used in principle to constrain the CD history and/or to identify the specific CD scenarios.

Next, we have performed an study in order to connect the redshift evolution of magnitude and sign of the bispectrum (studied in [191]) with the dominant physical processes during CD, namely Lyα coupling, and X-ray heating. For this we have considered a suite of simulated CD scenarios in our work [192]. We have analyzed the squeezed-limit triangle bispectrum for small k_1 mode ($k_1 \sim 0.16\,\mathrm{Mpc}^{-1}$), extracted from these simulated scenarios. For the first time, we have demonstrated that the redshift evolution of the sign and the magnitude of the 21-cm bispectrum can disentangle the dominating contributions from Ly coupling and X-ray heating of the IGM in a far more distinctive manner than the evolution of the global signal or the power spectrum. Our analysis also shows that the sign and the shape of the 21-cm bispectrum can distinctly tell us which one among these IGM processes were dominating at what cosmic time. This will allow us to independently probe the history of Cosmic Dawn and verify the same obtained from various global signal experiments, e.g., EDGES [263].

Further, we have performed a follow-up in depth investigation of the features in the large-scale 21-cm bispectrum during CD that has been observed in [192] by considering a wide range of properties (parameters) of the first light sources during the CD. The impact of the dominant physical processes during CD, Lyα coupling and X-ray heating, will depend on these source properties. The source properties are mainly determined via two major source parameters i.e. the minimum halo mass $M_{\mathrm{h,\,min}}$ and X-ray photon production efficiency f_{X}. In this work, for the first time, we study the impact of variation in these source parameters on the large scale ($k_1 = 0.16\,\mathrm{Mpc}^{-1}$) 21-cm bispectrum for all possible unique triangles in the Fourier domain. Our entire analysis is based on a suite of simulated 21-cm signal scenarios (with varying f_{X} and $M_{\mathrm{h,\,min}}$). Our detailed and comparative analysis of the power spectrum and bispectrum shows that the shape, sign and magnitude of bispectrum combinedly provides a better measure of the signal fluctuations and its non-Gaussianity compared to the power spectrum [193]. We also conclude that it is important to study the sequence of sign changes along with the variations in the shape and magnitude of the bispectrum throughout the CD history to arrive at robust conclusion about the dominant IGM processes at different cosmic times. We further observe that among the all possible unique k-triangles, the large scale non-Gaussianity in signal is better probed by the small k triangles in the squeezed limit and by triangles of similar shapes. This opens up the possibility of constraining the source parameters during the CD using 21-cm bispectrum.

Thus through an extensive and thorough analysis of the 21-cm bispectrum (using state-of-the-art large scale simulations of the signal) for all unique k-triangle shapes and sizes during both the CD and EoR and for a large variety of source models, we briefly conclude the following major points:

- We have established that the 21-cm signal from the CD-EoR is highly non-Gaussian. We further show that the 21-cm bispectrum can capture the intrinsic and time-evolving non-Gaussian fluctuations in the 21-cm signal from the CD-EoR.

- We also demonstrate for the first time that the bispectrum shape, sign and sequence of sign changes, capturing the time evolution of the non-Gaussianity, can distinctively probe the dominant physical process in the IGM at any cosmic time, which in turn is responsible for this non-Gaussianity in the signal.

- The various luminous sources which influences or dictates the IGM physics can be distinguished by the features of the large-scale 21-cm bispectrum.

- The sign of the bispectrum can tell us about the relative contrast of the fluctuations in the 21-cm signal with respect to its background. This is a unique feature of the bispectrum and cannot be obtained via the power spectrum, which is the dominantly used statistic to describe or probe the signal.

- Therefore, both the sign and shape of the bispectrum work as a more sensitive smoking gun for the dominant physical processes in the IGM induced by the specific source properties (or parameters) compared to the power spectrum.

6.2 Future scopes

The foundation of analyzing and interpreting the 21-cm signal from the CD-EoR, laid down in this thesis opens up a new and mostly uncharted avenue of probing this illusive period in the history of our Universe. The line of work initiated in this thesis can be further extended in the following directions:

- In this thesis we have explored the possibility of using 21-cm bispectrum as a confirmative probe to identify the dominant physical processes in the IGM during the CD. This approach can be further extended in the domain of the EoR as well, to identify the dominant IGM process during this era. The EoR 21-cm bispectrum can be further used to constrain the properties of the ionizing sources during this period.

- One can explore the possibility of using the 21-cm bispectrum to put tighter constraints on the CD model parameters using future observations with the next-generation telescopes e.g. SKA. Some effort in this line already been invested by [170–172] in the context of EoR 21-cm bispectrum. A more extensive analysis in the same line with realistic simulations of the telescope response, foregrounds, noise etc. can be done and this analysis can also be extended to the CD domain.

- The analysis of the impact of line-of-sight anisotropies intrinsically present in the signal bispectrum from the CD-EoR can be done more extensively by estimating all the higher order multipoles of this signal statistic. A thorough analysis of these higher order multipoles of the bispectrum can provide us a better insight into the physics of the IGM.

Appendices

Appendix A

A.1 Quasi-linear components of the redshift space 21-cm bispectra

The panels in Figure A.1 show the coefficients of different components of the quasi-linear model for redshift space bispectra defined by Equation (2.11). The four panels of Figure A.1 show the four coefficients defined in Equations (2.14) - (2.17) for the monopole moment of the bispectra i.e. for $m = 0$ and $\ell = 0$ in Equation (2.11).

Figure A.2 shows the ratio between $B_{\mu^4-\mathrm{RC}}$ and B^r for all unique triangle configurations at four different stages of the EoR and for four different k_1 modes. Figure A.3 shows the ratio between $B_{\mu^6-\mathrm{RC}}$ and B^r for all unique triangle configurations at four different stages of the EoR and for four different k_1 modes. The $B_{\mu^4-\mathrm{RC}}$ and $B_{\mu^6-\mathrm{RC}}$ are the two mostly minor correction terms which impact the EoR 21-cm signal bispectra in redshift space. These two figures show the relative contributions of the $B_{\mu^4-\mathrm{RC}}$ and $B_{\mu^6-\mathrm{RC}}$ groups of RC terms in the redshift space bispectra at different stages of the EoR.

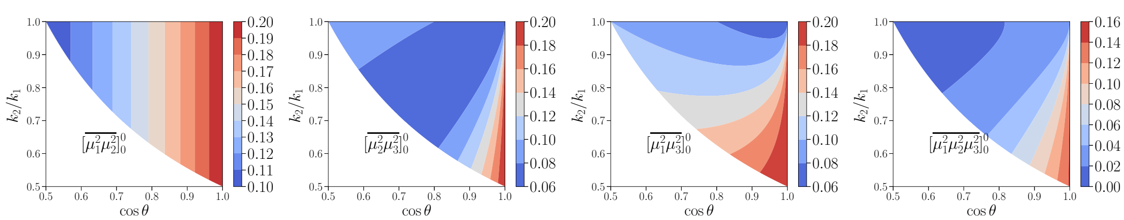

Figure A.1: These panels show the value of coefficients $\overline{[\mu_1^2\mu_2^2]}_0^0$, $\overline{[\mu_2^2\mu_3^2]}_0^0$, $\overline{[\mu_3^2\mu_1^2]}_0^0$ and $\overline{[\mu_1^2\mu_2^2\mu_3^2]}_0^0$ in the equation (2.11) for $m = 0$, $\ell = 0$.

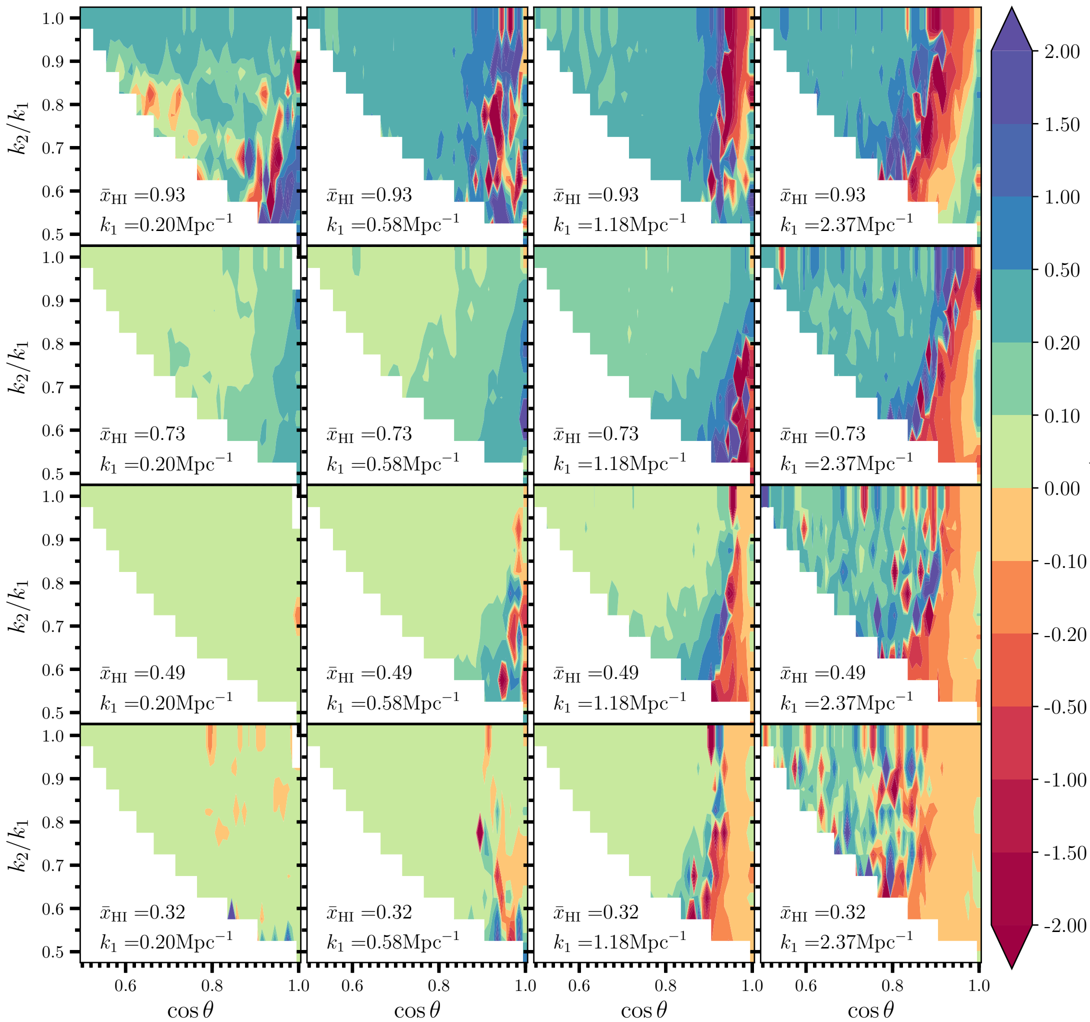

Figure A.2: The ratio between $B_{\mu^4-\mathrm{RC}}$ and B^r for all unique triangle configurations at four different stages of the EoR and for four different k_1 modes.

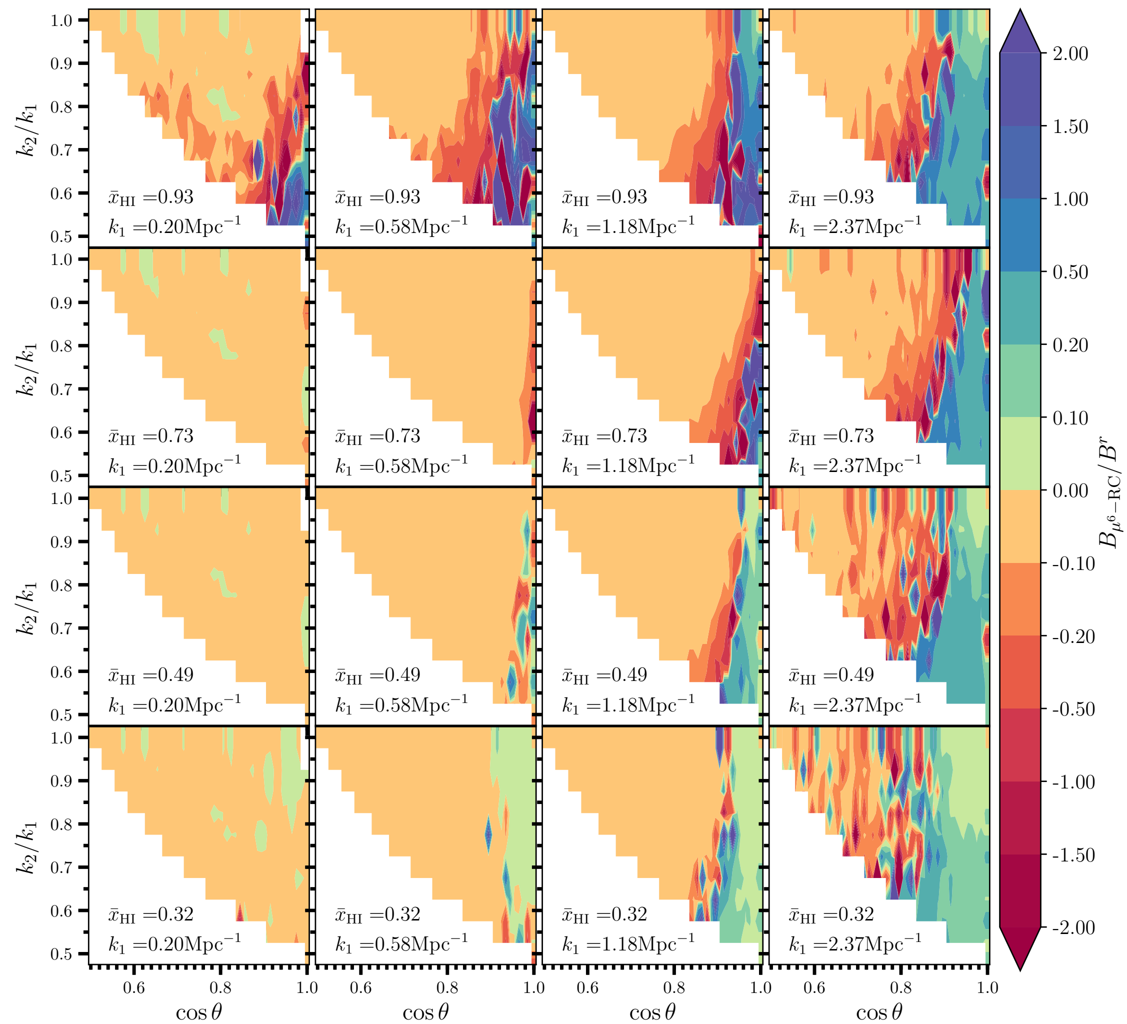

Figure A.3: The ratio between the $B_{\mu^6-\rm RC}$ and B^r for all unique triangle configurations at four different stages of the EoR and for four different k_1 modes.

References

[1] J.R. Pritchard and A. Loeb, *21 cm cosmology in the 21st century*, *Reports on Progress in Physics* **75** (2012) 086901 [1109.6012].

[2] G. Mellema, L. Koopmans, H. Shukla, K.K. Datta, A. Mesinger and S. Majumdar, *HI tomographic imaging of the Cosmic Dawn and Epoch of Reionization with SKA*, *Advancing Astrophysics with the Square Kilometre Array (AASKA14)* (2015) 10 [1501.04203].

[3] H. Jensen, K.K. Datta, G. Mellema, E. Chapman, F.B. Abdalla, I.T. Iliev et al., *Probing reionization with LOFAR using 21-cm redshift space distortions*, *Mon. Not. Roy. Astron. Soc.* **435** (2013) 460 [1303.5627].

[4] K.K. Datta, G. Mellema, Y. Mao, I.T. Iliev, P.R. Shapiro and K. Ahn, *Light-cone effect on the reionization 21-cm power spectrum*, *Mon. Not. Roy. Astron. Soc.* **424** (2012) 1877 [1109.1284].

[5] S. Bharadwaj, A. Mazumdar and D. Sarkar, *Quantifying the redshift space distortion of the bis-pectrum I: primordial non-Gaussianity*, *Mon. Not. Roy. Astron. Soc.* **493** (2020) 594 [https://academic.oup.com/mnras/article-pdf/493/1/594/32513251/staa279.pdf].

[6] B. Ryden, *Introduction to Cosmology*, Addison-Wesley (2003).

[7] *The inflationary universe. The quest for a new theory of cosmic origins*, January, 1997.

[8] S. Weinberg, *The first three minutes : a modern view of the origin of the universe*, 2nd updated edition (Basic Books, 1993) (1993).

[9] M. Carmeli, J.G. Hartnett and F.J. Oliveira, *The Cosmic Time in Terms of the Redshift*, *Foundations of Physics Letters* **19** (2006) 277 [gr-qc/0506079].

[10] R. Barkana and A. Loeb, *In the beginning: the first sources of light and the reionization of the universe*, *Physics Reports* **349** (2001) 125 [arXiv:astro-ph/0010468].

[11] J. Miralda-Escudé, *The Dark Age of the Universe*, *Science* **300** (2003) 1904 [astro-ph/0307396].

[12] S.D.M. White, J.F. Navarro, A.E. Evrard and C.S. Frenk, *The baryon content of galaxy clusters: a challenge to cosmological orthodoxy*, *Nature* **366** (1993) 429.

[13] T.A. McKay, E.S. Sheldon, D. Johnston, E.K. Grebel, F. Prada, H.-W. Rix et al., *Dynamical confirmation of sloan digital sky survey weak-lensing scaling laws*, *The Astrophysical Journal* **571** (2002) L85.

[14] R. Barkana, *Studying the sources of cosmic reionization with 21-cm fluctuations*, *Mon. Not. Roy. Astron. Soc.* **397** (2009) 1454 [0806.2333].

[15] P. Dayal and A. Ferrara, *Early galaxy formation and its large-scale effects*, *Physics Reports* **780** (2018) 1 [1809.09136].

[16] J.R. Pritchard and S.R. Furlanetto, *21-cm fluctuations from inhomogeneous X-ray heating before reionization*, *Mon. Not. Roy. Astron. Soc.* **376** (2007) 1680 [astro-ph/0607234].

[17] S.R. Furlanetto and J.R. Pritchard, *The scattering of Lyman-series photons in the intergalactic medium*, *Mon. Not. Roy. Astron. Soc.* **372** (2006) 1093 [astro-ph/0605680].

[18] R.H. Becker, X. Fan, R.L. White, M.A. Strauss, V.K. Narayanan, R.H. Lupton et al., *Evidence for Reionization at z˜6: Detection of a Gunn-Peterson Trough in a z=6.28 Quasar*, *Astron. J.* **122** (2001) 2850 [arXiv:astro-ph/0108097].

[19] A. Loeb, *How did the first stars and galaxies form?*, *American Journal of Physics* **79** (2010) .

[20] R. Barkana and A. Loeb, *In the beginning: the first sources of light and the reionization of the universe*, *Physics Reports* **349** (2001) 125 [astro-ph/0010468].

[21] S.R. Furlanetto, S.P. Oh and F.H. Briggs, *Cosmology at low frequencies: The 21 cm transition and the high-redshift Universe*, *Physics Reports* **433** (2006) 181 [arXiv:astro-ph/0608032].

[22] B.E. Robertson, S.R. Furlanetto, E. Schneider, S. Charlot, R.S. Ellis, D.P. Stark et al., *New Constraints on Cosmic Reionization from the 2012 Hubble Ultra Deep Field Campaign*, *Astrophys. J.* **768** (2013) 71 [1301.1228].

[23] B.E. Robertson, R.S. Ellis, S.R. Furlanetto and J.S. Dunlop, *Cosmic Reionization and Early Star-forming Galaxies: A Joint Analysis of New Constraints from Planck and the Hubble Space Telescope*, *Astrophys. J.* **802** (2015) L19 [1502.02024].

[24] T.R. Choudhury, A. Ferrara and S. Gallerani, *On the minimum mass of reionization sources*, *Monthly Notices of the Royal Astronomical Society: Letters* **385** (2008) L58 [https://academic.oup.com/mnrasl/article-pdf/385/1/L58/6203642/385-1-L58.pdf].

[25] V. Bromm and A. Loeb, *The formation of the first low-mass stars from gas with low carbon and oxygen abundances*, *Nature* **425** (2003) 812 [astro-ph/0310622].

[26] K. Lai, J.-S. Huang, G. Fazio, L.L. Cowie, E.M. Hu and Y. Kakazu, *The stellar population of lyα-emitting galaxies at z˜ 5.7*, *The Astrophysical Journal* **655** (2007) 704.

[27] S.L. Finkelstein, J.E. Rhoads, S. Malhotra and N. Grogin, *LYMAN ALPHA GALAXIES: PRIMITIVE, DUSTY, OR EVOLVED?*, *The Astrophysical Journal* **691** (2009) 465.

[28] G. Meynet and A. Maeder, *Stellar evolution with rotation-xi. wolf-rayet star populations at different metallicities*, *Astronomy & Astrophysics* **429** (2005) 581.

[29] P. Madau and M. Dickinson, *Cosmic Star-Formation History*, *Ann. Rev. Astron. Astrophys.* **52** (2014) 415 [1403.0007].

[30] S. Mitra, A. Ferrara and T.R. Choudhury, *The escape fraction of ionizing photons from high-redshift galaxies from data-constrained reionization models*, *Mon. Not. Roy. Astron. Soc.* **428** (2013) L1 [1207.3803].

[31] M.S. Elvis, B.J. Wilkes, J.C. McDowell, R.F. Green, J. Bechtold, S.P. Willner et al., *Atlas of quasar energy distributions*, *The Astrophysical Journal Supplement Series* (1994) .

[32] A. Laor, F. Fiore, M. Elvis, B.J. Wilkes and J.C. McDowell, *The soft x-ray properties of a complete sample of optically selected quasars. ii. final results*, *The Astrophysical Journal* **477** (1997) 93.

[33] D.E.V. Berk, G.T. Richards, A. Bauer, M.A. Strauss, D.P. Schneider, T.M. Heckman et al., *Composite quasar spectra from the sloan digital sky survey*, *The Astronomical Journal* **122** (2001) 549.

[34] C. Vignali, W. Brandt and D. Schneider, *X-ray emission from radio-quiet quasars in the sloan digital sky survey early data release: the αox dependence upon ultraviolet luminosity*, *The Astronomical Journal* **125** (2003) 433.

[35] D.J. Mortlock, S.J. Warren, B.P. Venemans, M. Patel, P.C. Hewett, R.G. McMahon et al., *A luminous quasar at a redshift of $z = 7.085$*, *Nature* **474** (2011) 616 [1106.6088].

[36] E. Bañados, C. Mazzucchelli, E. Momjian, A.-C. Eilers, F. Wang, J.-T. Schindler et al., *The discovery of a highly accreting, radio-loud quasar at $z = 6.82$*, *The Astrophysical Journal* **909** (2021) 80.

[37] F. Wang, J. Yang, X. Fan, J.F. Hennawi, A.J. Barth, E. Banados et al., *A luminous quasar at redshift 7.642*, *The Astrophysical Journal Letters* **907** (2021) L1.

[38] P. Madau and A. Meiksin, *The he ii lyman-alpha opacity of the universe*, *The Astrophysical Journal* **433** (1994) L53.

[39] D. Reimers, S. Köhler, L. Wisotzki, D. Groote, P. Rodriguez-Pascual and W. Wamsteker, *Patchy intergalactic heii absorption in he 2347-4342.-the possible discovery of the epoch of he-reionization*, *Arxiv preprint astro-ph/9707173* (1997) .

[40] J. Miralda-Escudé, M. Haehnelt and M.J. Rees, *Reionization of the inhomogeneous universe*, *The Astrophysical Journal* **530** (2000) 1.

[41] C.-A. Faucher-Giguere, A. Lidz, M. Zaldarriaga and L. Hernquist, *A new calculation of the ionizing background spectrum and the effects of he ii reionization*, *The Astrophysical Journal* **703** (2009) 1416.

[42] M. McQuinn, *The implications of gunn–peterson troughs in the he ii lyα forest*, *The Astrophysical Journal* **704** (2009) L89.

[43] G. Worseck, J.X. Prochaska, M. McQuinn, A. Dall'Aglio, C. Fechner, J.F. Hennawi et al., *The end of helium reionization at z 2.7 inferred from cosmic variance in hst/cos he ii lyα absorption spectra*, *The Astrophysical Journal Letters* **733** (2011) L24.

[44] F. Haardt and P. Madau, *Radiative Transfer in a Clumpy Universe. IV. New Synthesis Models of the Cosmic UV/X-Ray Background*, *Astrophys. J.* **746** (2012) 125 [1105.2039].

[45] G. Worseck, J.X. Prochaska, J.F. Hennawi and M. McQuinn, *Early and extended helium reionization over more than 600 million years of cosmic time*, *The Astrophysical Journal* **825** (2016) 144.

[46] T. Fragos, B. Lehmer, M. Tremmel, P. Tzanavaris, A. Basu-Zych, K. Belczynski et al., *X-Ray Binary Evolution Across Cosmic Time*, *Astrophys. J.* **764** (2013) 41 [1206.2395].

[47] A. Fialkov and R. Barkana, *The rich complexity of 21-cm fluctuations produced by the first stars*, *Mon. Not. Roy. Astron. Soc.* **445** (2014) 213 [1409.3992].

[48] T.R. Choudhury, *Analytical Models of the Intergalactic Medium and Reionization*, *Current Science* **97** (2009) 841 [0904.4596].

[49] D.N. Spergel, L. Verde, H.V. Peiris, E. Komatsu, M.R. Nolta, C.L. Bennett et al., *First-Year Wilkinson Microwave Anisotropy Probe (WMAP) Observations: Determination of Cosmological Parameters*, *Astrophys. J. Suppl.* **148** (2003) 175 [arXiv:astro-ph/0302209].

[50] E. Komatsu, J. Dunkley, M.R. Nolta, C.L. Bennett, B. Gold, G. Hinshaw et al., *Five-Year Wilkinson Microwave Anisotropy Probe Observations: Cosmological Interpretation*, *Astrophys. J. Suppl.* **180** (2009) 330 [0803.0547].

[51] E. Komatsu, K.M. Smith, J. Dunkley, C.L. Bennett, B. Gold, G. Hinshaw et al., *Seven-year Wilkinson Microwave Anisotropy Probe (WMAP) Observations: Cosmological Interpretation*, *Astrophys. J. Suppl.* **192** (2011) 18 [1001.4538].

[52] Planck Collaboration, P.A.R. Ade, N. Aghanim, C. Armitage-Caplan, M. Arnaud, M. Ashdown et al., *Planck 2013 results. XVI. Cosmological parameters*, *Astron. Astrophys.* **571** (2014) A16 [1303.5076].

[53] Planck Collaboration, N. Aghanim, Y. Akrami, M. Ashdown, J. Aumont, C. Baccigalupi et al., *Planck 2018 results. VI. Cosmological parameters*, *Astron. Astrophys.* **641** (2020) A6 [1807.06209].

[54] M. Colless, *First results from the 2dF Galaxy Redshift Survey*, in *Large-Scale Structure in the Universe*, G. Efstathiou and et al., eds., vol. 357, p. 105, January, 1999.

[55] M. Colless, *Redshift Surveys and Cosmology*, *arXiv e-prints* (1999) astro [astro-ph/9911326].

[56] J.A. Peacock, S. Cole, P. Norberg, C.M. Baugh, J. Bland-Hawthorn, T. Bridges et al., *A measurement of the cosmological mass density from clustering in the 2dF Galaxy Redshift Survey*, *Nature* **410** (2001) 169 [astro-ph/0103143].

[57] Planck Collaboration, R. Adam, N. Aghanim, M. Ashdown, J. Aumont, C. Baccigalupi et al., *Planck intermediate results. XLVII. Planck constraints on reionization history*, *Astron. Astrophys.* **596** (2016) A108 [1605.03507].

[58] X. Fan, M.A. Strauss, D.P. Schneider, R.H. Becker, R.L. White, Z. Haiman et al., *A Survey of $z > 5.7$ Quasars in the Sloan Digital Sky Survey. II. Discovery of Three Additional Quasars at $z > 6$*, *Astron. J.* **125** (2003) 1649 [arXiv:astro-ph/0301135].

[59] R. Barnett, S.J. Warren, G.D. Becker, D.J. Mortlock, P.C. Hewett, R.G. McMahon et al., *Observations of the Lyman series forest towards the redshift 7.1 quasar ULAS J1120+0641*, *Astron. Astrophys.* **601** (2017) A16 [1702.03687].

[60] M. Ouchi, K. Shimasaku, H. Furusawa, T. Saito, M. Yoshida, M. Akiyama et al., *Statistics of 207 Lyα Emitters at a Redshift Near 7: Constraints on Reionization and Galaxy Formation Models*, *Astrophys. J.* **723** (2010) 869 [1007.2961].

[61] Z.-Y. Zheng, J. Wang, J. Rhoads, L. Infante, S. Malhotra, W. Hu et al., *First Results from the Lyman Alpha Galaxies in the Epoch of Reionization (LAGER) Survey: Cosmological Reionization at $z \sim 7$*, *Astrophys. J.* **842** (2017) L22 [1703.02985].

[62] A.J. Taylor, L.L. Cowie, A.J. Barger, E.M. Hu and A. Songaila, *The Evolution of the Ultraluminous Lyα Luminosity Function over $z = 5.7$-6.6*, *Astrophys. J.* **914** (2021) 79 [2104.13382].

[63] G. Swarup, S. Ananthakrishnan, V.K. Kapahi, A.P. Rao, C.R. Subrahmanya and V.K. Kulkarni, *The Giant Metre-Wave Radio Telescope*, *Current Science, Vol. 60, NO.2/JAN25, P. 95, 1991* **60** (1991) 95.

[64] S. Yatawatta, A.G. de Bruyn, M.A. Brentjens, P. Labropoulos, V.N. Pandey, S. Kazemi et al., *Initial deep LOFAR observations of epoch of reionization windows. I. The north celestial pole*, *Astron. Astrophys.* **550** (2013) A136 [1301.1630].

[65] M.P. van Haarlem, M.W. Wise, A.W. Gunst, G. Heald, J.P. McKean, J.W.T. Hessels et al., *LOFAR: The LOw-Frequency ARray*, Astron. Astrophys. **556** (2013) A2 [1305.3550].

[66] V. Jelić, A.G. de Bruyn, M. Mevius, F.B. Abdalla, K.M.B. Asad, G. Bernardi et al., *Initial LOFAR observations of epoch of reionization windows. II. Diffuse polarized emission in the ELAIS-N1 field*, Astron. Astrophys. **568** (2014) A101 [1407.2093].

[67] F.G. Mertens, M. Mevius, L.V.E. Koopmans, A.R. Offringa, G. Mellema, S. Zaroubi et al., *Improved upper limits on the 21cm signal power spectrum of neutral hydrogen at z 9.1 from LOFAR*, Monthly Notices of the Royal Astronomical Society **493** (2020) 1662 [https://academic.oup.com/mnras/article-pdf/493/2/1662/32666766/staa327.pdf].

[68] S.J. Tingay, R. Goeke, J.D. Bowman, D. Emrich, S.M. Ord, D.A. Mitchell et al., *The Murchison Widefield Array: The Square Kilometre Array Precursor at Low Radio Frequencies*, Publ. Astron. Soc. Austral. **30** (2013) 7 [1206.6945].

[69] J.D. Bowman, I. Cairns, D.L. Kaplan, T. Murphy, D. Oberoi, L. Staveley-Smith et al., *Science with the Murchison Widefield Array*, Publ. Astron. Soc. Austral. **30** (2013) 31 [1212.5151].

[70] J.C. Pober, A.R. Parsons, J.E. Aguirre, Z. Ali, R.F. Bradley, C.L. Carilli et al., *Opening the 21 cm Epoch of Reionization Window: Measurements of Foreground Isolation with PAPER*, Astrophys. J. **768** (2013) L36 [1301.7099].

[71] A. Ewall-Wice, J.S. Dillon, A. Mesinger and J. Hewitt, *Detecting the 21 cm forest in the 21 cm power spectrum*, Mon. Not. Roy. Astron. Soc. **441** (2014) 2476 [1310.7936].

[72] D.R. DeBoer, A.R. Parsons, J.E. Aguirre, P. Alexander, Z.S. Ali, A.P. Beardsley et al., *Hydrogen epoch of reionization array (HERA)*, Publications of the Astronomical Society of the Pacific **129** (2017) 045001.

[73] G. Mellema, L.V.E. Koopmans, F.A. Abdalla, G. Bernardi, B. Ciardi, S. Daiboo et al., *Reionization and the Cosmic Dawn with the Square Kilometre Array*, Experimental Astronomy **36** (2013) 235 [1210.0197].

[74] L. Koopmans, J. Pritchard, G. Mellema, J. Aguirre, K. Ahn, R. Barkana et al., *The Cosmic Dawn and Epoch of Reionisation with SKA*, *Advancing Astrophysics with the Square Kilometre Array (AASKA14)* (2015) 1 [1505.07568].

[75] D.J. Griffiths, *Hyperfine splitting in the ground state of hydrogen*, American Journal of Physics **50** (1982) 698.

[76] G.B. Field, *Excitation of the Hydrogen 21-CM Line*, Proceedings of the IRE **46** (1958) 240.

[77] G. Rybicki and A. Lightman, *Lightman Radiative Processes in Astrophysics*, Wiley Online Library (01, 1979), 10.1002/9783527618170.

[78] M. Pospelov, J. Pradler, J.T. Ruderman and A. Urbano, *Room for New Physics in the Rayleigh-Jeans Tail of the Cosmic Microwave Background*, Phys. Rev. Lett. **121** (2018) 031103 [1803.07048].

[79] S. Bharadwaj and S.S. Ali, *The cosmic microwave background radiation fluctuations from HI perturbations prior to reionization*, *Mon. Not. Roy. Astron. Soc.* **352** (2004) 142 [arXiv:astro-ph/0401206].

[80] A. Loeb and M. Zaldarriaga, *Measuring the small-scale power spectrum of cosmic density fluctuations through 21 cm tomography prior to the epoch of structure formation*, Phys. Rev. Lett. **92** (2004) 211301.

[81] K.K. Datta, R. Ghara, A. Hoque and S. Majumdar, *Large H I optical depth and redshifted 21-cm signal from cosmic dawn*, Mon. Not. Roy. Astron. Soc. **509** (2022) 945 [2110.06925].

[82] J.R. Pritchard and A. Loeb, *Evolution of the 21cm signal throughout cosmic history*, Phys. Rev. **78** (2008) 103511 [0802.2102].

[83] S.A. Wouthuysen, *On the excitation mechanism of the 21-cm (radio-frequency) interstellar hydrogen emission line.*, Astron. J. **57** (1952) 31.

[84] J.R. Pritchard and S.R. Furlanetto, *Descending from on high: Lyman-series cascades and spin-kinetic temperature coupling in the 21-cm line*, Monthly Notices of the Royal Astronomical Society **367** (2006) 1057 [https://academic.oup.com/mnras/article-pdf/367/3/1057/3507365/367-3-1057.pdf].

[85] J.D. Bowman and A.E.E. Rogers, *A lower limit of $\Delta z > 0.06$ for the duration of the reionization epoch*, *Nature* **468** (2010) 796.

[86] J.D. Bowman, A.E.E. Rogers, R.A. Monsalve, T.J. Mozdzen and N. Mahesh, *An absorption profile centred at 78 megahertz in the sky-averaged spectrum*, Nature **555** (2018) 67 [1810.05912].

[87] S. Singh, R. Subrahmanyan, N.U. Shankar, M.S. Rao, A. Fialkov, A. Cohen et al., *First results on the epoch of reionization from first light with SARAS 2*, *The Astrophysical Journal* **845** (2017) L12.

[88] H.T.J. Bevins, E. de Lera Acedo, A. Fialkov, W.J. Handley, S. Singh, R. Subrahmanyan et al., *A comprehensive Bayesian reanalysis of the SARAS2 data from the epoch of reionization*, *Monthly Notices of the Royal Astronomical Society* **513** (2022) 4507 [https://academic.oup.com/mnras/article-pdf/513/3/4507/43754925/stac1158.pdf].

[89] A. Fialkov, R. Barkana and A. Cohen, *Constraining Baryon-Dark-Matter Scattering with the Cosmic Dawn 21-cm Signal*, *Phys. Rev. Lett.* **121** (2018) 011101 [1802.10577].

[90] A. Ewall-Wice, T.C. Chang, J. Lazio, O. Doré, M. Seiffert and R.A. Monsalve, *Modeling the Radio Background from the First Black Holes at Cosmic Dawn: Implications for the 21 cm Absorption Amplitude*, *Astrophys. J.* **868** (2018) 63 [1803.01815].

[91] R. Barkana, N.J. Outmezguine, D. Redigolo and T. Volansky, *Strong constraints on light dark matter interpretation of the edges signal*, *Phys. Rev. D* **98** (2018) 103005.

[92] A. Parsons, D. Backer, G. Foster, M. Wright, R. Bradley, N. Gugliucci et al., *The precision array for probing the epoch of re-ionization: Eight station results*, *Astronomical Journal* **139** (2010) 1468.

[93] T. Di Matteo, R. Perna, T. Abel and M.J. Rees, *Radio Foregrounds for the 21 Centimeter Tomography of the Neutral Intergalactic Medium at High Redshifts*, *Astrophys. J.* **564** (2002) 576 [arXiv:astro-ph/0109241].

[94] S.S. Ali, S. Bharadwaj and J.N. Chengalur, *Foregrounds for redshifted 21-cm studies of reionization: Giant Meter Wave Radio Telescope 153-MHz observations*, *Mon. Not. Roy. Astron. Soc.* **385** (2008) 2166 [0801.2424].

[95] G. Bernardi, A.G. de Bruyn, M.A. Brentjens, B. Ciardi, G. Harker, V. Jelić et al., *Foregrounds for observations of the cosmological 21 cm line. I. First Westerbork measurements of Galactic emission at 150 MHz in a low latitude field*, *Astron. Astrophys.* **500** (2009) 965 [0904.0404].

[96] A. Ghosh, J. Prasad, S. Bharadwaj, S.S. Ali and J.N. Chengalur, *Characterizing foreground for redshifted 21 cm radiation: 150 MHz Giant Metrewave Radio Telescope observations*, *Mon. Not. Roy. Astron. Soc.* **426** (2012) 3295 [1208.1617].

[97] G. Paciga, J.G. Albert, K. Bandura, T.-C. Chang, Y. Gupta, C. Hirata et al., *A simulation-calibrated limit on the H I power spectrum from the GMRT Epoch of Reionization experiment*, *Mon. Not. Roy. Astron. Soc.* **433** (2013) 639 [1301.5906].

[98] A.P. Beardsley, B.J. Hazelton, I.S. Sullivan, P. Carroll, N. Barry, M. Rahimi et al., *First Season MWA EoR Power spectrum Results at Redshift 7*, *Astrophys. J.* **833** (2016) 102 [1608.06281].

[99] L. Gleser, A. Nusser and A.J. Benson, *Decontamination of cosmological 21-cm maps*, *Mon. Not. Roy. Astron. Soc.* **391** (2008) 383 [0712.0497].

[100] V. Jelić, S. Zaroubi, P. Labropoulos, R.M. Thomas, G. Bernardi, M.A. Brentjens et al., *Foreground simulations for the LOFAR-epoch of reionization experiment*, *Mon. Not. Roy. Astron. Soc.* **389** (2008) 1319 [0804.1130].

[101] F.G. Mertens, A. Ghosh and L.V.E. Koopmans, *Statistical 21-cm signal separation via Gaussian Process Regression analysis*, *Mon. Not. Roy. Astron. Soc.* **478** (2018) 3640 [1711.10834].

[102] T.L. Makinen, L. Lancaster, F. Villaescusa-Navarro, P. Melchior, S. Ho, L. Perreault-Levasseur et al., *deep21: a deep learning method for 21 cm foreground removal*, *JCAP* **2021** (2021) 081 [2010.15843].

[103] J.C. Pober, A. Liu, J.S. Dillon, J.E. Aguirre, J.D. Bowman, R.F. Bradley et al., *What Next-generation 21 cm Power Spectrum Measurements can Teach us About the Epoch of Reionization*, *Astrophys. J.* **782** (2014) 66 [1310.7031].

[104] J.S. Dillon, A. Liu, C.L. Williams, J.N. Hewitt, M. Tegmark, E.H. Morgan et al., *Overcoming real-world obstacles in 21 cm power spectrum estimation: A method demonstration and results from early Murchison Widefield Array data*, *Phys. Rev.* **89** (2014) 023002 [1304.4229].

[105] A. Liu, A.R. Parsons and C.M. Trott, *Epoch of reionization window. I. Mathematical formalism*, *Phys. Rev.* **90** (2014) 023018 [1404.2596].

[106] A. Liu, A.R. Parsons and C.M. Trott, *Epoch of reionization window. ii. statistical methods for foreground wedge reduction*, *Phys. Rev. D* **90** (2014) 023019.

[107] Z.S. Ali, A.R. Parsons, H. Zheng, J.C. Pober, A. Liu, J.E. Aguirre et al., *PAPER-64 Constraints on Reionization: The 21 cm Power Spectrum at $z = 8.4$*, *Astrophys. J.* **809** (2015) 61 [1502.06016].

[108] M.F. Morales, *Power Spectrum Sensitivity and the Design of Epoch of Reionization Observatories*, *Astrophys. J.* **619** (2005) 678 [astro-ph/0406662].

[109] M. McQuinn, O. Zahn, M. Zaldarriaga, L. Hernquist and S.R. Furlanetto, *Cosmological Parameter Estimation Using 21 cm Radiation from the Epoch of Reionization*, *Astrophys. J.* **653** (2006) 815 [astro-ph/0512263].

[110] A. Datta, R. Bradley, J.O. Burns, G. Harker, A. Komjathy and T.J.W. Lazio, *Effects Of The Ionosphere On Ground-Based Detection Of The Global 21 CM Signal From The Cosmic Dawn And The Dark Ages*, *arXiv e-prints* (2014) arXiv:1409.0513 [1409.0513].

[111] E. Shen, D. Anstey, E. de Lera Acedo, A. Fialkov and W. Handley, *Quantifying ionospheric effects on global 21-cm observations*, *Mon. Not. Roy. Astron. Soc.* **503** (2021) 344 [2011.10517].

[112] A.R. Offringa, A.G. de Bruyn, M. Biehl, S. Zaroubi, G. Bernardi and V.N. Pandey, *Post-correlation radio frequency interference classification methods*, *Mon. Not. Roy. Astron. Soc.* **405** (2010) 155 [1002.1957].

[113] A.R. Offringa, J.J. van de Gronde and J.B.T.M. Roerdink, *A morphological algorithm for improving radio-frequency interference detection*, *Astron. Astrophys.* **539** (2012) A95 [1201.3364].

[114] L.R. Whitler, A. Beardsley and D. Jacobs, *The Effects of RFI on 21-cm Measurements of the Epoch of Reionization*, in *American Astronomical Society Meeting Abstracts #233*, vol. 233 of *American Astronomical Society Meeting Abstracts*, p. 349.17, January, 2019.

[115] A.H. Patil, S. Zaroubi, E. Chapman, V. Jelić, G. Harker, F.B. Abdalla et al., *Constraining the epoch of reionization with the variance statistic: simulations of the LOFAR case*, *Mon. Not. Roy. Astron. Soc.* **443** (2014) 1113 [1401.4172].

[116] C.A. Watkinson and J.R. Pritchard, *Distinguishing models of reionization using future radio observations of 21-cm 1-point statistics*, *Mon. Not. Roy. Astron. Soc.* **443** (2014) 3090 [1312.1342].

[117] C.A. Watkinson and J.R. Pritchard, *The impact of spin-temperature fluctuations on the 21-cm moments*, *Mon. Not. Roy. Astron. Soc.* **454** (2015) 1416 [1505.07108].

[118] A.H. Patil, S. Yatawatta, L.V.E. Koopmans, A.G. de Bruyn, M.A. Brentjens, S. Zaroubi et al., *Upper Limits on the 21 cm Epoch of Reionization Power Spectrum from One Night with LOFAR*, *Astrophys. J.* **838** (2017) 65 [1702.08679].

[119] K.K. Datta, T.R. Choudhury and S. Bharadwaj, *The multifrequency angular power spectrum of the epoch of reionization 21-cm signal*, *Mon. Not. Roy. Astron. Soc.* **378** (2007) 119 [arXiv:astro-ph/0605546].

[120] R. Mondal, S. Bharadwaj and K.K. Datta, *Towards simulating and quantifying the light-cone EoR 21-cm signal*, *Monthly Notices of the Royal Astronomical Society* **474** (2018) 1390 [1706.09449].

[121] R. Mondal, S. Bharadwaj, I.T. Iliev, K.K. Datta, S. Majumdar, A.K. Shaw et al., *A method to determine the evolution history of the mean neutral Hydrogen fraction*, *Monthly Notices of the Royal Astronomical Society* **483** (2019) L109 [1810.06273].

[122] N. Barry, M. Wilensky, C.M. Trott, B. Pindor, A.P. Beardsley, B.J. Hazelton et al., *Improving the Epoch of Reionization Power Spectrum Results from Murchison Widefield Array Season 1 Observations*, *Astrophys. J.* **884** (2019) 1 [1909.00561].

[123] M. Kolopanis, D. Jacobs, C. Cheng, A. Parsons, S. Kohn, J. Pober et al., *A simplified, lossless reanalysis of paper-64*, *The Astrophysical Journal* **883** (2019) 133.

[124] W. Li, J.C. Pober, N. Barry, B.J. Hazelton, M.F. Morales, C.M. Trott et al., *First Season MWA Phase II Epoch of Reionization Power Spectrum Results at Redshift 7*, *Astrophys. J.* **887** (2019) 141 [1911.10216].

[125] C.M. Trott, C.H. Jordan, S. Midgley, N. Barry, B. Greig, B. Pindor et al., *Deep multiredshift limits on Epoch of Reionization 21 cm power spectra from four seasons of Murchison Widefield Array observations*, *Monthly Notices of the Royal Astronomical Society* **493** (2020) 4711 [https://academic.oup.com/mnras/article-pdf/493/4/4711/32927265/staa414.pdf].

[126] The HERA Collaboration, Z. Abdurashidova, J.E. Aguirre, P. Alexander, Z.S. Ali, Y. Balfour et al., *First Results from HERA Phase I: Upper Limits on the Epoch of Reionization 21 cm Power Spectrum*, *arXiv e-prints* (2021) arXiv:2108.02263 [2108.02263].

[127] H. Merz, U.-L. Pen and H. Trac, *Towards optimal parallel PM N-body codes: PMFAST*, *New Astronomy* **10** (2005) 393 [astro-ph/0402443].

[128] J. Harnois-Déraps, U.-L. Pen, I.T. Iliev, H. Merz, J.D. Emberson and V. Desjacques, *High-performance P^3M N-body code: CUBEP^3M*, *Mon. Not. Roy. Astron. Soc.* **436** (2013) 540.

[129] M. Davis, G. Efstathiou, C.S. Frenk and S.D.M. White, *The evolution of large-scale structure in a universe dominated by cold dark matter*, *Astrophys. J.* **292** (1985) 371.

[130] P.S. Behroozi, R.H. Wechsler and H.-Y. Wu, *THE ROCKSTAR PHASE-SPACE TEMPORAL HALO FINDER AND THE VELOCITY OFFSETS OF CLUSTER CORES*, *The Astrophysical Journal* **762** (2012) 109.

[131] A. Maselli, A. Ferrara and B. Ciardi, *CRASH: a radiative transfer scheme*, *Mon. Not. Roy. Astron. Soc.* **345** (2003) 379 [arXiv:astro-ph/0307117].

[132] G. Mellema, I.T. Iliev, U.-L. Pen and P.R. Shapiro, *Simulating cosmic reionization at large scales - II. The 21-cm emission features and statistical signals*, *Mon. Not. Roy. Astron. Soc.* **372** (2006) 679 [arXiv:astro-ph/0603518].

[133] B. Semelin, E. Eames, F. Bolgar and M. Caillat, *21SSD: a public data base of simulated 21-cm signals from the epoch of reionization*, *Monthly Notices of the Royal Astronomical Society* **472** (2017) 4508 [https://academic.oup.com/mnras/article-pdf/472/4/4508/21077092/stx2274.pdf].

[134] Y.B. Zel'Dovich, *Gravitational instability: An approximate theory for large density perturbations.*, *Astronomy and astrophysics* **5** (1970) 84.

[135] F.R. Bouchet, S. Colombi, E. Hivon and R. Juszkiewicz, *Perturbative Lagrangian approach to gravitational instability.*, *Astron. Astrophys.* **296** (1995) 575 [astro-ph/9406013].

[136] A. Jenkins, *Second-order Lagrangian perturbation theory initial conditions for resimulations*, *Monthly Notices of the Royal Astronomical Society* **403** (2010) 1859 [https://academic.oup.com/mnras/article-pdf/403/4/1859/18576328/mnras0403-1859.pdf]

[137] M. Crocce, S. Pueblas and R. Scoccimarro, *Transients from initial conditions in cosmological simulations*, *Monthly Notices of the Royal Astronomical Society* **373** (2006) 369 [https://academic.oup.com/mnras/article-pdf/373/1/369/4187617/mnras0373-0369.pdf].

[138] S. Bharadwaj and P.S. Srikant, *HI Fluctuations at Large Redshifts: III - Simulating the Signal Expected at GMRT*, *Journal of Astrophysics and Astronomy* **25** (2004) 67 [arXiv:astro-ph/0402262].

[139] J. Peacock, *Cosmological Physics*, Cambridge Astrophysics Series, Cambridge University Press (1999).

[140] W.H. Press and P. Schechter, *Formation of galaxies and clusters of galaxies by self-similar gravitational condensation*, *The Astrophysical Journal* **187** (1974) 425.

[141] A. Jenkins, C.S. Frenk, S.D.M. White, J.M. Colberg, S. Cole, A.E. Evrard et al., *The mass function of dark matter haloes*, *Mon. Not. Roy. Astron. Soc.* **321** (2001) 372 [arXiv:astro-ph/0005260].

[142] R.K. Sheth and G. Tormen, *An excursion set model of hierarchical clustering: ellipsoidal collapse and the moving barrier*, *Mon. Not. Roy. Astron. Soc.* **329** (2002) 61 [arXiv:astro-ph/0105113].

[143] J.L. Tinker, B.E. Robertson, A.V. Kravtsov, A. Klypin, M.S. Warren, G. Yepes et al., *The Large-scale Bias of Dark Matter Halos: Numerical Calibration and Model Tests*, *Astrophys. J.* **724** (2010) 878 [1001.3162].

[144] W.A. Watson, I.T. Iliev, A. D'Aloisio, A. Knebe, P.R. Shapiro and G. Yepes, *The halo mass function through the cosmic ages*, *Monthly Notices of the Royal Astronomical Society* **433** (2013) 1230 [https://academic.oup.com/mnras/article-pdf/433/2/1230/4901588/stt791.pdf].

[145] S.R. Furlanetto, M. Zaldarriaga and L. Hernquist, *The Growth of H II Regions During Reionization*, *Astrophys. J.* **613** (2004) 1 [arXiv:astro-ph/0403697].

[146] J.R. Bond, S. Cole, G. Efstathiou and N. Kaiser, *Excursion Set Mass Functions for Hierarchical Gaussian Fluctuations*, *Astrophys. J.* **379** (1991) 440.

[147] S. Majumdar, G. Mellema, K.K. Datta, H. Jensen, T.R. Choudhury, S. Bharadwaj et al., *On the use of seminumerical simulations in predicting the 21-cm signal from the epoch of reionization*, *Mon. Not. Roy. Astron. Soc.* **443** (2014) 2843 [1403.0941].

[148] R. Mondal, S. Bharadwaj, S. Majumdar, A. Bera and A. Acharyya, *The effect of non-Gaussianity on error predictions for the Epoch of Reionization (EoR) 21-cm power spectrum*, *Mon. Not. Roy. Astron. Soc.* **449** (2015) L41 [1409.4420].

[149] O. Zahn, A. Mesinger, M. McQuinn, H. Trac, R. Cen and L.E. Hernquist, *Comparison of reionization models: radiative transfer simulations and approximate, seminumeric models*, *Mon. Not. Roy. Astron. Soc.* **414** (2011) 727 [1003.3455].

[150] A. Mesinger, S. Furlanetto and R. Cen, *21CMFAST: a fast, seminumerical simulation of the high-redshift 21-cm signal*, *Mon. Not. Roy. Astron. Soc.* **411** (2011) 955 [1003.3878].

[151] M.G. Santos, L. Ferramacho, M.B. Silva, A. Amblard and A. Cooray, *Fast large volume simulations of the 21-cm signal from the reionization and pre-reionization epochs*, *Mon. Not. Roy. Astron. Soc.* **406** (2010) 2421 [0911.2219].

[152] R.M. Thomas, S. Zaroubi, B. Ciardi, A.H. Pawlik, P. Labropoulos, V. Jelić et al., *Fast large-scale reionization simulations*, *Mon. Not. Roy. Astron. Soc.* **393** (2009) 32 [0809.1326].

[153] R. Ghara, T.R. Choudhury and K.K. Datta, *21 cm signal from cosmic dawn: imprints of spin temperature fluctuations and peculiar velocities*, *Mon. Not. Roy. Astron. Soc.* **447** (2015) 1806 [1406.4157].

[154] R. Ghara, G. Mellema, S.K. Giri, T.R. Choudhury, K.K. Datta and S. Majumdar, *Prediction of the 21-cm signal from reionization: comparison between 3D and 1D radiative transfer schemes*, *Mon. Not. Roy. Astron. Soc.* **476** (2018) 1741 [1710.09397].

[155] M. Zaldarriaga, S.R. Furlanetto and L. Hernquist, *21 Centimeter Fluctuations from Cosmic Gas at High Redshifts*, *Astrophys. J.* **608** (2004) 622 [arXiv:astro-ph/0311514].

[156] R. Barkana and A. Loeb, *A Method for Separating the Physics from the Astrophysics of High-Redshift 21 Centimeter Fluctuations*, *Astrophys. J.* **624** (2005) L65 [arXiv:astro-ph/0409572].

[157] A. Mesinger and S. Furlanetto, *Efficient Simulations of Early Structure Formation and Reionization*, *Astrophys. J.* **669** (2007) 663 [0704.0946].

[158] A. Lidz, O. Zahn, M. McQuinn, M. Zaldarriaga and L. Hernquist, *Detecting the Rise and Fall of 21 cm Fluctuations with the Murchison Widefield Array*, *Astrophys. J.* **680** (2008) 962 [0711.4373].

[159] Y. Mao, P.R. Shapiro, G. Mellema, I.T. Iliev, J. Koda and K. Ahn, *Redshift-space distortion of the 21-cm background from the epoch of reionization - I. Methodology re-examined*, *Mon. Not. Roy. Astron. Soc.* **422** (2012) 926 [1104.2094].

[160] S. Majumdar, H. Jensen, G. Mellema, E. Chapman, F.B. Abdalla, K.-Y. Lee et al., *Effects of the sources of reionization on 21-cm redshift-space distortions*, *Mon. Not. Roy. Astron. Soc.* **456** (2016) 2080 [1509.07518].

[161] S. Bharadwaj and S.K. Pandey, *Probing non-Gaussian features in the HI distribution at the epoch of re-ionization*, *Mon. Not. Roy. Astron. Soc.* **358** (2005) 968 [arXiv:astro-ph/0410581].

[162] N. Bartolo, E. Komatsu, S. Matarrese and A. Riotto, *Non-Gaussianity from inflation: theory and observations*, *Physics Reports* **402** (2004) 103 [astro-ph/0406398].

[163] R. Mondal, S. Bharadwaj and S. Majumdar, *Statistics of the epoch of reionization 21-cm signal - I. Power spectrum error-covariance*, *Mon. Not. Roy. Astron. Soc.* **456** (2016) 1936 [1508.00896].

[164] R. Mondal, S. Bharadwaj and S. Majumdar, *Statistics of the epoch of reionization (EoR) 21-cm signal - II. The evolution of the power-spectrum error-covariance*, *Mon. Not. Roy. Astron. Soc.* **464** (2017) 2992 [1606.03874].

[165] A.K. Shaw, S. Bharadwaj and R. Mondal, *The impact of non-Gaussianity on the error covariance for observations of the Epoch of Reionization 21-cm power spectrum*, *Mon. Not. Roy. Astron. Soc.* **487** (2019) 4951 [1902.08706].

[166] A.K. Shaw, S. Bharadwaj and R. Mondal, *The impact of non-Gaussianity on the Epoch of Reionization parameter forecast using 21-cm power-spectrum measurements*, *Mon. Not. Roy. Astron. Soc.* **498** (2020) 1480 [2005.06535].

[167] G.J.A. Harker, S. Zaroubi, R.M. Thomas, V. Jelić, P. Labropoulos, G. Mellema et al., *Detection and extraction of signals from the epoch of reionization using higher-order one-point statistics*, *Mon. Not. Roy. Astron. Soc.* **393** (2009) 1449 [0809.2428].

[168] H. Shimabukuro, S. Yoshiura, K. Takahashi, S. Yokoyama and K. Ichiki, *Studying 21cm power spectrum with one-point statistics*, *Mon. Not. Roy. Astron. Soc.* **451** (2015) 467 [1412.3332].

[169] K. Kubota, S. Yoshiura, H. Shimabukuro and K. Takahashi, *Expected constraints on models of the epoch of reionization with the variance and skewness in redshifted 21 cm-line fluctuations*, *Publ. Astron. Soc. Jap.* **68** (2016) 61 [1602.02873].

[170] R. Mondal, G. Mellema, A.K. Shaw, M. Kamran and S. Majumdar, *The Epoch of Reionization 21-cm bispectrum: the impact of light-cone effects and detectability*, *Mon. Not. Roy. Astron. Soc.* **508** (2021) 3848 [2107.02668].

[171] H. Tiwari, A.K. Shaw, S. Majumdar, M. Kamran and M. Choudhury, *Improving constraints on the reionization parameters using 21-cm bispectrum*, *JCAP* **2022** (2022) 045 [2108.07279].

[172] C.A. Watkinson, B. Greig and A. Mesinger, *Epoch of reionization parameter estimation with the 21-cm bispectrum*, *Mon. Not. Roy. Astron. Soc.* **510** (2022) 3838 [2102.02310].

[173] N. Kaiser, *Clustering in real space and in redshift space*, *Mon. Not. Roy. Astron. Soc.* **227** (1987) 1.

[174] A.J.S. Hamilton, *Linear Redshift Distortions: a Review*, in *The Evolving Universe*, D. Hamilton, ed., vol. 231 of *Astrophysics and Space Science Library*, p. 185, 1998 [arXiv:astro-ph/9708102].

[175] T. Matsubara, Y. Suto and I. Szapudi, *Light-cone effect on higher order clustering in redshift surveys*, *The Astrophysical Journal* **491** (1997) L1.

[176] R. Barkana and A. Loeb, *Light-cone anisotropy in 21-cm fluctuations during the epoch of reionization*, *Mon. Not. Roy. Astron. Soc.* **372** (2006) L43 [astro-ph/0512453].

[177] C. Alcock and B. Paczynski, *An evolution free test for non-zero cosmological constant*, *Nature* **281** (1979) 358.

[178] S. Bharadwaj and S.S. Ali, *On using visibility correlations to probe the HI distribution from the dark ages to the present epoch - I. Formalism and the expected signal*, *Mon. Not. Roy. Astron. Soc.* **356** (2005) 1519 [arXiv:astro-ph/0406676].

[179] P.R. Shapiro, Y. Mao, I.T. Iliev, G. Mellema, K.K. Datta, K. Ahn et al., *Will Nonlinear Peculiar Velocity and Inhomogeneous Reionization Spoil 21 cm Cosmology from the Epoch of Reionization?*, *Physical Review Letters* **110** (2013) 151301 [1211.2036].

[180] S. Majumdar, S. Bharadwaj and T.R. Choudhury, *The effect of peculiar velocities on the epoch of reionization 21-cm signal*, *Mon. Not. Roy. Astron. Soc.* **434** (2013) 1978 [1209.4762].

[181] S. Saiyad Ali, S. Bharadwaj and S.K. Pandey, *Probing the bispectrum at high redshifts using 21-cm HI observations*, *Mon. Not. Roy. Astron. Soc.* **366** (2006) 213 [astro-ph/0510118].

[182] C.A. Watkinson, S. Majumdar, J.R. Pritchard and R. Mondal, *A fast estimator for the bispectrum and beyond - a practical method for measuring non-Gaussianity in 21-cm maps*, *Mon. Not. Roy. Astron. Soc.* **472** (2017) 2436 [1705.06284].

[183] S. Majumdar, J.R. Pritchard, R. Mondal, C.A. Watkinson, S. Bharadwaj and G. Mellema, *Quantifying the non-Gaussianity in the EoR 21-cm signal through bispectrum*, *Mon. Not. Roy. Astron. Soc.* **476** (2018) 4007 [1708.08458].

[184] A. Hutter, C.A. Watkinson, J. Seiler, P. Dayal, M. Sinha and D.J. Croton, *The 21cm bispectrum during reionization: a tracer of the ionization topology*, *arXiv e-prints* (2019) arXiv:1907.04342 [1907.04342].

[185] C.A. Watkinson, S.K. Giri, H.E. Ross, K.L. Dixon, I.T. Iliev, G. Mellema et al., *The 21-cm bispectrum as a probe of non-Gaussianities due to X-ray heating*, *Mon. Not. Roy. Astron. Soc.* **482** (2019) 2653 [1808.02372].

[186] S.S. Ali, S. Bharadwaj and B. Pandey, *What will anisotropies in the clustering pattern in redshifted 21-cm maps tell us?*, *Mon. Not. Roy. Astron. Soc.* **363** (2005) 251 [arXiv:astro-ph/0503237].

[187] S. Majumdar, K.K. Datta, R. Ghara, R. Mondal, T.R. Choudhury, S. Bharadwaj et al., *Line-of-Sight Anisotropies in the Cosmic Dawn and Epoch of Reionization 21-cm Power Spectrum*, *Journal of Astrophysics and Astronomy* **37** (2016) 32 [1610.08180].

[188] R. Ghara, T.R. Choudhury and K.K. Datta, *21 cm signal from cosmic dawn: imprints of spin temperature fluctuations and peculiar velocities*, *Mon. Not. Roy. Astron. Soc.* **447** (2015) 1806 [1406.4157].

[189] A. Fialkov, R. Barkana and A. Cohen, *Reconstructing the Nature of the First Cosmic Sources from the Anisotropic 21-cm Signal*, *Physical Review Letters* **114** (2015) 101303 [1502.02731].

[190] S. Majumdar, M. Kamran, J.R. Pritchard, R. Mondal, A. Mazumdar, S. Bharadwaj et al., *Redshifted 21-cm bispectrum - I. Impact of the redshift space distortions on the signal from the Epoch of Reionization*, *Mon. Not. Roy. Astron. Soc.* **499** (2020) 5090 [2007.06584].

[191] M. Kamran, R. Ghara, S. Majumdar, R. Mondal, G. Mellema, S. Bharadwaj et al., *Redshifted 21-cm bispectrum - II. Impact of the spin temperature fluctuations and redshift space distortions on the signal from the Cosmic Dawn*, *Mon. Not. Roy. Astron. Soc.* **502** (2021) 3800 [2012.11616].

[192] M. Kamran, S. Majumdar, R. Ghara, G. Mellema, S. Bharadwaj, J.R. Pritchard et al., *Probing IGM Physics during Cosmic Dawn using the Redshifted 21-cm Bispectrum*, *arXiv e-prints* (2021) arXiv:2108.08201 [2108.08201].

[193] M. Kamran, R. Ghara, S. Majumdar, G. Mellema, S. Bharadwaj, J.R. Pritchard et al., *Redshifted 21-cm bispectrum: Impact of the source models on the signal and IGM physics from the Cosmic Dawn*, *arXiv e-prints* (2022) arXiv:2207.09128 [2207.09128].

[194] R.L. White, R.H. Becker, X. Fan and M.A. Strauss, *Probing the Ionization State of the Universe at z¿6*, *Astron. J.* **126** (2003) 1 [arXiv:astro-ph/0303476].

[195] M. Trenti, M. Stiavelli, R.J. Bouwens, P. Oesch, J.M. Shull, G.D. Illingworth et al., *The Galaxy Luminosity Function During the Reionization Epoch*, *Astrophys. J.* **714** (2010) L202 [1004.0384].

[196] H. Jensen, P. Laursen, G. Mellema, I.T. Iliev, J. Sommer-Larsen and P.R. Shapiro, *On the use of Lyα emitters as probes of reionization*, *Mon. Not. Roy. Astron. Soc.* **428** (2013) 1366 [1206.4028].

[197] T.R. Choudhury, E. Puchwein, M.G. Haehnelt and J.S. Bolton, *Lyman α emitters gone missing: evidence for late reionization?*, *Mon. Not. Roy. Astron. Soc.* **452** (2015) 261 [1412.4790].

[198] R. Bouwens, *High-Redshift Galaxy Surveys and the Reionization of the Universe*, in *Astrophysics and Space Science Library*, A. Mesinger, ed., vol. 423 of *Astrophysics and Space Science Library*, p. 111, 2016, DOI [1511.01133].

[199] K. Ota, M. Iye, N. Kashikawa, A. Konno, F. Nakata, T. Totani et al., *A New Constraint on Reionization from the Evolution of the Lyα Luminosity Function at*

$z \sim$ 6-7 Probed by a Deep Census of $z = 7.0$ Lyα Emitter Candidates to 0.3L^*, Astrophys. J. **844** (2017) 85 [1703.02501].

[200] M.A. Alvarez, P.R. Shapiro, K. Ahn and I.T. Iliev, *Implications of WMAP 3 Year Data for the Sources of Reionization*, *Astrophys. J.* **644** (2006) L101 [arXiv:astro-ph/0604447].

[201] S. Mitra, T.R. Choudhury and A. Ferrara, *Cosmic reionization after Planck*, Mon. Not. Roy. Astron. Soc. **454** (2015) L76 [1505.05507].

[202] R.J. Bouwens, G.D. Illingworth, P.A. Oesch, J. Caruana, B. Holwerda, R. Smit et al., *Reionization After Planck: The Derived Growth of the Cosmic Ionizing Emissivity Now Matches the Growth of the Galaxy UV Luminosity Density*, Astrophys. J. **811** (2015) 140 [1503.08228].

[203] J. Wang, H. Xu, T. An, J. Gu, X. Guo, W. Li et al., *Exploring the Cosmic Reionization Epoch in Frequency Space: An Improved Approach to Remove the Foreground in 21 cm Tomography*, Astrophys. J. **763** (2013) 90 [1211.6450].

[204] R. Mondal, S. Bharadwaj, I.T. Iliev, K.K. Datta, S. Majumdar, A.K. Shaw et al., *A method to determine the evolution history of the mean neutral Hydrogen fraction*, Monthly Notices of the Royal Astronomical Society **483** (2019) L109 [1810.06273].

[205] R. Mondal, A.K. Shaw, I.T. Iliev, S. Bharadwaj, K.K. Datta, S. Majumdar et al., *Predictions for measuring the 21-cm multifrequency angular power spectrum using SKA-Low*, Mon. Not. Roy. Astron. Soc. **494** (2020) 4043 [1910.05196].

[206] T.R. Choudhury, M.G. Haehnelt and J. Regan, *Inside-out or outside-in: the topology of reionization in the photon-starved regime suggested by Lyα forest data*, *Mon. Not. Roy. Astron. Soc.* **394** (2009) 960 [0806.1524].

[207] B. Greig and A. Mesinger, *21CMMC: an MCMC analysis tool enabling astrophysical parameter studies of the cosmic 21 cm signal*, Mon. Not. Roy. Astron. Soc. **449** (2015) 4246 [1501.06576].

[208] B. Greig, A. Mesinger and L.V.E. Koopmans, *Reionisation & Cosmic Dawn Astrophysics from the Square Kilometre Array: Impact of Observing Strategies*, *arXiv e-prints* (2019) arXiv:1906.07910 [1906.07910].

[209] R. Ghara, S.K. Giri, G. Mellema, B. Ciardi, S. Zaroubi, I.T. Iliev et al., *Constraining the intergalactic medium at $z \approx 9.1$ using LOFAR Epoch of Reionization observations*, Mon. Not. Roy. Astron. Soc. (2020) [2002.07195].

[210] R. Mondal, A. Fialkov, C. Fling, I.T. Iliev, R. Barkana, B. Ciardi et al., *Tight Constraints on the Excess Radio Background at* $z = 9.1$ *from LOFAR*, *arXiv e-prints* (2020) arXiv:2004.00678 [2004.00678].

[211] S.K. Giri, A. D'Aloisio, G. Mellema, E. Komatsu, R. Ghara and S. Majumdar, *Position-dependent power spectra of the 21-cm signal from the epoch of reionization*, *JCAP* **2019** (2019) 058 [1811.09633].

[212] C.M. Trott, C.A. Watkinson, C.H. Jordan, S. Yoshiura, S. Majumdar, N. Barry et al., *Gridded and direct Epoch of Reionisation bispectrum estimates using the Murchison Widefield Array*, *Publ. Astron. Soc. Austral.* **36** (2019) e023 [1905.07161].

[213] S. Yoshiura, H. Shimabukuro, K. Takahashi, R. Momose, H. Nakanishi and H. Imai, *Sensitivity for 21 cm bispectrum from Epoch of Reionization*, *Mon. Not. Roy. Astron. Soc.* **451** (2015) 266 [1412.5279].

[214] H. Shimabukuro, S. Yoshiura, K. Takahashi, S. Yokoyama and K. Ichiki, *21 cm line bispectrum as a method to probe cosmic dawn and epoch of reionization*, *Mon. Not. Roy. Astron. Soc.* **458** (2016) 3003 [1507.01335].

[215] A. Saxena, S. Majumdar, M. Kamran and M. Viel, *Impact of dark matter models on the EoR 21-cm signal bispectrum*, *Mon. Not. Roy. Astron. Soc.* **497** (2020) 2941 [2004.04808].

[216] C.A. Watkinson, C.M. Trott and I. Hothi, *The bispectrum and 21cm foregrounds during the Epoch of Reionization*, *arXiv e-prints* (2020) arXiv:2002.05992 [2002.05992].

[217] A. Mazumdar, S. Bharadwaj and D. Sarkar, *Quantifying the redshift space distortion of the bispectrum II: induced non-Gaussianity at second-order perturbation*, *Mon. Not. Roy. Astron. Soc.* **498** (2020) 3975 [2005.07066].

[218] A. Songaila and L.L. Cowie, *The Evolution of Lyman Limit Absorption Systems to Redshift Six*, *Astrophys. J.* **721** (2010) 1448 [1007.3262].

[219] E.J. Groth and P.J.E. Peebles, *Statistical analysis of catalogs of extragalactic objects. VII. Two- and three-point correlation functions for the high-resolution Shane-Wirtanen catalog of galaxies.*, *Astrophys. J.* **217** (1977) 385.

[220] J.N. Fry and P.J.E. Peebles, *Statistical analysis of catalogs of extragalactic objects. IX. The four-point galaxy correlation function.*, *Astrophys. J.* **221** (1978) 19.

[221] D. Brillinger and M. Rosenblatt, *Asymptotic theory of estimates of kth-order spectra*, *Proceedings of the National Academy of Sciences of the United States of America* **57** (1967) 206.

[222] A. Lidz, O. Zahn, M. McQuinn, M. Zaldarriaga, S. Dutta and L. Hernquist, *Higher Order Contributions to the 21 cm Power Spectrum*, *Astrophys. J.* **659** (2007) 865 [arXiv:astro-ph/0610054].

[223] R. Ghara, T.R. Choudhury and K.K. Datta, *21-cm signature of the first sources in the Universe: prospects of detection with SKA*, *Mon. Not. Roy. Astron. Soc.* **460** (2016) 827 [1511.07448].

[224] I.T. Iliev, G. Mellema, U.-L. Pen, J.R. Bond and P.R. Shapiro, *Current models of the observable consequences of cosmic reionization and their detectability*, *Mon. Not. Roy. Astron. Soc.* **384** (2008) 863 [arXiv:astro-ph/0702099].

[225] K.K. Datta, H. Jensen, S. Majumdar, G. Mellema, I.T. Iliev, Y. Mao et al., *Light cone effect on the reionization 21-cm signal - II. Evolution, anisotropies and observational implications*, *Mon. Not. Roy. Astron. Soc.* **442** (2014) 1491 [1402.0508].

[226] H.E. Ross, K.L. Dixon, R. Ghara, I.T. Iliev and G. Mellema, *Evaluating the QSO contribution to the 21-cm signal from the Cosmic Dawn*, *Mon. Not. Roy. Astron. Soc.* **487** (2019) 1101 [1808.03287].

[227] H.E. Ross, S.K. Giri, G. Mellema, K.L. Dixon, R. Ghara and I.T. Iliev, *Redshift-space distortions in simulations of the 21-cm signal from the cosmic dawn*, *Mon. Not. Roy. Astron. Soc.* **506** (2021) 3717 [2011.03558].

[228] G. Hinshaw, D. Larson, E. Komatsu, D.N. Spergel, C.L. Bennett, J. Dunkley et al., *Nine-year Wilkinson Microwave Anisotropy Probe (WMAP) Observations: Cosmological Parameter Results*, *Astrophys. J. Suppl.* **208** (2013) 19 [1212.5226].

[229] R.M. Thomas and S. Zaroubi, *Time-evolution of ionization and heating around first stars and miniqsos*, *Mon. Not. Roy. Astron. Soc.* **384** (2008) 1080 [0709.1657].

[230] R.M. Thomas and S. Zaroubi, *On the spin-temperature evolution during the epoch of reionization*, *Mon. Not. Roy. Astron. Soc.* **410** (2011) 1377 [1009.5441].

[231] R. Ghara, S.K. Giri, G. Mellema, B. Ciardi, S. Zaroubi, I.T. Iliev et al., *Constraining the intergalactic medium at $z \approx 9.1$ using LOFAR Epoch of*

Reionization observations, Mon. Not. Roy. Astron. Soc. **493** (2020) 4728 [2002.07195].

[232] P.S. Behroozi and J. Silk, *A Simple Technique for Predicting High-redshift Galaxy Evolution*, Astrophys. J. **799** (2015) 32 [1404.5299].

[233] G. Sun and S.R. Furlanetto, *Constraints on the star formation efficiency of galaxies during the epoch of reionization*, Mon. Not. Roy. Astron. Soc. **460** (2016) 417 [1512.06219].

[234] M. Fioc and B. Rocca-Volmerange, *PEGASE: a UV to NIR spectral evolution model of galaxies. Application to the calibration of bright galaxy counts.*, Astron. Astrophys. **326** (1997) 950 [astro-ph/9707017].

[235] C. Vignali, W.N. Brandt and D.P. Schneider, *X-Ray Emission from Radio-Quiet Quasars in the Sloan Digital Sky Survey Early Data Release: The α_{ox} Dependence upon Ultraviolet Luminosity*, Astron. J. **125** (2003) 433 [astro-ph/0211125].

[236] S. Gallerani, L. Zappacosta, M.C. Orofino, E. Piconcelli, C. Vignali, A. Ferrara et al., *X-ray spectroscopy of the $z = 6.4$ quasar SDSS J1148+5251*, Mon. Not. Roy. Astron. Soc. **467** (2017) 3590 [1702.07349].

[237] S. Martocchia, E. Piconcelli, L. Zappacosta, F. Duras, G. Vietri, C. Vignali et al., *The WISSH quasars project. III. X-ray properties of hyper-luminous quasars*, Astron. Astrophys. **608** (2017) A51 [1708.00452].

[238] S. Mineo, M. Gilfanov and R. Sunyaev, *X-ray emission from star-forming galaxies - I. High-mass X-ray binaries*, Mon. Not. Roy. Astron. Soc. **419** (2012) 2095 [1105.4610].

[239] N. Islam, R. Ghara, B. Paul, T.R. Choudhury and B.B. Nath, *Cosmological implications of the composite spectra of galactic X-ray binaries constructed using MAXI data*, Mon. Not. Roy. Astron. Soc. **487** (2019) 2785 [1905.10386].

[240] S.A. Wouthuysen, *On the excitation mechanism of the 21-cm (radio-frequency) interstellar hydrogen emission line.*, Astron. J. **57** (1952) 31.

[241] C.M. Hirata, *Wouthuysen-Field coupling strength and application to high-redshift 21-cm radiation*, Mon. Not. Roy. Astron. Soc. **367** (2006) 259 [astro-ph/0507102].

[242] R. Ghara and G. Mellema, *Impact of Ly α heating on the global 21-cm signal from the Cosmic Dawn*, Mon. Not. Roy. Astron. Soc. **492** (2020) 634 [1904.09999].

[243] S. Mittal and G. Kulkarni, *Ly α coupling and heating at cosmic dawn*, *Mon. Not. Roy. Astron. Soc.* **503** (2021) 4264 [2009.10746].

[244] J. Mirocha, H. Lamarre and A. Liu, *Systematic uncertainties in models of the cosmic dawn*, *arXiv e-prints* (2020) arXiv:2012.06588 [2012.06588].

[245] R. Ghara, K.K. Datta and T.R. Choudhury, *21 cm signal from cosmic dawn - II. Imprints of the light-cone effects*, *Mon. Not. Roy. Astron. Soc.* **453** (2015) 3143 [1504.05601].

[246] Q.-B. Ma, B. Ciardi, M.B. Eide, P. Busch, Y. Mao and Q.-J. Zhi, *Investigating X-Ray Sources during the Epoch of Reionization with the 21 cm Signal*, *Astrophys. J.* **912** (2021) 143 [2103.09394].

[247] S. Gallerani, L. Zappacosta and et al., *X-ray spectroscopy of the $z = 6.4$ quasar SDSS J1148+5251*, *Mon. Not. Roy. Astron. Soc.* **467** (2017) 3590.

[248] S. Martocchia, E. Piconcelli and et al., *The WISSH quasars project. III. X-ray properties of hyper-luminous quasars*, *Astron. Astrophys.* **608** (2017) A51.

[249] P.S. Behroozi and J. Silk, *A SIMPLE TECHNIQUE FOR PREDICTING HIGH-REDSHIFT GALAXY EVOLUTION*, *The Astrophysical Journal* **799** (2015) 32.

[250] G. Sun and S.R. Furlanetto, *Constraints on the star formation efficiency of galaxies during the epoch of reionization*, *Monthly Notices of the Royal Astronomical Society* **460** (2016) 417.

[251] C.M. Trott, B. Pindor, P. Procopio, R.B. Wayth, D.A. Mitchell, B. McKinley et al., *CHIPS: The Cosmological H I Power Spectrum Estimator*, *Astrophys. J.* **818** (2016) 139 [1601.02073].

[252] I. Hothi, E. Chapman, J.R. Pritchard, F.G. Mertens, L.V.E. Koopmans, B. Ciardi et al., *Comparing foreground removal techniques for recovery of the LOFAR-EoR 21 cm power spectrum*, *Mon. Not. Roy. Astron. Soc.* **500** (2021) 2264 [2011.01284].

[253] M. Mevius, F. Mertens, L.V.E. Koopmans, A.R. Offringa, S. Yatawatta, M.A. Brentjens et al., *A numerical study of 21-cm signal suppression and noise increase in direction-dependent calibration of LOFAR data*, *Mon. Not. Roy. Astron. Soc.* **509** (2022) 3693 [2111.02537].

[254] H. Gan, L.V. E Koopmans, F.G. Mertens, M. Mevius, A.R. Offringa, B. Ciardi et al., *Statistical analysis of the causes of excess variance in the 21 cm signal power spectra obtained with the Low-Frequency Array*, *arXiv e-prints* (2022) arXiv:2203.02345 [2203.02345].

[255] H.E. Ross, K.L. Dixon, R. Ghara, I.T. Iliev and G. Mellema, *Evaluating the QSO contribution to the 21-cm signal from the Cosmic Dawn*, *Mon. Not. Roy. Astron. Soc.* **487** (2019) 1101 [1808.03287].

[256] R. Mondal, A. Fialkov, C. Fling, I.T. Iliev, R. Barkana, B. Ciardi et al., *Tight constraints on the excess radio background at $z = 9.1$ from LOFAR*, *Mon. Not. Roy. Astron. Soc.* **498** (2020) 4178 [2004.00678].

[257] R. Ghara, S.K. Giri, B. Ciardi, G. Mellema and S. Zaroubi, *Constraining the state of the intergalactic medium during the Epoch of Reionization using MWA 21-cm signal observations*, *Mon. Not. Roy. Astron. Soc.* **503** (2021) 4551 [2103.07483].

[258] R. Ghara, G. Mellema and S. Zaroubi, *Astrophysical information from the Rayleigh-Jeans Tail of the CMB*, *JCAP* **2022** (2022) 055 [2108.13593].

[259] R. Ghara, K.K. Datta and T.R. Choudhury, *21 cm signal from cosmic dawn - II. Imprints of the light-cone effects*, *Mon. Not. Roy. Astron. Soc.* **453** (2015) 3143 [1504.05601].

[260] S.K. Giri, A. D'Aloisio, G. Mellema, E. Komatsu, R. Ghara and S. Majumdar, *Position-dependent power spectra of the 21-cm signal from the epoch of reionization*, *JCAP* **2019** (2019) 058 [1811.09633].

[261] R. Barkana and A. Loeb, *Unusually large fluctuations in the statistics of galaxy formation at high redshift*, *The Astrophysical Journal* **609** (2004) 474.

[262] A.K. Shaw, S. Bharadwaj, D. Sarkar, A. Mazumdar, S. Singh and S. Majumdar, *A fast estimator for quantifying the shape dependence of the 3D bispectrum*, *JCAP* **2021** (2021) 024 [2107.14564].

[263] J.D. Bowman, A.E.E. Rogers, R.A. Monsalve, T.J. Mozdzen and N. Mahesh, *An absorption profile centred at 78 megahertz in the sky-averaged spectrum*, *Nature* **555** (2018) 67 [1810.05912].